University of Nottingham
UK | CHINA | MALAYSIA

Classical and quantum fluid interfaces as simulators for gravity and the early Universe

Vitor Barroso Silveira

Supervised by Silke Weinfurtner

School of Mathematical Sciences
University of Nottingham

Thesis submitted to the University of Nottingham
for the degree of Doctor of Philosophy

September 2023

To my parents, Solange and Daniel.

Abstract

For the past few decades, gravity and early Universe analogue simulators have been used to experimentally replicate elusive processes and predictions of Quantum Field Theory (QFT) occurring on classical backgrounds of General Relativity using accessible physical systems, such as ultracold atoms, optical devices, and fluid surfaces. The analogies are typically devised by mapping the dynamics of small excitations on the analogue systems to the linear evolution of quantum fields on curved spacetimes. However, the territory of more intricate, interacting QFT problems remains largely unexplored by analogue simulations. This thesis extends the premises of gravity simulators on classical and quantum fluid interfaces to include non-linear processes and discusses suitable measurement schemes required for their development and experimental implementation.

We derive an effective field-theoretical description of the interfacial dynamics between two classical or quantum fluids. Our formalism can be used to systematically include non-linear terms in an effective Lagrangian for the interfacial height disturbances. This approach allows us to devise simulations for gravitational scenarios where scattering and decays are relevant, such as in the early Universe, and for fundamental phenomena of QFT in curved spacetimes (QFTCS). We then present a proof-of-principle non-linear Effective Field Theory (EFT) simulator in a classical liquid-liquid interface built to investigate the dynamical features of post-inflationary preheating. In this system, we show that suitable experimental control and repetition with a precise and accurate interfacial reconstruction enables the characterisation of the EFT through statistical measures, as previously realised in quantum simulators using Bose gases.

In our gravity simulators, the core physical observable is the interfacial height and measuring it is the utmost requirement for conducting experiments. Accordingly, we detail existing detection schemes and introduce a novel method based on Digital Holography. The latter is designed to reconstruct changes in the spatial profile of the interfacial height with unprecedented resolution and potential for applications at both room and low-temperature setups. Expanding on these measurement schemes, we generalise the particle detector concept in QFTCS to an analogue simulator. We specialise in a localised laser probe and consider its effective interaction with the analogue height field in thin films of superfluid helium-4. With this setup, we propose an experiment to extract the observer dependence in the response of a detector probing a thermal analogue field, in line with the circular-motion, finite-temperature Unruh effect.

Our experimental results show that liquid-liquid and liquid-gas interfaces, classical or not, hold great promise for analogue simulations tackling non-equilibrium gravitational scenarios and emulating fundamental aspects of QFTCS. Our work builds on the solid foundation laid by previous analogue black-hole and early Universe simulators to offer the stepping stones for a new generation of experiments using classical and quantum fluids that we anticipate will dive deeper into fundamental physics questions.

Acknowledgements

I would like to thank my supervisor, Silke, for your support and mentorship over the past four years, especially during the challenging times of the COVID-19 pandemic. Your scientific vision and outlook are inspiring, and I hope to continue learning from them. I sincerely appreciate your enduring efforts in building a diverse and inclusive research environment and making science more accessible. I am grateful for being part of your team in the Gravity Laboratory, which quickly became my academic home.

To current and former members of the Gravity Lab and its community of collaborators and partners, I extend my gratitude for all the feedback, discussions, and help during my PhD. I would like to especially thank Sebastian for always making time for helpful and riveting discussions. I also greatly appreciate the scientific guidance and assistance from our colleagues Tasos, Richard, Tony and Jorma from the Schools of Physics and Astronomy and Mathematical Sciences. The experiments presented in this thesis would not have happened without the incredible work of the technical team of the Physics Department, primarily through Terry, Tommy, Ian, Andy, Sionnach and Nick. I am incredibly thankful for your support.

The University of Nottingham has given me wonderful friends, some of whom I had the pleasure of working closely with during my PhD. Zack, thank you for making the long and intense hours in the lab much more fun amidst masks and loads of hand sanitiser; it was such a delight to learn from you and find support in your kindness throughout the PhD. August, your curiosity and ingenuity are incredibly inspiring, and the time spent working with you was truly fantastic. Cameron and Patrik, our time together was shorter, but I enjoyed every second of it; without your valuable and thorough comments, this thesis would not have come to fruition.

To the community of local and international Nottingham residents who received me so generously and warmly, I thank you for making my time here much more enjoyable and gifting me beautiful memories. My dear friends, mainly in Brazil but also scattered across the globe, your care and affection constantly reminded me of home and often gave me the incentive to keep moving forward, even from a distance. Whether we met in Nottingham or not, you know who you are and how special you've been.

À minha família, tenho somente a agradecer pelo apoio incondicional, o encorajamento incessante e os conselhos mais sábios, nos momentos mais necessários. Pai e mãe, posso somente tentar expressar o quão grato sou pelo perene esforço e cuidado que colocaram em me educar, e a dedicação em ajudar-me a conquistar o que tenho e tornar-me o que sou hoje.

A mi marido, Nacho, has sido el regalo más grande que Nottingham me ha dado. Eres mi garantia de constancia en los momentos más dificiles, y mi apoyo más presente, sin ti no habría completado esta etapa. Muchas gracias por tu amor, cuidado y cariño. No encuentro la forma de agradecerte y retribuir todo lo que me regalas a cada día.

A todos os que investiram seu tempo ou contribuíram financeiramente para que eu viesse a Nottingham, me resta somente agradecer imensamente e guaranti-los que o dever foi cumprido. Muito Obrigado!

List of Publications

[1] Barroso, V. S., Bunney, C. R. D., and Weinfurtner, S. Non-linear effective field theory simulators in two-fluid interfaces. *Journal of Physics: Conference Series*, 2531(1):012003, June 2023. [Chapter 2]

[2] Barroso, V. S., Geelmuyden, A., Fifer, Z., Erne, S., Avgoustidis, A., Hill, R. J. A., and Weinfurtner, S. Primary thermalisation mechanism of Early Universe observed from Faraday-wave scattering on liquid-liquid interfaces. arXiv e-prints, art. arXiv:2207.02199, July 2022. [Chapter 3]

[3] Barroso, V. S., Geelmuyden, A., Ajithkumar, S. C., Kent, A. J., and Weinfurtner, S. Multiplexed digital holography for fluid surface profilometry. *Applied Optics*, 62(27):7175–7184, September 2023 [Chapter 4]

[4] Bunney, C. R. D., Biermann, S., Barroso, V. S., Geelmuyden, A., Gooding, C., Ithier, G., Rojas, X., Louko, J., and Weinfurtner, S. Third sound detectors in accelerated motion. arXiv e-prints, art. arXiv:2302.12023, February 2023. [Chapter 5]

List of Figures

List of Abbreviations

BEC Bose-Einstein condensate . . . . . , 2, 3, 6, 45, 64, 75

BH black hole . . . . . , 13

DFT Discrete Fourier Transform . . . . . , 60, 61

DH Digital Holography . . . . . , 10, 79, 80, 87, 88, 101, 128, 130

EFT Effective Field Theory . . . . , 1, 4–10, 13, 16, 26, 28, 31–33, 41, 43–45, 52, 62, 75–77, 79, 103–105, 110, 127–130

FCD Fast-Checkerboard Demodulation . . . . . , 81, 88

FFT Fast Fourier Transform . . . . . , 60

FIR finite impulse response . . . . . , 83

FLRW Friedmann – Lemaître – Robertson – Walker . . . . . , 27–29

FTP Fourier Transform Profilometry . . . . . , 10, 79–82, 84, 85, 93, 101, 102, 128

GR General Relativity . . . . . , 1, 5, 7

KG Klein-Gordon . . . . . , 8, 25, 28, 31, 109, 110, 115

PCA Principal Component Analysis . . . . . , 93, 94, 97–101

QCD Quantum Chromodynamics . . . . . , 4

QFT Quantum Field Theory . . . . . , 1, 5–8, 24, 25, 31, 44, 61, 63, 110, 115, 129

QFTCS Quantum Field Theory in Curved Spacetimes , 1, 2, 4, 8–10, 103, 127, 129

RK Runge-Kutta . . . . . , 141, 142

RMS root mean square . . . . . , 96, 98

SFD spatial-frequency domain . . . . . , 80, 83, 86, 90, 91, 95, 97, 99, 100

SSI synthetic Schlieren imaging . . . . . , 81

THD Total Harmonic Distortion . . . . . , 55, 75

List of Symbols

Physical Constants

$\hbar$	Reduced Planck constant	$1.054\,571\,82 \times 10^{-34}\,\mathrm{J\,s}$
h	Planck constant	$6.626\,070\,15 \times 10^{-34}\,\mathrm{J\,s}$
k_B	Boltzmann constant	$1.380\,649 \times 10^{-23}\,\mathrm{J\,K^{-1}}$
ϵ_0	Permittivity of free space	$8.854\,187\,812\,8 \times 10^{-12}\,\mathrm{F\,m^{-1}}$
μ_0	Permeability of free space	$1.256\,637\,062\,1 \times 10^{-6}\,\mathrm{N\,A^{-2}}$
c	Speed of light in vacuum	$2.997\,924\,58 \times 10^{8}\,\mathrm{m\,s^{-1}}$
G	Gravitational constant	$6.674\,30 \times 10^{-11}\,\mathrm{N\,kg^{-2}\,m^{2}}$
g_0	Acceleration of gravity on Earth	$9.806\,65\,\mathrm{m\,s^{-2}}$

Other Symbols

Functions and Operators

Contents

Chapter 1

Introduction

At the interface between General Relativity (GR) and Quantum Field Theory (QFT), two of the most significant physical theories of the 20th century, lies Quantum Field Theory in Curved Spacetimes (QFTCS), which, in the words of Birrell and Davies [5], may be regarded as *"an approximation to an as yet inaccessible theory of quantum gravity."* In QFTCS, quantum fields propagate on a classical spacetime background that is a solution of Einstein's field equations. Regardless of its intermediate-theory status, QFTCS presents us with a variety of intriguing and mesmerising results, such as Hawking radiation and the Unruh effect, pointing towards the complexity of the interplay between QFT and GR. These physical processes are expected to occur in scenarios where direct experimentation is unfeasible, limiting empirical verification to purely observational evidence, if any. Accordingly, despite recent experimental proposals, e.g. [6], the predictions of the field remain largely untested and empirically unverified.

In an attempt to shed light on this issue and bring insights to the field, analogue gravity simulators [7, 8] appeared as candidates to mimic these processes emerging in QFTCS using accessible physical systems. These simulators for gravity and the early Universe are nowadays valuable tools for investigating elusive phenomena in possibly unreachable scenarios [9]. In general, the analogies are created by describing small excitations on the simulator through an Effective Field Theory (EFT), which, in turn, can be mapped to the dynamics of quantum fields propagating on flat or curved spacetimes of GR. Building on the similarities and equivalences between the simulator and the target system, various spacetime geometries can be engineered and analogue experiments devised with them.

Since the beginning of analogue gravity, with the publication of Unruh's seminal article *"Experimental Black Hole Evaporation?"* [10] in 1981, the field experienced a remarkable surge in progress. Unruh's proposal of acoustic hydrodynamical analogues of black hole horizons and their evaporation [11, 12] inspired further development in many directions. Four decades later, the field has grown considerably and produced

significant results that nowadays resonate amongst several areas in Physics [7, 9]. The role of analogue simulators as testing grounds for field theories has been solidified by experimental verification in various domains, such as ultra-cold atoms, fluids, and optical systems. Analogue gravity has come a long way from its beginnings and now encompasses increasingly complex physical systems. We now present a brief overview of its history, in line with the timeline definitions of Field [13], and background literature discussions of Jacquet et al. [9] and Almeida and Jacquet [14].

1.1 Analogue gravity: a historical prelude

Initially, Unruh established in [10] an analogy between two seemingly distant theoretical frameworks, namely fluid dynamics and QFTCS. In the former, the author considered linearised acoustic excitations on a background transonic fluid flow, i.e., a flow with subsonic and supersonic regions [15]. Unruh then showed that the dynamical equations determining the evolution of sound waves in this flow type correspond to those of massless scalar fields propagating on a black hole spacetime geometry, where the speed of light is replaced by the speed of sound in the fluid. In other words, the transition region between subsonic and supersonic flows would emulate a black hole horizon for sound waves, i.e., a dumb hole. Unruh's work set the tone for the subsequent *theory era* of analogue gravity [13], which lasted until 2008 when the first experimental implementations followed.

During this period of intensive theoretical efforts, a community with diverse background expertise developed a series of possible analogue setups and speculations on their experimental viability. Notably, the field welcomed major contributions in the early 2000s. Schützhold and Unruh [16] were the first to propose using surface-wave dynamics on fluid flows as the framework for emulating various analogue black-hole geometries. Around the same time, Novello et al. [17] assembled a collection of studies on analogue simulators for gravity and cosmology in condensed-matter systems, including the challenges and particularities of implementing them in Bose-Einstein condensates (BECs), superfluids and optical setups. Soon after [17], Volovik and Press [18] discoursed about the creation of entire analogue universes using a quantum liquid, superfluid ^{3}He.

Throughout its *theory era* (1981-2008, [13]), analogue gravity spontaneously turned its focus to simulating Hawking radiation and finding its footprint on analogue horizons [9]. In this context, Almeida and Jacquet [14] remark that a more general notion of Hawking radiation, denoting a class of scattering Hawking-like processes around effective horizons, were collectively referred to by the umbrella-term *Hawking effect*. This expectation of observing the Hawking effect and identifying its essential features [19] culminated with the first experimental implementations of analogue gravity

in 2008. These inaugurate what Field [13] calls the *experimental era*, which primarily concentrated on detecting the Hawking effect in (1+1)-dimensional analogue black holes, with few exceptions [20–22].

Early in 2008, Philbin et al. [23] reported the first analogue horizon using pulsed light in an optical fibre. A few months later, Rousseaux et al. [24] showed that surface waves on a transcritical open-channel water flow could also emulate an effective one-dimensional horizon. Later, in a similar setup, Weinfurtner et al. [25] registered in 2011 the observation of the stimulated Hawking spectrum. The following decade brought up several contributions to the field, again focused on consolidating the theoretical predictions and generalising the conditions for the Hawking effect around arbitrary horizons. These included experiments not only in new systems, such as bulk crystals [26], BECs [27, 28] and polariton superfluids [29], but also novel key results in open-channel flows [30] and optical fibres [31–33].

This *experimental era* of analogue gravity pushed it to become an empirically driven field, with steady theoretical support along the way, e.g., see [14] and references therein. While analogue experiments on the Hawking effect continue to this day [34–39], 2017 marked a turning point in the field. In that year, Torres et al. [40] presented the first analogue rotating black hole in a hydrodynamical system, registering the amplification of surface waves upon scattering through a "draining bathtub" vortex flow. Their results agree with the picture of *superradiance* around rotating black holes, as proposed by Zel'Dovich [41, 42] in his semi-classical generalisation of the Penrose process [43]. Later on, Braidotti et al. [44] observed the phenomenon by creating a vortex flow on a fluid of light.

By adding an extra spatial dimension to the analogy, Torres et al. [40] opened a new avenue for the investigation of (2+1)-dimensional effective geometries, as seen in the experiments that followed [44–47]. However, Field [13] notes that the year 2017 marked a shift not only in the experimental trends but also in the interests of the involved community, which perhaps started using these analogue simulators *"not to provide confirmation for the existence of an astrophysical phenomenon like Hawking radiation, but to detect more generalised phenomena and/or to explore the behaviour of the analogue systems."* In reference to the transition and emergence of these new research goals, Almeida and Jacquet [14] label this period as the *autonomous phase* of analogue gravity.

Over the past few years, this *autonomous phase* has been recording steady progress in the study mentioned above of (1+1) and (2+1)-dimensional analogue black holes. However, a new line of investigation centred around simulating early Universe scenarios has gained momentum. Many experiments appeared in the context of condensed matter, primarily using ultracold systems. Pioneered by the early work of Hung et al. [22], in 2013, Eckel et al. [48] re-ignited this research branch in 2018, followed by

several others [49–53]. This consistent branching-out of the field over the past two decades speaks for its versatility and potential in exploring as yet uncharted territories in the physics of the simulators and the target astrophysical systems.

Despite the philosophical controversy surrounding the limitations and validity of the results in the field, see e.g. [13, 14, 54–56], it is now clear that the agenda of the research programme has extrapolated its original purpose of finding confirmation for astrophysical phenomena. Instead, Almeida and Jacquet [14] argue that: *"It may also be that analogue gravity will be proved useful to discover new field theoretic effects, although only time will settle the matter. These new trends in the field have grown in strength at different paces as theoretical work is becoming more and more driven by experiments. It inspires a reassessment of the role and application of analogue gravity in quantum field theory research."*

Analogue gravity no longer purely concerns a *pursuit of analogies* with QFTCS around black hole geometries. Instead, it currently takes a multi-faceted and interdisciplinary pace, in effect *simulating* general aspects of target systems with possible astrophysical origins. Accordingly, in this thesis, we shall adopt a slight change in nomenclature, as put forward by Weinfurtner [57], referring to the systems in analogue gravity as *gravity or early Universe simulators*. Furthermore, we argue that these systems are *EFT simulators*, as, in practice, they can be used for the open-ended exploration of whole sets of field theories that may or may not have direct astrophysical counterparts. We end this discussion by stressing that our historical recollection of analogue gravity is certainly not exhaustive, and we refer the interested reader to [7–9, 13, 14] for in-depth presentations.

1.2 Effective Field Theory simulators

In physics, it is common to encounter situations where a comprehensive theoretical framework is not yet available to explain a phenomenon. Effective Field Theories (EFTs) [58] have become an invaluable tool in such scenarios, offering a practical approach to understanding physical systems at different scales while more fundamental theories develop. EFTs provide a systematic method for modelling interactions and phenomena that occur at specific energy or distance scales without requiring a complete understanding of the underlying microscopic dynamics. This adaptable framework simplifies calculations and allows accurate predictions and insights into experimental outcomes. Historical examples [59], such as Fermi's theory of weak interactions and the chiral perturbation theory in Quantum Chromodynamics (QCD), demonstrate the effectiveness of EFTs in successfully describing and predicting experimental results before more encompassing theories were established. Although the application domain of EFTs is usually that of quantum theories, classical physics may also benefit

from its techniques. Some notable examples include the non-relativistic approximation of GR [59] and the effective relativistic description of hydrodynamics [60, 61].

In the context of this thesis, we borrow the terminology and refer to the emergent field theories in accessible physical systems as EFTs. In analogue simulators, they result from suitable reductions and approximations of the dimensions and degrees of freedom of an underlying theory. When thinking of mathematical equivalences, e.g. [10, 16], they must further recover an effective relativistic field theory embedded in a suitable spacetime geometry, which may have astrophysical relevance [7, 17, 18]. Conversely, the EFT may describe the generalised dynamics of a physical phenomenon, for instance, extrapolating mathematical analogies to include dispersive and dissipative aspects [62–64]. Since EFTs result from the coarse-graining of a possibly unknown microscopic theory, the outcomes of the effective description are independent of the underlying properties of the system. Hence, they may present themselves as universal in a set of compatible physical settings [58, 65]. Accordingly, this effective approach becomes a powerful tool for investigating phenomena or dynamical features appearing across different systems whose theoretical frameworks are impractical or overly intricate for calculating emerging effects.

These fundamental aspects of EFTs played a central role in developing quantum simulators in condensed matter systems [66]. In parallel with the early experimental age of analogue gravity, the idea of realising such quantum simulations became a tangible possibility, as reviewed by Bloch et al. [67]. Similarly to gravity analogues, ultracold-atom systems can be used to devise effective free-particle or interacting Hamiltonians that simulate the many-body dynamics of less experimentally viable quantum systems. Indeed, Schweigler et al. [68] showed that the statistical machinery of EFTs, particularly through correlation functions of order higher than two, could be used to experimentally characterise the dynamics and interactions of the collective degrees of freedom in a one-dimensional condensate. Their approach is capable of informing the essential features of the system while avoiding the intricate and, sometimes, impractical task of completely determining complex many-body states. Zache et al. [69] further display a systematic procedure for this experimental characterisation via equal-time correlations of interacting EFTs arising in quantum many-body systems. As expected from an effective framework, the authors argue that the microscopic details of the system will not impact the quantum simulations of the emerging QFT.

An empirically driven, field-theoretical approach to quantum many-body systems offers the possibility of simulating problems that cannot be calculated with current theoretical and computational techniques [69]. Following this argument, various experiments using ultracold-atom systems have been tackling poorly understood and challenging non-equilibrium processes through quantum simulations. Some remarkable examples using out-of-equilibrium Bose gases are noteworthy, as they include the

observation of universal self-similar scaling [70–73], akin to turbulence cascades, and the extraction of the irreducible two- and four-point vertex correlators of a quantum effective action in strongly interacting far-from-equilibrium samples [74]. The authors in [70, 71, 73] further note that these processes are also relevant in early Universe scenarios. Hence, the programme of quantum simulators could be extended to tackle these settings, intersecting with the domain of analogue gravity simulators in this way [57].

The aforementioned success of quantum simulators in systematically approaching non-equilibrium physics raises the question: Can analogue simulators be used for investigating the dynamical effects of out-of-equilibrium and interacting QFTs in astrophysical and cosmological settings? Weinfurtner [57] ponders that recent early-universe simulators in ultracold-atom systems [51, 53] indicate a positive answer to this question, and argues that a new goal for gravity simulators as a whole would be *"to venture beyond what we can calculate."* The latter statement refers to problems that cannot be exactly solved with available theoretical frameworks or numerically simulated on a computer. One notable example of such a problem in cosmology is that of false vacuum decay [75], a conceptual model for the origin of our Universe before the Big Bang through phase transitions of a relativistic field in a metastable state. Experimental proposals of analogue quantum simulators for this process have recently appeared [76, 77] exploiting interacting EFTs emerging in BECs. As contemplated by Weinfurtner [57], these experiments - if feasible - offer a prospect of valuable phenomenological input to narrow down the relevant dynamical features and further improve the model in cosmology.

When developing both quantum simulators in condensed matter and gravity simulators in various systems, we identify some common and crucial features and advantages. Firstly, it is essential to understand the limitations of the emergent EFT. To achieve this, we need to create a theoretical framework that captures the dynamics of the target system while recognising the validity of its description. Additionally, we must ensure repeatability and control in the experiments. By maintaining strict control over the experimental parameters, we can guarantee consistency, reproducibility, and the use of the statistical machinery of EFTs. Moreover, we need detection methods that can accurately measure and precisely resolve physical observables. Finally, a tunable parameter space in the experimental setup allows us to explore various regimes of the EFT systematically and simulate gravity and early Universe target scenarios with them.

1.3 A new generation of simulators on fluid interfaces

As presented in our historical prelude, Unruh's original proposal [10] involving acoustic horizons in fluids paved the way for the inception of analogue gravity. However, the experimental implementation of Unruh's concept presented a practical challenge. In many liquids, the speed of sound is typically of the order of hundreds of metres per second [15], rendering the creation and control of acoustic horizons through transonic fluid flows experimentally impractical. Furthermore, detecting bulk excitations within these fast-moving liquids would present significant technical difficulties. Building on these ideas, Schützhold and Unruh [16] introduced a novel approach by considering surface waves on background fluid flows. As previously discussed, this shift in perspective opened the door to analogue black-hole experiments in fluids replicating the Hawking effect, superradiance, and quasi-normal ringdown. These pioneering results highlighted the adaptability of fluid interfaces in simulating various astrophysical scenarios.

In analogue simulators using classical hydrodynamical systems, viscous dissipation may overwhelm the dynamics and hinder the observation of the target phenomenon. Conversely, quantum fluids, such as liquid helium-3 and helium-4, display similar EFT descriptions as their classical counterparts but offer alternative simulation settings with negligible viscosity. Recently, Švančara et al. [78] used superfluid helium-4 to experimentally verify the creation of a macroscopic analogue rotating black hole with quantised vorticity. Their work is yet another example of the broad range of possibilities in using both classical and quantum fluid interfaces as gravity simulators.

A wide range of fluids, each with unique physical and chemical properties, are readily available, presenting a natural opportunity for open-ended empirical exploration of analogue scenarios. Elaborating on this prospect, Fifer et al. [79] propose an early Universe simulator that uses two immiscible, weakly magnetised liquids. They show that the interfacial dynamics could emulate inflationary scenarios when the two-fluid sample is placed in strong magnetic field gradients. The authors suggest using a small and closed sample cell to precisely control the setup and prevent evaporation and contamination of the interface, thereby ensuring consistency and repeatability of the fluid experiment. These features would allow the use of field-theoretical statistical tools to analyse the results and characterise the effective dynamics simulating inflation. However, like other fluid analogues, Fifer et al. [79] primarily focused on mimicking and generalising non-interacting QFTs around the backgrounds of GR under the real conditions of an experiment.

Instead, our work expands on the solid foundation of previous analogue gravity experiments and proposals to develop EFT simulations on fluids for problems and scenarios that, so far, have only been implemented in Bose gases, as previously presented.

We seize the non-linearities inherent in fluid dynamics to devise the first interacting field theory simulators on liquid-liquid and liquid-gas interfaces. These are unique and adaptable platforms for probing the robustness of fundamental phenomena in the presence of non-idealised features, such as dispersion and dissipation. In contrast with ultracold-atom systems, continuous monitoring and measurement of the samples are readily available in fluid experiments, allowing the direct observation of the onset of non-linearities and their subsequent evolution. We use these properties to experimentally simulate post-inflationary dynamical features of the early Universe on a liquid-liquid interface.

The characterisation of the interacting interfacial dynamics in fluid simulators is ultimately limited by the detection methods employed in experiments. We examine this aspect in our work, presenting the current standard schemes and noting that they cannot resolve the initial state of the interface. Under non-equilibrium conditions, the connection between the initial and final states of a system is still not fully understood [80]. Hence, aiming at future experiments that track the entire dynamical evolution of the EFT, we develop a novel detection technique capable of measuring nanometric fluctuations in fluid surfaces. The methods presented here reconstruct an entire spatial region of the interface through snapshots of the sample and are applicable in both room and low-temperature setups.

Despite the useful aspects of our measurement schemes, we require a different type of detection for the prospect of investigating the particle detectors concept in QFTCS. For that, we propose using a localised laser detector, as put forward by Gooding et al. [81], to measure quasi-particle surface excitations (third sound) in thin films of superfluid helium-4, which are analogous to a massless Klein-Gordon (KG) field in Minkowski spacetime. In essence, an effective interaction term arises between the probing (laser) and analogue (interfacial height) fields, allowing a generalised definition of a continuous particle detector. We use this correspondence to examine the difference between the responses of circularly accelerated and inertial detectors as an analogy to the Unruh effect [82]. However, a crucial difference appears in our simulator in comparison with the standard formulation of the Unruh effect: the analogue field is at a thermal state determined by the non-zero temperature of the superfluid helium sample. This deviation required further development of the QFT description supporting the proposal to account for the thermality of the analogue field in helium [83].

In the gravity simulators discussed in this thesis, we show that a solid grasp of the relevant EFT allows one to examine beyond the correspondence with the target scenario to quantify deviations from the idealised phenomenon. In our early Universe experimental simulations, we understand the validity and limitations of the effective description, which we use to study a non-equilibrium, post-inflationary process while considering the inherent dissipative and dispersive properties of the simulator. On the

other hand, the accelerated observer proposal in superfluid helium displays a deviation that leads to an extension of the underlying assumptions of the target process, possibly revealing entirely new features of the Unruh effect. Going hand-in-hand with these theoretical aspects, we argue that the precision and accuracy of extracting the simulated field dynamics are central to the characterisation and further refinement of the emergent EFT. In the following chapters, we will detail the development and prospects of this new generation of simulators in classical and quantum fluid interfaces.

1.4 Outline

This thesis will display the theoretical, experimental and phenomenological development of new kinds of interacting field theory simulators using the emergent dynamics of liquid-liquid and liquid-gas interfaces. Based on the discussion presented above, the chapters are divided as follows.

In Chapter 2, we systematically derive a generalised EFT from the interfacial dynamics between two fluids. Initially, we lay down the properties and assumptions of the underlying simulator, defining our concept of two-fluid systems and the approximations required to effectively operate with them. We then consider setups of fluids in closed sample cells in the absence of background stationary flows. From the equations of motion governing each fluid, we follow the literature in Fluid Dynamics to derive a Lagrangian description of the inviscid interfacial dynamics, allowing for non-linear terms. This formulation defines our EFT for the height disturbances at the two-fluid interface, which we use to examine approximate cases that simulate QFTCS settings, as usually carried out in analogue gravity. Understanding the limitations of our derivation in accounting for realistic and non-idealised aspects of the physical system at hand, we finally discuss their inclusion in the effective description by modifying the EFT and its equations of motion accordingly.

We then move to experimental investigations in Chapter 3, where we detail the creation and implementation of a non-linear EFT simulator for non-equilibrium processes in the early Universe using a biphasic liquid system. Our chosen target is a post-inflationary thermalisation model in cosmology known as preheating. Our discussion starts with an overview of the role of non-equilibrium conditions in the early Universe, motivating our choice of target process. We then apply the theoretical framework derived in Chapter 2 to argue that driving Faraday instabilities on the two-fluid system can emulate dynamical aspects of an interacting field theory. Next, we present the experimental setup, its implementation and the methods used for acquiring and processing data. The results are then discussed and interpreted under the lenses of preheating dynamics, showing that its key aspects are captured by our non-linear EFT simulator. We finally reason that our experiments are a proof-of-principle for the use

of fluid simulators for examining dynamical features of non-equilibrium phenomena in the early Universe.

In Chapter 4, we present detection methods used for measuring the profile of fluid interfaces, which is naturally required for the experimental development of EFTs whose observable is the interfacial height. After a brief summary of existing fluid profilometry methods, we specialise to two cases. We first introduce a widely-known technique referred to as Schlieren Fourier Transform Profilometry (FTP), focusing on the numerical pipeline and its adaptation to the setup presented in Chapter 3. Our discussion then turns to a novel method, which we developed based on Digital Holography (DH) and the digital reconstruction procedure of FTP. We present the experimental setup and the supporting interferometric theory, followed by the new analysis using statistical methods or catered data acquisition. In conclusion, we display experimental results supporting the method.

Chapter 5 extends our EFT simulators into the domain of quantum fluids with an experimental proposal for probing observer dependence between particle detectors. We begin with a short discussion on the target scenario in QFTCS, where inertial and accelerated observers are known to disagree on the particle content of empty space, a phenomenon known as the Unruh effect. We then move to the underlying system: thin films of superfluid helium-4. The linearised dynamics of small surface fluctuations on the film, or third sound, is examined under the scope of the Lagrangian formulation of Chapter 2, revealing an emergent EFT of third-sound quasi-particles, akin to massless scalar fields in Minkowski spacetime. We then introduce a different type of non-linearity to define a quasi-particle detector through an effective interaction between a laser field and the superfluid sample. Finally, we show that moving the detector along a circular trajectory yields an acceleration-dependent signal. We conclude by presenting the proposed experimental setup and estimating the expected outcomes.

1.5 Statement of Originality

This thesis is a result of my own work, done in collaboration with members of the research group and other academic partners, in and out of the University of Nottingham. Below, I disclaim the related publications and contributions to the work in each chapter.

- Chapter 2 is based on [1]. I initially extended the non-linear Lagrangian formalism from the work of Miles [84, 85] to two-fluid interfaces. With other group members, we improved the description and included capillary effects. I adapted the linear damping model in [86] and [87, 88] to the annular geometry.

- Chapter 3 is based on [2], the outcome of lasting efforts of almost ten people, relying on the technical support team of the School of Physics & Astronomy to build the experiment. I actively participated in the experimental implementation of the current design and data acquisition, prepared the biphasic liquid samples, and conducted the digital reconstruction and subsequent analysis.

- Chapter 4 is partially based on [3] and the interface reconstruction scheme employed in the experiment of Chapter 3. The latter is extended and adapted from the work of Wildeman [89]. In the portion related to [3], my contributions were in developing the acquisition and processing pipelines and analysing and interpreting results. August Geelmuyden, Silke Weinfurtner and I disclose as inventors the UK Patent Application Number GB2214343.2, filed by The University of Nottingham and partly related to [3].

- Chapter 5 is based on [4]. This work also results from an extended collaboration. I implemented the numerical calculations and contributed to mapping the QFT and EFT descriptions, the estimates of experimental parameters, and the interpretation of results.

Chapter 2

Effective Field Theories on fluid interfaces

The present chapter contains a systematic description of the analytical methods used for obtaining an emerging Effective Field Theory (EFT) from the underlying interfacial dynamics between two fluids. Initially, a series of simplifying assumptions are made to derive a generalised model for the non-linear, inviscid evolution of interfacial modes. From there, we discuss the possible gravitational and early Universe scenarios where our derived EFT can be used. Finally, we conclude with a discussion on the challenges of modifying the EFT to include more realistic features, such as dissipation and boundary effects, which are relevant to the experimental setups considered in this thesis. Some of the contents of this chapter were extracted from, or based on, the work "Non-linear effective field theory simulators in two-fluid interfaces" [1] carried out in collaboration with Cameron R. D. Bunney and Silke Weinfurtner.

2.1 Two-fluid systems: properties and assumptions

We begin by defining our understanding of *two-fluid systems*, their assumed features and the approximations adopted throughout. Generally, the model presented herein applies to any set of two immiscible, homogeneous fluids in incompressible and viscous motion, either liquids or gases, whose dynamics are described by the Navier-Stokes equations [90]. In certain limits, our formalism also applies to liquid helium films. Unless otherwise stated, we will disregard stationary background flow velocities, such as the bathtub vortex and the open channel flow, both successfully used in previous experiments simulating black hole (BH) phenomena [25, 40, 47, 91–93]. Instead, we concentrate on closed systems with rigid boundaries, where interfacial waves arise from noise sources [4] or external forcing [2, 79]. We stress that, when necessary, we may approximate the theory or add to the assumptions to discuss specific cases. A brief description of the required properties follows below.

2.1.1 Immiscibility

The requirement of immiscibility allows us to define the concept of an interface between the two media. We adopt a coarse-grained view of the molecular motion that dictates the *smooth* transition between both fluids in such a way that an effective two-dimensional description of this region arises. However, as we will use in Chapter 3, by including a macroscopic depiction of the interface, which is valid when its roughness is negligible compared to the characteristic scales of the system [94], the microscopic dynamics still plays a role and may be incorporated by means of stochastic fluctuations [90, 95, 96]. Accordingly, the two-dimensional interface between two fluids is never at rest but instead is constantly displaying the random interplay of the underlying molecular forces [94, 97].

2.1.2 Homogeneity

A homogeneous fluid is one that admits no local changes in its density ρ. Hence, the density is uniform throughout its volume, i.e., $\rho(\boldsymbol{x}) \equiv \rho$. In most experimental applications where our discussion applies, especially in the case of classical fluids, this condition is readily satisfied by working with uncontaminated samples of pure liquids or homogeneous mixtures of liquids at fixed temperatures. This also includes liquid Helium-4, where two fluid phases (normal and superfluid) coexist below the superfluid transition temperature (lambda-point), as described by Landau's two-fluid model [98, 99], the resulting mixture can be treated as homogeneous.

2.1.3 Incompressibility

Although incompressibility is a familiar assumption in the context of fluid dynamics, it may always be interpreted as a condition on the flow velocity relative to the speed of sound in the medium. In fact, fluids are generally compressible, but for those with low compressibility coefficients, such as water, oils and most liquid solvents, the speed of sound is considerably large, especially when compared to gases [90]. As mentioned in Chapter 1, the speed of propagation of surface waves and the flow velocities achievable in a laboratory are typically a few orders of magnitude smaller than the speed of sound in the same media. Thus, for such flows, the ratio between the typical flow and sound speeds, or the *Mach number*, is much smaller than one [15], and they can be regarded as incompressible. Since our treatment in this thesis focuses on interfacial instead of bulk phenomena, as originally proposed by W. Unruh [10], incompressible flows will be the theoretical backdrop for the analogue simulators in fluids discussed here.

2.1.4 Viscosity

In fluid dynamics, viscosity can greatly complicate the analytical study of fluids through the Navier-Stokes equations at various regimes of *Reynolds number*[1], from creeping to turbulent flows [15, 98]. Similar to compressibility, viscosity is ubiquitous to liquids and gases, but it may be neglected depending on the specific properties of the flow at hand. White claims that *"when a flow is both frictionless and irrotational, pleasant things happen"* [15]. The author refers to the study of potential flows, which simplify the dynamical equations describing the bulk motion of the fluids by disregarding viscosity and vorticity. Under these conditions, the former can be accounted for by considering a thin viscous layer adjoining the boundaries of the fluid container [90]. These are called boundary layers, and their thickness is proportional to the square root of the kinematic viscosity ν [100], which is defined as the ratio between (dynamic) viscosity μ and density ρ of the fluid. The flow velocity within them admits a description in terms of rotational components, whose contributions are only non-negligible in the vicinity of the boundaries. In practice, the appropriate choice of fluids with low viscosity can result in the desired and *pleasant* mathematical modelling benefits of a potential flow[2]. For most of the following content, we will treat inviscid flows and, later on, correct for dissipative (viscous) effects.

2.1.5 Capillarity

As stated in subsection 2.1.1, we are restricted to a set of two immiscible fluids, which allows an interface to be identified [94]. Such interfaces are free to deform and change their shape, but in a way that minimises their surface energy [97]. Surface (or interfacial) tension σ provides a measure of the amount of energy necessary to change the interface by one unit of area. As its name indicates, it does not appear in the bulk equations of motion of fluids but through appropriately set boundary conditions at a fluid-fluid interface. In liquid analogue simulators, it usually modifies the linear dispersion of waves with a "superluminal" or free-particle term [16], which dominates for small wavelengths, i.e., in the order of the typical length where surface tension and gravity forces are comparable, known as the capillary length. As we will discuss in Chapter 3, capillary effects can hardly be neglected in experiments. Viscosity and capillarity may lead to the appearance of non-negligible curvature of the interface (meniscus) around solid walls. The effect of menisci cannot be readily accounted

[1] The Reynolds number Re is a dimensionless quantity used to characterise viscous flows, e.g., it is used to quantitatively identify the transition between laminar and turbulent flows. It is typically defined as $\mathrm{Re} = \rho u L/\mu$, where u is the flow speed, L is a characteristic length scale of the system, and ρ and μ are the density and viscosity of the fluid.

[2] An appropriate choice of *common* liquid samples implicitly requires that they are *Newtonian fluids*, for which an externally applied shear stress linearly results in a strain rate in the fluid. In this case, their *constant* proportionality coefficient is denoted by (dynamic) viscosity coefficient μ.

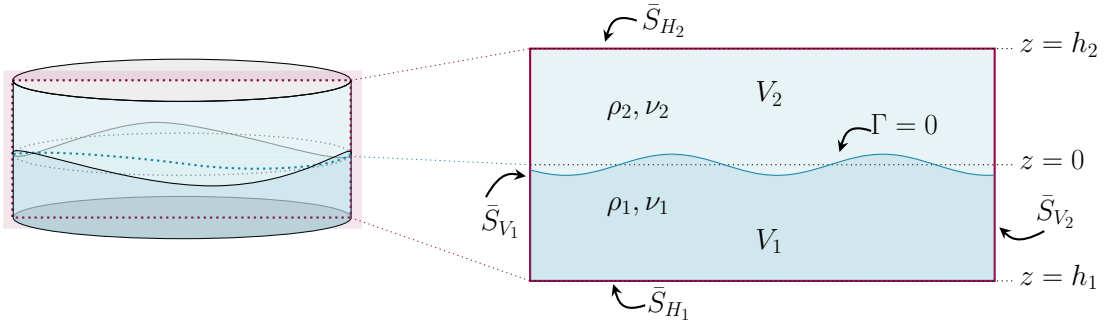

Figure 2.1: (Left) Illustration of an example basin with cylindrical geometry enclosing two immiscible fluids. A vertical plane (shaded red) slices the cell across its diameter. (Right) Depiction of the rectangular cross-section of the cylindrical two-fluid cell. Solid lines indicate rigid boundaries $\bar{S}_B$. Top and bottom plates at $z = h_j$ act as horizontal boundaries $\bar{S}_{H,j}$. Vertical walls are shown by $\bar{S}_{V,l}$. The interface is indicated by the surface $\Gamma = 0$ (solid blue curve).

for in the modelling, reinforcing the importance of empirically testing the EFT to examine their relevance. Additionally, the dramatically varying interfacial tension due to potential contaminants and surfactants at the interface may hinder repeatability in preparing fluid samples and reproducibility of experimental results [94].

2.2 Fluid-fluid interfacial dynamics: the setup

We can now turn to the description of the emerging dynamics at the interface between two fluids enclosed in a basin (or fluid cell), both satisfying the assumptions presented in Section 2.1. We allow the geometry of the cell to be arbitrary in the direction perpendicular to the vertical coordinate z, which is aligned with the constant acceleration of gravity on Earth, $\boldsymbol{g_0} = -g_0\hat{\boldsymbol{z}}$. The horizontal cross-section of the basin has area Σ and is mapped by a set of two-dimensional coordinates $\boldsymbol{x} = (x, y)$ orthogonal to the vertical direction ($\hat{\boldsymbol{z}}$). A depiction of an example fluid cell with cylindrical geometry is shown in Figure 2.1.

For our proposed closed system, in the absence of a stationary background flow, the time-averaged interface is static and located at $z = 0$. One has the option of inducing motion on the fluid cell through an arbitrary external forcing, which induces an acceleration $\boldsymbol{F}(t) = F_0(t)\hat{\boldsymbol{z}} + \tilde{\boldsymbol{F}}(t)$, with $\tilde{\boldsymbol{F}} \cdot \hat{\boldsymbol{z}} = 0$. This results in a horizontal acceleration $\tilde{\boldsymbol{F}}(t)$ and a combined vertical acceleration $\boldsymbol{g}(t) = -(g_0 - F_0(t))\hat{\boldsymbol{z}} \equiv -g(t)\hat{\boldsymbol{z}}$, which can generate waves on the interface with disturbed height $\xi(t, \boldsymbol{x})$ and parametrised by a surface $\Gamma(t, \boldsymbol{x}, z) = z - \xi(t, \boldsymbol{x}) = 0$ (see Figure 2.1). The top and bottom lids of the cell ($\bar{S}_{H_1}$ and $\bar{S}_{H_2}$), respectively at $z = h_2$ and $z = h_1 = -|h_1|$, vertically confine the denser fluid phase (denoted 1) and the lighter one (denoted 2), both with uniform densities ρ_1 and $\rho_2 < \rho_1$, respectively. The volume of each fluid is

then $V_j = |h_j|\Sigma$.

In accordance with the continuity equation [90], incompressibility requires that the velocity $\boldsymbol{u}_j$ of fluid j is divergenceless, i.e.,

$$\frac{D\rho_j}{Dt} + (\nabla \cdot \boldsymbol{u}_j)\,\rho_j = 0 \implies \nabla \cdot \boldsymbol{u}_j = 0. \tag{2.1}$$

Here, the flow's material derivative reads $\frac{D\rho_j}{Dt} = \frac{\partial \rho_j}{\partial t} + \boldsymbol{u}_j \cdot \nabla$. With no further assumptions, the solutions to the equation above can be written in terms of Helmholtz decomposed velocity fields, i.e., they are formed of irrotational (potential) and rotational components [101], as follows,

$$\boldsymbol{u}_j = \nabla \phi_j + \boldsymbol{U}_j, \tag{2.2}$$

with $\boldsymbol{U}_j = \nabla \times \boldsymbol{A}_j$ [3]. Thus, the potential ϕ_j must fulfil

$$\nabla^2 \phi_j = 0, \text{ in } V_j, \tag{2.3}$$

and Equation 2.1 is identically satisfied by $\boldsymbol{U}_j$. In line with Prandtl's boundary layer theory assumptions [90, 100, 102], we expect that the rotational components of the velocity fields are only non-negligible in a thin viscous layer around the solid boundaries of the basin.

Before turning to the equations of motion for the velocity fields, we must specify the appropriate set of boundary conditions for our system. A condition of impenetrability on all rigid (non-porous) boundaries $\bar{S}_B$ (see Figure 2.1) requires that the velocity vanishes along their outwardly directed normal unit vectors $\hat{\boldsymbol{n}}_B$, that is,

$$\hat{\boldsymbol{n}}_B \cdot \boldsymbol{u}_j|_{\bar{S}_B} = 0 \Rightarrow \hat{\boldsymbol{n}}_B \cdot \nabla \phi_j|_{\bar{S}_B} = -\,\hat{\boldsymbol{n}}_B \cdot \boldsymbol{U}_j|_{\bar{S}_B}\,. \tag{2.4}$$

Additionally, as conventionally assumed when considering viscous flows [90, 103], we impose the no-slip condition on all rigid boundaries, i.e., the fluids cling to the walls of the basin due to viscosity[4]. In other words, the velocity components tangential to the boundaries must vanish, hence, according to Equation 2.2,

$$\hat{\boldsymbol{n}}_B \times \boldsymbol{u}_j|_{\bar{S}_B} = 0 \Rightarrow \hat{\boldsymbol{n}}_B \times \nabla \phi_j|_{\bar{S}_B} = -\,\hat{\boldsymbol{n}}_B \times \boldsymbol{U}_j|_{\bar{S}_B}\,. \tag{2.5}$$

At the interface $\Gamma = 0$, we further require that the particles in the fluid are advected

[3] Since the divergence of the curl is zero, this choice is always justified.

[4] We note that this choice of boundary condition, although widely accepted, may not always be guaranteed in an experimental setup around the contact line between an interface and the boundaries, see [104, 105] and references therein for an in-depth discussion. In fact, the physical and chemical properties of the walls determine the validity of this assumption, and it is not uncommon to observe a degree of slipping when interfacial waves are large enough.

by the flow [90, 101]. The previous statement is usually referred to as the kinematic boundary condition at the moving interface, and it translates into stating that fluid particles on the interface remain part of it and move along the flow. Hence, the advection condition over the parametric surface Γ is

$$\frac{D\Gamma}{Dt} \equiv \frac{\partial \Gamma}{\partial t} + \boldsymbol{u}_j \cdot \nabla \Gamma = 0, \text{ on } \Gamma = 0. \tag{2.6}$$

It is worth remarking that the equation above constitutes two equations, one in each fluid j, and, by noting that $\nabla \Gamma = \hat{\boldsymbol{z}} - \nabla \xi$, it expands to

$$\frac{\partial \xi}{\partial t} = \frac{\partial \phi_j}{\partial z} - \nabla \phi_j \cdot \nabla \xi + U_{j,z} - \boldsymbol{U}_j \cdot \nabla \xi, \text{ on } z = \xi(t, \boldsymbol{x}), \tag{2.7}$$

where $U_{j,z}$ denotes the $z-$component of the rotational velocity $\boldsymbol{U}_j$.

We now examine the bulk motion of each fluid, which is governed by a set of Navier-Stokes equations, as follows,

$$\rho_j \left[\frac{\partial \boldsymbol{u}_j}{\partial t} + (\boldsymbol{u}_j \cdot \nabla) \boldsymbol{u}_j \right] = \nabla \cdot \overleftrightarrow{\boldsymbol{\pi}}_j + \boldsymbol{f}_j, \tag{2.8}$$

where $\overleftrightarrow{\boldsymbol{\pi}}_j$ and $\boldsymbol{f}_j$ are the stress tensor and an externally applied force density on fluid j [90, 106]. The former encompasses both viscous and static (pressure) stresses *within* the fluid and is given by

$$\overleftrightarrow{\boldsymbol{\pi}}_j = -p_j \mathbf{1} + \mu_j \left(\nabla \boldsymbol{u}_j + (\nabla \boldsymbol{u}_j)^T \right), \tag{2.9}$$

where p_j and μ_j are the pressure and dynamic viscosity in fluid j, and $(\nabla \boldsymbol{u}_j)^T$ denotes the transpose of the tensor field obtained from the vector gradient of the velocity $\boldsymbol{u}_j$ (see Appendix A). The identity matrix is denoted $\mathbf{1}$, and the last term in Equation 2.9 may be expressed in terms of the strain rate tensor $\overleftrightarrow{\boldsymbol{\varepsilon}}_j = \frac{1}{2} \left(\nabla \boldsymbol{u}_j + (\nabla \boldsymbol{u}_j)^T \right)$.

In the presence of interfacial tension and viscosity, when the fluid phases are in motion, stress appears at the interface. These conditions can be modelled by examining the behaviour of the stress tensor across the interface, which results in the following stress balance equation [100][5]

$$\hat{\boldsymbol{n}}_\Gamma \cdot \overleftrightarrow{\boldsymbol{\pi}}_1 \Big|_{\Gamma=0^-} - \hat{\boldsymbol{n}}_\Gamma \cdot \overleftrightarrow{\boldsymbol{\pi}}_2 \Big|_{\Gamma=0^+} = -\hat{\boldsymbol{n}}_\Gamma \left(\sigma \nabla \cdot \hat{\boldsymbol{n}}_\Gamma \right), \tag{2.10}$$

[5] Equation 2.10 is obtained by assuming a uniform interfacial tension coefficient σ across the interface. Spatial gradients on $\sigma(\boldsymbol{x})$ introduce tangential stress, and the right-hand-side of the equation gets corrected by $-\nabla \sigma(\boldsymbol{x})$.

where $\hat{\boldsymbol{n}}_\Gamma$ is the normal unit vector at the interface defined as

$$\hat{\boldsymbol{n}}_\Gamma = \frac{\nabla\Gamma}{|\nabla\Gamma|} = \frac{\hat{\boldsymbol{z}} - \nabla\xi}{\sqrt{1+|\nabla\xi|^2}}. \tag{2.11}$$

From Equation 2.10, we can obtain a jump condition for the normal stress on the interface and a continuity condition for the tangential stress, which, respectively, read

$$\hat{\boldsymbol{n}}_\Gamma \cdot \left(\overleftrightarrow{\boldsymbol{\pi}}_1\Big|_{\Gamma=0^-} - \overleftrightarrow{\boldsymbol{\pi}}_2\Big|_{\Gamma=0^+} \right) \cdot \hat{\boldsymbol{n}}_\Gamma = -\sigma\nabla\cdot\hat{\boldsymbol{n}}_\Gamma, \tag{2.12}$$

$$\hat{\boldsymbol{n}}_\Gamma \cdot \left(\overleftrightarrow{\boldsymbol{\pi}}_1\Big|_{\Gamma=0^-} - \overleftrightarrow{\boldsymbol{\pi}}_2\Big|_{\Gamma=0^+} \right) \times \hat{\boldsymbol{n}}_\Gamma = 0. \tag{2.13}$$

The complete formulae of both conditions in terms of the velocity components and pressures are shown in Appendix A.

Provided with the equations presented in the current section, we will now specialise to two particular regimes. The first concerns the inviscid non-linear evolution of interfacial waves in the presence of an arbitrary vertical forcing term, i.e., $\boldsymbol{F}(t) = F_0(t)\hat{\boldsymbol{z}}$ and $\tilde{\boldsymbol{F}} = \boldsymbol{0}$. In the second, we will examine the relaxation of standing waves in the absence of external forcing to derive a linear model for the damping of the interfacial modes in a specific geometry of the fluid cell.

2.3 Non-linear inviscid interfacial dynamics

In the following discussion, we will consider the dynamical evolution of the fluid-fluid interface through an inviscid flow generated by an external vertical forcing applied on the fluid cell. The flow will be entirely described by the velocity potentials in each fluid, ϕ_1 and ϕ_2, and the viscous (boundary-layer) components $\boldsymbol{U}_1$ and $\boldsymbol{U}_2$ will be assumed negligible. The combined time-dependent acceleration $g(t)$ discussed above enters Equation 2.8 as a conservative field upon the following identification: $\boldsymbol{f}_j = -\nabla\left(\rho_j g(t) z\right)$.

For negligible viscosities, the normal stress condition at the interface (2.12) reduces to the Young-Laplace law [97], which states that the pressure difference across the interface is proportional to its surface curvature, i.e.,

$$-\left(p_1|_{\Gamma=0^-} - p_2|_{\Gamma=0^+}\right) = -\sigma\nabla\cdot\hat{\boldsymbol{n}}_\Gamma = -\sigma\nabla\cdot\left(\frac{\nabla\Gamma}{|\nabla\Gamma|}\right) = \sigma\nabla\cdot\left(\frac{\nabla\xi}{\sqrt{1+|\nabla\xi|^2}}\right), \tag{2.14}$$

where σ denotes the interfacial-tension coefficient between the two fluids. By computing the difference between the Navier-Stokes equations (2.8) in each fluid, evaluating it at the interface and simplifying with the assumptions above, we obtain the following set of equations determining the inviscid, non-linear dynamics of the interface

(see Appendix A for derivation):

$$\nabla^2\phi_j = 0, \qquad \text{in } V_j, \tag{2.15a}$$

$$\hat{\boldsymbol{n}}_B \cdot \nabla\phi_j|_{\bar{S}_B} = 0, \qquad \text{on } \bar{S}_B, \tag{2.15b}$$

$$\frac{\partial\xi}{\partial t} = \frac{\partial\phi_j}{\partial z} - \nabla\phi_j \cdot \nabla\xi, \quad \text{on } z = \xi(t,\boldsymbol{x}), \tag{2.15c}$$

$$\left[\frac{\partial}{\partial t}\left(\rho_1\phi_1 - \rho_2\phi_2\right) + \frac{\rho_1}{2}\left(\nabla\phi_1\right)^2 - \frac{\rho_2}{2}\left(\nabla\phi_2\right)^2\right]_{z=\xi}$$
$$+ (\rho_1 - \rho_2)g(t)\xi - \sigma\nabla\cdot\left(\frac{\nabla\xi}{\sqrt{1+|\nabla\xi|^2}}\right) = 0, \text{ on } z = \xi(t,\boldsymbol{x}). \tag{2.15d}$$

The equations above determine the non-linear interfacial dynamics in the absence of viscous dissipation. In the following discussion, we will use them as a reference in order to express the dynamical evolution in terms of a variational problem. Ultimately, we shall obtain a Lagrangian formulation of the dynamics in terms of the interfacial height ξ, which is our primary observable in this description.

2.3.1 Variational approach to the kinematic boundary-value problem

The set of equations (2.15a), (2.15b) and (2.15c) comprises a kinematic boundary-value problem, which may be derived by requiring the stationarity of the following action functional [84, 101],

$$I_j = \frac{(-1)^{j+1}}{2\Sigma}\iiint_{V_j}\left(\nabla\phi_j\right)^2 \mathrm{d}\Sigma\ \mathrm{d}z - \frac{1}{\Sigma}\iint\frac{1}{|\nabla\Gamma|}\frac{\partial\xi}{\partial t}\,\phi_j|_{z=\xi}\,\mathrm{d}\Sigma, \tag{2.16}$$

where $\mathrm{d}\Sigma \equiv \mathrm{d}^2\boldsymbol{x}$ is the area element of the horizontal cross-section and is such that $\Sigma = \iint \mathrm{d}\Sigma$. In [1] (and in Appendix A), the variation of action I_j with respect to ϕ_j is shown to recover the appropriate set of kinematic boundary-value equations.

In [84], Miles seems to have missed the curvature denominator $|\nabla\Gamma|$ in Equation 2.16, but according to the derivation of Serrin [101] for the Dirichlet problem, this term is necessary to recover Equation 2.15c without the need of any approximations or perturbative expansions. We will show that this term contributes to quartic nonlinearities, leaving Miles's results consistent since the author focuses on cubic ones in [84]. The fluid-relative sign in front of the first integral is necessary to recover the appropriate Equation 2.15c in the upper phase, fluid 2, where the normal at the interface is opposite to that of fluid 1.

We now consider Laplace's equation (2.15a) with boundary conditions (2.15b) on the geometry of the fluid cell. It admits discretised solutions $\{\psi_{j,a}(\boldsymbol{x},z)\}_a$ on each

fluid j and the symmetry of the basin allows us to decouple these eigenfunctions into vertical $f_{j,a}(z)$ and horizontal $\chi_a(\boldsymbol{x})$ components. Thus, we decompose them as $\psi_{j,a}(\boldsymbol{x}, z) = \chi_a(\boldsymbol{x}) f_{j,a}(z)$, with

$$f_{j,a}(z) = \frac{\cosh[k_a(z - h_j)]}{\cosh(k_a h_j)}, \tag{2.17}$$

for k_a such that

$$\left(\nabla^2 + k_a^2\right) \chi_a(\boldsymbol{x}) = 0, \text{ with } \hat{\boldsymbol{n}} \cdot \nabla \chi_a|_{\partial\Sigma} = 0, \tag{2.18}$$

where $\chi_a(\boldsymbol{x})$ are spatial eigenfunctions of the horizontal Laplacian, and we leave implicit that $\nabla \equiv \nabla_{\boldsymbol{x}}$. We construct the $z-$component in (2.17) to identically satisfy the boundary conditions at the top and bottom lids of the cell, namely $\partial_z \phi_j(t, \boldsymbol{x}, z = h_j) = 0$. We further require that the set of functions $\{\chi_a\}_a$ is orthonormal on the cross-section Σ, i.e.,

$$\iint \mathrm{d}\Sigma \; \chi_a(\boldsymbol{x}) \chi_b(\boldsymbol{x}) = \Sigma \delta_{ab}. \tag{2.19}$$

We can now express the velocity potentials in the basis of orthonormal spatial eigenfunctions $\chi_a(\boldsymbol{x})$ with coefficients given by time-dependent generalised coordinates $\phi_{j,a}(t)$ multiplied by the respective $f_{j,a}(z)$, as follows,

$$\phi_j(t, \boldsymbol{x}, z) = \sum_a \phi_{j,a}(t) f_{j,a}(z) \chi_a(\boldsymbol{x}) = \sum_a \phi_{j,a}(t) \psi_{j,a}(\boldsymbol{x}, z). \tag{2.20}$$

We further assume that a decomposition in the basis of $\chi_a(\boldsymbol{x})$ also applies to the height fluctuations $\xi(t, \boldsymbol{x})$, i.e.,

$$\xi(t, \boldsymbol{x}) = \sum_a \xi_a(t) \chi_a(\boldsymbol{x}). \tag{2.21}$$

Along these lines, we choose a representation of the generalised coordinates ξ_a and $\phi_{j,a}$ as column vectors of infinite dimension, namely $\boldsymbol{\Phi}_j \equiv \{\phi_{j,a}\}$ and $\boldsymbol{\Xi} \equiv \{\xi_a\}$, and for the basis vector, $\boldsymbol{X} \equiv \{\chi_a\}$.

In vector notation, we may express equations (2.20) and (2.21) in terms of a dot product of vectors, e.g., $\xi(t, \boldsymbol{x}) = \boldsymbol{\Xi}^{\mathrm{T}} \boldsymbol{X}$, where $\boldsymbol{\Xi}^{\mathrm{T}}$ denotes the transpose of $\boldsymbol{\Xi}$. Then, the action functional in (2.16) reads

$$I_j = \frac{1}{2} \boldsymbol{\Phi}_j^{\mathrm{T}} \mathbf{K}_j \boldsymbol{\Phi}_j - \frac{1}{2} \dot{\boldsymbol{\Xi}}^{\mathrm{T}} \mathbf{D}_j \boldsymbol{\Phi}_j, \tag{2.22}$$

where $\mathbf{K}_j \equiv \left[\mathrm{k}_{ab}^{(j)}\right]$ and $\mathbf{D}_j \equiv \left[\mathrm{d}_{ab}^{(j)}\right]$ are two square matrices defined in terms of integrals of products of χ_a, ψ_a and ξ_a, given explicitly in Section A.3 of Appendix A. An underlying assumption permeates the derivation of these terms. Namely, we consider

interfacial height fluctuations $\xi(t, \boldsymbol{x})$ much smaller than the depth of both fluids, i.e., $|\xi| \ll |h_j|$. Hence, we perturbatively expand all appropriate quantities in powers of a small parameter $\delta_j \equiv \left|\frac{\xi}{h_j}\right| \ll 1$, keeping contributions up to second-order in δ_j.

The variation of the action I_j with respect to $\mathbf{\Phi}_j$ (see Section A.3 in Appendix A) results in the kinematic boundary condition (2.15c) in matrix notation, as follows,

$$\mathbf{\Phi}_j = \mathbf{K}_j^{-1}\mathbf{D}_j^{\mathrm{T}}\dot{\mathbf{\Xi}} \equiv \mathbf{L}_j\dot{\mathbf{\Xi}}, \tag{2.23}$$

where $\mathbf{K}_j^{-1}$ denotes the inverse of the symmetric matrix $\mathbf{K}_j$ and $\mathbf{D}_j^{\mathrm{T}}$ is the transpose of $\mathbf{D}_j$. In Equation A.34 of Appendix A, we show the exact form of the combined square matrix $\mathbf{L}_j \equiv \left[\mathrm{l}_{ab}^{(j)}\right]$. Consistently, to a leading-order approximation, the equation above recovers the linearised dynamics result (cf. [106]), i.e.,

$$\dot{\xi}_a = k_a \tanh(k_a|h_1|)\phi_{1,a} = -k_a \tanh(k_a|h_2|)\phi_{2,a}. \tag{2.24}$$

Finally, we note that Equation 2.23 maps the time-variations of the interfacial height modes $\dot{\xi}_a$ into velocity potential modes $\phi_{j,a}$ at the interface. The dependence of $\mathrm{l}_{ab}^{(j)}$ on the modes ξ_a (see Equation A.34) allows us to interpret Equation 2.23 as the nonlinear generalisation of Equation 2.24.

2.3.2 Lagrangian formulation

As previously discussed, equations (2.15c) and (2.15d) dictate the dynamics of the interfacial modes between the two fluids. Luke [107] established a widely used variational principle to recover these equations of motion. In his approach, a Lagrangian is obtained from the integrated fluid pressures p_j over their own volumes V_j. However, here we follow the method of Miles [84, 85], where the kinetic and potential energies of the fluids at play are considered instead. We construct a Lagrangian from their difference using the spectral decomposition in equations (2.20) and (2.21), and their respective matrix representations. As shown in [84, 85], we expect the results of this approach to correspond to a decomposition of Equation 2.15d in terms of interfacial modes ξ_a, followed by a perturbative expansion of it for small parameter $\delta_j = \left|\frac{\xi}{h_j}\right|$ and small slopes $|\nabla\xi|^2 \ll 1$.

We begin defining the kinetic energy T_j of fluid j from its velocity field (cf. §10 of [108]), and employing relation (2.23) to express it in terms of the interfacial height modes ξ_a, as follows,

$$\frac{T_j}{\Sigma} = \frac{\rho_j}{2\Sigma}\iiint_{V_j} \mathrm{d}\Sigma\mathrm{d}z\,|\boldsymbol{u}_j|^2 = \frac{(-1)^{j+1}}{2}\rho_j\mathbf{\Phi}_j^{\mathrm{T}}\mathbf{K}_j\mathbf{\Phi}_j = \frac{(-1)^{j+1}}{2}\rho_j\dot{\mathbf{\Xi}}^{\mathrm{T}}\mathbf{L}_j^{\mathrm{T}}\mathbf{K}_j\mathbf{L}_j\dot{\mathbf{\Xi}}, \tag{2.25}$$

where we used the definition of $\mathbf{K}_j$ (see Equation A.24). We further define a new

matrix that conveniently simplifies the equations, as follows,

$$\mathbf{L}_j^{\mathrm{T}}\mathbf{K}_j\mathbf{L}_j = \mathbf{D}_j(\mathbf{K}_j^{-1})^{\mathrm{T}}\mathbf{K}_j\mathbf{L}_j = \mathbf{D}_j\mathbf{L}_j \equiv \mathbf{A}_j.$$

Its exact form is given in Equation A.35 of Appendix A. Accordingly, the total kinetic energy of the fluids read

$$\frac{T}{\Sigma} = \frac{1}{2}\dot{\boldsymbol{\Xi}}^{\mathrm{T}}\left(\rho_1\mathbf{A}_1 - \rho_2\mathbf{A}_2\right)\dot{\boldsymbol{\Xi}}. \tag{2.26}$$

Additionally, we must consider the potential energy V, which can be obtained from the effective gravitational energy, $\rho_j g(t) z$, integrated over deformations $\xi(t,\boldsymbol{x})$ of the resting interface at $z=0$, and the surface energy term as a result of the non-vanishing interfacial tension σ. Hence, the energy reads (cf. §10, §265 of [108])

$$\begin{aligned}\frac{V}{\Sigma} &= \frac{1}{2\Sigma}\iint \mathrm{d}\Sigma\ \left[\left(\rho_1-\rho_2\right)g(t)\xi^2 + 2\sigma\left(|\nabla\Gamma|-1\right)\right] \\ &= \frac{1}{2\Sigma}\iint \mathrm{d}\Sigma\ \left[\left(\rho_1-\rho_2\right)g(t)\xi^2 + \sigma\left(|\nabla\xi|^2 - \frac{1}{4}|\nabla\xi|^4 + \cdots\right)\right].\end{aligned} \tag{2.27}$$

The above definition for the potential energy V is such that it vanishes in the absence of interfacial waves $\xi(t,\boldsymbol{x})$, and can be understood as a change in the total potential energy of the fluids due to changes on the interface. The quartic (last) term in (2.27) will introduce additional non-linear contributions to the Lagrangian and may be expressed in the spectral decomposition (2.21) as

$$\frac{1}{4\Sigma}\iint \mathrm{d}\Sigma\ |\nabla\xi|^4 \equiv \frac{1}{4}\sum_{a,b,c,d}\mathcal{B}_{abcd}\xi_a\xi_b\xi_c\xi_d, \tag{2.28}$$

where $\mathcal{B}_{abcd}$ are coefficients computed from products of $\nabla\chi_a$ and defined in Equation A.37 of Appendix A.

Finally, with both the kinetic and potential energies at hand, we can define the complete Lagrangian that determines the dynamics of the interfacial height modes ξ_a, as follows

$$\begin{aligned}\frac{L}{\Sigma} = \frac{1}{2}\sum_a\left(\frac{\rho_1}{k_aT_{1,a}} + \frac{\rho_2}{k_aT_{2,a}}\right)\left(\dot{\xi}_a^2 - \omega_a^2(t)\xi_a^2\right) + \frac{1}{2}\sum_{a,b,c}\left(\rho_1\mathcal{A}^{(1)}_{cab} - \rho_2\mathcal{A}^{(2)}_{cab}\right)\xi_c\dot{\xi}_a\dot{\xi}_b \\ + \frac{1}{4}\sum_{a,b,c,d}\left[\left(\rho_1\mathcal{A}^{(1)}_{cdab} + \rho_2\mathcal{A}^{(2)}_{cdab}\right)\dot{\xi}_a\dot{\xi}_b + \frac{\sigma}{2}\mathcal{B}_{abcd}\xi_a\xi_b\right]\xi_c\xi_d,\end{aligned} \tag{2.29}$$

where

$$\omega_a^2(t) = \frac{(\rho_1-\rho_2)g(t) + \sigma k_a^2}{\rho_1\coth(k_a|h_1|) + \rho_2\coth(k_a|h_2|)}k_a, \tag{2.30}$$

and $T_{j,a} \equiv \tanh(k_a|h_j|)$. We note that the dispersion relation for an interfacial mode

ξ_a in linear dynamics becomes time-dependent and is given by the frequency $\omega_a(t)$ (cf. [106]). When varied with respect to ξ_a, the Lagrangian (2.29) results in the non-linear equations of motion for the interface in the presence of external vertical forcing $F_0(t)$, which is contained within the effective gravity term $g(t) = g_0 - F_0(t)$.

We will later show through an example scenario that the coefficients $\mathcal{A}^{(j)}_{cab}$ and $\mathcal{A}^{(j)}_{cdab}$ in (2.29) may be understood as momentum conservation constraints. In other words, a given primary ξ_a mode with spatial wavenumber k_a will interact with other modes with a "strength" given by these non-linear coefficients, similar to the conservation rules in vertices of Quantum Field Theory (QFT) [109]. On the other hand, in our systems of interest, the boundaries introduce finite-size effects, resulting in a discrete spectrum of wavenumbers k_a, further restraining the available interactions.

2.4 EFT simulators in ideal cases

In the particular case of both phases with the same depth, i.e., $h_2 = |h_1| \equiv h_0$, and in the absence of external forcing, so that $F_0(t) \equiv 0$, we can write the dispersion (2.30) as follows,

$$|\omega_a| = \frac{c}{h_0}\sqrt{(1+\ell_c^2 k_a^2)\, k_a h_0 \tanh(k_a h_0)}, \text{ with } \ell_c \equiv \sqrt{\frac{\sigma}{(\rho_1-\rho_2)g_0}}. \tag{2.31}$$

Here, ℓ_c is called the capillary length, and $c \equiv \sqrt{A_{12}\, g_0 h_0}$ is the speed of long-wavelength gravity interfacial waves, with the Atwood number [15] given by $A_{12} \equiv (\rho_1 - \rho_2)/(\rho_1 + \rho_2)$. The form of the dispersion above is convenient because it highlights the limiting behaviours relevant to our discussion, and we depict them in Figure 2.2. In the long-wavelength regime, the interfacial modes have wavelengths much longer than the depth h_0 of the fluids, hence they are usually referred to as "shallow-water" waves [90, 100]. Accordingly, it holds that $k_a h_0 \ll 1$ and we can use the small argument approximation for the hyperbolic tangent in the equation above, $\tanh(k_a h_0) \approx k_a h_0$. For appropriate conditions where $h_0 \gg \ell_c$, and thus $k_a \ell_c \ll 1$, the quadratic term in the dispersion (2.31) can be neglected, and the waves are said to be gravity waves, i.e., the action of gravity determines their dynamics. The dispersion of such waves is then linear, $\omega_a = c k_a$, and they propagate with speed c. Conversely, in the short-wavelength limit, where $k_a h_0 \gg 1$, we have $\tanh(k_a h_0) \approx 1$, and the dispersion acquires a cubic term inside the square root. For high enough wavenumbers for which $k_a \ell_c \gg 1$, this term prevails and gives the characteristic capillary dispersion scaling $k^{3/2}$ [90] (see Figure 2.2).

When considering a free surface ($\rho_1 \gg \rho_2, \rho_2 \to 0$), Schützhold and Unruh showed in [16] that the equations of motion for long-wavelength surface waves are mathemat-

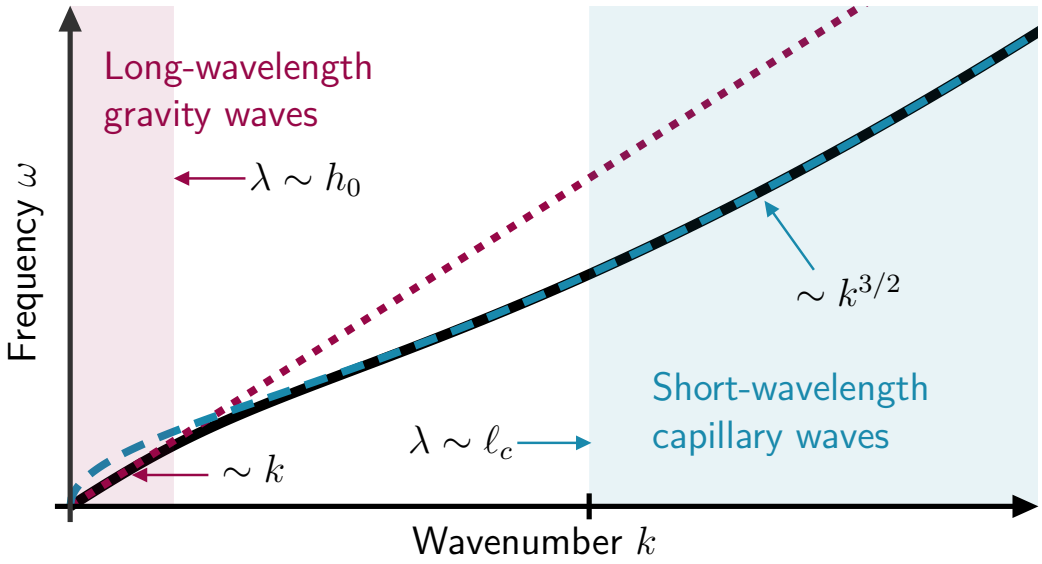

Figure 2.2: Depiction of interfacial wave dispersion (2.31) (thick, solid black line). The trend of linear dispersion $\omega \sim k$ is shown by the dotted red line, while that of short-wavelength gravity-capillary dispersion $\omega \sim \sqrt{(1+\ell_c^2 k^2)k}$ is displayed by the dashed blue line. Arrows indicate their asymptotic behaviours for small and large wavenumber k. The domains of validity of both approximations are shown by the red (gravity waves) and blue (capillary waves) shaded regions.

ically equivalent to the dynamics of a massless Klein-Gordon (KG) field on an effective $(2+1)-$dimensional spacetime. Their work opened an avenue for the development of gravity and early Universe simulators on fluid interfaces, and, building up on their work, we discuss now some limiting cases of the equations derived in Section 2.2, wherein one finds similar mathematical equivalences. Throughout this section, unless otherwise stated, we keep the assumption that both fluids have the same depth and consider long-wavelength gravity waves, such that their wavenumbers k_a satisfy $k_a h_0 \ll 1$ and $k_a \ell_c \ll 1$.

2.4.1 Analogue massless scalar field in flat spacetime

Under the above conditions, we see that the dispersion relation (2.31) reads

$$\omega_a = c k_a, \tag{2.32}$$

a linear dispersion relation as in Quantum Field Theory (QFT). Further, with the decomposition (2.21), the modes ξ_a satisfy to leading order the following equation of motion

$$\ddot{\xi}_a + c^2 k_a^2 \xi_a = 0 \Leftrightarrow \frac{1}{c^2}\partial_t^2 \xi - \nabla^2 \xi = 0. \tag{2.33}$$

This corresponds to the dynamical evolution of a massless KG field in a $(2+1)-$dimensional Minkowski spacetime with an effective speed of light $c = \sqrt{A_{12}\, g_0 h_0}$.

For systems where the top phase is a gas or vapour, we can take $\rho_1 \gg \rho_2$, so that the Atwood number A_{12} tends to unity, resulting in an EFT for surface waves on an inviscid fluid [16]. We will discuss this case in more detail in Chapter 5, where this correspondence is used for simulating quantum processes that can take place on flat spacetimes, such as the Unruh effect [82], on a static and homogeneous superfluid helium free surface, as proposed in [4, 83].

2.4.2 A simulator for inflationary cosmology

In the presence of arbitrary external forcing $F_0(t) \neq 0$, the linearisation of the equations in Section 2.3 for small interfacial wave amplitudes and negligible capillary effects allows us to identify $\phi_1|_{z=\xi} = -\,\phi_2|_{z=\xi} = \phi_0$ at the interface. We now promote this interfacial velocity potential ϕ_0 to the main field, such that Equation 2.15d reads

$$(\rho_1 + \rho_2)\frac{\partial}{\partial t}\phi_0 + (\rho_1 - \rho_2)g(t)\xi = 0. \tag{2.34}$$

With the decompositions (2.20) and (2.21) at the interface, the spatial eigenfunctions $\psi_{j,a}(\boldsymbol{x}, \xi)$ reduce to $\chi_a(\boldsymbol{x})$ to leading order. Hence, the equation above becomes

$$\begin{aligned} \sum_a \left(\dot{\phi}_{0,a} + A_{12}\; g(t)\xi_a(t)\right)\chi_a(\boldsymbol{x}) = 0, \\ \implies \dot{\phi}_{0,a} + A_{12}\; g(t)\xi_a(t) = 0. \end{aligned} \tag{2.35}$$

Differentiating (2.35) with respect to time yields

$$\ddot{\phi}_{0,a}(t) + A_{12}\; \dot{g}(t)\xi_a(t) + A_{12}\; g(t)\dot{\xi}_a(t) = 0. \tag{2.36}$$

We want to examine the dynamics of the modes $\phi_{0,a}$ and, thus, remove any instances of ξ_a. First, we note that the linearised kinematic condition (2.7) yields $\dot{\xi}(t) = k_a \tanh(k_a h_0)\phi_{0,a} = (h_0 k_a^2)\phi_{0,a}$ in the long-wavelength limit. Second, (2.35) can be rearranged as $\xi_a = -\dot{\phi}_{0,a}/(A_{12}\; g(t))$. With both these expressions, our scalar field ϕ_0 satisfies the following equation of motion

$$\ddot{\phi}_{0,a} - \frac{\dot{g}(t)}{g(t)}\dot{\phi}_{0,a} + A_{12}\; g(t)h_0 k_a^2 \phi_{0,a} = 0. \tag{2.37}$$

At this stage, we note that, with the following identifications, $\omega_a^2(t) = c^2\left(1 - \frac{F_0(t)}{g_0}\right)k_a^2$ and $a^{-2} \equiv \left(1 - \frac{F_0(t)}{g_0}\right)$, and by relabelling the mode number from a to d to avoid confusion, the equation above can be rewritten as:

$$\ddot{\phi}_{0,d} - \frac{\dot{g}(t)}{g(t)}\dot{\phi}_{0,d} + \omega_d^2(t)\phi_{0,d} = 0, \tag{2.38a}$$

$$c^{-2}\ddot{\phi}_{0,d} + 2c^{-2}\frac{\dot{a}(t)}{a(t)}\dot{\phi}_{0,d} + \frac{k_d^2}{a^2(t)}\phi_{0,d} = 0, \tag{2.38b}$$

where $c = \sqrt{A_{12}\ g_0 h_0}$ is the speed of propagation of long-wavelength waves.

Let us briefly consider a massive scalar field in a $(2+1)-$dimensional Friedmann – Lemaître – Robertson – Walker (FLRW) spacetime [5, 110], described by the following metric and Lagrangian density, respectively,

$$\mathrm{d}s^2 = g_{\mu\nu}\mathrm{d}x^\mu \mathrm{d}x^\nu = -c^2\mathrm{d}t^2 + a^2(t)\mathrm{d}\mathbf{x}^2, \tag{2.39a}$$

$$\mathcal{L} = -\frac{1}{2}\sqrt{-g}\left(\nabla_\mu\phi\nabla^\mu\phi + (mc)^2\phi^2\right), \tag{2.39b}$$

where $g = \det g_{\mu\nu}$. The stationary variation of (2.39b) with respect to ϕ results in

$$\Box\phi - (mc)^2\phi = 0, \tag{2.40}$$

which for the metric above reduces to

$$c^{-2}\ddot{\phi} + 2c^{-2}\frac{\dot{a}}{a}\dot{\phi} - \frac{1}{a^2}\nabla^2\phi + (mc)^2\phi = 0. \tag{2.41}$$

Note that, because of the $(2+1)-$dimensional spacetime, a factor of two in the term $2\frac{\dot{a}}{a}\dot{\phi}$ appears.

We can now establish a connection between equations (2.38b) and (2.41), which allows us to interpret the former as the equation of motion of a massless, minimally coupled scalar field in an effective $(2+1)-$dimensional FLRW spacetime spectrally decomposed as $\phi(t,\mathsf{x}) = \sum_d \phi_d(t)\chi_d(\mathsf{x})$, with $(\nabla^2 + k_d^2)\chi_d = 0$. However, this mathematical equivalence relies on the shallow-water approximation in the simulator. For arbitrary wavelengths, the analogue scale factor $a(t)$ would instead depend on the spatial wavenumber k, i.e., $a(t) \to a_k(t)$, which is characteristic of a rainbow universe [79, 111]. As in the case of [79], the effective scale factor $a(t)$ can be modulated by appropriately choosing the external forcing $F_0(t)$, allowing this correspondence to be used in investigating the evolution of analogue scalar fields in inflationary scenarios.

As a final comment on this case, we note that Equation 2.35 provides an interpretation of the field ξ as the conjugate momentum of the analogue field ϕ_0 at the interface. Under the present assumptions, we obtained the relation $\dot{\xi}_d = (h_0 k_d^2)\phi_{0,d}$, which upon differentiation yields

$$\ddot{\xi}_d = h_0 k_d^2 \dot{\phi}_{0,d}. \tag{2.42}$$

By using (2.35), we find again the equation of motion for the modes ξ_d,

$$\ddot{\xi}_d + c^2 \frac{k_d^2}{a^2(t)} \xi_d = 0. \tag{2.43}$$

In contrast with (2.33), the equation above describes the dynamics of the conjugate momentum of the analogue relativistic field ϕ_0 in an effective FLRW spacetime with the speed of light replaced by the long-wavelength speed c. Whereas (2.33) is the equation of motion of the analogue scalar field ξ in a Minkowski metric with an effective speed of light given by the speed of interfacial wave propagation. These various interpretations showcase the flexibility of using two-fluid systems in devising analogue scenarios relevant, for example, in the context of cosmology.

2.4.3 Nonlinear EFT simulator

In the following, we will specialise in the case of a harmonic external forcing $F(t) = F_0 \cos(\Omega t)$[6], for which the equation of motion of the modes ξ_a (2.43) reads

$$\ddot{\xi}_a + k_a^2 c^2 \left(1 - \frac{F_0}{g_0} \cos(\Omega t)\right) \xi_a = 0 \tag{2.44a}$$

$$\Rightarrow \frac{1}{\tilde{c}^2} \ddot{\xi}_a + \left(k_a^2 + \lambda^2 k_a^2 F_0 \sin^2(\omega_0 t)\right) \xi_a = 0, \tag{2.44b}$$

where we identified $\Omega \equiv 2\omega_0$, $\tilde{c}^2 \equiv A_{12}\ (g_0 - F_0) h_0$ and $\lambda^2 \equiv 2/(g_0 - F_0)$. Similar to (2.33), the equation above when $F_0 = 0$ may be understood as that of a massless KG field propagating on a $(2+1)-$dimensional Minkowski spacetime, but now with an effective speed of light $\tilde{c}$. We note that the analogue field ξ interacts with a spatially uniform mechanical forcing $\Phi^2(t)$ through a derivative coupling in a potential of the form $-\frac{1}{2}\lambda^2 \Phi^2 (\nabla \xi)^2$. Upon identifying $\Phi(t) \equiv \sqrt{F_0} \sin(\omega_0 t)$, Equation 2.44b follows readily.

Equation 2.44a has the standard form of the Mathieu equation [112, 113], which is known to yield exponentially unstable solutions in time in various fields in physics, from fluid dynamics [106, 114] and engineering [115, 116] to models of the early Universe [117, 118]. Generally, when systems manifest these particular solutions, they are referred to as undergoing parametric amplification or resonance. In fluid interfaces, the resonant modes are specifically called Faraday instabilities in reference to Faraday's foremost contributions to their understanding [114]. Along the lines of our previous discussion, we can establish a parallel between our EFT for interfacial waves and models for the thermalisation of the early Universe after inflation. In particular, we now discuss the case of slow-roll inflation [119].

[6] Here, we implicitly require that $F_0 < g_0$, i.e., the amplitude of the external oscillating acceleration must not overcome Earth's gravitational acceleration g_0.

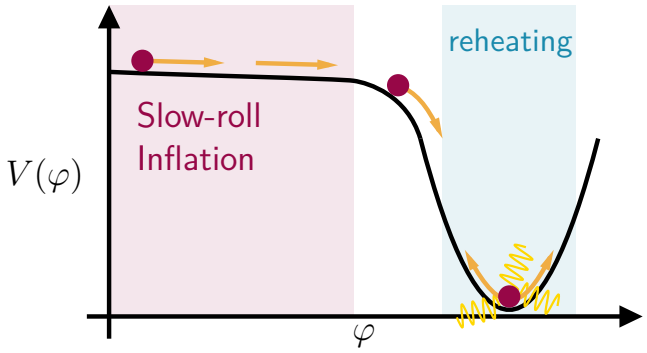

Figure 2.3: Illustration of the conceptual picture of slow-roll inflation. The classical evolution of the inflaton field φ is represented by the red ball. As inflation ends, reheating starts, and the field parametrically oscillates around the minimum of its potential and slowly loses its kinetic energy through parametric resonance and the subsequent decay into matter $\psi-$particles (yellow waves). Inspired by [120].

In the context of cosmology, chaotic inflation models [119] predict that a scalar field φ, commonly known as the inflaton, is subjected to a slow-roll potential $V(\varphi)$, and sources inflation on a spatially homogeneous and isotropic spacetime (FLRW geometry) characterised by a scale factor $a(t)$ and Hubble parameter $H \equiv \dot{a}/a$. Throughout this process, the inflationary expansion of the Universe determines the classical background evolution of the scalar field. Eventually, as inflation concludes, the inflaton transitions from the potential-dominated region and enters a phase of oscillations around the global minimum of $V(\varphi)$, initiating the reheating process. We examine the interaction between the inflaton φ and a massless bosonic field ψ coupled through the interaction potential $-\frac{1}{2}\lambda\varphi^2\psi^2$. A depiction of this picture is shown in Figure 2.3.

At the end of inflation, slow-roll models assume that the inflaton would then oscillate around a minimum of the potential $V(\varphi)$, which we consider here to be quadratic, i.e., $\frac{1}{2}m_\varphi^2\varphi^2$. It then follows that the classical evolution of the field is well approximated by $\varphi(t) \approx \Phi(t)\sin(m_\varphi t)$, where $\Phi(t)$ is a nearly constant amplitude. In this kinetic-dominated regime, the energy of the inflaton is transferred to the matter fields ψ through their interaction, resulting in the following equation of motion for ψ_k modes [117, 120]

$$\ddot{\psi}_k + 3H\dot{\psi}_k + \left(\frac{k^2}{a^2(t)} + \lambda^2\varphi^2(t)\right)\psi_k = 0. \tag{2.45}$$

In that period, the spacetime is usually regarded as a nearly Minkowski metric with $a(t) \sim 1$ and $\dot{a}(t) \sim 0$ [119]. Hence, the Hubble-friction term in the equation above becomes negligible and the modes evolve according to

$$\ddot{\psi}_k + \left(k^2 + \lambda^2\Phi^2\sin^2(m_\varphi t)\right)\psi_k = 0 \tag{2.46a}$$

$$\Rightarrow \ddot{\psi}_k + \left(k^2 + \frac{1}{2}\lambda^2\Phi^2 - \frac{1}{2}\lambda^2\Phi^2\cos(2m_\varphi t)\right)\psi_k = 0, \tag{2.46b}$$

recovering again a Mathieu-type equation as in (2.44).

Unstable solutions of the Mathieu equation appear in instability bands in the frequency domain [112], which requires that, for wavenumbers k inside them, their modes ψ_k experience parametric resonance and evolve as

$$\psi_k(t) \propto \exp(\mu_k m_\varphi t), \tag{2.47}$$

where μ_k are known as Floquet coefficients [113]. In the initial stages of reheating, when the inflaton oscillation amplitude Φ is still large, and hence $\lambda^2\Phi^2$ is large, a broad band of k-modes undergoes parametric amplification, which characterises the so-called preheating stage [117]. This unstable evolution leads to an explosive production of $\psi-$particles with exponentially growing occupation number density n_k, i.e., $n_k \propto \exp(2\mu_k m_\varphi t)$. Preheating results in a far-from-equilibrium state, where elementary particle decays dominate, bringing on succeeding stages of reheating and, ultimately, the required thermalisation of the early Universe [119].

Given the equivalence between equations (2.44) and (2.46b), we can now conceive a simulator of the non-trivial interacting features of preheating using parametrically excited Faraday instabilities. Within the approximations and assumptions of this section, the Lagrangian (2.29) to second-order in small amplitudes ξ_a reads

$$\frac{L}{\Sigma} = \overbrace{\frac{\rho_1+\rho_2}{2h_0}\sum_a \frac{1}{k_a^2}\left(\dot{\xi}_a^2 - \omega_a^2(t)\xi_a^2\right)}^{L^{(0)}} + \underbrace{\frac{\rho_1-\rho_2}{2}\sum_{a,b,c}\mathcal{A}^{(0)}_{cab}\xi_c\dot{\xi}_a\dot{\xi}_b + \frac{\rho_1+\rho_2}{4}\sum_{a,b,c,d}\mathcal{A}^{(0)}_{cdab}\dot{\xi}_a\dot{\xi}_b\xi_c\xi_d}_{L^{(1)}}, \tag{2.48}$$

with $\omega_a^2(t) = (A_{12}\ g(t)h_0)k_a^2$. We denote the quadratic Lagrangian by $L^{(0)}$ and higher-order terms by $L^{(1)}$. The Euler-Lagrange equations for a mode ξ_a result in a non-linear equation of motion, which reduces to (2.44a) to leading order. It is worth noting that the equations obtained from the Lagrangian above are only valid for long-wavelength gravity waves, in this way restricting the available wavenumbers of this approximate dynamics. A more general picture should include the complete dispersion to allow for arbitrary wavenumbers, as we will discuss in Chapter 3. Still, we can devise a scenario where a low-wavenumber interfacial mode is parametrically amplified and evolves dominantly with respect to the others. Its exponentially growing amplitude triggers the cubic and quartic interactions in Equation 2.48, hence exciting other modes.

Within this framework, in addition to the correspondence between the interfacial height ξ and a KG field on a flat spacetime, the emerging EFT, as described by Lagrangian (2.48), can be employed to examine the onset of interactions in a simulator for preheating and the initial phases of thermalisation in the early Universe [2]. We must note, however, that the boundary conditions (2.4) imposed on the field ξ limit the values of k_a to those that fit the geometry of the fluid cell. In other words, the confined interface of our proposed system can only accommodate a reduced density of states ξ_a.

We now illustrate the implications of this discretisation through an example case. Consider a fluid cell with a rectangular cross-section with sides ℓ_0 and ℓ_0/α, i.e., $(x, y) \in [0, \ell_0] \times [0, \ell_0/\alpha]$ and $\Sigma = \ell_0^2/\alpha$. The quantity α can assume any positive real value and represents the horizontal aspect ratio of the fluid cell. In this geometry, the spatial eigenfunctions $\chi_a(\boldsymbol{x})$ satisfying (2.18) read

$$\chi_a(x, y) = 2 \cos\left(\frac{\pi m_a x}{\ell_0}\right) \cos\left(\frac{\pi \alpha n_a y}{\ell_0}\right), \tag{2.49}$$

where $m_a,\ n_a \in \mathbb{N} \cup \{0\}$ such that $m_a^2 + (\alpha n_a)^2 = N_a > 0$. The corresponding eigenvalues of $\chi_a(\boldsymbol{x})$ are $k_a = \frac{\sqrt{N_a}\pi}{\ell_0}$. By labelling the unique pair of non-negative integers (m_a, n_a) with a counter a, we can uniquely identify interfacial modes $\xi_a(t)$ with a non-degenerate spectrum and wavevector $\boldsymbol{k}_a = \frac{\pi}{\ell_0}(m_a \hat{\boldsymbol{x}} + \alpha n_a \hat{\boldsymbol{y}})$. In the case of squared cross-section, in which $\alpha = 1$, a degeneracy arises from the invariance of $\sqrt{N_a}$ under the action $(m_a, n_a) \mapsto (n_a, m_a)$; see [1] for a discussion of this particular case. In this configuration, long-wavelength waves must satisfy $\sqrt{N_a} \ll \frac{\ell_0}{\pi h_0}$, which is attainable in setups with large vertical to horizontal aspect ratio ℓ_0/h_0.

We can use χ_a of the form (2.49) to compute the coefficients $\mathcal{A}^{(0)}_{cab}$ and $\mathcal{A}^{(0)}_{cdab}$ in Section A.3, from what we find

$$\mathcal{A}^{(0)}_{cab} \propto \delta_{m_c,|m_a \pm m_b|}\ \delta_{n_c,|n_a \pm n_b|}, \tag{2.50a}$$

$$\mathcal{A}^{(0)}_{cdab} \propto \delta_{|m_c \pm m_a|,|m_d \pm m_b|}\ \delta_{|n_c \pm n_a|,|n_d \pm n_b|}, \tag{2.50b}$$

where δ_{ab} is the Kronecker delta. Equations (2.50) act as conservation rules for the Lagrangian (2.48). The delta relations above reduce the modes contributing to the summations in $L^{(1)}$ and effectively restrict those appearing in the cubic and quartic terms. For instance, the cubic constraint requires that a mode with wavenumber k_c can only interact with wavenumbers k_a and k_b, if $m_c = |m_a \pm m_b|$ and $n_c = |n_a \pm n_b|$. We illustrate this process using the mode with the longest wavelengths in both directions in Figure 2.4. We can further draw a comparison between our interacting EFT and QFT, as the deltas in equations (2.50) are equivalent to vertex conservation rules in the latter.

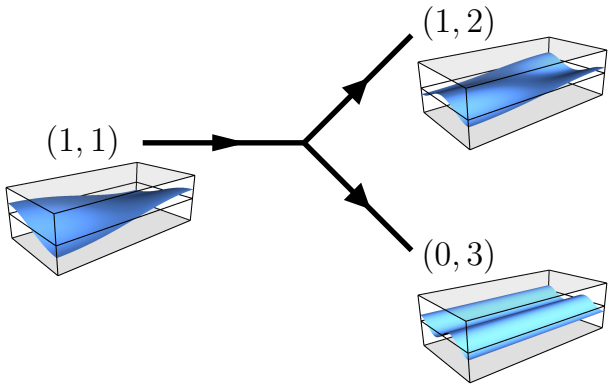

Figure 2.4: Depiction of a possible interfacial mode decay for $(m_c, n_c) = (1, 1)$ into $(m_a, n_a) = (1, 2)$ and $(m_b, n_b) = (0, 3)$ through a cubic interaction. The blue surfaces show the interface height for these modes with arbitrary amplitudes. The bounding boxes denote the boundaries of a fluid cell with aspect ratio $\alpha = 2$, and a thin rectangular contour indicates the resting interface position. It is straightforward to check that these modes satisfy the conservation rule (2.50a).

Finally, at the level of equations of motion, an interfacial mode $\xi_a(t)$ evolves non-linearly according to

$$\ddot{\xi}_a + \omega_a^2(t)\xi_a + \frac{2h_0k_a^2}{\rho_1 + \rho_2}\left[\frac{d}{dt}\left(\frac{\partial L^{(1)}}{\partial \dot{\xi}_a}\right) - \frac{\partial L^{(1)}}{\partial \xi_a}\right] = 0, \tag{2.51}$$

where $L^{(1)}$ corresponds to cubic and higher-order terms in the Lagrangian (2.48). As proposed in [2], by appropriately selecting a dominant mode, it is possible to streamline this equation to retain solely terms arising from quartic interactions in the Lagrangian. Consequently, one can simulate models resembling ϕ^4 particle decay scenarios during reheating. In a broader sense, the formalism presented herein provides an avenue to explore the dynamical features of interacting field theories.

2.5 EFT modifications for more realistic features

In the previous sections, a series of assumptions discussed in Section 2.1 were adopted in order to obtain the EFT presented and employ it in analogue scenarios. It should not come as a surprise, however, that in our target systems, a plethora of other physical phenomena may play a role in the dynamics of the interface. This could be understood as a collateral outcome for using the intricate framework of fluid dynamics to devise EFT simulators, with the understanding that, as the name suggests, the *effective* description may fall short in accounting for certain aspects of the underlying physics. Regardless, informed by experimental observations and theoretical predictions in the background literature, we venture into improving our model for at least some of these more realistic features. Throughout, we keep in mind that experimental results

will ultimately ascertain the adequacy of our EFT in accurately describing the system while discerning the core underlying concepts.

In the previous section, we never specified the initial conditions for the equations of motion derived. Unless a well-defined initial state is imprinted on the interface through a prior process, such as parametric resonance, sloshing or a mechanical wave generator, one could postulate that the interface is initially at rest, i.e., $\xi = 0$ and $\dot{\xi} = 0$. However, in our discussions in subsection 2.1.1 and subsection 2.1.5, we argued that the effective coarse-graining of the interface does not eliminate the underlying microscopic dynamics but instead allows us to treat the macroscopic surface as a fluctuating object [90, 94, 97]. These random variations from an equilibrium "rest" (and flat) state may be understood by means of the fluctuation-dissipation theorem [121]. The inherent viscous properties of fluids in equilibrium, which naturally dissipate their energy, are in *detailed balance* with inter-molecular fluctuations.

Several authors have investigated the characteristic spectrum of these surface fluctuations with thermal origin in fluids, see e.g. [90, 95, 96, 122–124]. Simulations [96, 125, 126] and experiments [127–129] have confirmed the suitability and accuracy of these models in describing the high-frequency, short-wavelength ($> 1\,\mathrm{kHz}$) end of the surface spectrum, where waves are strongly damped. Unfortunately, for experiments interested in the low-frequency, long-wavelength range, thermality may not be the primary source of fluctuations and the models mentioned above become unfit for predicting the behaviour of fluid surfaces. In fact, it is well-known that laboratory environments tend to display non-negligible noise levels, especially at lower frequencies. These may come from various unpredictable sources, such as street traffic, machinery, and building resonance. This wide variety of contributing environmental factors adds to the challenge of modelling the fluctuating interface in the regimes of interest to our proposed simulators.

Our chosen approach is to incorporate the microscopic features of the interface through an experimentally informed model, which we discuss further in Chapter 3, compensating for the lack of a satisfactory theoretical description. We assume that the two-fluid interface is flat and at rest *on average*, i.e., $\langle \xi \rangle = 0$ and $\left\langle \dot{\xi} \right\rangle = 0$, and we leave the mean $\langle \cdot \rangle$ purposefully unspecified, as it can be taken over long times or over a statistical ensemble. Further, we incorporate the fluctuating nature of the interface by promoting all its modes ξ_a to central random variables with non-vanishing variance $\langle \xi_a^2 \rangle \neq 0$, which, along with their distribution, should be directly inferred from observations. In practice, we modify the equations of motion for the interfacial modes to include a stochastic noise term η_a [121], which, to linear order, sources them as follows

$$\ddot{\xi}_a + 2\gamma_a \dot{\xi}_a + \omega_a^2(t)\xi_a = \eta_a. \tag{2.52}$$

Note the inclusion of linear damping γ_a to the equation above. Even in the absence of other environmental noise sources, dissipation continuously acts as a noise source by means of the fluctuation-dissipation theorem. Thus, we acknowledge its contribution through a linear damping term, which we now discuss in the framework of fluid dynamics.

Miles notes in [84] that the Lagrangian formulation presented in subsection 2.3.2 can be appropriately modified to include a linear damping term through Rayleigh's dissipation function [130], as follows,

$$Q_0 = \sum_a \left(\rho_1 \coth(k_a|h_1|) + \rho_2 \coth(k_a|h_2|)\right) \gamma_a \dot{\xi}_a^2. \tag{2.53}$$

It modifies the Euler-Lagrange equations of a mode ξ_a with an extra term,

$$\frac{\mathrm{d}}{\mathrm{d}t}\left(\frac{\partial L}{\partial \dot{\xi}_a}\right) - \frac{\partial L}{\partial \xi_a} = -\frac{\partial Q_0}{\partial \dot{\xi}_a}, \tag{2.54}$$

where L is the Lagrangian (2.29). Extensive literature on fluid dynamics has tackled the problem of obtaining an experimentally compatible formula for the damping of free-surface waves in cylindrical and rectangular basins [86–88, 131–138]. More recently [87, 88], authors have extended previous models to understand the effects of dissipation in slightly viscous two-fluid interfaces within systems with boundaries[7].

We follow an *ad-hoc* approach to dissipation as proposed in [86] with modifications to account for the liquid-liquid interface. In the method of Case and Parkinson [86], the mechanical energy balance is examined, and it requires that the variation in time of the total mechanical energy (i.e., kinetic and potential energies) corresponds to the total rate of dissipation in the fluids [108]. In the case of two liquids, the balance equation reads [87]

$$\frac{\mathrm{d}}{\mathrm{d}t}\left(T_1 + T_2 + V\right) = -2\sum_{j=1,2} \mu_j \iint_{V_j} \mathrm{d}V_j \; \overleftrightarrow{\boldsymbol{\varepsilon}}_j : \overleftrightarrow{\boldsymbol{\varepsilon}}_j \quad \equiv -2\sum_{j=1,2} F_j, \tag{2.55}$$

where T_j and V are the kinetic and potential energies, as in equations (2.25) and (2.27), respectively. The term on the right-hand side of the above equation contains the contraction of the strain rate tensor in each fluid, defined as $\overleftrightarrow{\boldsymbol{\varepsilon}}_j : \overleftrightarrow{\boldsymbol{\varepsilon}}_j \equiv \varepsilon_{j,kl}\varepsilon_{j,lk}$. The left-hand side of Equation 2.55 can be expressed in terms of interfacial modes using the formalism of the previous section, approximated to leading order in ξ_a (linear dynamics). Therefore, the damping rates can be estimated by assuming an unstable decay of standing waves on the interface and comparing both sides of the Equation 2.55.

As we will later show, computing the F_j integrals of both fluids using solely the linear

[7] Practically, we are referring to fluids with kinematic viscosities in the range of few $\mathrm{mm\,s^{-1}}$, such as most liquid solvents [15].

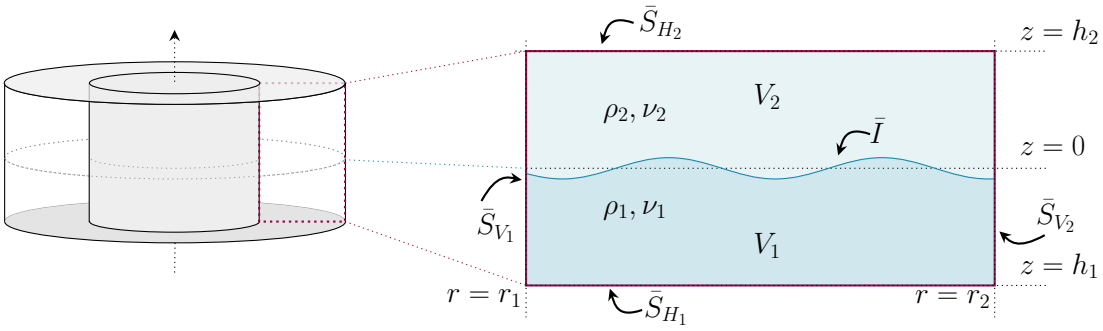

Figure 2.5: (Left) Illustration of an annular-cylinder basin or a cylindrical shell. (Right) Depiction of the rectangular cross-section of the two-fluid cell. Solid lines indicate rigid boundaries $\bar{S}_B$. Top and bottom plates at $z = h_j = (-1)^j |h_j|$ act as horizontal boundaries $\bar{S}_{H_j}$. Vertical walls at $r = r_s$ are shown by $\bar{S}_{V_s}$, for $s = 1, 2$. The average resting interface at $z = 0$ is indicated by $\bar{I}$.

potential flow solutions of Section 2.3 results in the so-called interior damping rate (see e.g. [106]), which informs us of the dissipation in the body of the liquids [90]. However, it is consistently shown in the literature that the formula for interior damping falls short in matching experimentally extracted damping rates, especially in the case of small cylindrical basins [86, 87, 133–135]. This known discrepancy motivates a modification of the inviscid potential solutions through the inclusion of small rotational viscous contributions, which would remain valid for liquids with small kinematic viscosities. We will now restrict the discussion to the damping of interfacial waves forming on cylindrical geometries, which will be relevant to the content of Chapter 3. Along the lines of [86, 87], we will revise the underlying ideas behind them and extend the analysis to liquid-liquid interfaces in an annular geometry, where the inner cylinder introduces an extra boundary damping term.

2.5.1 Damping of standing interfacial waves in cylindrical geometries

Our derivation in this section will extend the most recent results for linear damping in liquid-liquid interfaces in cylindrical basins presented in [87], which is in itself based on [86]. For that, we consider an annular two-fluid cell (see Figure 2.5) with inner and outer radii r_1 and r_2, respectively, satisfying all the properties required in Section 2.2. The main assumption underlying the following discussion is that the flows of both fluids are well described by a linear approximation of the inviscid theory presented in Section 2.3 in the absence of external forcing, corrected by small viscous contributions included through rotational velocity components.

We employ the aforementioned assumption of standing waves on the interface to examine the behaviour of a single mode at frequency ω_a and damped at rate γ_a.

Within the premise of low-viscosity fluids, the damping is *a priori* assumed to be much smaller than the typical frequency, i.e., $\gamma_a \ll \omega_a$, subject to later verification. Momentarily, we treat the velocities and interfacial height as complex fields, keeping in mind that these observables are real-valued and taking their absolute values when computing the energies in Equation 2.55. Provided that the potential flow satisfies the set of equations (2.15) to leading order in small interfacial height fluctuations ξ (see Appendix A), it follows that the single mode evolution for some initial interfacial amplitude ξ_a reads

$$\xi(t,r,\theta) = \chi_a(r,\theta)\xi_a \mathrm{e}^{-i\omega_a t-\gamma_a t}, \tag{2.56a}$$

$$\phi_j(t,r,\theta,z) = i(-1)^j \frac{\omega_a - i\gamma_a}{k_a} \frac{\cosh\left[k_a(z-h_j)\right]}{\sinh(k_a|h_j|)} \chi_a(r,\theta)\xi_a \mathrm{e}^{-i\omega_a t-\gamma_a t}, \tag{2.56b}$$

and

$$\chi_a(r,\theta) = \sqrt{\Sigma} N_a R_a(r)\cos(m_a\theta), \tag{2.56c}$$

with $\Sigma = \pi(r_2^2 - r_1^2)$ and

$$R_a(r) = Y'_{m_a}(k_a r_1)\, J_{m_a}(k_a r) - J'_{m_a}(k_a r_1)\, Y_{m_a}(k_a r), \tag{2.56d}$$

where k_a are the zeros of $R'_a(r_2) = 0$, and [139]

$$N_a^{-2} = \frac{2}{\pi k_a^2}\left[\left(1 - \frac{m_a^2}{k_a^2 r_2^2}\right)\left(\frac{J'_{m_a}(k_a r_1)}{J'_{m_a}(k_a r_2)}\right)^2 - \left(1 - \frac{m_a^2}{k_a^2 r_1^2}\right)\right]. \tag{2.56e}$$

In this cylindrical geometry, an interfacial mode here labelled by a is instead characterised by a unique pair of integers, namely the azimuthal mode m_a and the order n_a of the zero k_a.

Having the exact linear inviscid solutions above, we can turn to the viscous corrections, which we assume to be non-negligible only around thin boundary layers of thickness $\ell_j = \sqrt{\nu_j/|\omega_a|}$ in each fluid [90, 100]. In these conditions, the rotational components $\boldsymbol{U}_j$ must approximately satisfy the following equations:

$$(2.1) \implies \nabla \cdot \boldsymbol{U}_j = 0, \quad \text{in } V_j, \tag{2.57a}$$

$$(2.4) \implies \hat{\boldsymbol{n}}_B \cdot \boldsymbol{U}_j|_{\bar{S}_B} = 0, \quad \text{on } \bar{S}_B, \tag{2.57b}$$

$$(2.5) \implies \hat{\boldsymbol{n}}_B \times \boldsymbol{U}_j|_{\bar{S}_B} = -\hat{\boldsymbol{n}}_B \times \nabla\phi_j|_{\bar{S}_B}, \quad \text{on } \bar{S}_B, \tag{2.57c}$$

$$(2.7) \implies U_{j,z}|_{z=0} = 0, \quad \text{on } \bar{I}, \tag{2.57d}$$

$$(2.13) \implies \mu_1\, \partial_z\left(\hat{\boldsymbol{n}}_\Gamma \times \boldsymbol{U}_1\right)|_{z=0} = \mu_2\, \partial_z\left(\hat{\boldsymbol{n}}_\Gamma \times \boldsymbol{U}_2\right)|_{z=0}, \quad \text{on } \bar{I}, \tag{2.57e}$$

$$(2.8) \implies -i\,\mathrm{sgn}(\omega_a)\boldsymbol{U}_j = \ell_j^2 \nabla^2 \boldsymbol{U}_j. \tag{2.57f}$$

We further note that the velocities of both fluids are continuous across the inter-

face [106] and, thus, their tangential components match, i.e.,

$$(\hat{\boldsymbol{n}}_\Gamma \times \boldsymbol{u}_1)|_{z=0} = (\hat{\boldsymbol{n}}_\Gamma \times \boldsymbol{u}_2)|_{z=0}\,, \text{ on } \bar{I}. \tag{2.57g}$$

Since these velocities should only contribute around the viscous boundary layers, it is convenient to operate with a new set of dimensionless coordinates $\zeta_{j,B}$, which span along the direction of the normal vectors $\hat{\boldsymbol{n}}_B$ of the boundaries and the interface, increasing towards the inside of the fluids. We define them as follows,

$$\zeta_{j,B} = \begin{cases} (-1)^j (h_j - z)/\ell_j, & \text{near } \bar{S}_{H_j} \\ (-1)^s (r_s - r)/\ell_j, & \text{near } \bar{S}_{V_s} \\ (-1)^j z/\ell_j, & \text{near } \bar{I} \end{cases}. \tag{2.58}$$

We note that, since the ℓ_j's are assumed small compared to the dimensions of the basin, the set of normal coordinates above is of order unity around the boundary layers and rapidly scales to infinity far from the walls.

Using equations (2.57) and this new set of coordinates, one can show that the boundary layer velocities around solid boundaries $\bar{S}_B$ are well approximated by (see Appendix A for derivation)

$$\boldsymbol{U}_{j,B} = -\nabla_{\parallel_B}\phi_j\big|_{\bar{S}_B} \exp\left(-\Delta\zeta_{j,B}\right), \tag{2.59}$$

where $\Delta = \frac{1-i\ \mathrm{sgn}(\omega_a)}{\sqrt{2}}$. $\nabla_{\parallel_B}$ denotes the gradient vector on tangential coordinates of the rigid boundary $\bar{S}_B$, and it is then clear that $\boldsymbol{U}_{j,B}$ does not have a component along the normal $\hat{\boldsymbol{n}}_B$ to leading order, as required by Equation 2.57c. Similarly, at the interface $\bar{I}$,

$$\boldsymbol{U}_{j,I} = (-1)^j \frac{1}{\rho_j\sqrt{\nu_j}} \left(\frac{1}{\rho_1\sqrt{\nu_1}} + \frac{1}{\rho_2\sqrt{\nu_2}}\right)^{-1} \nabla_{\boldsymbol{x}} \left(\phi_1 - \phi_2\right)_{z=0} \exp\left(-\Delta\zeta_{j,I}\right). \tag{2.60}$$

Again, the term $\nabla_{\boldsymbol{x}}$, denoting the gradient on the $\boldsymbol{x}$ horizontal coordinates, indicates that $\boldsymbol{U}_{j,I}$ does not have a component along the normal of the interface to leading order, as required by (2.57d).

With all pieces of the problem set, we can go back to the mechanical energy balance equation (2.55). The left-hand side can be computed from the equations for both kinetic and potential energies ((2.25) and (2.27)), and reduces to

$$\frac{\mathrm{d}}{\mathrm{d}t}\left(T_1 + T_2 + V\right) = -2\gamma_a \left(\frac{\rho_1}{T_{1,a}} + \frac{\rho_2}{T_{2,a}}\right) \frac{\omega_a^2}{k_a} \Sigma \left|\xi_a\right|^2 \mathrm{e}^{-2\gamma_a t}. \tag{2.61}$$

On the other hand, the dissipation integrals $2F_j$ can be simplified by expanding the

contraction $\overleftrightarrow{\varepsilon}_j : \overleftrightarrow{\varepsilon}_j$ to recover the usual form of Lamb's dissipation integrals (see [108], §329). The integrals effectively reduce to two terms: the first approximately reads

$$2F_{j,r} = \rho_j \nu_j \sum_B \iiint_{\delta V_{j,B}} \mathrm{d}V_j \left| \nabla \times \boldsymbol{U}_{j,B} \right|^2, \tag{2.62a}$$

where the summation over B indicates contributions from the boundary layer components around $\bar{S}_{H_j}$, $\bar{S}_{V_s}$ and $\bar{I}$, which are relevant inside small volumes $\delta V_{j,B}$ near the boundaries due to the rapid exponential decays in the velocities. The second term is a surface integral over all the boundaries of each fluid's volume, but it can be shown to reduce to a single contribution at the interface, given by

$$2F_{j,I} = 4(-1)^j \rho_j \nu_j \iint_{\bar{I}} \mathrm{d}\Sigma \left[\frac{\partial \phi_j}{\partial z} \nabla_{\boldsymbol{x}} \cdot \left(\nabla_{\boldsymbol{x}} \phi_j + \boldsymbol{U}_{j,I} \right) \right]_{z=0}. \tag{2.62b}$$

Lengthy but straightforward computations of all integrals above follow in line with §D in [87]. By comparing the integration results with (2.61), we find that the total damping can be written in terms of the contributions of each energy dissipation term, as follows

$$\gamma_a = \gamma_{a,\mathrm{int}} + \gamma_{a,I} + \gamma_{a,H} + \gamma_{a,V}, \tag{2.63a}$$

where each component is given below:

$\gamma_{a,\mathrm{int}}$ The interior damping $\gamma_{a,\mathrm{int}}$ is the simplest of terms, as it can be derived from the inviscid solution alone, see, e.g., equation (4.20) in [106], where the authors obtain the same formula using the time-averaged rate of dissipation of Landau & Lifshitz [90] in §25. Herreman *et al.* note in [87], however, that an extra boundary layer contribution appears in the same order at liquid-liquid interfaces, in contrast with the results of Case & Parkinson for a free-surface [86]. We then separate this damping into two terms $\gamma_{a,\mathrm{int}_{\mathrm{inv}}}$ and $\gamma_{a,\mathrm{int}_{\mathrm{BL}}}$ obtained from Equation 2.62b,

$$\gamma_{a,\mathrm{int}_{\mathrm{inv}}} = 2 \frac{\rho_1 \nu_1 \coth(k_a |h_1|) + \rho_2 \nu_2 \coth(k_a |h_2|)}{\rho_1 \coth(k_a |h_1|) + \rho_2 \coth(k_a |h_2|)} k_a^2, \tag{2.63b}$$

$$\gamma_{a,\mathrm{int}_{\mathrm{BL}}} = -2 \left(\frac{\sqrt{\nu_1} + \sqrt{\nu_2}}{\dfrac{1}{\rho_1 \sqrt{\nu_1}} + \dfrac{1}{\rho_2 \sqrt{\nu_2}}} \right) \frac{\coth(k_a |h_1|) + \coth(k_a |h_2|)}{\rho_1 \coth(k_a |h_1|) + \rho_2 \coth(k_a |h_2|)} k_a^2. \tag{2.63c}$$

Although these are considered higher-order terms, scaling with ℓ_j^2 or ν_j, it is worth keeping them because the inviscid component $\gamma_{a,\mathrm{int}_{\mathrm{inv}}}$ provides a baseline comparison for boundary-layer corrections, as it is the only non-vanishing dissipation term for irrotational interfacial (and surface) waves [90, 106, 108].

$\gamma_{a,I}$ At the interface, the boundary layer velocity applied to Equation 2.62a results in the leading contribution,

$$\gamma_{a,I} = \frac{\sqrt{|\omega_a|}k_a}{2\sqrt{2}} \left(\frac{1}{\rho_1\sqrt{\nu_1}} + \frac{1}{\rho_2\sqrt{\nu_2}} \right)^{-1} \frac{(\coth(k_a|h_1|) + \coth(k_a|h_2|))^2}{\rho_1 \coth(k_a|h_1|) + \rho_2 \coth(k_a|h_2|)} \tag{2.63d}$$

This damping dominates at order ℓ_j or $\sqrt{\nu_j}$ and does not exist to leading order for free-surface waves, as in [86] and [134].

$\gamma_{a,H}$ The horizontal solid walls also display boundary-layer contributions obtained from Equation 2.62a and the damping reads

$$\gamma_{a,H} = \frac{\sqrt{|\omega_a|}k_a}{2\sqrt{2}} \frac{\dfrac{\rho_1\sqrt{\nu_1}}{\sinh^2(k_a|h_1|)} + \dfrac{\rho_2\sqrt{\nu_2}}{\sinh^2(k_a|h_2|)}}{\rho_1 \coth(k_a|h_1|) + \rho_2 \coth(k_a|h_2|)}. \tag{2.63e}$$

This term also dominates over interior damping, as it scales with ℓ_j or $\sqrt{\nu_j}$.

$\gamma_{a,V}$ Finally, at vertical solid walls, we find again from Equation 2.62a a term at order ℓ_j or $\sqrt{\nu_j}$ at each boundary at r_1 and r_2, as follows,

$$\gamma_{a,V} = \frac{\sqrt{|\omega_a|}}{4\sqrt{2}} \sum_{s=1,2} \frac{\pi r_s N_a^2 R_a^2(r_s) \left(\rho_1\sqrt{\nu_1}\mathcal{G}_{1,a}(r_s) + \rho_2\sqrt{\nu_2}\mathcal{G}_{2,a}(r_s) \right)}{\rho_1 \coth(k_a|h_1|) + \rho_2 \coth(k_a|h_2|)}, \tag{2.63f}$$

with

$$\mathcal{G}_{j,a}(r_s) = \left(1 + \frac{m_a^2}{k_a^2 r_s^2}\right) \coth(k_a|h_j|) - \left(1 - \frac{m_a^2}{k_a^2 r_s^2}\right) \frac{k_a|h_j|}{\sinh^2(k_a|h_j|)}.$$

Out of the presented formulae, this is the only one sensitive to the horizontal geometry of the basin. In fact, regardless of the shape of the cell's cross-section, equations (2.63b), (2.63c), (2.63d) and (2.63e) recover the results in [87], cf. equations (2.66) and (D19). Equation 2.63f is also valid for a regular cylinder and recovers the results of [87] by appropriately modifying R_a and N_a to a cylinder of radius r_2 and taking $r_1 \to 0$.

To illustrate the qualitative behaviour of this model for damping, we consider an example set of fluids with typical physical properties shown in Figure 2.6. As noted in [87], the damping is minimum when both phases have the same depth, i.e., $h_2 = -h_1 = h_0$. Hence, we specialise in this case to numerically evaluate and confirm our assumptions. Figure 2.6(a) verifies that the interior damping may represent a small fraction of the total, especially for low wavenumbers. As expected, deep-water waves, with $k_a h_0 \gg 1$, experience not only more interior damping but more damping in general, as evidenced in Figure 2.6(b). This statement is surprisingly valid also for the

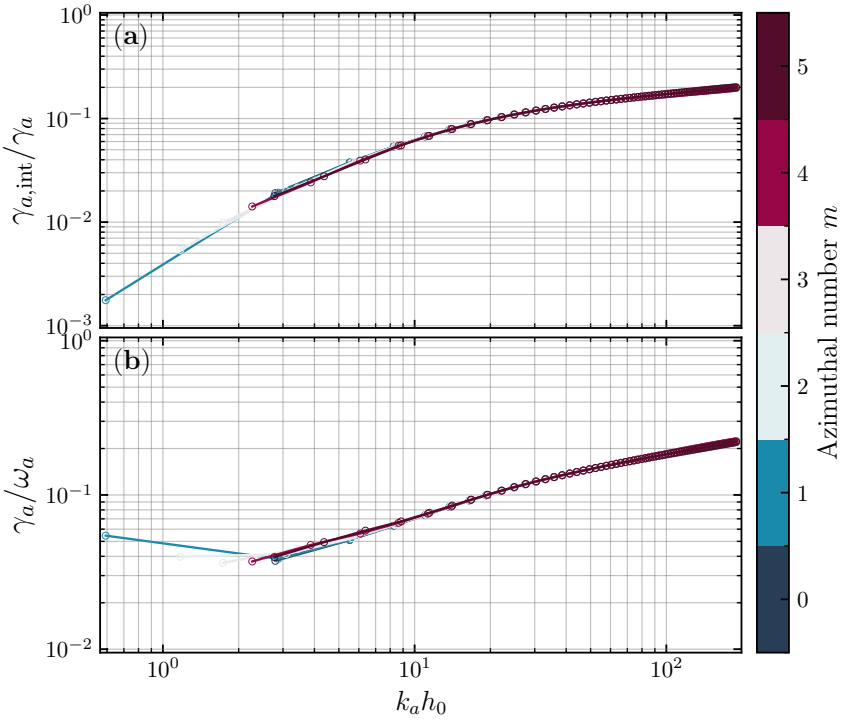

Figure 2.6: Depiction of damping model of equations (2.63) in annular geometry for the first 70 wavenumbers of azimuthal numbers from 0 to 5. Different colours reference the azimuthal numbers m, and each circle denotes the $n-$th order eigenvalue, i.e., k_a is the n_a-th zero of the equation $R'_{m_a}(r_2) = 0$. The higher wavenumbers are densely populated and thus visually overlap for different m's in the plots. In $(\mathbf{a})$, we display the ratio of the interior damping γ_{int} with the total γ_a of each mode k_a. In $(\mathbf{b})$, the ratio of the total damping γ_a with the corresponding dispersion frequency ω_a of each mode k_a. In both panels, the quantities are shown as functions of the dimensionless product $k_a h_0$. For both plots, we choose the following illustrative values: $\rho_1 = 1200\,\mathrm{kg\,m^{-3}}$, $\rho_2 = 900\,\mathrm{kg\,m^{-3}}$, $\nu_1 = 3\,\mathrm{mm^2\,s^{-1}}$, $\nu_2 = 2\,\mathrm{mm^2\,s^{-1}}$, $\sigma = 5\,\mathrm{mN\,m^{-1}}$, $r_2 = 2r_1 = 4\,\mathrm{cm}$, and $h_2 = -h_1 = h_0 = 5\,\mathrm{mm}$.

first few shallow-water modes that fit the geometry, i.e., k_a with $m_a = 0, 1, 2$ and $n_a = 0, 1$. This is a known property of surface waves in small basins [86, 131, 136], and it can be understood in terms of the boundary layer thickness $\ell_a \propto 1/\sqrt{\omega_a}$, which is larger for lower frequencies. In this picture, long wavelengths will experience more damping from their low-frequency flow around the boundaries ($k_a h_0 \ll 1$ in Figure 2.6), whereas short wavelengths tend to be damped by the bulk motion of the fluids since their decreasingly thin boundary layers have less influence on their motion ($k_a h_0 \gg 1$ in Figure 2.6). In the chosen range of wavenumbers, Figure 2.6(b) shows that the assumption of perturbatively small damping compared to the frequency of a mode, i.e., $\gamma_a/\omega_a \ll 1$, seems to hold comfortably.

2.6 Remarks and overview

In the present Chapter, we discussed the theoretical framework behind the construction of EFT simulators using fluid interfaces. We defined the properties and assumptions essential for this development. Working with a series of convenient approximations, we derived a Lagrangian model entirely described by height and velocity variations at the two-fluid interface. Limiting cases of our model can then be used to devise various simulators for gravitational scenarios, as discussed in Section 2.4. We recovered previously proposed linear simulators for flat [4] and cosmological [79] spacetimes and built upon them to lay the groundwork for investigating interacting field theories. Nevertheless, one must be aware that the assumptions required for some of the derivations in sections 2.2 and 2.4 may be overly restrictive, or even unattainable, in experimental realisations. Appropriate modifications of the formalism can improve the description of the underlying physical system used as a simulator and, in turn, reveal novel aspects of the emerging EFT.

We specifically note that the results presented here are valid for systems where the contact angle along the contact line between the fluid-fluid interface and the solid walls is approximately $90°$. However, capillarity is a ubiquitous property of fluids, and the meniscus forming at the edges of the interface can hardly be ignored. In particular, a curved meniscus with a velocity-dependent contact angle causes a consistent deviation between observed damping rates and theoretical predictions not accounting for capillarity, as thoroughly observed in standard references in the field, e.g., [86, 132, 136, 140–142], but also more recently in [143–148]. Many of the methods employed in modifying the theory accordingly are strongly phenomenological and numerical, and cannot yield formulas for damping such as those presented in subsection 2.5.1 and derived in [87]. In certain cases, specific fluids and materials for the basin can be used to reduce the formation of a meniscus. For instance, this was the case in [87, 88, 149], for which a capillary-free dissipation model for low-frequency modes recovered the observed damping with good accuracy. We note, however, that it is not always possible to fine-tune the system to reduce the meniscus, and we must accept the limitations of analytically predicting the damping in such conditions.

Chapter 3

A non-linear EFT simulator: experimental investigations

We build upon one of the cases discussed in Section 2.4 of Chapter 2 and devise a hydrodynamical experiment to simulate interacting field theories. In the following, we will describe a non-linear Effective Field Theory (EFT) simulator on a liquid-liquid interface. Our proposed target system is a theory for the post-inflationary thermalisation of the early Universe, known as preheating, previously discussed in subsection 2.4.3. We will detail the underlying physical phenomenon that appears in both the simulator and the target, namely parametric instabilities, which we describe through the EFT model derived in Chapter 2. The experimental implementation and methods are then presented, followed by a discussion of the results. The contents of this chapter are based on the preprint "Primary thermalisation mechanism of early universe observed from Faraday-wave scattering on liquid-liquid interfaces." [2], the fruit of a long collaboration with Zack Fifer, August Geelmuyden, Sebastian Erne, Anastasios Avgoustidis, Richard J A Hill, and Silke Weinfurtner.

3.1 Non-equilibrium conditions in the early Universe

Experimental evidence indicates that the Universe is homogeneous, isotropic, flat, and continuously expanding [119]. However, the precise connection between the initial singularity of the Big Bang and the observed Universe remains unclear. Inflationary scenarios are at the centre of the significant efforts of modern cosmology in understanding this link. During inflation, gravity acts as a repulsive force, causing the Universe to undergo accelerated expansion. Several inflationary models exist, with varying levels of complexity and degrees of freedom. A simple model involves a scalar field, known as the inflaton, whose classical evolution of its macroscopic condensate recovers an appropriate equation of state to source inflation. For suitable choices of potential,

the field evolves slowly in a potential-dominated era while driving inflation. As the potential energy of the inflaton is converted into kinetic energy, inflation ends, and the field oscillates around the minimum of its potential. The end of inflation leaves a cold and empty universe, very different from the thermal Universe filled with matter that we see today. Hence, the inflationary evolution necessitates a subsequent process of *reheating* [117].

Mukhanov argues that the *"theory of reheating is far from complete (...) [and] the overall picture of inflaton decay depends crucially on the underlying particle physics theory beyond the Standard Model"* [119]. The author then reasons that our interest should be in the final outcome of it, that is, a thermal Friedman Universe with the large-scale structures seen in the present. Investigating toy models for reheating can provide insights into the intermediate stages between inflation and the thermal Universe observed today. During the early phases of reheating, the oscillating inflaton field parametrically amplifies its quantum fluctuations and other coupled matter fields, resulting in an explosive production of particles known as preheating [150]. This process exhibits an initial exponential growth of the occupation numbers in a low-momentum region, called the primary band, followed by a secondary amplification period with higher momentum modes growing at even larger rates [151].

Upon the completion of preheating, a far-from-equilibrium state is established and eventually thermalises, completing the reheating period. However, this thermalisation process results in the loss of significant information about the initial conditions that led to it. Thus, understanding the role of out-of-equilibrium processes in the early Universe may shed light on its initial structure. This necessitates a comprehensive description of the time evolution of Quantum Field Theory (QFT), which cannot be achieved using standard perturbative solution methods based on early and late-time asymptotic behaviours or small deviations from equilibrium [80]. The statistical machinery of EFTs, particularly through the characterisation and evolution of arbitrary-order correlation functions, offers a tool to systematically study these out-of-equilibrium states, as demonstrated in pioneering work on ultra-cold atoms systems [67–69].

Preheating represents one example of the wide-ranging far-from-equilibrium processes that exist in nature, encompassing phenomena such as turbulence in fluids, the formation of storms and the growth of snowflakes [152]. As discussed in Chapter 1, these systems have been out of the scope of classical experimental analogues for gravity and cosmology, and only recently appeared in quantum simulators, e.g., see [71, 73, 74]. Here, we extend the premise of these analogues, and instead of concentrating efforts on operating in a linear regime, we devise and build an experiment that seizes the non-linear dynamics inherent to interfacial waves in fluids to simulate aspects of quantum fields placed in nonequilibrium configurations. With the non-linear EFT presented in subsection 2.4.3, we create a primary instability through the

external parametric driving of the fluid interface and show that certain interfacial modes experience an effective interaction Lagrangian [109], whose onset of non-linearities is investigated. By repeatedly running the experiment, we form a statistical ensemble of the observable, the interfacial height ξ, which allows us to use the methods introduced in [68, 69] for Bose-Einstein condensates (BECs) to validate the EFT of interfacial mode-mode interactions in our system.

3.2 Effective model for interfacial instabilities

The investigation of surface instabilities in liquids induced by an external vibration source has a long history, tracing back to Faraday's pioneering work in 1831 when he first observed it in a water-filled cylindrical glass [114]. Faraday discovered that the unstable surface waves oscillate at half the frequency of the external driver, a phenomenon known as parametric resonance. This behaviour has since been extensively studied and identified in a wide range of physical systems [153], and can be responsible for dramatic events, such as the collapse of bridges [115], the rolling of ships at sea [116], and the thermalisation of our Universe 13.8 billion years ago [117, 118, 150].

In general, when a periodic forcing with frequency ω_{d} acts on these systems, their spectral response exhibits unstable resonance bands at specific frequencies [112]. These unstable bands occur at integer multiples of $\omega_0 \equiv \omega_{\mathrm{d}}/2$ and, within them, parametric amplification happens at a common exponential rate. However, the dominant growth appears at ω_0, the so-called primary instability. As the amplitudes increase, non-linear effects may become significant and restrict the amplification process. As briefly discussed in Chapter 2, the interface between two fluids subjected to a vertical oscillatory acceleration is no different to Faraday's original system and thus undergoes parametric resonance [106].

We showed in subsection 2.4.3 that the interfacial dynamics of a vertically oscillating two-fluid system recovers the Mathieu equation [112], which is a particular form of a more general set of periodically driven equations, or Hill's equations [113]. Here, we keep the assumptions that both fluids have the same depth and sinusoidal forcing acts on the sample cell, but now we allow modes with arbitrary wavelengths and linear damping. Hence, the linear evolution of interfacial modes ξ_a is described by

$$\ddot{\xi}_a + 2\gamma_a \dot{\xi}_a + \omega_a^2(t)\xi_a = 0. \tag{3.1}$$

with

$$\omega_a^2(t) = \frac{(\rho_1 - \rho_2)g(t) + \sigma k_a^2}{\rho_1 + \rho_2} k_a \tanh(k_a h_0). \tag{3.2}$$

Although less familiar, the equation above is also of the Mathieu form, given that

$g(t) = g_0 - F_0 \cos(\omega_d t)$. See Section A.4 in Appendix A for variable definitions that reduce it to the standard dimensionless form of the Mathieu equation [112, 113].

3.2.1 Floquet analysis

A general approach to Hill's equations, and thus Mathieu equations as well, is through Floquet's theorem [112, 113], which states that they admit two solutions of the form $\xi_\pm(t) = \exp(\pm(\lambda + i\beta)t)\zeta(t)$, where $(\lambda + i\beta)$ are complex Floquet exponents, and ζ are periodic functions with period $2\pi/\omega_d$, as a consequence of the periodicity of $F_0(t)$. The two solutions correspond to positive and negative real parts of the Floquet exponents, and their response is said to be harmonic if $\beta = \pm\omega_d$, or subharmonic if $\beta = \pm\omega_d/2$. In both cases, this analysis predicts that, for a fixed driving amplitude F_0, some of the available interfacial k_a-modes experience an unstable evolution, i.e., they display exponential growth or decay. If we write the periodic component $\zeta(t)$ as a Fourier series with constant coefficients $\{\zeta_n\}$, i.e., $\zeta(t) = \sum_n \zeta_n \exp(in\omega_d t)$, then the exponentially unstable solution can be written as follows,

$$\xi_a = \sum_{n=-\infty}^{\infty} \zeta_{a,n} \exp\left(\lambda_a t + in\frac{\omega_d}{2}t\right), \text{ with } \lambda_a > 0. \tag{3.3}$$

By applying this form to Equation 3.1, one obtains an eigenvalue problem, whose eigenvectors are given by the amplitudes $\{\zeta_{a,n}\}_n$ and the eigenvalues are λ_a [106, 112]. See Section B.1 in Appendix B for the derivation and discussion of the numerical procedure. In the following, we employ the definition $\omega_d \equiv 2\omega_0$, and refer to ω_0 as the primary instability frequency.

Before turning to the analysis of solutions (3.3), we briefly revise the geometrical traits of our system. As in our derivation for a damping model in subsection 2.5.1, we consider that the two immiscible fluids are confined in an annular cylinder basin. This geometry suggests that interfacial modes can be decomposed on the basis of spatial eigenfunctions $\chi_a(r, \theta)$ of the 2D Laplacian on the annular disk with Neumann boundary conditions at vertical walls $r = r_1$ and $r = r_2$, given in Equation 2.56c. The $\theta-$dependence in the modes is labelled by an integer m_a, the azimuthal number, ranging from $-\infty$ to ∞. Intuitively, it corresponds to the number of troughs and crests in a standing wave in the angular direction. Additionally, the zeros obtained from the first derivative of the radial component $R_a(r)$ at the boundaries yield the wavenumber k_a of the mode. Another nonnegative integer label applies in this case: the order n_a of the zero corresponding to k_a. As in the case of Bessel functions, n_a indicates the number of times the radial function $R_a(r)$ crosses zero in the interval $r_1 \leq r \leq r_2$. Because the pair of numbers (m_a, k_a) is unique [139], we can also uniquely label the interfacial annular modes by (m_a, n_a), i.e., their numbers of azimuthal peaks and radial

nodes, respectively. In the following, we use the label a to indicate general modes and the pair (m_a, n_a) when referring to specific mode numbers.

In Figure 3.1, we show the numerical results of the Floquet instability analysis with the fluid, mechanical and geometrical properties characteristic of the experiment that we will present in the next section (see Table 3.1). The typical form of instability charts is shown in panels (a) and (b), cf. [112], with solid lines denoting the critical amplitudes F_0 with respect to gravity g_0 where modes k_a can cross between the unstable (shaded) and stable evolution bands. We say the modes undergo parametric resonance (or instability or amplification) in the shaded regions. As expected from Equation 3.3, we observe in Figure 3.1 instability bands around all integer multiples of half the driving frequency, ω_0, and their corresponding wavenumbers. We also note that the width of these resonance regions decreases as the frequency increases. Indeed, a general result of Floquet analysis is decreasingly small instability coefficients for increasing

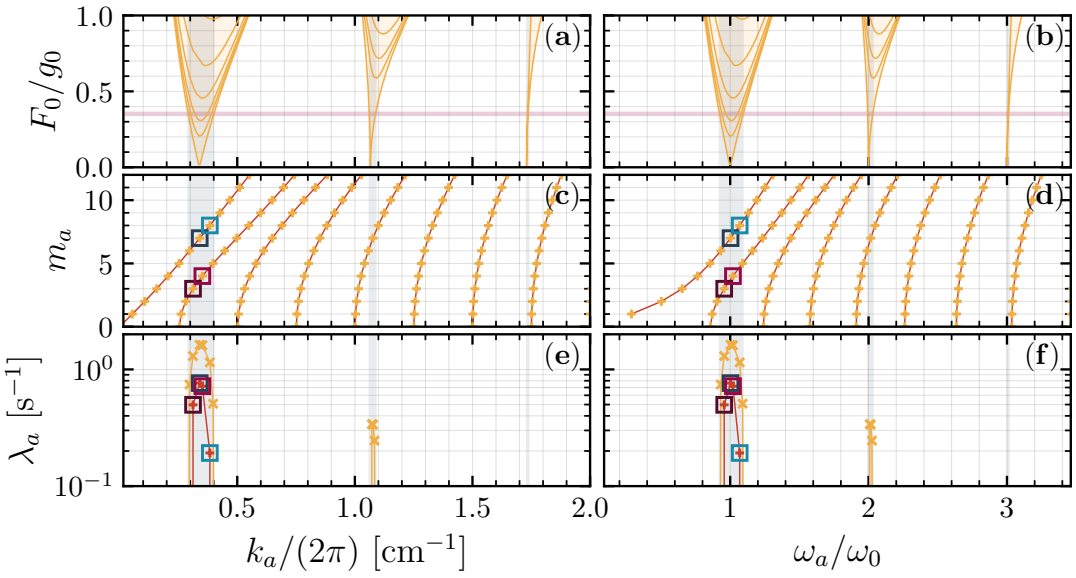

Figure 3.1: In $(\mathbf{a})$ and $(\mathbf{b})$, we display the instability charts for the critical forcing amplitudes F_0/g_0 as a function of the wavenumber and frequency of the modes, respectively. Inside the shaded yellow regions, the modes experience unstable evolution. Solid yellow lines denote the transition to the stable regions with increasing damping, with the innermost line having the stronger damping. The lowest outermost curves have no damping and serve as a boundary between the stability domains. The average amplitude of the experiment $F_0 = 0.352(5)g_0 = 3.45(5)\,\mathrm{m\,s^{-2}}$ is shown by the horizontal shaded line. Its intersection with the outermost instability curves creates a band, which we represent by a shaded grey vertical region in all panels. For reference, panels $(\mathbf{c})$ and $(\mathbf{d})$ have the estimated discretised spectrum of wavenumbers k_a and corresponding frequencies ω_a of the azimuthal modes m_a in the spatial eigenfunctions $\chi_a(r,\theta)$. The lines in $(\mathbf{c})$ and $(\mathbf{d})$ connect wavenumbers k_a with constant order n_a, starting from zero. In $(\mathbf{e})$ and $(\mathbf{f})$, the instability coefficients λ_a for $F_0 = 0.352(5)g_0$ in the case without damping (yellow line) and with the damping model γ_a of subsection 2.5.1. Coloured squares highlight the predicted unstable modes in the presence of damping.

frequencies [112].

This chart has two critical features in its application to our system. First, for a fixed forcing F_0, damping effectively narrows the instability bands. It also shifts their centres towards higher momenta, as seen by the higher yellow curves crossing the purple line of constant acceleration. Another perspective is that when considering two modes with similar wavenumbers $k_a \sim k_b$ but with different damping rates, the one more damped needs a higher forcing amplitude F_0 than the less damped one. This concept has been observed in experiments, e.g., [106, 154]. The second feature concerns the reduced density of states in our system. As discussed in Chapter 2, the confined geometry of the basin enforces a discretisation of the eigenvalues of the 2D Laplacian, i.e., the solutions $\chi_a(r,\theta)$ as in Equation 2.18, through boundary conditions at the walls. For higher momenta, we observed in Figure 2.6, and here in Figure 3.1(c-d), the interfacial wavenumbers k_a are densely packed and increasingly close to each other. However, the modes are coarsely spaced for lower k_a. This coarsening at low momenta results in fewer modes fitting inside the most prominent instability bands, i.e., those at lower frequencies. Hence, in our context, a broader instability band centred around low momenta will not necessarily entail a broad band of modes undergoing parametric amplification, as it would be in a system without boundaries and with a continuous spectrum.

Finally, we stress that the lines of constant damping are merely for conceptual rigour. In reality, the modes present varying damping rates according to their wavenumbers, as discussed in subsection 2.5.1. Hence, even inside a narrow frequency resonance band, modes may dampen at different rates. We depict this variation in Figure 3.1(e-f), where the Floquet instability coefficients λ_a were computed using the average forcing amplitude of the experimental setup. We first disregarded any dissipation (yellow crosses) and observed that, in the first resonance band, the modes $(m_a, n_a) = \{(3,1),(4,1),(5,1),(6,0),(7,0),(8,0)\}$ display positive coefficients λ_a, and hence should undergo exponential growth in the absence of damping. Also, in the second band, for azimuthal numbers $m_a < 12$, the modes $(m_a, n_a) = \{(6,4),(7,4),(8,4)\}$ were unstable. Conversely, when using the damping model of Equation 2.63 (red crosses and coloured squares), we noted a strong suppression of the instabilities in higher wavenumbers. In fact, the only remaining unstable modes were $(m_a, n_a) = \{(3,1),(4,1),(7,0),(8,0)\}$.

From the results in Figure 3.1(e-f), we see that the modes $(4,1)$ and $(7,0)$ sit very close to each other in the centre of the primary instability band with predicted wavenumbers $k_{4,1} \simeq (2\pi)0.35\,\mathrm{cm}^{-1}$ and $k_{7,0} \simeq (2\pi)0.34\,\mathrm{cm}^{-1}$, respectively. Their amplification rates λ_a, however, are not exactly the same, especially when damping is present. In the absence of damping (yellow crosses in Figure 3.1(e-f)), their estimated rates are $\lambda_{4,1} \simeq 1.61\,\mathrm{s}^{-1}$ and $\lambda_{7,0} \simeq 1.62\,\mathrm{s}^{-1}$. The damping model in Equation 2.63

predicts decay rates for these modes of $\gamma_{4,1} \simeq 0.92\,\mathrm{s}^{-1}$ and $\gamma_{7,0} \simeq 0.88\,\mathrm{s}^{-1}$, and hence their instability rates reduce to $\lambda_{4,1} \simeq 0.70\,\mathrm{s}^{-1}$ and $\lambda_{7,0} \simeq 0.74\,\mathrm{s}^{-1}$ (red and dark blue squares in Figure 3.1). Quantitatively, this means that if both interfacial modes have the same amplitude as the driver starts, after 100 cycles of oscillation, the amplitude of the mode $(7,0)$ will be approximately 2.13 times larger than that of $(4,1)$. In practice, due to the fluctuating character of the interface, as introduced in Chapter 2, we will see that the modes will not start from the same initial state amplitude, and it is possible to explore conditions where the unstable evolution of one of the modes dominates over the others.

3.2.2 Dominant and subdominant non-linear instabilities

Within the assumptions of this chapter, the interfacial evolution of the modes is determined by the truncated non-linear Lagrangian (2.29), which reduces to

$$\frac{L}{\Sigma} = \frac{1}{2}\sum_a \frac{\rho_1+\rho_2}{k_a \tanh(k_a h_0)}\left(\dot{\xi}_a^2 - \omega_a^2(t)\xi_a^2\right) + \frac{1}{2}\sum_{a,b,c}(\rho_1-\rho_2)\,\mathcal{A}_{cab}\xi_c\dot{\xi}_a\dot{\xi}_b + \frac{1}{4}\sum_{a,b,c,d}\left[(\rho_1+\rho_2)\,\mathcal{A}_{cdab}\dot{\xi}_a\dot{\xi}_b + \frac{\sigma}{2}\mathcal{B}_{abcd}\xi_a\xi_b\right]\xi_c\xi_d, \quad (3.4)$$

with coefficients

$$\mathcal{A}_{cab} = \mathbb{C}_{cab}\left(1 + \frac{k_c^2 - k_a^2 - k_b^2}{2k_a k_b \tanh(k_a h_0)\tanh(k_b h_0)}\right), \quad (3.5a)$$

$$\mathcal{A}_{cdab} = -\frac{k_a\tanh(k_a h_0) + k_b\tanh(k_b h_0)}{k_a k_b \tanh(k_a h_0)\tanh(k_b h_0)}\left(\mathbb{D}_{abcd} + \mathbb{D}_{cdab}\right) + \frac{1}{2}\sum_e \frac{(k_e^2+k_a^2-k_c^2)(k_e^2+k_b^2-k_d^2)}{k_a T_{j,a} k_b T_{j,b} k_e T_{j,e}}\mathbb{C}_{cae}\mathbb{C}_{deb}, \quad (3.5b)$$

and Raleigh's dissipation function [130]

$$\frac{Q_0}{\Sigma} = \sum_a \frac{\rho_1+\rho_2}{\tanh(k_a h_0)}\gamma_a\dot{\xi}_a^2. \quad (3.5c)$$

We stress that the Lagrangian above implicitly entails that, in the infinite discretised spectrum of interfacial waves, the evolution of a single mode is intertwined with the dynamics of infinitely many others. This unveils the inherent complexity of interacting systems, and such an impractical aspect of a non-linear description is what motivates us to approach it from an even more approximate perspective. We then limit this endless intricacy to the study of dominant-subdominant counterparts of the interfacial dynamics, as proposed in [155, 156]. Following the final discussion of the previous section, we now devise a scenario where, in a set of interfacial modes $\{\xi_a\}$ undergoing

parametric resonance, one of them, ξ_D, grows dominantly over the others. Specifically, we require the amplitude of the latter to be at least one order of magnitude (10 times) larger than that of the former ones, i.e., $|\xi_D| \gg |\xi_a|$, for $a \neq D$.

As argued in the example of subsection 2.4.3, the coefficients $\mathcal{A}_{cab}$, $\mathcal{A}_{cdab}$ and $\mathcal{B}_{cdab}$ act as momentum conservation constraints. As shown in their definitions above and in Equation A.37, they are proportional to integrals of products of the spatial functions $\chi_a(r,\theta)$ over the horizontal cross-section of the basin. For instance, the cubic coefficient $\mathbb{C}_{cab}$ reads

$$\mathbb{C}_{cab} = \frac{1}{\Sigma}\iint \mathrm{d}r\ r\mathrm{d}\theta \chi_c\chi_a\chi_b \propto \int_{-\pi}^{\pi} \mathrm{d}\theta \cos(m_c\theta)\cos(m_b\theta)\cos(m_a\theta) \propto \delta_{m_c,\pm|m_a\pm m_b|}. \tag{3.6}$$

Thus, similarly to Equation 2.50 for the rectangular basin, in cylindrical geometries, the following constraints apply,

$$\mathcal{A}_{cab} \propto \delta_{m_c,\pm|m_a\pm m_b|}, \tag{3.7a}$$

$$\mathcal{A}_{cdab}, \mathcal{B}_{cdab} \propto \delta_{\pm m_c \pm m_d, \pm m_a \pm m_b}. \tag{3.7b}$$

Note, however, that no explicit restrictions on the second mode number n_a, and hence k_a, appear, in contrast with the rectangular symmetry. In the cylindrical case, the coefficients satisfying the delta relations above have to be computed numerically, and their values will determine the constraints on the wavenumbers.

In the presence of the dominant mode ξ_D, we now consider that the self-interaction of the remaining modes ξ_a is negligible compared to ξ_D. Hence, from the Euler-Lagrange equations for the system above, one finds the corresponding equations of motion for an arbitrary mode ξ_a, including ξ_D itself, which read

$$\begin{aligned}
&\ddot{\xi}_a + 2\gamma_a\dot{\xi}_a + \omega_a^2(t)\xi_a \\
&\quad + \frac{1}{2}A_{12}k_a\tanh(k_ah_0)\left[(2\mathcal{A}_{DDa} - \mathcal{A}_{aDD})\,\dot{\xi}_D^2 + 2\mathcal{A}_{DDa}\xi_D\ddot{\xi}_D\right] \\
&\quad + \frac{1}{2}k_a\tanh(k_ah_0)\left[(2\mathcal{A}_{DDDa} - \mathcal{A}_{aDDD})\,\xi_D\dot{\xi}_D^2 + \mathcal{A}_{DDDa}\xi_D^2\ddot{\xi}_D\right] \\
&\quad - \frac{1}{2}\frac{\sigma}{\rho_1+\rho_2}k_a\tanh(k_ah_0)\mathcal{B}_{DDDa}\xi_D^3 \simeq \eta_a(t),
\end{aligned} \tag{3.8}$$

where $A_{12} = (\rho_1 - \rho_2)/(\rho_1 + \rho_2)$ is the Atwood number. We have included a new quantity $\eta_a(t)$, which is a stochastic noise term as discussed in Chapter 2. It encompasses the coarse-graining of the microscopic dynamics, which is dominated by random molecular motion, resulting in a jittering interface. We note two interesting cases of the equation above, which we analyse through a generic formula for the dynamics of

ξ_a given by

$$\ddot{\xi}_a + (2\gamma_a + \tilde{\gamma}_a[\xi])\,\dot{\xi}_a + \left(\omega_a^2(t) + \tilde{\delta}_a[\xi]\right)\xi_a = \eta_a(t) + \tilde{\eta}_a[\xi], \tag{3.9}$$

with nonlinear damping $\tilde{\gamma}_a[\xi]$, frequency detuning $\tilde{\delta}_a[\xi]$ and source $\tilde{\eta}_a[\xi]$ terms appropriately identified in each case.

First, since the amplitude of the dominant mode grows larger than all others, it is reasonable to consider that its evolution is not influenced by the remaining interfacial modes. Naturally, this assumption can only be valid as long as their amplitudes are not comparable to the dominant one. Hence, by disregarding its interaction with other modes, ξ_D will approximately satisfy Equation 3.9 upon identifying $a \equiv D$ and with the following nonlinear terms

$$\tilde{\gamma}_D[\xi] \approx -\gamma_D k_D \tanh(k_D h_0)\tilde{\mathcal{A}}_D \xi_D^2, \tag{3.10a}$$

$$\tilde{\delta}_D[\xi] \approx \frac{1}{2} k_D \tanh(k_D h_0)\left[\tilde{\mathcal{A}}_D(\dot{\xi}_D^2 - \omega_D^2(t)\xi_D^2) - \frac{\sigma}{\rho_1+\rho_2}\tilde{\mathcal{B}}_D \xi_D^2\right], \tag{3.10b}$$

$$\tilde{\eta}_D[\xi] \approx 0, \tag{3.10c}$$

where $\tilde{\mathcal{A}}_D \equiv \mathcal{A}_{DDDD}$ and $\tilde{\mathcal{B}}_D \equiv \mathcal{B}_{DDDD}$. As Miles points out in [85], the equation of a single self-interacting and dominant interfacial mode resembles that of a parametrically forced and viscously damped pendulum in weakly nonlinear motion, with an effective length proportional to $k_D^{-1}\coth(k_D h_0)$. The fluid system, however, offers the possibility of interaction between the various pendulum-like interfacial modes.

In the second case, we consider a mode ξ_a whose azimuthal number is the same as that of the dominant, i.e., $m_a \equiv m_D$. Thus, the quadratic terms in Equation 3.8 will vanish unless $m_D = 0$ by virtue of the angular conservation conditions Equation 3.7, i.e., $\mathcal{A}_{DDa}, \mathcal{A}_{aDD} \propto \delta_{m_D,\pm|m_D \pm m_D|} \equiv 0$, for $m_D \neq 0$. In our discussion, we do not consider the case of an axisymmetric ($m = 0$) dominant mode, i.e., $m_D \neq 0$, as it is the only one interacting with itself at cubic order in the Lagrangian, and thus experiences stronger non-linear frequency detuning and damping, even for small amplitudes [154]. Under these conditions, the dynamical evolution of a subdominant mode ξ_a follows from Equation 3.9, with non-linear coefficients given by

$$\tilde{\gamma}_a[\xi] \approx 0, \tag{3.11a}$$

$$\tilde{\delta}_a[\xi] \approx 0, \tag{3.11b}$$

$$\tilde{\eta}_a[\xi] \approx \frac{1}{2} k_a \tanh(k_a h_0)\left[\mathcal{A}_{DDDa}\xi_D\ddot{\xi}_D + (2\mathcal{A}_{DDDa} - \mathcal{A}_{aDDD})\dot{\xi}_D^2 - \frac{\sigma}{\rho_1+\rho_2}\mathcal{B}_{DDDa}\xi_D^2\right]. \tag{3.11c}$$

The equations above indicate that the dominant mode sources the motion of ξ_a through $\tilde{\eta}_a$. We also note that the infinitely many discretised matrix components $\mathcal{A}_{cdab}$ and $\mathcal{B}_{cdab}$ reduced to the three elements shown above, i.e., $\mathcal{A}_{DDDa}$, $\mathcal{A}_{aDDD}$ and $\mathcal{B}_{DDDa}$.

The predictions of the models presented in this section, both for the instability and non-linear analysis, will be put in contrast with experimental observations later in this chapter. We will also discuss how some of the non-idealised aspects of our experiment that are not accounted for in the modelling appear. Regardless of the limitations of piecing together an EFT and comparing it to an experiment, we will show that dynamical features of the target system may still be observed under the scope of the proposed EFT. In the following section, we discuss the experiment that allowed us to empirically verify these statements and validate the theory through statistical methods.

3.3 Experimental setup and methods

A general view of the setup is depicted in Figure 3.2. A fluid sample cell (1) containing two immiscible liquids is placed on a shaking platform suspended by four springs and guided by four metal rods with pneumatic air bearings (4). Compressed air flows through the bearings, allowing the platform to move virtually frictionless and composing a spring-mass system forced by a voice-coil actuator (3). The rods, springs and the actuator's coil base are firmly attached to an outer metal frame, placed on an active noise-cancelling table. These components form the mechanical vibration system that oscillates the fluid cell. Independently connected to the outer frame, an array of 225 densely packed red LEDs (2) illuminates the sample from below. Their light goes through the glass windows of the cell and the fluids, reflects from a 45° mounted mirror (5), and finally reaches a camera (6) in the distance. These components form our imaging system.

A static checkerboard pattern sits on the light source and is imaged by the camera. As waves form at the two-fluid interface, the images of the pattern are distorted in a way that allows us to reconstruct its 3D profile through a modified detection scheme that we will discuss later in this section and in Chapter 4. Experimental control and acquisition were done through a centralised script interfacing with a data acquisition card[1], allowing for the automated and synchronised repetition of individual runs. In Figure 3.3, we illustrate the timeline of 1500 realisations in one experiment and the pipeline of acquisition and analysis. The associated datasets will be presented and explored throughout this chapter. In the following, we discuss the different components of the experimental design and the technical methods used for running the experiment, acquiring data and processing it.

[1] National Instruments DAQ PCIeX card

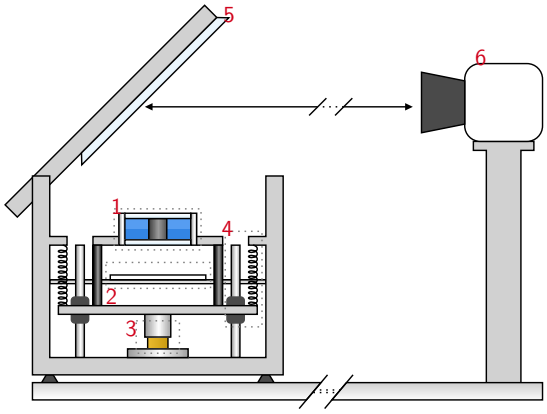

Figure 3.2: Illustrative schematics of the experimental setup, with dashed rectangles indicating its main components. (1) Annular cylinder two-fluid sample cell. (2) Back-lighting LED array with a checkerboard pattern on top. (3) Voice-coil actuator used for driving the spring-mass system. (4) Springs attached to the outer frame and lower vibration plate, which is allowed to move vertically due to pneumatic air bearings guided by vertical rods. (5) 45-degree slanted mirror for imaging the sample. (6) Camera used for recording the interface from a large distance.

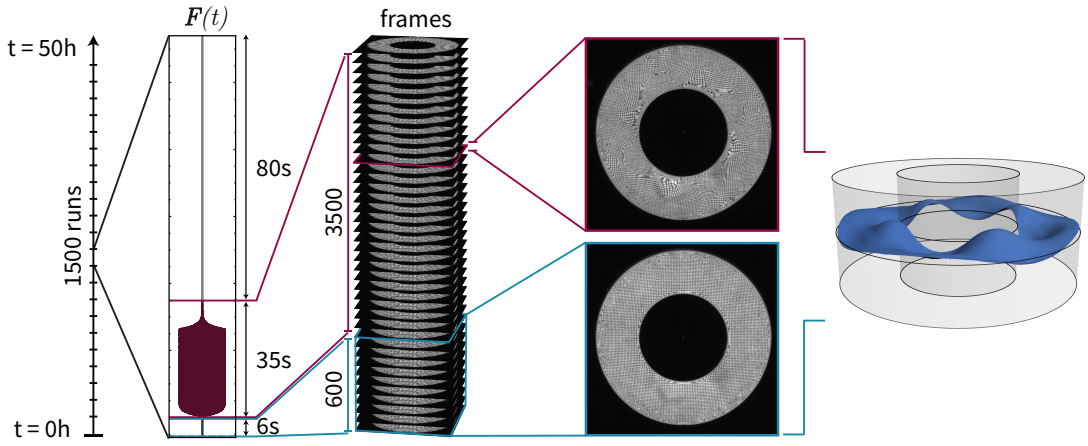

Figure 3.3: Overview of the experimental acquisition and processing pipelines. Columns from left to right: (First) Portrayal of the 50-hour long timeline of 1500 runs with approximately 120 seconds each. (Second) Typical acceleration profile $\boldsymbol{F}(t)$ of the sample cell during a repetition, with an initial resting time of 6 seconds (turquoise region), followed by 160 oscillations of the platform plus the decay period, resulting in 35 seconds of vibration and relaxation of the system (maroon region). Finally, the sample is allowed to rest for a dead time of 80 seconds (grey region). (Third) Depiction of the acquired array of frames with images of the two-fluid interface at a rate of 100 frames per second during the first two sections of each repetition. (Fourth) The first 600 images are used to create a time-averaged reference of the resting interface, shown in the lower turquoise square. In each repetition, a dim LED indicator was turned on with the actuator to signal the start of the driving period, allowing for synchronising the images with the acceleration data. The subsequent 3500 frames where the indicator appears are then individually compared with the reference. A sample image of the driven interface is shown in the top maroon square. (Last) Three-dimensional profile of the two-fluid interface obtained from the sample and reference images after digital processing.

3.3.1 Vibration platform and mechanical performance

In order to evaluate and monitor the mechanical performance of the vibration platform, three-axis acceleration measurements were acquired over time from an accelerometer mounted to the fluid cell plate. We denote the forcing that the actuator produced on the fluid cell by $\boldsymbol{F}(t)$ and decompose it into a vertical amplitude, $F_0(t)$, and a component in the horizontal direction, $\tilde{\boldsymbol{F}}(t)$, with amplitude $\tilde{F}_r \equiv |\tilde{\boldsymbol{F}}|$. A sample measurement of $\boldsymbol{F}(t)$ is shown in Figure 3.4, where we see in panel (a) that $F_0(t)$ displays the typical transient envelope of a driven damped oscillator around resonance [157, 158]. After a few seconds of driving, the vertical acceleration reaches a steady sinusoidal state $F_0(t) \approx F_0 \cos(\omega_\mathrm{d} t)$, with approximately constant amplitude F_0 and frequency ω_d. Once the actuator turns off at 26 seconds, the system dampens back to its resting position, granting $F_0(t)$ with a characteristic exponential decay tail.

Since the maximum sinusoidal response happens around the resonance, we find it by sweeping through various driving frequencies until a maximum steady-state oscillation amplitude F_0 is reached. We can extract it from the measured quantity $F_0(t)$ by

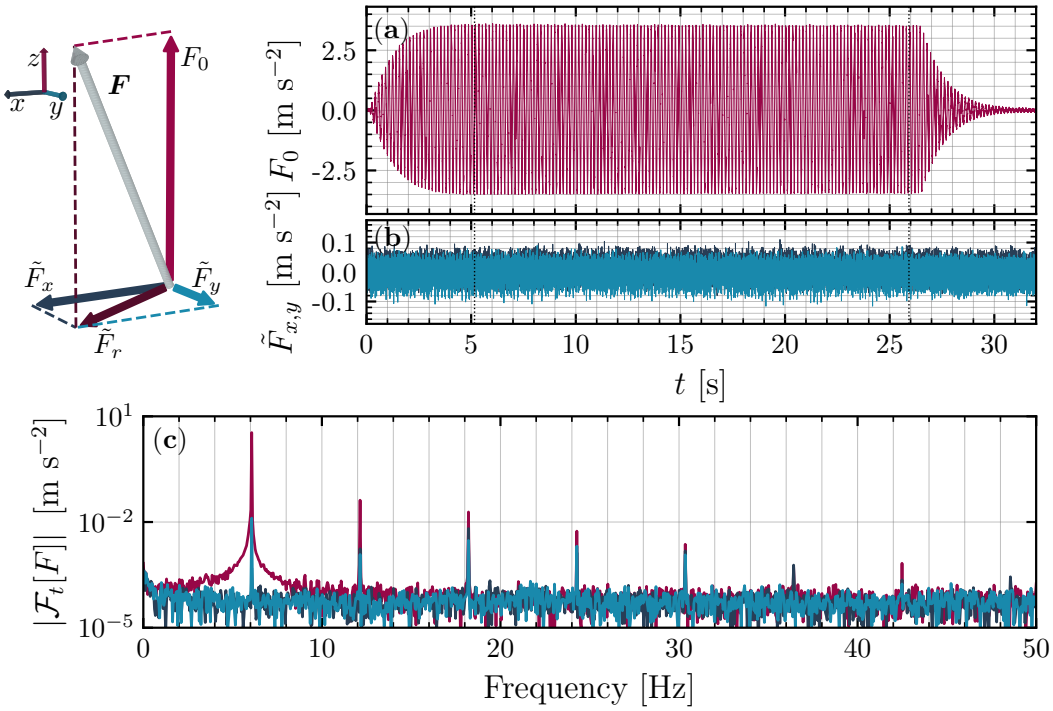

Figure 3.4: (Top left) Depiction of the forcing acceleration vector $\tilde{\boldsymbol{F}}$ with an exaggerated deviation from the $z-$direction. Typical acceleration profiles measured in an example experimental run in the vertical and horizontal directions are shown in $(\mathbf{a})$ and $(\mathbf{b})$, respectively, with matching colours as the vectors on the left. In $(\mathbf{c})$, we display the frequency spectrum of each component over a window between 5 and 26 seconds relative to the onset of the drive at $t = 0$ obtained from the Fourier transform in time, $\mathcal{F}_t[F]$. The fundamental resonance frequency of the oscillation was at 6.07 Hz, coinciding with the dominant spectral component.

computing its Fourier transform in time, $\mathcal{F}_t[F_0](\omega)$, and examining its spectrum, where an amplitude peak should appear around the oscillation frequency. In Figure 3.4(c), the Fourier spectrum of all three acceleration components is shown. As expected, the most prominent peak appears at $\omega_{\rm d} = (2\pi)6.07\,{\rm Hz}$, and its amplitude corresponds to that of the steady-state oscillation, i.e., $F_0 = |\mathcal{F}_t[F_0](\omega_{\rm d})|$. A similar analysis applies to the oscillation amplitudes of horizontal components.

We evaluated the quality and performance of our bespoke vibration platform through two measures. First, we required that the oscillating acceleration exhibited a steady-state profile as sinusoidal as possible, i.e., the Total Harmonic Distortion (THD) of the oscillator was minimal. The THD of a signal is defined as the ratio between its amplitude accumulated over all harmonics and that of the fundamental frequency [159, 160], i.e.,

$$\mathrm{THD} = \frac{\sqrt{\sum_{n\geq 2} A^2_{n\omega_f}}}{A_{\omega_f}}, \tag{3.12}$$

where $A_{n\omega_f}$ denotes the signal amplitude of the $n-$th harmonic of the fundamental frequency ω_f. This quantity measures to what degree a signal deviates from an exact sinusoidal profile. Hence, for sine or cosine waves, the THD is zero, whereas, for instance, a periodic rectangular wave has $\mathrm{THD} \approx 48.4\%$ [159]. In our system, the amplitudes $A_{n\omega_f}$ are obtained from the Fourier spectrum of the acceleration through the procedure described before (peaks in Figure 3.4(c)).

Second, to keep proximity with the theory presented in Chapter 2, we needed to confine the motion of the sample cell to the vertical direction, i.e., reduce the horizontal components of the acceleration $\boldsymbol{F}(t)$. For that, the outer frame was built on adjustable levelling feet, which, together with accelerometer measurements, enabled its alignment with respect to the $z-$direction, i.e., the axis of gravity. Following industry standards [161], we measured the deviation of $\boldsymbol{F}(t)$ from $\hat{\boldsymbol{z}}$ by the cross-axis ratio,

$$\mathrm{r_{acc}} = \frac{\tilde{F}_r}{F_0}, \tag{3.13}$$

i.e., the ratio between the horizontal and vertical oscillation amplitudes at the driving frequency.

For all 1500 repetitions during the experiment, both measures and the vertical amplitude F_0 are shown in Figure 3.5. In panel (d), we also display the measured ambient temperature for reference. In panel (b), we observe a consistent distribution of the cross-axis ratio $\mathrm{r_{acc}}$, which averaged to $0.396\% \pm 0.004\%$. These values are way better than the industry standard of 10% [161] in our frequency range and comparable to those in [162], reassuring the performance quality of our vibration platform in reducing cross-axis motion. Similarly, the THD in panel (c) averaged to $1.34\% \pm 0.008\%$ (cf. [162]), reinforcing that the steady oscillation profile throughout the entire exper-

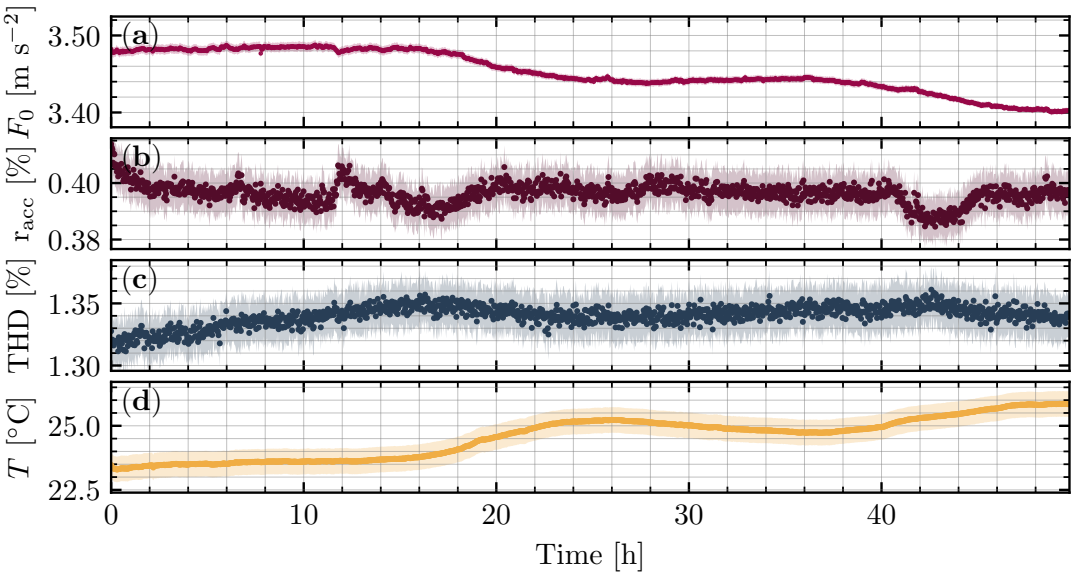

Figure 3.5: Mechanical performance measures of the vibration platform over 1500 realisations during approximately 50 hours. All measures were computed with values extracted during the steady-state region of the oscillations, and each marker corresponds to one repetition. In $(\mathbf{a})$, we show the evolution over the experiment of the vertical acceleration amplitude F_0 extracted from the fundamental frequency at $6.07\ \mathrm{Hz}$. Similarly, $(\mathbf{b})$ and $(\mathbf{c})$ respectively display the cross-axis ratio $\mathrm{r_{acc}}$ of (3.13) and total harmonic distortion (THD) of (3.12). The ambient temperature T throughout the experiment is shown in $(\mathbf{d})$ for reference. In all panels, the shaded regions indicate the uncertainty of the respective quantities.

iment is indeed close to an ideal sinusoidal one. Both quantities indicate that the acceleration of the vibration platform in the steady-state region can be well approximated by $\boldsymbol{F}(t) = F_0 \cos(\omega_\mathrm{d} t)\hat{\boldsymbol{z}}$. Finally, we note that a clear trend appears in the driving amplitude F_0 (see Figure 3.5(a)), which we could also identify in the ambient temperature (Figure 3.5(d)). However, this evident correlation between these two quantities does not seem to have affected the cross-axis motion or the harmonic quality of the vibration system. Additionally, regardless of its trend, the amplitudes throughout the experiment remained within $\pm 1.5\%$ of the average $3.45\,\mathrm{m\,s^{-2}}$. As we will later discuss, these variations in the acceleration amplitudes did not result in any dramatic deviation from the expected interfacial dynamics. Accordingly, the desired qualitative behaviour persisted throughout the repetitions, and quantitative deviations were accounted for when using the theoretical model.

3.3.2 Sample cell, biphasic solution and their properties

The two liquids were completely sealed in a custom closed annular cylinder basin with depth $2h_0 = 35\,\mathrm{mm}$, as in Figure 2.5. The inner and outer cylinders of the sample cell, with radii $r_1 = 20\,\mathrm{mm}$ and $r_2 = 40\,\mathrm{mm}$, were machined from solid nylon, and the transparent top and bottom windows were machined from transparent polycarbonate.

In order to precisely control the relative fluid depths and ensure an uncontaminated sample cell, the basin was filled using threaded Luer lock [163] adapters and precision syringes. This procedure also prevented air bubbles from appearing while ensuring an unpolluted interface.

When selecting the fluids used in this setup, some considerations were necessary to guarantee that the assumptions in Chapter 2 were, at least partially, fulfilled. The condition of immiscibility is readily satisfied by many binary fluid systems, e.g. [88, 164, 165], with varying degrees of interfacial tension and viscosity. We chose a biphasic solution consisting of an ethanol-water (organic) phase as the upper fluid and a potassium carbonate (aqueous) phase as the lower fluid [166]. The homogeneous mixture between water and aliphatic alcohols, such as ethanol, can undergo phase separation through a process called *salting out*, where an inorganic salt, such as potassium carbonate, is added to the mixture. The high ionic strength of the dissolved salt pushes alcohol molecules away from their hydrogen-bonded water molecules. The solution eventually reaches a liquid-liquid equilibrium, where the salt concentration is negligible in the organic phase and similarly for the alcohol in the aqueous phase.

Since the water molecules are highly soluble in both solutions, the interface between them is smeared and largely dependent on the concentrations of each component. Following the procedure described in [166], we observed a visible interface in a solution prepared with the concentration in line 2 of Table 1 in [166]. Accordingly, each kilogram of the biphasic solution was prepared with $310\,\mathrm{g}$ of ethanol (Fisher Chemical: E/0600DF/15), $540\,\mathrm{g}$ of distilled water (Gibco™ 15230001), and $150\,\mathrm{g}$ of anhydrous potassium carbonate (Fisher Chemical: P/4080/60). The preparation is done in controlled conditions to prevent contaminants in the bulk of each phase and deposits at their interface. The dissolution of the salt in the ethanol-water mixture is exothermic and raises the temperature of the solutions from room temperature ($20\,^\circ\mathrm{C}$) to approximately $30\,^\circ\mathrm{C}$. Thus, the final biphasic solution was allowed to settle for several hours to cool down before samples were taken from the lower and upper phases to fill the sample cell.

For reference, some physical properties of both phases are shown in Table 3.1 with their estimated uncertainties. The densities ρ_j were measured using density bottles (BRAND® BLAUBRAND®: BR43328), and their kinematic viscosities ν_j, using a U-tube viscometer (Poulten Selfe™: 1619/02) for low-viscosity fluids. The interfacial tension σ between the liquids was estimated using the pendant drop method [167]. Finally, a digital refractometer (Kern: ORF) was used to measure the refractive indices n_j of each phase.

Table 3.1: Measured fluid properties (ρ_j: density; ν_j: kinematic viscosity; n_j: optical density or refractive index; σ: interfacial tension of the liquid-liquid interface) with their uncertainty at $20\,^{\circ}\mathrm{C}$. The index $j = (1, 2)$ labels the separate fluid phases.

Property	Fluid 1 (lower phase)	Fluid 2 (upper phase)
ρ_j $[\mathrm{kg\,m^{-3}}]$	$1276(10)$	$907(7)$
ν_j $[\mathrm{mm^2\,s^{-1}}]$	$2.35(3)$	$3.28(1)$
n_j $[\,]$	$1.385(2)$	$1.364(2)$
σ $[\mathrm{mN\,m^{-1}}]$	$2.5(5)$	

3.3.3 Imaging system and detection scheme

To reconstruct the profile of the two-fluid interface, we employed a variant of the two-dimensional Fourier Transform Profilometry [89], adapted to the particularities of our setup. A brief presentation of the literature underlying this method will be given in Chapter 4, while here we discuss its implementation in our setup. As shown in Figure 3.2, a camera (Phantom® VEO 640) is placed at a distance of $1.5\,\mathrm{m}$ from the slanted mirror, hence effectively sitting $1.8\,\mathrm{m}$ away from the light source, imaging a region of approximately $10\,\mathrm{cm}$ by $10\,\mathrm{cm}$. This large aspect ratio between the pattern-camera distance and the field of view prevents optical distortions and aberrations in the digital images of the setup, which is a requirement of the method [168]. A bespoke array of bright red LEDs allows for enough light to go through the semi-transparent checkerboard pattern and reach the camera. This condition is also important, as the method is sensitive to the contrast between dark and bright spots of the pattern [169]. The colour of the LEDs was appropriately chosen to match the peak response wavelength of the camera sensor.

We note the periodicity of the checkerboard reference pattern in Figure 3.3 and express its image I_0 as follows [89],

$$I_0(\mathbf{x}) = \mathrm{Re}\left\{\exp\left(i\boldsymbol{k_1}\cdot\mathbf{x} + i\boldsymbol{k_2}\cdot\mathbf{x}\right)\right\}, \tag{3.14a}$$

where $\boldsymbol{k_1}$ and $\boldsymbol{k_2}$ are wavevectors identifying the spatial frequencies of the pattern in the horizontal and vertical directions of the image, whose pixel coordinates are $\mathbf{x}$. As the basin oscillates, waves appear on the two-fluid interface and, from the top view of the cell, cause the pattern to appear distorted, as in Figure 3.3. We interpret this distortion as a modulation in the phase of an image I_t, as follows,

$$I_t(\mathbf{x}) = \mathrm{Re}\left\{\exp\left(i\boldsymbol{k_1}\cdot(\mathbf{x}+\delta\mathbf{x}) + i\boldsymbol{k_2}\cdot(\mathbf{x}+\delta\mathbf{x})\right)\right\}, \tag{3.14b}$$

where $\delta\mathbf{x}$ denotes an apparent shift in the pattern position caused by the curved interface. We will detail in Chapter 4 how this shift can be extracted from the modulated frame I_t by digitally processing it in comparison with the reference I_0. Additionally, we will show that it can then be approximately related to the gradient of the interfacial height change $\xi(t, \boldsymbol{x})$ by [168]

$$\delta\mathbf{x} \approx -h_p \left(1 - \frac{n_2}{n_1}\right) \nabla\xi, \tag{3.14c}$$

where n_j is the refractive index of fluid layer j, and h_p is the apparent distance between the background pattern and the interface given by $h_p = h_0 + n_1 d_p + \ell_w n_1/n_w$, with d_p the physical distance between the pattern and the bottom of the cell, and ℓ_w and n_w are the thickness and refractive index of the bottom window. We further note that our setup requires a modification of the standard method [89, 168]: as the sample platform oscillates, the pattern-basin distance d_p becomes time-dependent. We compute it approximately from the acceleration data through $d_p(t) \approx d_0 - F_0(t)/\omega_\mathrm{d}^2$, where d_0 is the pattern-basin average resting position.

This detection scheme effectively yields the difference between the interfacial height ξ at the time of the target frame and at the reference time (see subsection 4.2.3 for details). In our setup, at each repetition, we obtain the latter by averaging the first 600 images acquired before the actuator starts driving the system, as illustrated in Figure 3.3. The advantage of this approach against using a single-image reference is twofold. First, it averages out the detection noise of the camera sensor, effectively reducing the overall noise of the reference image. Second, it averages out modulations in individual images caused by small fluctuations of the undisturbed interface, creating a virtually flat interfacial height reference.

In the present dataset, the images have a square aspect ratio of 1024 by 1024 pixels. The high-contrast images combined with the careful alignment of the imaging system allow us to determine the centres and radii of the inner and outer cylinders with precision down to one pixel. If alignment is appropriately performed, the centres of both cylinders should coincide in the image. With the physical size difference between inner and outer radii, we determined that one pixel corresponds to $\ell_\mathrm{px} = 86.6(6)\,\mu\mathrm{m}$. This value can then be used as a scale conversion between the digitally extracted apparent spatial shift $\delta\mathbf{x}_\mathrm{px}$, given in pixel units, and the physical shift $\delta\mathbf{x}$, given in length units, that can be used in Equation 3.14c to recover the physical interfacial height ξ.

3.3.4 Data Analysis and spectral decomposition

With the methods above, we could reconstruct the three-dimensional profile of the two-fluid interface with respect to its averaged undisturbed position at $z = 0$ for each repetition of the experiment, as in the last column of Figure 3.3. The output of the numerical reconstruction of the nth run of the experiment was an array corresponding to the interfacial height changes $\xi(t, \boldsymbol{x})$ in cartesian coordinates $\boldsymbol{x} = (x, y)$ of the image grid. Given the geometry of the fluid cell, we interpolated the height array into a grid of polar coordinates $\boldsymbol{x} = (r, \theta)$ defined in between the cylindrical walls, effectively carrying out a coordinate transformation of ξ. In this transformation $(x, y) \to (r, \theta)$, the cartesian grid with $N \times N$ elements and coordinates $X_j = j/\ell_{\mathrm{px}}$ and $Y_l = l/\ell_{\mathrm{px}}$, for $j, l \in (0, 1, \cdots N-1)$, was mapped into another grid with $N_r \times N_\theta$ elements and coordinates $R_j = r_1 + (r_2 - r_1)j/(N_r - 1)$ and $\Theta_l = \pi\,(-1 + 2l/(N_\theta - 1))$, for $j \in (0, 1, \cdots N_r - 1)$ and $l \in (0, 1, \cdots N_\theta - 1)$. For the experiment presented here, $N = 1024$, $N_r = 200$ and $N_\theta = 128$. As previously mentioned, the interfacial height was reconstructed throughout the driving period of the repetitions, with duration $T_0 = 35\,\mathrm{s}$. Image acquisition was performed at 100 frames per second, resulting in a total of $N_t = 3500$ frames per experimental run. After the coordinate transformation, the $n-$th repetition had an associated array with digitally reconstructed height field $\Xi_n[i, j, l] = \xi^{(n)}(T_i, R_j, \Theta_l)$, for $j \in (0, 1, \cdots N_r - 1)$, $l \in (0, 1, \cdots N_\theta - 1)$ and the time array $T_i = iT_0/(N_t - 1)$, with $i \in (0, 1, \cdots N_t - 1)$.

The spectral decomposition of the real-valued interfacial height $\xi(t, r, \theta)$ may be written in our model as

$$\xi(t, r, \theta) = \mathrm{Re}\left\{\sqrt{\Sigma} \sum_{m,n\geq 0} N_{mn} R_{mn}(r) \xi_{mn}(t) e^{im\theta}\right\}, \tag{3.15}$$

where we adopted the azimuthal and radial-node numbers m and n of the cylindrical mode-decomposition as labels for the interfacial modes. Now, the generalised coordinates ξ_{mn} are complex-valued, hence the real part in the equation above. The equation does not correspond exactly to what can be extracted from experimental data but serves as a reference to the quantities we want to obtain from it. Our analysis pipeline starts with the reconstructed height of a single repetition $\xi_R(t, r, \theta)$ in correspondence with ξ above. First, we fix the time and radial components and perform a Discrete Fourier Transform (DFT) [160], implemented through the Fast Fourier Transform (FFT) algorithm [170], in the angular direction, denoted $\xi_{R,m}(t, r) \equiv \mathcal{F}_\theta[\xi_R(t, r, \theta)](t, r, m)$. Since ξ_R is a real-valued signal, its DFT is symmetric, i.e., even in the azimuthal numbers, $\xi_{R,m} = \xi_{R,-m}$ [160]. Thus, it suffices to consider only one of the branches in the spectrum, which we chose to be $m \geq 0$.

Accordingly, the decomposition of the reconstruction reads

$$\xi_R(t,r,\theta) = \mathrm{Re}\left\{\sum_{m\geq 0} \xi_{R,m}(t,r)e^{im\theta}\right\}, \tag{3.16a}$$

where $\xi_{R,m}$ are complex-valued Fourier coefficients.

For the second step of the analysis, we inspect the time-frequency spectrum of a single azimuthal amplitude $\xi_{R,m}$ at fixed radii. A time DFT of this quantity yields its Fourier decomposition as follows,

$$\xi_{R,m}(t,r) = \sum_{\omega} \tilde{\xi}_{R,m}(\omega,r)e^{-i\omega t}, \tag{3.16b}$$

in the discrete set of N_t frequencies ω in the interval $2\pi(N_t/T_0)\times[-1/2, 1/2)$ [160]. At each radial point, the amplitude $\tilde{\xi}_{R,m}(\omega,r)$ informs us of the frequency content of each azimuthal mode in the duration of one repetition. It is also possible to build a root mean squared (RMS) quantity with it, defined by the average $|\tilde{\xi}_{R,m}|_r(\omega) = \sqrt{\langle|\tilde{\xi}_{R,m}|^2\rangle_r}$, where $\langle\cdot\rangle_r$ denotes the average over the radial coordinate. Another way of investigating the time-frequency dependence of azimuthal waves is through a spectrogram, or scaleogram, of the signal [171]. It consists of a representation of the frequency spectrum as it varies with time and is particularly useful for signals whose frequencies themselves or their amplitudes change over time. We opt to do this procedure by employing continuous wavelets [171], which, in essence, work as a moving band-pass window in the Fourier domain centred around specific frequencies (scales), thus mapping their variations over time. In other words, the outcome of this analysis is a time-dependent envelope $b_{m,\omega}(t,r)$ around ω satisfying

$$\begin{aligned}\xi_{R,m}(t,r) &= \sum_{\omega>0}\left(b_{m,\omega}(t,r)e^{-i\omega t} + b_{m,-\omega}(t,r)e^{i\omega t}\right)\\ \implies \xi_R &= \mathrm{Re}\left\{\sum_{\omega>0,m\geq 0}\left(b_{m,\omega}(t,r)e^{-i(\omega t-m\theta)} + b_{m,-\omega}(t,r)e^{i(\omega t+m\theta)}\right)\right\}.\end{aligned} \tag{3.16c}$$

As defined above, the instantaneous amplitudes $b_{m,\pm\omega}$ are in analogy with quasi-particle amplitudes in QFT and denote counter-clockwise (positive frequency) and clockwise (negative frequency) propagating waves. In this sense, Equation 3.16c simply states that a standing azimuthal wave ξ_m may be decomposed as two interfering waves propagating in opposite directions.

The equations above constitute the core of our data analysis, which allowed us to extract the theoretically relevant quantities from the experimental reconstruction. We should note that the radial dependence has not yet been considered, but it will play a role in the later discussions of the results section. By comparing equations (3.16)

with Equation 3.15, we expect that quantities $b_{m,\omega}$ may be approximated by

$$b_{m,\omega}(t,r) \propto \sum_{n\geq 0} \tilde{b}_{m,\omega_{mn}}(t) R_{mn}(r) \delta_{\omega_{mn},\omega}, \tag{3.17}$$

for some undetermined instantaneous amplitudes $\tilde{b}_{m,\omega}(t)$, and the Kronecker delta restricts the (m,n) modes whose dispersion frequency ω_{mn} are close to ω. This is an approximation in the sense that, as previously discussed, the existence of a meniscus with vertical walls and viscous boundary layers at the interface result in a deviation from the theoretically modelled profile in terms of cylindrical Bessel functions satisfying Neumann boundary conditions. Nonetheless, the overall trend of the radial wave should resemble that of $R_{mn}(r)$ and hence display an oscillatory behaviour within the slice $r_1 < r < r_2$. Thus, we opted to examine the radial dependence through the Fourier transform, i.e., $\mathcal{F}_r[b_{mn}(t,r)](t,k_r)$. It should be stressed that the spectrum obtained from this operation is only indicative of the typical wavelengths in the signal, and the radial wavenumber k_r does not equal the mode wavenumber k_{mn}. We argue, however, that this analysis can be used to draw qualitative conclusions from the data in the absence of a more refined digital decomposition in terms of radial eigenfunctions.

3.3.5 Statistical measures

The fluctuating stochastic behaviour of the two-fluid interface will inevitably cause variations between the 1500 repetitions. Due to the intermolecular interactions at the interface, this feature would persist even in an idealised situation where all noise sources are eliminated, and experimental parameters are kept constant. Hence, the set of reconstructed interfacial height profiles composes a statistical ensemble of randomly distributed variables. The various amplitudes obtained from the spectral decomposition of the measured quantity, as described above, can also be treated in a similar fashion. Along the lines of our EFT, we propose utilising the statistical machinery commonly employed in field theories to our setup. In particular, we operate with two-point functions and the factorisation of higher-order correlation functions [121].

Let $\{X_i\}$ be a set of randomly distributed variables forming a statistical ensemble, which could correspond in our system to a set of azimuthal mode amplitudes ξ_m or envelopes $b_{m,\omega}$. We denote ensemble averages by $\langle\cdot\rangle$ and define the statistical moment, or full correlation function, of a subset of N variables $\boldsymbol{X} = (X_1, \ldots, X_N)$ as

$$G^{(N)}(\boldsymbol{X}) = \langle X_1 \cdots X_N \rangle. \tag{3.18}$$

If the components of the vector $\boldsymbol{X}$ are all random independent variables amongst them, this quantity has the distinguishable property of completely factorising in terms

of products of lower order moments $G^{(N')}$, with $N' < N$ [121]. In quantum systems, the components of $\boldsymbol{X}$ may be the mode amplitudes of a quantum field or a collection of quantum many-body states. Hence, in these cases, factorising correlation functions indicate independent degrees of freedom and thus the absence of interactions between them [109, 172]. Further, quantum Gaussian states, and more generally, Gaussian ensembles of independent random variables, are fully characterised by their mean and variance. In other words, they are fully characterised by their first two moments $G^{(1)}(\boldsymbol{X})$ and $G^{(2)}(\boldsymbol{X})$, so all higher-order correlations $G^{(N)}(\boldsymbol{X})$, for $N > 2$, can be entirely factorised in terms of $G^{(1)}(\boldsymbol{X})$ and $G^{(2)}(\boldsymbol{X})$. For a quantum system, this is equivalent to applying the Wick decomposition [172].

In more general conditions, where interactions play a role, the evolution of the random variables $\boldsymbol{X}$ is tainted by non-linearities in their equations of motion, such as in our system, ultimately breaking their statistical independence. Hence, the full correlation functions $G^{(N)}$ can be decomposed into [121, 172]

$$G^{(N)}(\boldsymbol{X}) = \langle X_1 \cdots X_N \rangle_{\mathrm{c}} + \langle X_1 \cdots X_N \rangle_{\mathrm{d}} \equiv G_{\mathrm{c}}^{(N)}(\boldsymbol{X}) + G_{\mathrm{d}}^{(N)}(\boldsymbol{X}). \tag{3.19}$$

Here, we have employed the notation of quantum systems, where the first term $G_{\mathrm{c}}^{(N)}$ denotes the connected part of the correlation functions, also called statistical cumulants. In QFT, $G_{\mathrm{c}}^{(N)}$ corresponds to the contributions from connected Feynman diagrams, hence the name, with N external lines which cannot be broken down into two-point correlators. Thus, we refer to the second term $G_{\mathrm{d}}^{(N)}$ as the disconnected correlation function, i.e., the component that can be fully factorised in terms of correlation functions with order $N' < N$. There exists no simple formula for the cumulants at all orders N, but they can be computed recursively from the cumulant generating function, see §2.7 of [121].

It is possible to show that Gaussian ensembles have vanishing cumulants for $N > 2$ [121]. For a scalar normally distributed variable X, the mean μ and variance σ^2 of its distribution are identically given by the first and second statistical cumulants, $G_{\mathrm{c}}^{(1)}(X) = \langle X \rangle \equiv \mu$ and $G_{\mathrm{c}}^{(2)}(X) = \langle X^2 \rangle - \langle X \rangle \langle X \rangle \equiv \sigma^2$, respectively. In fact, Marcinkiewicz shows that a scalar random variable has all its cumulants of order $N > 2$ vanishing if, and only if, it is normally distributed; otherwise, it must have an arbitrary non-Gaussian distribution with an infinite number of nonzero cumulants [173]. This property of cumulants is in direct contrast with moments of arbitrary order, which are not expected to vanish, even for normally distributed random variables. Notably, since $G_{\mathrm{c}}^{(N)} = G^{(N)} - G_{\mathrm{d}}^{(N)}$ contains moments of all orders $N' \leq N$, there is little to be learned from $G_{\mathrm{c}}^{(N+1)}$ if its predecessor $G_{\mathrm{c}}^{(N)}$ provides sufficient information about the distribution. For this reason, Gardiner argues that *"higher-order cumulants contain information of decreasing significance, unlike higher-order moments"* [121].

Given the useful properties of cumulants in characterising statistical distributions, we use them to define a measure of non-Gaussianity, in line with the work of Schweigler et al. in a 1D BEC [68]. We choose to operate with the ensemble of experimentally distributed instantaneous complex amplitudes $b_{m,\omega}$ of a given azimuthal mode m around a frequency ω, and define our measure from their self-correlation functions at order N as follows,

$$M^{(2N)}_{m,\omega}(t,r) \equiv \frac{G^{(N)}_{\mathrm{c}}\left(|b_{m,\omega}|^2\right)}{G^{(N)}\left(|b_{m,\omega}|^2\right)} = \frac{\left\langle \left(b^*_{m,\omega} b_{m,\omega}\right)^N \right\rangle_{\mathrm{c}}}{\left\langle \left(b^*_{m,\omega} b_{m,\omega}\right)^N \right\rangle} \,. \tag{3.20}$$

Here, we compute the correlation of order $N > 1$ with the squared absolute values $|b_{m,\omega}|^2$ to ensure that the measure above is real-valued.

Since the numerator (cumulant) vanishes if the correlation functions fully factorise, the quantity should be zero upon the null hypothesis, which requires that the complex degrees of freedom $b_{m,\omega}$ are normally distributed around zero. In this sense, $M^{(2N)}_{m,\omega}$ provides a quantitative indicator for the deviation of the measured distribution of $b_{m,\omega}$ from a featureless Gaussian. We further note that the measure $M^{(2N)}_{m,\omega}$ varies in time and radius, as shown in Equation 3.20. This allows us to track the distributional properties of the ensemble of repetitions of $b_{m,\omega}(t,r)$ as the system evolves. In particular, regardless of the initial amplitude distribution and its corresponding factorisation $M^{(2N)}_{m,\omega}$, the linear evolution of $b_{m,\omega}$, entirely independent of other interfacial modes, requires its distributional properties not to change over time. Otherwise, in the presence of non-linear interactions, these degrees of freedom are not independent random variables anymore and hence develop connected correlation functions between them. This automatically changes the distributional properties of the modes $b_{m,\omega}$, which, in turn, alters the value of our measure $M^{(2N)}_{m,\omega}$. Consequently, we can study the onset of non-linearities in our system through the dynamics of a single mode by examining the time evolution of its factorisation measure $M^{(2N)}_{m,\omega}$.

3.4 Results

Following the discussion of the previous section, we now present the observations and results of the experiment previously introduced. We begin by scrutinising a single sample run to gain intuition over the interfacial dynamics at play before extending certain conclusions to the ensemble of repetitions. For this example repetition, Figure 3.6 depicts the data analysis pipeline of subsection 3.3.4. The interpolated interfacial height in cylindrical coordinates reconstructed from the experiment is shown in Figure 3.6(a) for a fixed time frame near the stopping of the driving. Along the angular (horizontal) direction, we observe a clear sinusoidal signal with four troughs and crests, consistent with an azimuthal mode number of four, i.e., $m = 4$. Perpendicularly in the radial

(vertical) direction, the waves appear to cross zero once, which is, in turn, compatible with the radial order number one, i.e., $n = 1$. This inspection hints that the dominant mode is $(m, n) = (4, 1)$, with predicted wavenumber $k_{41} = (2\pi)0.35\,\mathrm{cm}^{-1}$.

Initially, we examine the Fourier coefficients of the decomposition into azimuthal modes (3.16a) through their root-mean-squared values over all radii, as defined in the previous section. Their time evolution is shown for the first ten azimuthal numbers in Figure 3.6(b). As expected from the visual inspection of panel (a), $\xi_{m=4}$ reaches the largest amplitudes during the experimental repetition, displaying an evident unstable growth. It is also clear that the azimuthal numbers 7 and 8 become unstable, which is in agreement with the prediction from Floquet analysis of the linear model (see Figure 3.1). However, to confidently state that these modes are undergoing parametric amplification, we must examine the characteristic frequencies, if any, where the instabilities happen. We also observed a consistent presence of $m = 1$, referred to as the sloshing mode [135], and it appears due to the horizontal cross-axis motion of the sample cell, albeit reduced to under 0.5% (see Figure 3.5(b)). In our analysis, we disregard contributions from the azimuthally symmetric mode $m = 0$, or the average of ξ in θ, as it is overwhelmed by the vertical displacement of the basin.

Complementarily, Figure 3.6(c) displays the radial RMS of the time Fourier transformed amplitudes $\tilde{\xi}_m$, representing the frequency spectrum of the modes ξ_m. Around the primary frequency ω_0, corresponding to half the driving frequency ω_d, the azimuthal numbers $m = 4,\ 7,$ and 8 appear with amplitudes several orders of magnitude larger than the noise background at $\sim 0.5\,\mu\mathrm{m}$, confirming that they undergo parametric amplification. The frequency content of $m = 1$ is spread through many frequencies, with a stronger presence at the driving frequency $2\omega_0$, again consistent with the dynamics of sloshing resonance [135]. We further note that all azimuthal modes Figure 3.6(c) display a faint but non-vanishing contribution around $2\omega_0$, which is likely due to the harmonic creation of waves by the meniscus at the vertical walls, as observed in [146, 174].

Finally, the last quantity of our analysis process is the time-dependent envelope $b_{m,\omega}(t)$ of an azimuthal number m around a frequency ω. We show the radial RMS of these amplitudes around the positive primary frequency ω_0 in Figure 3.6(d). There are three distinct sets of modes based on the predictions of the Floquet analysis for linear dynamics in subsection 3.2.1. First, we distinguish the dominant mode $(m, n) = (4, 1)$ (solid maroon line), which evidently displays a log-linear growth until the driver shuts down, indicating an unstable evolution of the form $\propto \exp(\lambda_{4,1}t)$, as anticipated for a parametrically excited wave as in Equation 3.3. Second, the dashed lines in Figure 3.6 specify the other modes that appeared under the primary resonance band in the instability chart of Figure 3.1. By the time the external driving stops, all of these modes are at least one order of magnitude smaller than the dominant

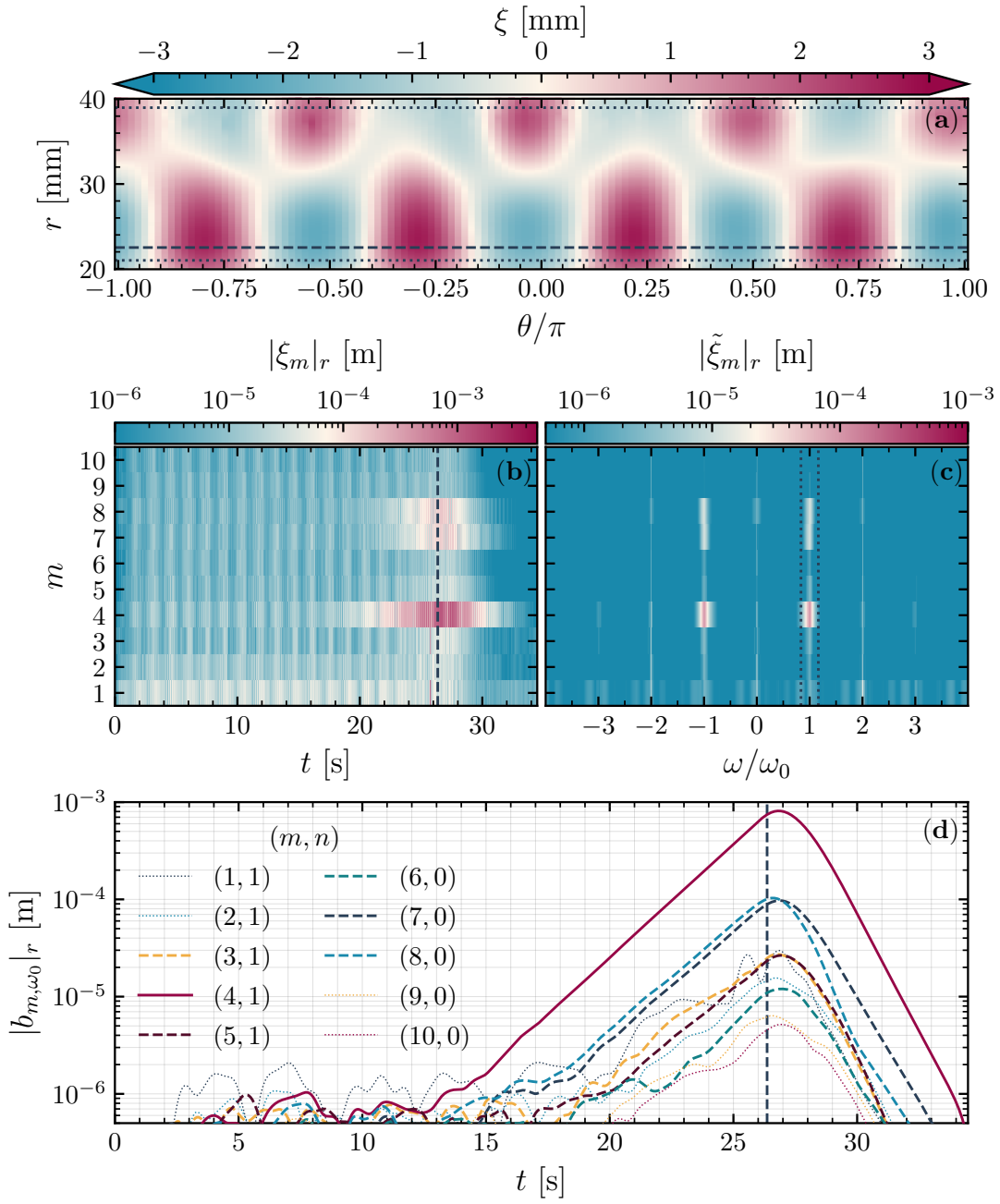

Figure 3.6: Overview of the data analysis pipeline. In $(\mathbf{a})$, a representative time frame t_0 of the reconstructed interfacial height $\xi(t_0, r, \theta)$ in cylindrical coordinates for a single repetition. Dotted horizontal lines indicate the regions where the meniscus between the interface and the vertical walls appear. The fixed radius $r_0 = 22.5\,\mathrm{mm}$ used in a subsequent analysis is displayed by the dashed horizontal line. In $(\mathbf{b})$ and $(\mathbf{c})$, we show the radial RMS of the Fourier coefficients $|\xi_m|_r(t)$ and $|\tilde{\xi}_m|_r(\omega)$, as defined in equations (3.16), for the first ten non-zero azimuthal modes. The instant where the external driver stops is indicated by the vertical dashed line in $(\mathbf{b})$ and $(\mathbf{d})$. The horizontal axis of $(\mathbf{c})$ is given in multiples of the primary frequency $\omega_0 = (2\pi)3.035\,\mathrm{Hz}$. In $(\mathbf{d})$, we show the radial RMS of the time-varying amplitudes $b_{m,\omega}$ around the positive branch of the primary frequency $+\omega_0$. The legend indicates the corresponding azimuthal numbers m and orders n to each curve. In the three last panels, the amplitude scales are logarithmic.

$(4,1)$ mode. Within them, the log-linear growth of the curves for $(8,0)$, $(7,0)$ and $(5,1)$ suggests that they are also amplified in an exponential fashion, with the former two reaching amplitudes more than three times larger than the remaining modes. Conversely, $(6,0)$ and $(3,1)$ display inconsistent growth, not necessarily compatible with that of parametric instabilities. This behaviour is shared with the third set of modes in Figure 3.6, shown as dotted lines. In particular, we observe the sloshing wave $(1,1)$ increasing inconsistently, likely due to interactions with its dominant resonance at $2\omega_0$.

Generally, the picture we draw from Figure 3.6 for the evolution of individual modes is consistent with the following description of the collective interfacial dynamics. As one or more modes undergo parametric instability and increase in amplitude, some of the infinitely many terms in the non-linear Lagrangian (2.48) may become non-negligible. Thus, modes outside resonance bands may also experience an unstable evolution due to interactions with parametrically resonant ones, sometimes several orders of magnitude larger. Naturally, this is due to happen at all frequencies and wavenumbers, eventually reaching a stage where the exponential amplification of the primary instabilities cannot be sustained. It is, however, impractical to map and describe all interactions between interfacial modes. Given that the behaviour demonstrated in Figure 3.6 consistently appeared throughout all 1500 repetitions, we then restrict our investigation to the nonlinear dynamics of the azimuthal mode $m = 4$. We note that, although the other modes predicted in subsection 3.2.1 were also excited, $m = 4$ dominates, likely due to the initial random fluctuations of the interface, which might have been larger for this mode than for others.

3.4.1 Unstable evolution of the dominant mode

Around the primary resonance band at ω_0, the evolution of the dominant mode is encapsulated in the time-dependent envelope b_{4,ω_0}. The standing waves of the dominant mode $m = 4$ can be seen by the four crests on the interface in Figure 3.7(d). Their instantaneous amplitudes corresponding to the counter-clockwise waves are displayed in logarithmic scale in Figure 3.7(f) for all 1500 experimental repetitions (in light blue), and two qualitatively distinct realisations are highlighted to stress distinguishable stages of the evolution. Initially, the noise level (in dark green) of our detection method overwhelms the signal until the instabilities emerge out of it between 10 and 17 seconds. A consistent log-linear amplification trend (blue) appears in all repetitions, displaying exponential growth rates throughout. After the external driving is shut down, the mode envelopes of all runs are seen to follow a log-linear decay trend (in maroon), consistent with viscous exponential damping. Some repetitions quickly transition to the final damping stage (orange), while others reach a critical

amplitude and saturate, see the upper curve in Figure 3.7(f). The bounded unstable growth appearing in the latter case is inconsistent with a single-mode linear evolution, as presented in subsection 3.2.1, and, instead, indicates that the energy continuously provided by the driving actuator is being scattered into other modes in the system. This behaviour has been observed in various experiments and is the core principle behind non-linear Faraday instabilities, see, e.g. [156, 175–180].

From the mode amplitudes in Figure 3.7(f), we extracted the slopes in the growth (blue) and decay (maroon) regions by performing linear fits of the log-linear trends in each. We label the fitted amplification and damping rates by the azimuthal and order numbers of the dominant mode, $(4, 1)$, as $\lambda_{4,1}$ and $\gamma_{4,1}$, respectively. In Figure 3.8, we display their results for the 1500 repetitions along with the monitored values of the driving amplitude F_0 and the ambient temperature T. As observed in Figure 3.5,

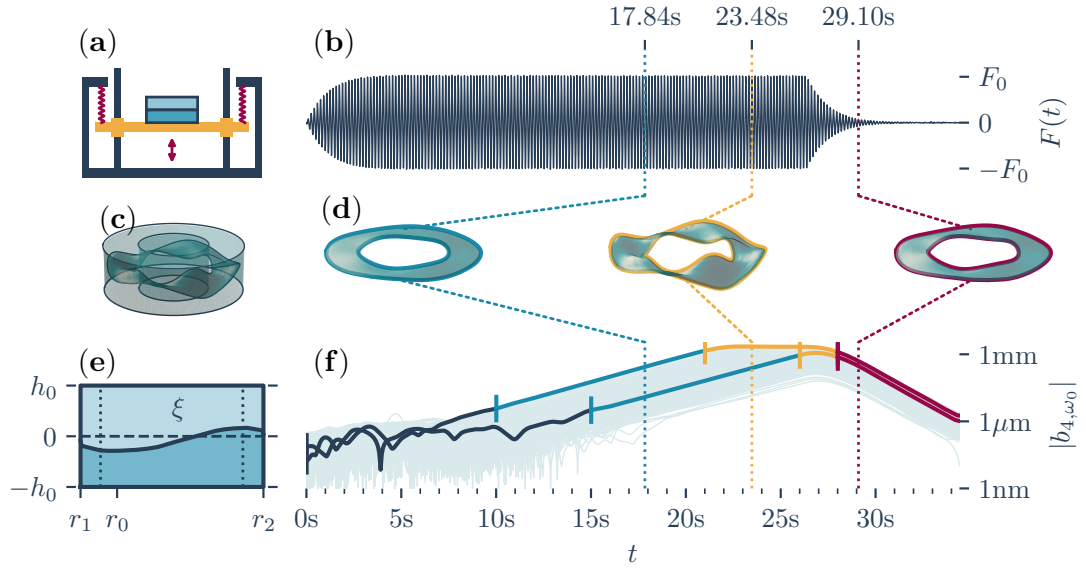

Figure 3.7: In $(\mathbf{a})$, an illustrative depiction of the driving setup previously explained is shown. A typical profile of the measured vertical acceleration $F_0(t)$ over time appears in $(\mathbf{b})$. In $(\mathbf{c})$, we portray the geometry of the fluid cell with the experimentally reconstructed interface. Three rendered snapshots in time of the observed interfacial waves are shown in $(\mathbf{d})$. In $(\mathbf{e})$, the cross-section of the fluid cell in $(\mathbf{c})$: at fixed azimuthal angle θ_0 depicting the interfacial height $z = \xi(t, r, \theta_0)$ in comparison with the horizontal walls at $\pm h_0$. The dashed, vertical lines indicate the radii where the steep curvature of the menisci between the interface and the vertical walls at r_1 and r_2 decreases the sensitivity of the detection method. In $(\mathbf{f})$, instantaneous amplitudes b_{m,ω_0} in logarithmic scale of the dominant azimuthal mode $m = 4$, at the primary resonance frequency ω_0, for 1500 repetitions (light blue) at fixed radius $r_0 = 24\text{mm}$. Out of the ensemble of repetitions, two qualitatively distinct runs are highlighted in bold with coloured regions showing different parts of the dynamics: (dark green) detection method noise floor, (turquoise) log-linear unstable growth, (orange) transition from amplification-dominated to damping-dominated dynamics and (red) log-linear unstable decay. The difference in the two realisations is due to random variations between their initial states.

an evident correlation between some of the quantities and the ambient temperature appears. In panel (c), we observe a drift between the driving amplitude and temperature around $3.44\,\mathrm{m\,s^{-2}}$ and $25\,^{\circ}\mathrm{C}$, likely due to the various thermal responses of the mechanical components of the vibration system (springs, actuator, metal bolts, etc.). However, this behaviour seems to modulate an overall linear relation over the observed ranges.

Similarly, the damping rates $\gamma_{4,1}$ in Figure 3.8(b) and (g) display a clear inverse correlation with the ambient temperature, which we attribute to a change in the temperature of the fluid sample. The dissipation model (2.63) presented in subsection 2.5.1 shows the direct dependence of the damping rate with the kinematic viscosities and densities of the liquid phases, and both properties manifestly scale inversely proportional to temperature [15]. In our experiment, it is unlikely that the densities varied so drastically to explain the reduction of almost 6% in damping over an increase of only $3\,^{\circ}\mathrm{C}$, whereas the kinematic viscosities may have reduced more significantly. Using reference values for solutions with similar concentrations [181, 182], we estimate that, by increasing the temperature of the biphasic sample from $20\,^{\circ}\mathrm{C}$ to $25\,^{\circ}\mathrm{C}$, their densities ρ_j would reduce by less than 0.2%, while their kinematic viscosities ν_j would reduce as much as 10%. Interfacial tension only enters the damping formula indirectly through the dispersion frequency of the mode, and a similar analysis leads us to expect a negligible variation over this temperature range, as for the density[2]. An in-depth study of the rheological properties of the two-fluid system would be necessary to confidently explain the observed variations, but we consider it to be out of the scope of this thesis. In addition, this study underlines the need for precise temperature control in hydrodynamical experiments.

While the damping rates evidently scale with the measured temperature, the amplification rate $\lambda_{4,1}$ does not display this behaviour in Figure 3.8(a). Instead, we observe a stronger correlation with the vertical driving amplitude F_0, particularly around $25\,^{\circ}\mathrm{C}$, where the driver exhibits a hysteresis (see panel (c)). Besides, in Figure 3.8(f), the distribution of $\lambda_{4,1}$ over the duration of the experiment could not be as well explained by the temperature variations as the other quantities presented. These observations are in agreement with the statement of Kumar & Tuckerman [106] that for small damping, $\gamma_{mn} \ll \omega_{mn}$, and small waves (linear evolution), Faraday instabilities are well described by a linearly damped Mathieu equation [156]. In this case, the overall

[2]For these estimates, we are considering that the two phases are purely formed by solutions of potassium carbonate-water and ethanol-water. We are also disregarding changes in the triphasic liquid-liquid equilibrium between the components, see [183] for experimental results. As a reference, when the temperature of pure water (see Appendix A of [15]) is raised from $20\,^{\circ}\mathrm{C}$ to $30\,^{\circ}\mathrm{C}$, its density ρ reduces by approximately 0.2%, while its kinematic viscosity ν reduces by 20%. We could not find references for the interfacial tension between the liquid phases. However, for biphasic solutions of water and 1-butanol [184], whose interfacial tension is similar to that of our system, the referred increase in temperature of $5\,^{\circ}\mathrm{C}$ causes variations of less than 1% in the measured interfacial tension.

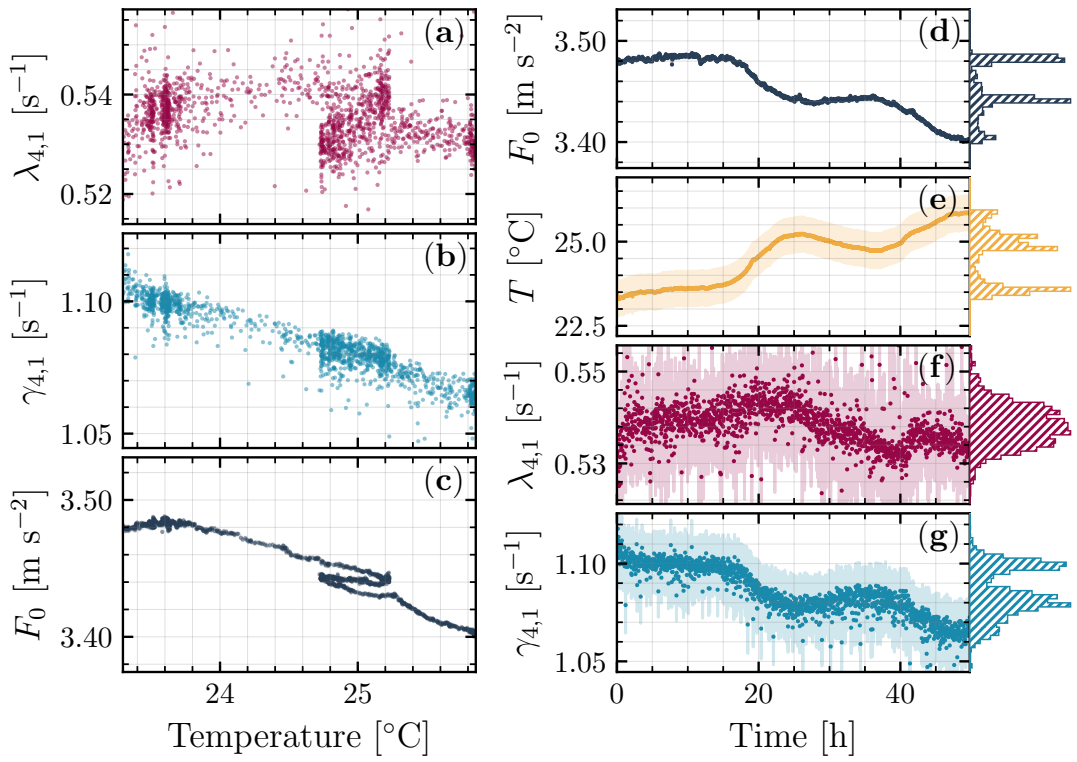

Figure 3.8: Panels (**a**), (**b**) and (**c**) display the fitted growth and decay rates, and the vertical acceleration of the cell as functions of the measured environmental temperature. In (**d**), the measured amplitudes of the vertical driver acceleration F_0 throughout each repetition are shown. Panel (**e**) displays the average environmental temperature near the platform during each run. In (**f**) and (**g**), the fitted exponential amplification and decay rates for the azimuthal number $m = 4$ around ω_0, λ (blue dots) and γ (red dots), respectively, by the elapsed time since the first experimental run. Their respective average values with one standard deviation are $\langle\lambda_{4,1}\rangle = 0.536(9)$ s^{-1} and $\langle\gamma_{4,1}\rangle = 1.084(12)$ s^{-1}. The shaded regions indicate the uncertainty in the measured or fitted values. At the right-hand side of panels (**d**) to (**g**), we display the histograms of their quantities.

mode amplification rate λ_{mn} can be approximated by the difference between an inviscid rate α_{mn}, obtained from the undamped Mathieu equation, and the damping rate γ_{mn}, i.e., $\lambda_{mn} \approx \alpha_{mn} - \gamma_{mn}$. Kovacic et al. [112] show that for small external forcing, as in our experiment, the instability rate α_{mn} scales linearly with F_0, i.e., $\alpha_{mn} \propto F_0$. Since the latter reduces with temperature, $F_0 \propto -T$, then the former also does $\alpha_{mn} \propto -T$. Accordingly, with the unverified assumption that α_{mn} and γ_{mn} exhibit similar temperature dependence, we postulate that, by computing their difference, the resulting temperature scaling of λ_{mn} is ultimately reduced, as observed in the experiment for the dominant mode $(m, n) = (4, 1)$.

It should be noted that, even when accounting for the above-mentioned variations of up to $\pm 5\%$ in the kinematic viscosity values due to temperature, the damping model introduced in subsection 2.5.1 falls short in recovering the observed rates. For the dominant mode, the empirical average damping (with one standard devia-

tion uncertainty) was $\gamma_{4,1}^{(E)} = 1.084(12)\,\mathrm{s}^{-1}$(see Figure 3.8), with an overall variation through all runs of $\pm\Delta\gamma_{4,1}^{(E)} = \pm 0.03\,\mathrm{s}^{-1}$. Conversely, the model in Equation 2.63, yields $\gamma_{4,1}^{(M)} = 0.898\,\mathrm{s}^{-1}$ with uncertainty of $\pm\Delta\gamma_{4,1}^{(M)} = \pm 0.044\,\mathrm{s}^{-1}$, hence about 17% smaller than the observed rate, on average. As discussed in Chapter 2, this discrepancy has been observed extensively in the background literature (see e.g. [147] and references therein) and is expected from the presence of a meniscus between the two-fluid interface and the vertical walls. For instance, experimental results include [146], where the authors identify an "empirical factor" attributed to capillarity around the walls and that multiplies their theoretical model by 1.25. Regardless, by following an experimentally-informed approach and using the observed damping rates $\gamma_{4,1}$ and forcing amplitudes F_0 in the linear Floquet analysis of subsection 3.2.1, we obtain an average amplification rate $\lambda_{4,1}^{(M)} = 0.528(15)\,\mathrm{s}^{-1}$, which is in good agreement with the observed one, $\lambda_{4,1}^{(E)} = 0.536(9)\,\mathrm{s}^{-1}$.

We stress that the results presented here illustrate the aforementioned complexity of modelling and carrying out experiments with fluid systems. Nonetheless, the inspection of appropriately monitored quantities allows us to identify theoretical predictions that are reproduced in an experiment, as well as possible limitations of the description. Ultimately, we now comprehend that the variations observed in the experiment, mainly due to temperature changes, do not hinder the effect of Faraday resonance and can be properly modelled through a phenomenological strategy. Along these lines, we can transfer the knowledge gathered in this study of the linear evolution through Floquet analysis to now investigate the onset of non-linearities in our system, as implied by the saturation of the dominant mode envelopes in Figure 3.7(f).

3.4.2 Self-interacting dynamics and secondary instabilities

Continuing our examination of the dominant mode through the instantaneous amplitudes b_{4,ω_0} shown in Figure 3.7(f), we now inspect their ensemble distributions at four phases of the experimental repetitions in Figure 3.9(a). In the first stage, we observe normally distributed amplitudes (at 7 seconds) as expected from white detection noise. As the driving continues, at later times, they develop more intricate, non-Gaussian distributions. The experimental self-correlation function $G^{(2)}(|b_{4,\omega_0}|) = \langle |b_{4,\omega_0}|^2 \rangle$ is shown in Figure 3.9(b) by the dark solid line. Using the nonlinear model of Equation 3.10 for a self-interacting dominant mode, we have simulated the ensemble of repetitions using the observed damping rates and measured acceleration profiles with the fluid properties of Table 3.1, see Section B.2 in Appendix B. For the numerical solutions of the equations of motion, we chose a random initial state sampled from the experimental normalised distribution during the linear regime (between 12 and 20 seconds). Hence, the only free parameter was the standard deviation of this initial distribution, which

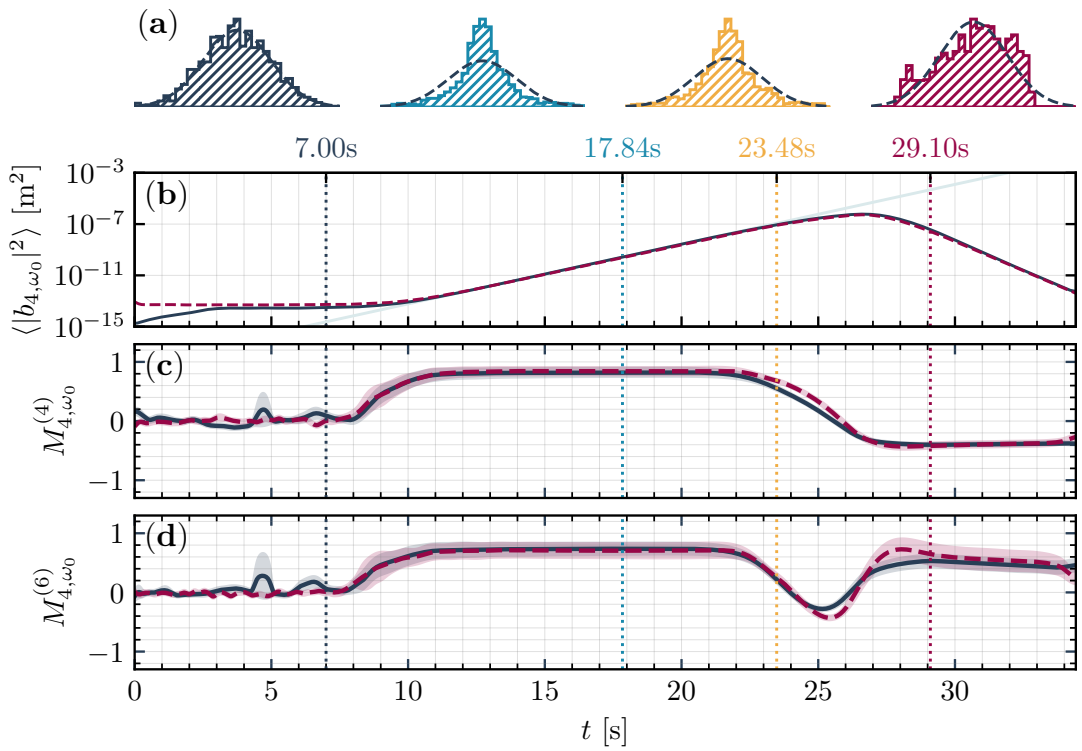

Figure 3.9: In (**a**), we exhibit the ensemble distributions of the real part of the amplitudes $b_{m,\omega_0}(t, r_0)$ of the $m = 4$ mode at four different times (vertical dotted lines): the noise-floor (dark grey), the log-linear unstable growth (light blue), the non-linear period (yellow) and the decay (maroon). The second-order self-correlation function $\langle |b_{4,\omega_0}|^2 \rangle$ for the experiment (dark grey) and the numerical simulation (maroon) are shown in (**b**). Panels (**c**) and (**d**) depict the statistical measures $M^{(2N)}_{m,\omega}$ for $N = 2, 3$ computed from experimental data (dark grey) and simulations (maroon), with bootstrapped bands of one standard deviation.

was appropriately chosen so that the simulated self-correlation $\langle |b_{4,\omega_0}|^2 \rangle$ was in best agreement with the experimental one.

The maroon dashed curve in Figure 3.9(b) displays the self-correlation function for these numerical results. The overlap between experimental and simulated curves confirms that our effective nonlinear model appropriately recovers the average dominant mode evolution. As discussed in subsection 3.3.5, the presence of interactions modifies the distributional properties of the ensemble over time. To characterise the deviation from a featureless Gaussian and identify the onset of non-linearities, we employ the measures of non-Gaussianity defined in Equation 3.20. In Figure 3.9(c) and (d), solid dark lines show $M^{(2N)}_{m,\omega}$ for the mode $m = 4$, around the primary resonance frequency ω_0, at orders $N = 2$ and $N = 3$. In the white noise-dominated region, before 8 seconds, the correlations can be fully factorised, and, as expected, the measure vanishes. We incorporate this feature in our simulated mode through a Gaussian noise floor added to the numerical results, which are shown by the maroon curves in all panels of Figure 3.9.

As the signal emerges from the background noise in the repetitions, all curves gradually increase and stabilize at a non-zero value, indicating an initial distribution of interfacial waves that is not Gaussian. Between 10 and 21 seconds, the ensemble shows the expected linear evolution at small amplitudes. However, at around 22 seconds, some repetitions in Figure 3.7(f) reach a critical amplitude, causing abrupt changes in both measures. This deviation suggests a departure from a linear evolution, which should preserve the distribution. Before the time indicated by the yellow dashed line in Figure 3.9, the simulated and experimental curves match for $M^{(4)}_{m,\omega}$ and $M^{(6)}_{m,\omega}$ within the 1σ-confidence intervals (shaded regions). Conversely, in the non-linear region, both non-Gaussianity measures display a small quantitative discrepancy between simulation and experiment. Our model, however, shows that the self-interaction of the dominant parametrically amplified mode is a prevailing source of nonlinearity. Were the external driving to continue for longer, the interface would form stationary patterns, as commonly observed in experimental studies of nonlinear Faraday resonance [175–177]. Here, we investigate the onset of these nonlinearities prior to the saturation of the amplitudes. In this regime, the dominant parametrically unstable mode scatters into a limited number of modes, leading to the growth of secondary instabilities with higher wavenumber. This feature is at the centre of a correspondence with preheating dynamics in the early Universe, which we explore now.

Going beyond self-interactions, we showed in subsection 3.2.2 that a dominant primary Faraday instability, here $\xi_{4,1}$ with wavenumber $k_0 \equiv k_{4,1} \approx (2\pi)0.35\,\mathrm{cm}^{-1}$, can source the dynamics of a secondary mode $\xi_{4,n}$, with wavenumber $k_1 \equiv k_{4,n}$, through the equation of motion (3.9) with non-linear terms (3.11). At the level of the Lagrangian, they correspond to terms proportional to $\xi_{4,n}\xi_{4,1}\dot{\xi}^2_{4,1}$ and $\xi^2_{4,1}\dot{\xi}_{4,1}\dot{\xi}_{4,n}$ with nonvanishing coefficients. In this case, the only remaining degree of freedom is the order n of the wavenumber k_1. Hence, accompanying the primary instability $(m,n) = (4,1)$(solid dark line in Figure 3.10(a)), we observe the growth of a secondary mode $(m,n) = (4,7)$ with $k_1 \approx (2\pi)1.77\,\mathrm{cm}^{-1}$ at the $3\omega_0$-resonance band (dashed dark line). These quantities are displayed in Figure 3.10(a) as the radial Fourier transform $\tilde{b}_{4,\omega}(t,k_r)$ as in Equation 3.17 of the instantaneous amplitudes $b_{4,\omega}(t,r)$, with radial wave-number k_r.

As displayed in Figure 3.10(a) for a sample repetition, our numerical model (maroon lines) accurately captures the non-linear features of the observed mode-mode interaction between primaries (solid lines) and secondaries (dashed lines). Equation 3.11 shows that the primary instability sources the equations of motion of the secondary mode with cubic terms. Since the primary evolves as $\xi_{4,1} \sim \exp\left(\lambda_{4,1}t - i\omega_0 t\right)$, its cubic sourcing scales as $\sim \exp\left(3\lambda_{4,1}t - 3i\omega_0 t\right)$, and hence the secondary mode around the frequency $3\omega_0$ should become unstable with amplification rate $\sim 3\lambda_{4,1}$. We extract the slopes (plotted as light blue lines) for the simulated primary $\lambda^{(M)}_0$ and secondary $\lambda^{(M)}_1$

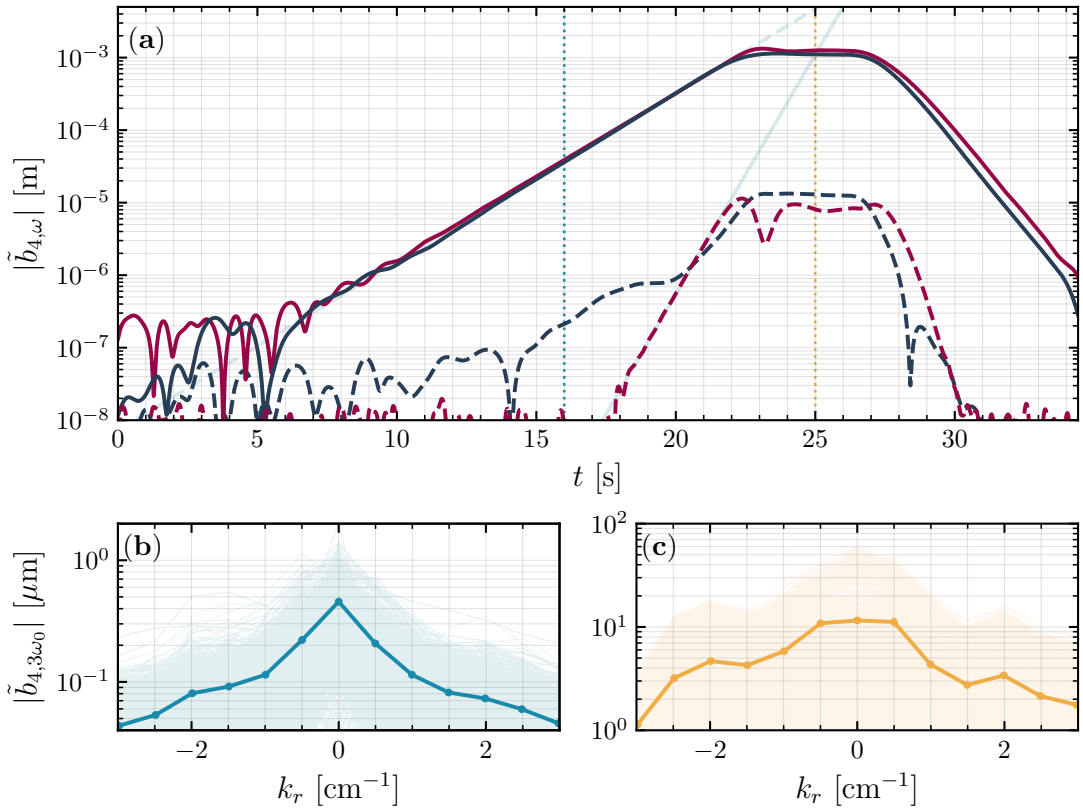

Figure 3.10: Radially Fourier transformed instantaneous amplitudes, $\tilde{b}_{4,\omega}(t, k_r)$, at various ω and k_r, of experimentally reconstructed (dark lines) and simulated (red lines) data are shown in $(\mathbf{a})$. The primary instabilities with wavenumber k_0 around ω_0 are displayed as solid lines, and the secondary instabilities with wavenumber k_1 around $3\omega_0$ are depicted by dashed lines. Solid light blue lines indicate the log-linear fit of the growth region of the simulated $|\tilde{b}_{4,\omega_0}(t, k_0)|$ and $|\tilde{b}_{4,3\omega_0}(t, k_1)|$, with growth rates $\lambda_0 = 0.52\,\mathrm{s}^{-1}$ and $\lambda_1 = 1.48\,\mathrm{s}^{-1} \approx 2.85\lambda_0$, respectively, verifying the $3:1$ ratio predicted by preheating mechanism (see main text for details). Panels $(\mathbf{b})$ and $(\mathbf{c})$ show the radial spectra of the experimental amplitudes $\tilde{b}_{4,3\omega_0}(t, k_r)$ for all realisations at two different times, matching the colours of the dotted vertical lines in $(\mathbf{a})$. Darker lines show the ensemble average of the quantities in both panels. The horizontal axis of $(\mathbf{b})$ and $(\mathbf{c})$ follow the resolution of the numerical Fourier transform. Hence the values of $k_0/(2\pi) \approx 0.35\,\mathrm{cm}^{-1}$ and $k_1/(2\pi) \approx 1.77\,\mathrm{cm}^{-1}$ are approximated by the closest binned value, i.e., $k_{r,0} \sim 0.5\,\mathrm{cm}^{-1}$ and $k_{r,1} \sim 2\,\mathrm{cm}^{-1}$.

instabilities, obtaining the ratio $\lambda_1^{(M)}/\lambda_0^{(M)} = 2.85$ for the run displayed in Figure 3.10, and then for the entire simulated ensemble, for which we obtain $\left\langle \lambda_1^{(M)}/\lambda_0^{(M)} \right\rangle = 3.06$. In the experimental data, the secondary instability at $3\omega_0$ (dark-blue dashed curve) in Figure 3.10(a) results from an overlap between a harmonic of the primary mode with low k_0 and the secondary with high k_1, whose radial spectrum cannot be separated. Thus, when examining the slope of the experimental amplitude $\tilde{b}_{4,3\omega_0}(t, k_1)$, we observe a contribution from the primary growth λ_0 to the pure secondary instability with rate λ_1, which should follow the simulated model (maroon dashed curve). The relative contribution of the modes depends on their random initial state and hence varies between experimental repetitions. The outcome of this mode superposition

is a modulated secondary growth that cannot be reliably compared with the slopes extracted from our model.

As outlined in subsection 3.2.2, our effective description of the interfacial dynamics in our system qualifies it as an analogue simulator for mode-mode scattering through quartic interactions and, as such, offers a platform to experimentally investigate aspects of preheating models. Similar to our quartic non-linear terms in the EFT Lagrangian, Berges & Serreau [151] investigate a model for preheating as presented in subsection 2.4.3 but with a ψ^4-type interaction in the Lagrangian of the matter field ψ. By using approximate analytical and numerical techniques, they identify a signature of preheating as the decay of modes amplified through the primary resonance into secondary instabilities. Particularly, the latter is predicted to appear with an integer multiple of the frequency and slope of the former. From the discussion above, we see that this feature appears in the simulations of our non-linear model but is not as evident in the empirical data, and more experiments are needed to confirm this feature, showing the same difficulty in observing the modelled amplification rates for the BEC simulator discussed in [185]. Nevertheless, as predicted for preheating models in BECs [186], in Figure 3.10(b) and (c) the qualitative picture of this early-Universe process emerges. We observe the broadening of the primary resonance at k_0 and subsequent occupation of secondary instabilities through the scattering to higher wavenumber modes k_1.

3.5 Summary and discussion

Based on the theoretical model of Chapter 2, we presented the experimental investigation of a non-linear EFT for the interfacial dynamics between two immiscible liquids. We presented the setup that allowed a consistent repetition of 1500 runs with fixed specifications in a well-controlled environment. By monitoring the mechanical performance and the ambient temperature, we have quantitatively established the reliability of the repetitions. In particular, a dependence between the response of the mechanical oscillator and temperature was identified (Figure 3.5), seemingly affecting only the amplitude of the acceleration but not the cross-axis motion and Total Harmonic Distortion (THD), both of which were well-within or better than the accepted industry standards. Despite the observed changes, the measured vertical acceleration varied within $\pm 1.5\%$ of its average, which in no way hindered the formation of Faraday waves on the interface.

With continuous image acquisition during each repetition, we could reconstruct the time evolution of interfacial height changes ξ with enough resolution to observe wave amplification spanning over three orders of magnitude, from micro to millimetres. With an appropriate spectral decomposition of the data, we distinguished the unstable evolution of individual azimuthal modes around the primary resonance band (Figure 3.6). A

dominant interfacial wave appeared invariably in all repetitions with azimuthal number $m = 4$ and amplitudes at least 10 times larger than the remaining modes. Focusing on the evolution of the dominant mode, the amplification and damping rates were extracted by fitting the log-linear behaviour of the instantaneous amplitude b_{4,ω_0} during the growth and decay periods. Once again, the laboratory temperature was seen to correlate with damping but not so clearly with the amplification rates (Figure 3.8). We argued that the variations in the former are consistent with thermally-induced changes in the physical properties of the fluids, particularly the viscosities. Further, linear Floquet analysis was used to offer an explanation for the overall insensitivity of the fitted amplification rates with temperature.

Using the experimentally extracted decay rates for the dominant mode, we found that the damping model presented in Chapter 2 underestimated the observed damping by about 17%. Supported by previous experimental studies reporting this discrepancy, we concluded that it was likely due to capillary effects around the vertical walls, which were not accounted for by the model, as stated in Chapter 2. We leave the inclusion of these effects for future work through, e.g., the semi-analytical and numerical approach presented in [147]. From the experimental side, different liquids could be used to create the biphasic sample, e.g. [87, 187], and reduce boundary-layer damping at low frequencies. It should be noted, however, that to reduce the formation of a meniscus around the contact line and hence suppress its dissipation, it is not enough to simply change the set of two fluids used but also consider their interaction with the vertical walls. For instance, the roughness of the material of the basin plays a dramatic role in the reduction of dissipation through capillary-viscous boundary layers [94, 97].

Once it was clear that the 1500 repetitions displayed consistent behaviour, we examined the distributional properties of the ensemble of measured instantaneous amplitudes of the dominant mode. For that, we used higher-order correlation functions to compute measures of non-Gaussianity using experimental and simulated amplitudes (Figure 3.9). The latter was obtained from a numerical ensemble evolving according to the self-interacting nonlinear dynamics of the dominant mode. The agreement between empirical and theoretical measures shows that our approximate non-linear model successfully describes the evolution of the primary instability. Additionally, it confirms that the statistical machinery employed here can be utilised in characterising the emerging EFT throughout the entire evolution of the ensemble.

Finally, we strengthened the conceptual connection with the target scenario, preheating, by investigating the appearance of secondary instabilities through the decay of the dominant mode (Figure 3.10). In our system, this feature of preheating dynamics appeared through the growth in occupation of a higher-wavenumber mode at three times the primary frequency. Complementarily, the reduced quartic Lagrangian obtained in our model was shown to reproduce this behaviour in the evolution of the

secondary mode. Our findings are in agreement with the preheating scenario put forward by Berges & Serreau [151] and other theoretical analogue preheating proposals in ultra-cold atoms [185, 188].

The results presented here show that features of inflationary preheating can be observed by parametrically driving nonlinearities in a strongly interacting and damped system and can be directly related to the underlying field-theoretical model of interactions. We consider this approach an initial step in the characterisation of EFTs in classical simulators, where the entire time evolution of the system is available, and the onset of nonlinearities can be investigated, limited only by detection precision and data analysis uncertainty. Ultimately, motivated by perhaps elusive theoretical models, our expectation is that more experimental simulators tackle the challenges of understanding far-from-equilibrium scenarios in both classical, as in here, and quantum systems, as in [71, 73, 74]. In this process, their results may be used to improve the model and learn more about the nonlinear physics of the simulator.

For fluid dynamics, we maintain that experimental studies of surface and interfacial phenomena may benefit from the statistical machinery and conceptual intuition of EFTs. With appropriate detection schemes, one could examine the complexity of the stochastic interfacial dynamics emerging from the coarse-graining of the molecular theory. In the context of nonlinear Faraday instabilities, although being a 200-year-old field, the study of specific interaction channels and pattern formation could be improved through the data analysis and modelling tools presented here.

Chapter 4

Detection methods for fluid profilometry

In previous chapters, we showed that interfacial height fluctuations in classical and quantum fluids play a central role in devising Effective Field Theory (EFT) simulators for gravity and the early Universe. Accordingly, the experimental realisation of these analogues in fluids relies on measuring the 3D profile of the interface and monitoring its time evolution. Here, we first review the application of a standard method of digital reconstruction of fluid interfaces, which was employed in the experimental setup discussed in Chapter 3. Later, we present a novel reconstruction scheme based on Digital Holography (DH), designed to operate at room temperature and below, envisioning future experiments using superfluid helium. The contents of this Chapter regarding digital holography are based on the work *"Multiplexed digital holography for fluid surface profilometry"* [3], developed with August Geelmuyden, Sreelekshmi C. Ajithkumar, Anthony J. Kent, and Silke Weinfurtner.

4.1 Fluid profilometry methods

The study of interfacial phenomena and surface flows in fluids requires advanced detection schemes that can reveal the intricacies of these systems. Over the past few decades, many of these methods have emerged, driven by significant advancements in computer vision and the need for efficient profilometry techniques in automated production lines. Currently, widely-employed object profilometry methods [189] include correlating images taken from slightly different angles, analysing the deformations of periodic patterns and time-of-flight imaging. Many of these have been adapted for applications in fluid samples, see, e.g., [190] for a modern review of techniques for free-surface flow measurements. We note, in particular, the Schlieren Fourier Transform Profilometry (FTP) proposed by Wildeman [89], which became known for its optimal

computational performance and straightforward experimental implementation, being extensively applied in the past few years. By placing a periodic pattern on the background of a transparent fluid sample, this method circumvents the main issue with pattern projection techniques in fluids [191, 192]: the liquid must often be contaminated with an opaque or fluorescent dye, potentially changing its physicochemical properties, as reported in [193]. Here, we will review the main aspects of this technique relevant to its implementation in the setup of Chapter 3 and refer to its references for a comprehensive discussion.

Despite the advantages of Schlieren FTP, its application is limited by the size and spatial frequency of the physical periodic pattern under the sample and the imaging system, for instance, requiring specific lighting of the background and suitable optical access and camera-lens combinations [190]. Practically, this technique may not be appropriate for studies seeking to resolve nanometric fluid profile measurements, such as for thin films of superfluid helium or surface fluctuations in liquids at room temperature. Envisioning future analogue simulators using fluid samples at smaller scales and/or lower temperatures, we devise a new optical detection scheme that combines digital processing aspects of FTP with a digital holographic experimental setup. In parallel with the aforementioned profilometry methods, Digital Holography (DH) has been a powerful tool in the context of microscopy and topography of nanostructures [194, 195]. Building upon its principles, we will show that multiple interference fringe patterns can be generated, and the numerical procedure employed in Schlieren FTP for analysing periodic signals can be used to digitally reconstruct the profile of a fluid surface.

4.2 Schlieren Fourier Transform profilometry

Fourier Transform Profilometry (FTP) was first proposed by Takeda & Mutoh [191] as a technique for digitally reconstructing the three-dimensional profile of reflective objects. In its original formulation, the method involved projecting a periodic pattern on the target sample, whose surface profile variations would deform the projected fringes. A camera displaced from the projector by a known distance would then acquire snapshots of the system. By comparing these images with an undeformed reference fringe pattern, Takeda & Mutoh showed it was possible to recover the shape of the object. The appeal of their method was in its straightforward analysis and the ingenuity in noting that the periodic images appear as isolated signals in the spatial-frequency domain (SFD). Hence, from the Fourier transformed snapshots of reference and deformed patterns, one could retrieve the profile of the object, hence the name FTP.

Naturally, the technique expanded into an entire field of its own, with extensive theoretical and computational developments, see [196] and references therein. The

applications of FTP eventually reached the domain of fluid dynamics, with the reconstruction of free-surface waves on fluids, notably in the work of Cobelli et al. [192]. In the same year, Moisy et al. [168] extended the principles of synthetic Schlieren imaging (SSI) [197] for the same purposes. In their method, a random backdrop pattern is placed under a fluid sample, where waves appear on the free surface. A Schlieren image[1] is then synthetically generated by digitally contrasting a distorted image of the sample with an undistorted one, similar to the procedure in FTP.

More recently, Wildeman [89] proposed a merged approach between FTP and SSI, which the author calls Fast-Checkerboard Demodulation (FCD), and we refer to it as Schlieren FTP. Wildeman maintains the experimental configuration of SSI, where a camera placed at a known distance from the sample records a pattern under the fluid, as shown in Figure 3.2 for the experimental setup of Chapter 3. However, the author proposes replacing the random dot pattern typically used in SSI with a periodic checkerboard backdrop reminiscent of the fringe-pattern projection in FTP. In general, the intensity profile of this undisturbed checkboard pattern reads

$$I_0(\mathbf{r}) = \mathcal{C}_0 + \mathcal{C}_1 \left[\cos(\mathbf{k_1} \cdot \mathbf{r}) + \cos(\mathbf{k_2} \cdot \mathbf{r})\right], \tag{4.1}$$

where $\mathbf{r}$ denotes the horizontal coordinate along the pattern, $\mathbf{k_1}$ and $\mathbf{k_2}$ are two distinct spatial wavevectors determining the repetition frequency of the pattern in direct space, and $\mathcal{C}_0$ and $\mathcal{C}_1$ are two arbitrary intensities. In Chapter 3, the horizontal coordinate is denoted by $\mathbf{x}$ instead of $\mathbf{r}$ to avoid confusion with the radial coordinate r of the basin's geometry. We also used an alternative periodic pattern formula for clarity in the discussion of subsection 3.3.3. Nevertheless, the following discussion applies generally to any spatially periodic pattern, as discussed in [89].

From the point of view of the camera, when surface waves appear in the fluid sample, the pattern is disturbed and effectively shifted. These deformations can be represented by a horizontal apparent-displacement field $\boldsymbol{\delta}(\mathbf{r})$. The essence of SSI and FTP is in noting that the intensity of the disturbed pattern $I(\mathbf{r})$ is given by a displaced view of the reference $I_0(\mathbf{r})$, i.e., $I(\mathbf{r}) = I_0\left(\mathbf{r} + \boldsymbol{\delta}(\mathbf{r})\right)$. Hence, the first step of these methods is to quantitatively retrieve $\boldsymbol{\delta}(\mathbf{r})$. Then, this displacement field needs to be related to the physical deformations on the surface of the sample.

In practice, images of the pattern are discretised intensity maps of Equation 4.1 and are often not exactly periodic. Thus, their Fourier transform is likely to include digital processing features, such as harmonics or aliasing [160]. Accordingly, a more realistic representation of the image $\mathbf{Y}(\mathbf{r})$ of a disturbed pattern $I(\mathbf{r})$ in terms of a harmonic

[1] Schlieren imaging [198, 199] refers to a visualisation technique for density changes or bulk flows in fluid samples, such as air and inhomogeneous liquids. The images typically display dark or bright streaks where sudden changes happen in the flow, as for shock waves when a bullet moves through air. Hence the name *Schlieren*, which translates to *streaks*, in German.

series would be

$$\mathbf{Y}(\mathbf{r}) = \sum_{p,q} \mathcal{A}_{p,q} \exp[i(p\mathbf{k_1} + q\mathbf{k_2}) \cdot (\mathbf{r} + \boldsymbol{\delta}(\mathbf{r}))] \equiv \mathbf{Y_0}(\mathbf{r} + \boldsymbol{\delta}), \tag{4.2}$$

where p, q are integer counters, and the amplitudes $\mathcal{A}_{p,q}$ must satisfy $\mathcal{A}^*_{-p,-q} = \mathcal{A}_{p,q}$, since $\mathbf{Y}$ is real-valued. Here, we see that the displacement field $\boldsymbol{\delta}(\mathbf{r})$ acts as frequency modulation (FM) around specific carrier frequencies $\mathbf{k}_m \in (p\mathbf{k_1} + q\mathbf{k_2})$, analogous to FM radio transmission [89]. An alternative perspective comes by noting that the signal $g_m(\mathbf{r})$ of a carrier $\mathbf{k}_m$ in Equation 4.2 may be expressed as a planar phase $\mathbf{k}_m \cdot \mathbf{r}$ modulated by a spatially-varying phase $\phi_m(\mathbf{r})$, i.e,

$$g_m(\mathbf{r}) = \mathcal{A}_m \exp[i\mathbf{k}_m \cdot \mathbf{r} + \phi_m(\mathbf{r})]. \tag{4.3}$$

Clearly, the following correspondence applies: $\phi_m = \mathbf{k}_m \cdot \boldsymbol{\delta} = k_{m,x}\delta_x + k_{m,y}\delta_y$, with $\mathbf{k}_m = k_{m,x}\hat{\boldsymbol{x}} + k_{m,y}\hat{\boldsymbol{y}}$ and $\boldsymbol{\delta} = \delta_x\hat{\boldsymbol{x}} + \delta_y\hat{\boldsymbol{y}}$. Hence, to recover both components of $\boldsymbol{\delta}$, we need the phases ϕ_m of two (misaligned $\mathbf{k}_m \times \mathbf{k}_{m'} \neq 0$) carrier frequencies in the least.

In the particular cases of $\mathbf{k}_m = \mathbf{k}_1$ and $\mathbf{k}_{m'} = \mathbf{k}_2$, we obtain a 2×2 system of equations relating the phase modulations ϕ_1 and ϕ_2 around these carriers with the components of $\boldsymbol{\delta}$. By inverting it, we find the latter as

$$\delta_x(\mathbf{r}) = \frac{k_{2y}\phi_1(\mathbf{r}) - k_{1y}\phi_2(\mathbf{r})}{k_{1x}k_{2y} - k_{1y}k_{2x}}, \tag{4.4a}$$

$$\delta_y(\mathbf{r}) = \frac{k_{2x}\phi_1(\mathbf{r}) - k_{1x}\phi_2(\mathbf{r})}{k_{1y}k_{2x} - k_{1x}k_{2y}}. \tag{4.4b}$$

With the equation above, it is possible to obtain the displacement field from two observed phases. In what follows, we will discuss the numerical procedure, called Fourier demodulation [169], for digital recovery of these phases from distorted images of a periodic pattern. We will then present the implementation of this Schlieren FTP method to the two-fluid system of Chapter 3, focusing on how the displacement field $\boldsymbol{\delta}$ relates to the interfacial profile ξ.

4.2.1 Fourier demodulation and phase recovery

We parametrise an image $\mathbf{Y}$ of the pattern as a map of intensity evaluated in the grid of pixels labelled by positive integers (i, j), with positions $\mathbf{r}_{ij} = (x_i, y_j)$. Hence, the image is denoted $\mathbf{Y} = (Y_{ij}) \equiv I(\mathbf{r}_{ij})$ and, similarly, for the phase, $\phi^{(m)}_{ij} = \phi_m(\mathbf{r}_{ij})$. The planar phases $\mathbf{k}_m \cdot \mathbf{r}$ in Equation 4.2 appear in the Fourier spectrum of Y_{ij} as localised intensity peaks centred at the carrier frequencies $\mathbf{k}_m$, i.e., $\mathcal{F}[\exp(i\mathbf{k}_m \cdot \mathbf{r})](\mathbf{k}) \propto \delta(\mathbf{k} - \mathbf{k}_m)$. Provided with some function $G_m(\mathbf{k})$ that is non-vanishing around the carrier

frequency $\mathbf{k}_m$ only, we define a Fourier filter $F_m \equiv \mathcal{F}^{-1} G_m(\mathbf{k}) \mathcal{F}$ around the peak at $\mathbf{k}_m$. Depending on the properties of $G_m(\mathbf{k})$, the filter should allow us to isolate a signal of the form (4.3), i.e.,

$$g_m(\mathbf{r}) = \mathcal{A}_m e^{i\mathbf{k}_m \cdot \mathbf{r} + \phi_m(\mathbf{r})} \simeq F_m[\mathbf{Y}](\mathbf{r}) = \left\{ \mathcal{F}^{-1}[G_m] * \mathbf{Y} \right\}(\mathbf{r}). \tag{4.5}$$

In the above equation, we noted that the filtered image $F_m[\mathbf{Y}]$ can be regarded as a convolution of the inverse Fourier transform of the function G_m and the image $\mathbf{Y}$. In other words, the degree to which the filtered image $F_m[\mathbf{Y}]$ retrieves the ideal signal g_m depends not only on the form of $G_m(\mathbf{k})$ in spatial-frequency domain (SFD), but also on its response in direct space, given by $\mathcal{F}^{-1}[G_m](\mathbf{r})$.

It is shown in [200] that the best choice of G_m to reduce errors induced by digital filtering is a finite impulse response (FIR) filter [160]. That is, the function G_m and its inverse Fourier transform $\mathcal{F}^{-1}[G_m]$ both have negligible gain outside a finite region in SFD and direct space[2]. Accordingly, our choice of function $G_m(\mathbf{k})$ is such that it is 1 inside a disk $|\mathbf{k} - \mathbf{k}_m| \leq k_{c,m}$, for some spatial frequency cutoff $k_{c,m}$, and smoothly goes to zero within the interval $k_{c,m} < |\mathbf{k} - \mathbf{k}_m| < 1.1\ k_{c,m}$. To isolate the signals of the peaks, we must appropriately select the size of the filters $G_m(\mathbf{k})$, given by $k_{c,m}$, so they do not overlap [89]. In our method, based on the neighbouring noise background of a peak at $\mathbf{k}_m$ and its distance to others, we select a cutoff $k_{c,m}$ large enough so that as many of its modulations as possible are within G_m without intersecting with suitable filters around other peaks. It should be noted that the size of the filter in SFD, determined by $k_{c,m}$, also delimits the maximum wavenumber that can be resolved in the reconstructed phase ϕ_m [191], i.e., $|\nabla \phi_m(\mathbf{r})| \lesssim k_{c,m}$.

Finally, with a suitable choice of filter, we select a filtered reference image $(Y_0)_{ij}$, i.e., $F_m[Y_0]_{ij}$, to recover the phase variations $\Delta\phi_{ij}^{(m)}$ with respect to it. The outcome is then:

$$\Delta\phi_{ij}^{(m)} = \mathrm{Im}\left\{ \log\left[(F_m[Y]_{ij})(F_m[Y_0]_{ij})^* \right] \right\}. \tag{4.6}$$

Numerically, this equation will only yield values between $-\pi$ and π. Thus, if the change in phase $\Delta\phi_{ij}^{(m)}$ is larger than one period of 2π, then a phase unwrapping algorithm, such as that of [202], is required. One way to avoid the issue of phase wrappings is to consider changes in phase from some reference time t_0 to the time t in question. If the position of the carrier does not drift from t_0 to t, i.e. $\mathbf{k}_m(t_0) = \mathbf{k}_m(t)$, then, the reconstructed phase difference reads $\Delta\phi_{ij}^{(m)} \equiv \phi_{ij}^{(m)}(t) - \phi_{ij}^{(m)}(t_0)$.

[2]For instance, a common non-FIR filter used in image processing is a tophat, defined as $\Pi_m(\mathbf{k}) = \Theta(k_{c,m} - |\mathbf{k} - \mathbf{k}_m|)$, i.e., it is 1 for $|\mathbf{k} - \mathbf{k}_m| < k_{c,m}$, and zero elsewhere. Its inverse Fourier transform is given by $\mathcal{F}^{-1}[\Pi_m] \propto \exp(i\mathbf{k}_m \cdot \mathbf{r}) J_1(k_{c,m}|\mathbf{r}|)/|\mathbf{r}|$, which extends over all direct space. Hence, a convolution with this function integrates over contributions from all values of $\mathbf{r}$, brought by the infinite response of the Bessel function $J_1(k_{c,m}|\mathbf{r}|)$. Instead, to avoid this issue, an FIR filter can be appropriately constructed to approximate the ideal tophat response in SFD while keeping a negligible gain outside a finite region in direct space, e.g., through the Remez algorithm [201].

Given a sequence of images $\{Y_{ij}(t_n)\}_{n=1}^{N}$ taken at equidistant times spaced by a fixed $\delta t \equiv t_{n+1} - t_n$, there are two canonical choices for the reference time t_0. First, one may choose t_0 as a constant reference, e.g. the first camera frame. We shall refer to this approach as the *absolute reconstruction*. Alternatively, one can choose the previous image as the reference, i.e. $t_0 = t - \delta t$. We shall refer to this approach as the *relative reconstruction*. Lastly, we shall refer to the full reconstructed phase $\phi_{ij}^{(m)}$ using a synthetic reference image of a plane wave $\exp(i\mathbf{k}_m \cdot \mathbf{r})$, e.g., a digitally generated checkerboard pattern, as *synthetic reconstruction*, which is always determined up to a global phase wrapping value ℓ_m. These digital phase recovery procedures are general and independent of the experimental method used to generate a periodic signal. In Chapter 3, we employed an absolute reconstruction using an initial reference, as detailed in subsection 3.3.3. In Section 4.3, we will show the usage of the relative reconstruction in a different type of setup.

4.2.2 Implementation in the two-fluid system

As briefly introduced in subsection 3.3.3 of Chapter 3, we employed the Schlieren FTP method discussed above as a detection of interfacial waves between two liquid phases. With the procedure of the previous section, we can digitally reconstruct the phases around the carrier frequencies of a disturbed pattern and, in turn, use Equation 4.4 to compute the displacement field $\boldsymbol{\delta}$. In the following, we use the properties of the experimental implementation of Chapter 3 to adapt the results of Moisy et al. [168] for the relation between $\boldsymbol{\delta}$ and the interfacial height ξ. A depiction of the setup is shown in Figure 4.1, with the interface located at $z = \xi(t, \mathbf{r})$.

Moisy et al. [168] detail the long derivation of the displacement field $\boldsymbol{\delta}$ in the case of waves on a free surface in a single fluid, i.e., without an upper phase and top window, in comparison to our setup. They showed that the displacement is proportional to the gradient of the surface profile ξ and can be well approximated by

$$\boldsymbol{\delta} = \tilde{h}\nabla\xi, \quad \text{with } \left(\tilde{h}\right)^{-1} = \left(1 - \frac{n_2}{n_1}\right)^{-1} h_p^{-1} - H^{-1} > 0, \tag{4.7}$$

where $h_p = h_0 + n_1 d_p + \ell_w n_1/n_w$ is the apparent pattern-surface distance, and H is the pattern-camera distance. We argue, however, that their results can be adapted to our system. It is straightforward to see that, in our setup (see values in Figure 4.1), $H \gg (1 - n_2/n_1)\, h_p$ and, thus, $\tilde{h} \simeq (1 - n_2/n_1)\, h_p$.

Under the conditions of our system, the light rays leaving the checkerboard pattern, going through the sample, and reaching the camera, must exit the fluid surface almost exactly parallel to the vertical axis. By combining this large camera-pattern distance with a telecentric lens-camera configuration, this condition is enhanced, and virtu-

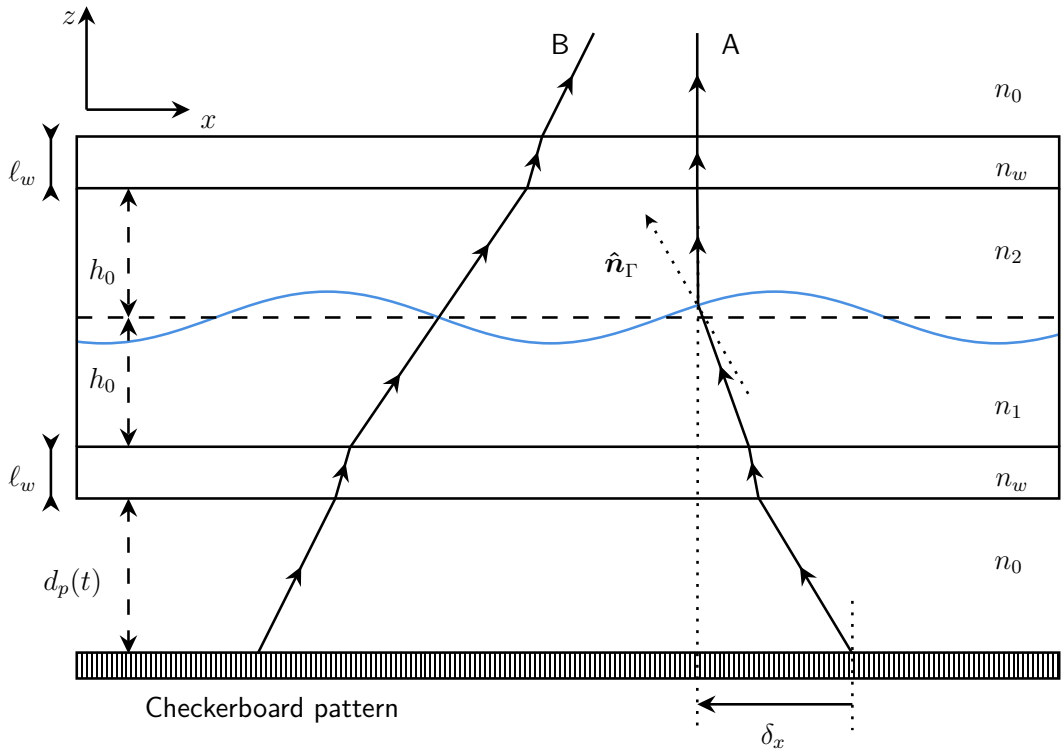

Figure 4.1: Ray tracing of Schlieren FTP method in two-fluid system of Chapter 3. Distances and angles are not to scale and are mere depictions of the model. The refracting trajectories of two indicative light rays originating at the checkerboard pattern are shown. Ray A exits the top window parallel to the vertical axis z, while Ray B leaves at an angle. For a camera placed at $H = 1.8\,\mathrm{m}$ from the pattern, only type-A rays reach the camera, which images an effective displacement δ_x of the pattern along the $x-$direction. A checkerboard pattern sits at a time-dependent distance $d_p(t) = d_0 - F_0(t)/\omega_\mathrm{d}^2$ from the bottom lid of the two-fluid cell, with $d_0 = 10\,\mathrm{cm}$. Inside the basin, the deformed interface $\Gamma = z - \xi(t, \mathbf{r})$ is indicated by a blue line. A dashed line shows the average resting interface at $z = 0$. Both liquid phases have an average depth of $h_0 = 17.5\,\mathrm{mm}$, and the denser and lighter fluids have refractive indices $n_1 = 1.385$ and $n_2 = 1.364$, respectively. The top and bottom lids have thickness $\ell_w = 6\,\mathrm{mm}$ and are made of a transparent material with refractive index $n_w = 1.51$. The surrounding medium is air, with refractive index $n_0 = 1$.

ally all light reaching the camera sensor comes from rays parallel to the optical axis. Accordingly, in our setup, only rays of type A in Figure 4.1 would contribute to the distorted view of the pattern, while light rays of type B, leaving the top window at an angle, would never reach the camera sensor. In other words, a distorted image of our setup can be well approximated by rays that exit the interface parallel to the $z-$axis. Hence, the light rays cross the top window of the cell along its vertically-directed normal $\hat{\boldsymbol{n}}_w = \hat{\boldsymbol{z}}$, and refraction there can be neglected altogether. Consequently, this configuration is effectively equivalent to that of Moisy et al. [168] for free surface waves, and Equation 4.7 can be used in our experiment.

4.2.3 Numerical reconstruction of the interface

In the previous sections, we showed the procedure to recover the phases modulating the carrier frequencies of the checkerboard pattern and their relation to the displacement field through Equation 4.4. We also presented how the latter relates to the gradient of the interfacial height between the two fluids in our experimental setup of Chapter 3. Hence, if correctly inverted, Equation 4.7 should yield a digital reconstruction of the interfacial profile ξ. For this inversion, we employ a straightforward algebraic operation in SFD, as in [203], by first taking the divergence of Equation 4.7 and, then, computing the Fourier transform. That is,

$$\begin{aligned}\mathcal{F}\left[\nabla\cdot\boldsymbol{\delta}\right] &= \mathcal{F}\left[\nabla\cdot\left(\tilde{h}\nabla\xi\right)\right]\\ \implies 0 = \mathcal{F}[\nabla^2\xi] - \frac{1}{\tilde{h}}\mathcal{F}[\nabla\cdot\boldsymbol{\delta}] &= -|\mathbf{k}|^2\mathcal{F}[\xi] - \frac{1}{\tilde{h}}(-i\mathbf{k})\cdot\mathcal{F}[\boldsymbol{\delta}]\\ \implies \xi = \frac{1}{\tilde{h}}\mathcal{F}^{-1}&\left[\frac{(i\mathbf{k})\cdot\mathcal{F}[\boldsymbol{\delta}]}{|\mathbf{k}|^2}\right]. \quad (4.8)\end{aligned}$$

The equation above provides a systematic mapping between the apparent displacement field and the interfacial height profile. It should be noted that Equation 4.7 is insensitive to spatially homogeneous changes in ξ over time. If the interface shifts by a constant amount, $\xi(t,\mathbf{r}) \to \xi_0(t) + \xi(t,\mathbf{r})$, its gradient remains the same since $\nabla\xi_0(t) \equiv 0$. Hence, the displacement $\boldsymbol{\delta}$ is not affected by $\xi_0(t)$, and Equation 4.8 cannot retrieve this constant shift.

In summary, the numerical procedure for the reconstruction of the interface for the setup discussed in Chapter 3 is carried out as follows:

1. Reference and target images, $\mathbf{Y_0}$ and $\mathbf{Y}$, respectively, are obtained from the experiment.

2. Using the reference, the two misaligned carrier frequencies $\mathbf{k}_1$ and $\mathbf{k}_2$ are identified in the Fourier domain (SFD) by their intensity peaks, and spectral filters $G_1(\mathbf{k})$ and $G_2(\mathbf{k})$ are respectively defined to isolate the signals of each carrier peak. The final image filters are then computed $F_m = \mathcal{F}^{-1}G_m\mathcal{F}$, for $m = 1, 2$ labelling the carriers.

3. Two reference signals as in Equation 4.3 are then computed by filtering $\mathbf{Y_0}$, i.e., $g_{0,m}(\mathbf{r}) = F_m[\mathbf{Y_0}]$, for $m = 1, 2$.

4. Step 3 is repeated with the target image $\mathbf{Y}$ to compute the modulated filtered signals $g_m(\mathbf{r}) = F_m[\mathbf{Y}]$.

5. The phases ϕ_m modulating the carriers are recovered using the numerical equivalent of Equation 4.6, given by $\phi_m = \texttt{unwrap}(\texttt{angle}(g_m\ g^*_{0,m}))$, where the

function `angle` numerically evaluates the phase of the input between $-\pi$ and π, while `unwrap` performs the spatial unwrapping of the retrieved phase.

6. The vector components of the apparent spatial displacement $\boldsymbol{\delta}$ are computed from Equation 4.4 using the phases ϕ_1 and ϕ_2 obtained in step 5, and the values of $\mathbf{k}_1$ and $\mathbf{k}_2$ determined in step 2.

7. Finally, the interfacial height profile ξ is obtained by the integration procedure of Equation 4.8 using the displacement $\boldsymbol{\delta}$ computed in 6.

4.3 Digital Holographic profilometry

In 1948, Gabor [204] introduced the revolutionary concept of holography in optics, marking a significant milestone in the field of imaging and three-dimensional visualisation. Through diffraction theory, Gabor's breakthrough allowed the complete reconstruction of optical wavefronts and the extraction of three-dimensional information from two-dimensional holograms [205, 206]. Later on, with the invention and development of computer processors and CCD cameras, digital holography (DH) emerged with methods for digitally reconstructing holograms, retrieving phase and amplitude information from images obtained from interferometric setups [207, 208]. Rapidly evolving technological advances led to subsequent innovations, such as quantitative phase measurements through off-axis DH, as put forward by Cuche et al. [209]. In off-axis DH, the reference and probe arms of an interferometric setup, e.g. Michelson or Mach-Zender, are purposefully misaligned to generate a linear fringe pattern carrying information on the profile of the sample imaged by the probe arm.

Over the past decades, the field of digital holography gained momentum, and its applications as a metrology tool now extend over a broad range of areas, from the study of living organisms in micro-biology to the profile inspection of nano-materials [194, 195]. One of the key recent developments in DH is the concept of multiplexing; see [210] for a comprehensive review. Multiplexed DH relies on simultaneously recording multiple holograms from the same sample by modifying or adding optical components according to the desired application. This was shown to effectively increase the storage capacity of holograms [211–213] and improve their reconstruction performance [214, 215] and resolution [216]. We note, however, that applications of off-axis multiplexed digital holography to fluid measurement are scarce, especially outside the realm of microscopy.

Here, we develop a method for reconstructing the profile of fluid surfaces evolving in time by extending fluid profilometry and off-axis DH multiplexing techniques. In a Michelson interferometry setup, when one arm probes a liquid sample, the resulting hologram becomes a superposition of multiple interference patterns, each having phases proportional to the liquid surface profile. In our specific configuration, the

fluid acts as a cavity, generating multiplexed holograms. This study introduces a systematic approach to extracting the fluid surface profile from the modulations on the carrier peaks within each pattern. As for the Fast-Checkerboard Demodulation (FCD) method, these carrier peaks can be distinctly identified within the spatial frequency domain. Through intentional off-axis adjustments of the beam paths, we effectively enhance the separation of these carriers in the frequency domain. We can recover slight variations on the fluid surface with a digital reconstruction of their phase changes between consecutive time frames.

We consider a Michelson interferometer, as commonly employed in off-axis Digital Holography (DH), shown in Figure 4.2. In this configuration, a beam splitter divides an input laser beam with wavelength λ into two arms after it has been expanded to the required width. A reference is created by reflecting one of the arms from a mirror (M_r), while the other probes the fluid sample. This probe beam partially reflects from the fluid surface and a mirror placed under it (M_b). To create a variety of linear interference patterns, we employ the general off-axis DH procedure of slightly misaligning the reference with respect to the probe arm. As the beams recombine in the beam-splitter, their resulting interferograms (or holograms) are captured by a digital camera (C). Since this setup exploits the partial reflections from a sample, it can be referred to as DH reflectometry, as discussed in [217, 218] for the profile reconstruction of semi-transparent wafers. In the following, we briefly examine the relations between the height profile of the sample and the fringe patterns that appear due to the optical path differences among the different components of the probing beam.

4.3.1 Phase shifts and fluid height profile

We first examine the various rays types present in the setup of Figure 4.2 and their optical paths as they travel through an air-fluid interface at $z = h(t, \mathbf{r})$. Consider a ray that originates at an initial height $z = H$, with a transverse horizontal coordinate $\mathbf{r}$, and progresses down towards the fluid. Upon reaching the interface, the ray undergoes partial transmission and partial reflection, and we refer to it as an F-type ray. The transmitted ray proceeds through the fluid and arrives at a submerged plane mirror M_b situated at the bottom of the basin. This arrangement results in the fluid interface and the mirror working as a cavity, producing an assortment of partially reflected rays, denoted as B_j and labelled by the number j of internal reflections within the fluid (see depiction in Figure 4.2). The probe arm — comprising F and B_j rays — merges at the beam-splitter with the reference arm R, originating from the reflection off mirror M_r. This combination generates a beam featuring four families of interferograms: RF, RB_j, FB_j, and $B_\ell B_j$. For any given ray pair AB, their phase difference $\Phi_{AB} =$

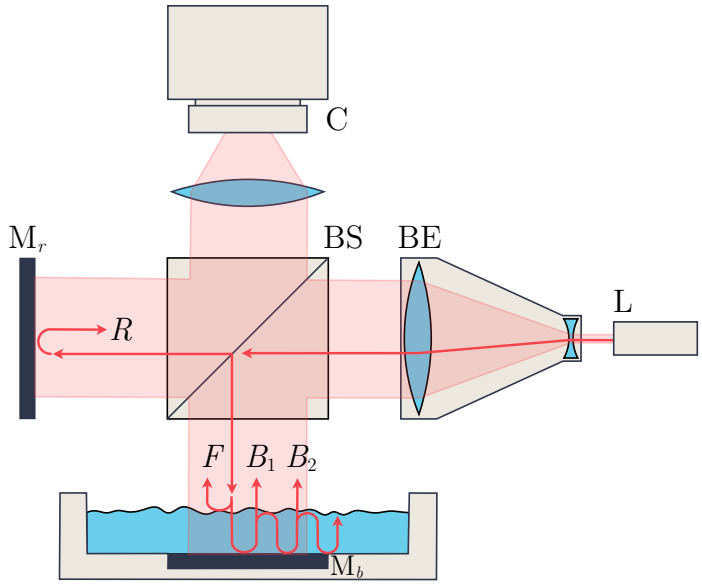

Figure 4.2: General schematics of proposed setup. A laser source (L) emits a collimated beam that expands to the desired diameter by passing through a Beam Expander (BE). A Beam Splitter (BS) divides the beam into two, namely a probe going through the fluid sample and a reference (R), both reflecting from adjustable mirrors (M). The reflected trajectories recombine in the beam splitter, and the resulting beam is captured by a camera (C). In the illustration, the multiple beams reflected from the fluid surface (F) and the probe mirror (B_1, B_2) contribute to the multiple interference peaks discussed in subsection 4.3.1. [3]

$\Phi_A - \Phi_B$ is directly proportional to their optical path differences. The camera C captures this combined beam, generating an image $\mathbf{Y} = (Y_{ij})$, which portrays the total intensity profile of all the interferograms at positive integer pixel positions (i, j). It is assumed that all phase differences Φ_{AB} exhibit minor modulations $\phi^{(AB)}(t, \mathrm{r})$ around a stationary planar phase $\mathbf{k}_{AB} \cdot \mathbf{r}$. That is, $\Phi_{AB}(t, \mathbf{r}) = \phi^{(AB)}(t, \mathbf{r}) + \mathbf{k}_{AB} \cdot \mathbf{r}$, so that

$$Y_{ij} = Y_0 \left(1 + \sum_{\substack{AB \\ A \neq B}} \mathcal{A}_{AB} \exp\left(i\mathbf{k}_{AB} \cdot \mathbf{r}_{ij} + i\phi_{ij}^{(AB)} \right) \right), \tag{4.9}$$

where Y_0 is an arbitrary average intensity, and the amplitudes $\mathcal{A}_{AB}$ are given below and, like the phases, result from propagating the electromagnetic waves through the media and computing their combined intensities [217, 219]. Naturally, the image $\mathbf{Y}$ is real-valued and, thus, for each pair AB in the summation of Equation 4.9, there is a conjugate BA, for which $\mathbf{k}_{BA} = -\mathbf{k}_{AB}$, $\mathcal{A}_{BA} = \mathcal{A}_{AB}$ and $\phi_{ij}^{(BA)} = \phi_{ij}^{(AB)}$. In the context of digital holography, $\mathbf{k}_{BA}$ is referred to as the twin signal of $\mathbf{k}_{AB}$.

We assume that the incident beam has its optical axis perpendicular to the plane of the fluid interface and can reflect off three surfaces: the reference and bottom mirrors, and the surface of the sample. Now, if both mirrors are slightly tilted with respect to the incident optical axis $\hat{\mathbf{z}}$, then their normal unit vectors $\mathbf{m}_b$ and $\mathbf{m}_r$ are such that

$\mathbf{m}_b \cdot \hat{\mathbf{r}} \ll 1$ and $\mathbf{m}_r \cdot \hat{\mathbf{r}} \ll 1$. For small surface slopes, i.e., $|\nabla h| \ll 1$, it follows that the phase differences carried by each family of holograms read

$$\Phi_{RF} = 2k_0 n_1 \left(h + \mathbf{m}_r \cdot \mathbf{r} + \Delta H\right), \tag{4.10a}$$

$$\Phi_{RB_j} = 2k_0[(n_1 - jn_2)h + (n_1\mathbf{m}_r - jn_2\mathbf{m}_b) \cdot \mathbf{r} + n_1\Delta H], \tag{4.10b}$$

$$\Phi_{FB_j} = 2k_0 n_2[jh + j\mathbf{m}_b \cdot \mathbf{r}], \tag{4.10c}$$

$$\Phi_{B_\ell B_j} = 2k_0 n_2[(\ell - j)h + (\ell - j)\mathbf{m}_b \cdot \mathbf{r}], \tag{4.10d}$$

where $\Delta H \equiv H_R - H$ is the arm length difference between the reference H_R and the probe H beams, and $k_0 \equiv 2\pi/\lambda$ is the laser wavenumber. Here, n_1 and n_2 denote the refractive indices of the surrounding medium (e.g., air) and the fluid, respectively. The relative amplitudes corresponding to each family of interferograms read

$$\mathcal{A}_{RF} = \mathcal{A}_0\, r_{21}, \tag{4.11a}$$

$$\mathcal{A}_{RB_j} = \mathcal{A}_0\, (1 - r_{21}^2) r_{21}^{j-1}, \tag{4.11b}$$

$$\mathcal{A}_{FB_j} = \mathcal{A}_0\, (1 - r_{21}^2) r_{21}^{j}, \tag{4.11c}$$

$$\mathcal{A}_{B_\ell B_j} = \mathcal{A}_0\, (1 - r_{21}^2)^2 r_{21}^{\ell+j-2}, \tag{4.11d}$$

where $r_{21} = \frac{n_2 - n_1}{n_1 + n_2}$ is the reflection coefficient between the two media, and $\mathcal{A}_0$ denotes a common constant amplitude prefactor. The phases (4.10) and amplitudes (4.11) above agree with those derived in [217]. We refer to [220] for a complete discussion and derivation of these equations in general configurations.

By comparing the phases in Equation 4.10 with Equation 4.9, it follows that the planar phases $\mathbf{k}_{AB} \cdot \mathbf{r}$ are proportional to $\mathbf{m}_b \cdot \mathbf{r}$ and $\mathbf{m}_r \cdot \mathbf{r}$. Hence, when the mirrors have a non-vanishing tilt in their normal vectors $\mathbf{m}_r$ and $\mathbf{m}_b$, the resulting image Y_{ij} captured by the camera will follow Equation 4.9 and exhibit a collection of distinguishable fringe patterns with spatial repetition frequency given by the various $\mathbf{k}_{AB}$ vectors. We will soon describe a process to numerically simulate the image using Equation 4.9, and an example frame of this procedure is shown in panel (a) of Figure 4.3. We denote the two-dimensional Fourier transform of the image $\mathbf{Y}$ as $\hat{\mathbf{Y}} = \mathcal{F}[\mathbf{Y}]$, which we use to inspect the SFD containing the spectrum of holograms. For reference, the SFD of the simulated image in Figure 4.3(a) is given in panel (b) of the same figure. Equation 4.10 also reveals how the interfacial height $h(t, \mathbf{r})$ acts as a modulation signal around the spatial carrier $\mathbf{k}_{AB}$ of all holographic families AB. Hence, variations $\delta\phi_{AB}$ in the phase

of a carrier due to changes δh on the fluid interface are given by

$$\left(\frac{\delta\phi_{AB}}{2\pi}\right) = 2\alpha_{AB}\left(\frac{\delta h}{\lambda}\right),\ \alpha_{AB} = \begin{cases} n_1, & \text{for } AB = RF; \\ j\ n_2, & \text{for } AB = FB_j; \\ n_1 - j\ n_2, & \text{for } AB = RB_j. \end{cases} \tag{4.12}$$

The dimensionless phase-prefactors α_{AB} above relate the observed phase modulations with the interfacial height changes and have distinct values for each family of interferograms AB.

Suppose the various holograms can be individually resolved in an intensity map of the form (4.10). In that case, we may refer to the resulting image as a Multiplexed Off-axis Digital Holography signal [211]. In this context, multiplexing implies that individual interferograms simultaneously measuring the same sample can be combined within a single snapshot of intensity due to their separation in SFD. While existing digital holography techniques have leveraged the multitude of rays arising from partial reflection, known as Digital Holographic Reflectometry [217, 218], a key distinction emerges in comparison to the approach outlined here. Introducing a tilt of the submerged mirror permits the arbitrary separation and isolation of off-axis holograms from the same group of partially reflected rays. Capitalising on this property, a straightforward Michelson interferometer (see Figure 4.2) enables simultaneous and autonomous surface measurements via the multiplexing process. Essentially, our approach presents an extension of digital holographic reflectometry by incorporating off-axis multiplexing principles without requiring additional optical components. Due to the mirror tilts, distinct holograms will capture marginally shifted regions of the fluid interface. Consequently, the reconstructed profile h_{AB} for a hologram AB relates to the real fluid surface profile h through $h_{AB}(t, \mathbf{r}) = h(t, \mathbf{r} + \boldsymbol{\delta}_{AB})$, where $\boldsymbol{\delta}_{AB}$ represents a spatial displacement linked to the physical tilt between rays A and B (see Figure 4.3).

4.3.2 Numerical phase-tracing and simulated holograms

As with the previous detection method, we can assess the proposed model through a numerical simulation emulating the outcome of an experimental acquisition. The algorithm executes the iterative propagation of a mesh of rays through a mathematical model of the configuration in Figure 4.2. In this simulation, we define the two mirrors as inclined planes at $z = -\mathbf{m}_b \cdot \mathbf{r}$ and $z = -\mathbf{m}_r \cdot \mathbf{r}$ while parametrising the interface $z = h(t, \mathbf{r})$ using an analytic function $h(t, \mathbf{r})$. The input beam is described as a bundle of rays initially propagating parallel to each other towards the sample and reference mirror from an initial position defined as a Cartesian mesh. Each ray in the mesh is then propagated until it intersects a surface, either a mirror or the fluid interface. At

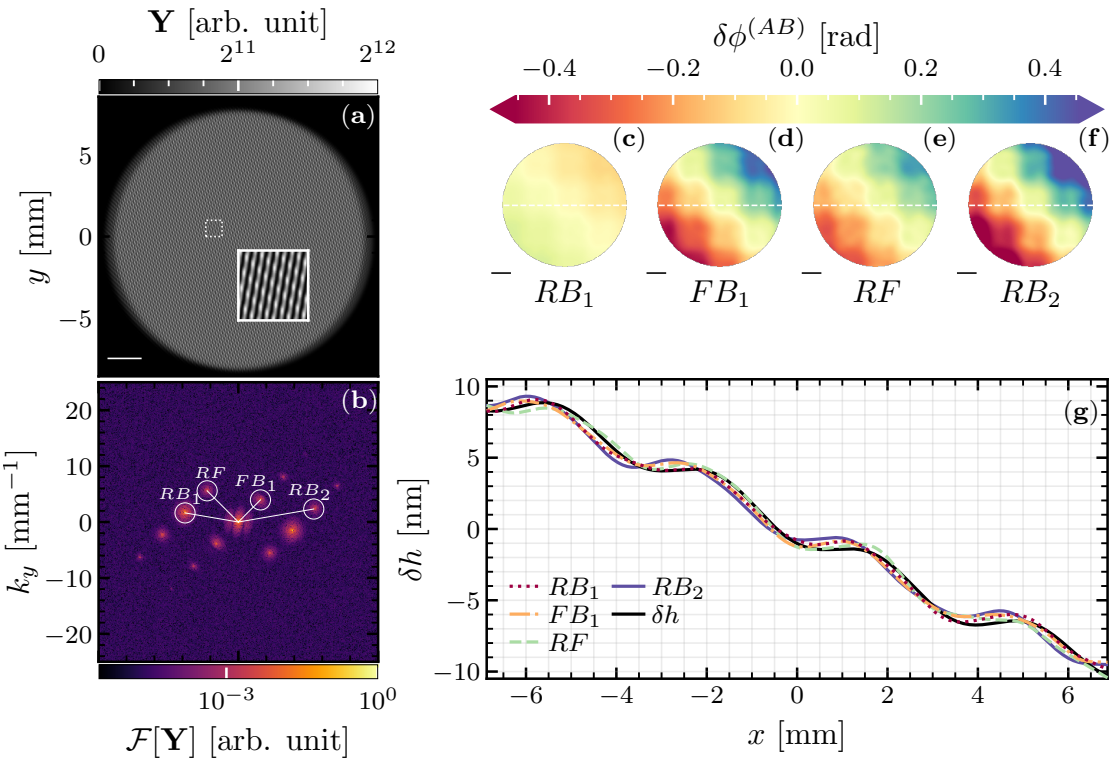

Figure 4.3: In $(\mathbf{a})$, we display a numerically simulated intensity image $\mathbf{Y}$ with an inset of the fringe patterns (white dashed rectangle). A white line on the lower-left corner depicts a length of $2\,\mathrm{mm}$. The spatial Fourier transform $\hat{\mathbf{Y}}$ of $\mathbf{Y}$ is shown in $(\mathbf{b})$, where the brightness of each pixel is proportional to the logarithmic amplitude $\log|\hat{\mathbf{Y}}|$. As expected from the real-valued image $\boldsymbol{Y}$, its Fourier spectrum in $(\mathbf{b})$ is symmetric on the wavevector $\mathbf{k}$, i.e., $|\hat{\mathbf{Y}}|(-\mathbf{k}) = |\hat{\mathbf{Y}}|(\mathbf{k})$. White lines are drawn to illustrate the carrier frequencies for the holograms RB_1, RF, FB_1 and RB_2 of order $+1$ in line with Equation 4.10. In $(\mathbf{c}) - (\mathbf{f})$, we show the phase differences $\delta\phi^{(AB)}$ between two consecutive time frames for the four hologram types AB with a shared colour bar. The visibly correlated spatial dependence of the phases is proportional to the change in fluid height $\delta h(\mathbf{r})$ by Equation 4.12. Spatial slices of the phases at $y = 0$ (white dashed lines) in $(\mathbf{c}) - (\mathbf{f})$ are shown in $(\mathbf{g})$ already converted to height variations δh using the prefactors α_{AB}. The black line indicates the ground-truth height change δh used to generate the simulation. The spatial displacement between the reconstructed curves and the ground truth confirms the expected shift due to the relative tilts between the sample and reference mirrors. The simulated image has 1024×1024 pixels with size $16.8\ \mu\mathrm{m}$ by $16.8\ \mu\mathrm{m}$ and the resolution in Fourier space is $\delta k = 0.06\,\mathrm{mm}^{-1}$.

the latter, the rays satisfy the Fresnel boundary conditions, which are used to separate them into reflected and transmitted components [219]. The refracted rays are then reflected by the bottom mirror and return to the interface, where the process repeats. The wave amplitudes are appropriately modified by the reflection and transmission coefficients between the media, while the phases acquire contributions proportional to the travelled distance. Finally, the returning rays are collected at the detector plane at $z = H$ within a defined number of iterations N_i. By adding all the rays and interpolating them to the original Cartesian mesh, we are left with the combined intensity for ray types R, F, and $\{B_j\}$. From the final intensity profile, we generate a

synthetic image of the form (4.9). This iterative loop for spatial ray tracing can be evolved in time at intervals δt to obtain a set of consecutive frames equally spaced in time. The outcome of this process, which yields the change in interfacial height profile $\delta h(t_0, \mathbf{r}) = h(t_0, \mathbf{r}) - h(t_0 - \delta t, \mathbf{r})$ between two consecutive times of standing waves in a square basin, is showcased in Figure 4.3.

4.3.3 Peak identification and prefactor estimates

In line with the previous detection method, the digital recovery of phases from our setup is done through the canonical approach of Fourier Demodulation [191]. In the context of digital holography, it receives the name Angular Method [221] in reference to the retrieved *angular* phase. Here, for all practical purposes, the demodulation procedure is the same as described in subsection 4.2.1 for the checkerboard pattern. The only striking difference is the existence of several carrier peaks instead of just two. The numerical simulation shows that the families of holograms AB will have corresponding intensity peaks in the Fourier domain around carrier frequencies $\mathbf{k}_{AB}$. Following the notation of subsection 4.2.1, we conveniently label each peak in the spectrum by an integer m and refer to the phase obtained from its modulation as $\Delta\phi_{ij}^{(m)}$, given by Equation 4.6. We also stress that, despite the same digital recovery procedure, the phase in the digital holographic setup is directly proportional to interfacial height h profile, as per Equation 4.12. Whereas, for the FTP configuration, it is proportional to the spatial gradient of the height.

In order to consistently apply the phase-to-height relations in Equation 4.12, we must know to which family a peak belongs before converting its phase into the interfacial profile. We discuss here two distinct approaches that can be used for peak identification and prefactor estimation. The first involves an experimental procedure relevant during data acquisition and will be elaborated upon when discussing experimental results in Section 4.3.4. In cases where manipulating the experimental setup is neither feasible nor desirable, the second method may be employed. This alternative procedure relies on a statistical tool known as Principal Component Analysis (PCA) [222, 223]. We demonstrated that if a reconstructed phase $\phi_{ij}^{(m)}(t)$ can effectively capture changes in the surface height $h(\mathbf{r}_{ij}, t)$, it can be expressed as $\phi^{(m)} = 2k_0\alpha_m h$. Under this assumption, the experimentally obtained phases $\phi_{ij}^{(m)}(t)$ from a collection of M holograms must scale proportionally to the fluid height profile $h(t, \mathbf{r}_{ij})$, as in Equation 4.12. In vector notation, we can represent this relationship as

$$\mathbf{\Phi} = (2k_0 h)\boldsymbol{\alpha}, \tag{4.13}$$

where $\mathbf{\Phi} = \left(\phi^{(0)}, \ldots, \phi^{(M-1)}\right)$ denotes a vector comprising M reconstructed phases, and $\boldsymbol{\alpha} = (\alpha_0, \ldots, \alpha_{M-1})$ represents a vector of phase-prefactors α_m following Equa-

tion 4.12. Naturally, this relation is anticipated to be affected by noise and processing errors, which originate from the reconstruction process alone and do not faithfully represent the real fluid surface profile h.

For simplicity, in the following, we consider the spatial average of the phases, denoted $\phi^{(m)}(t) \equiv \langle \phi_{ij}^{(m)}(t, \mathbf{r}_{ij}) \rangle_{ij}$. In this case, the phase-vector $\mathbf{\Phi}(t)$ in Equation 4.13 is a function of time only. To apply the PCA [223], we must first make sense of the statistical problem at hand. Given the set of M experimentally obtained phases $\mathbf{\Phi}(t)$, we wish to find a function $f(t)$ that maximally correlates with the time evolution of the components in $\mathbf{\Phi}(t)$. For that, we compute the eigenvalues λ_a and corresponding eigenvectors $\mathbf{v}_a$ of the $M \times M$ time-averaged covariance matrix of $\mathbf{\Phi}(t)$ with elements $C_{\ell m}$, i.e., $C_{\ell m}\mathbf{v}_{a,\ell} = \lambda_a \mathbf{v}_{a,m}$. The elements of the matrix are given by

$$C_{\ell m} = \left\langle \left(\phi^{(\ell)} - \langle \phi^{(\ell)} \rangle_t\right) \left(\phi^{(m)} - \langle \phi^{(m)} \rangle_t\right) \right\rangle_t , \tag{4.14}$$

where $\langle \cdot \rangle_t$ denotes the average in time. It follows from the PCA that the principal component of the covariance matrix, i.e., the eigenvector $\mathbf{v}_p$ with eigenvalue λ_p much larger than all others, is such that $\mathbf{\Phi} = \lambda_0 f(t) \mathbf{v}_p$, for some undetermined constant λ_0. From Equation 4.13, we see that $f(t) = 2k_0 h(t)$ and $\boldsymbol{\alpha} = \lambda_0 \mathbf{v}_p$. Accordingly, the time evolution of the height $h(t)$ could be expressed in terms of a phase $\phi^{(m)}(t)$ through the $m-$th component of $\mathbf{v}_p$, denoted $v_p^{(m)}$, as

$$h(t) = \frac{\phi^{(m)}(t)}{2k_0 \lambda_0 v_p^{(m)}}. \tag{4.15}$$

Here, the phases can be obtained from the experiment, and the principal component from the PCA, while the only undetermined quantity is λ_0. We can specify the latter if one of the components of $\boldsymbol{\alpha}$ is previously known, so that $\lambda_0 = \alpha_m / v_p^{(m)}$.

Finally, we introduce the normalised eigenvalue of the principal component $\mathbf{v}_p$,

$$\mathrm{sg}_p \equiv \frac{\lambda_p}{\sum_a \lambda_a}. \tag{4.16}$$

This quantity is a measure of how well the time evolution of the phases in $\mathbf{\Phi}(t)$ can be represented by a single quantity $h(t)$ along the direction of $\mathbf{v}_p$ [222]. We refer to sg_p as the confidence of the PCA, and it assumes values between 0 and 1. If $\mathrm{sg}_p = 1$, then all variations in the data $\mathbf{\Phi}$ fall along the principal component $\mathbf{v}_p$, whereas, for $\mathrm{sg}_p = 0$, the data does not correlate with $\mathbf{v}_p$. Provided that the multiplexed holograms and their respective phases are indeed described by the model of Equation 4.10, then PCA could be used to obtain the phase prefactors α_m and, ultimately, the change in height from the principal component.

4.3.4 Experimental results

We employ the configuration shown in Figure 4.2 as a surface profilometer for liquid samples over a circular area. Our setup uses a diode-pumped solid-state laser source with wavelength $532\,\mathrm{nm}$ and power of $1\,\mathrm{mW}$. The beam expander augments the circular beam to a diameter of approximately $18\,\mathrm{mm}$. A liquid sample fills a square basin of side $84\,\mathrm{mm}$ with a 2" mirror at its bottom and is placed $30\,\mathrm{mm}$ below the beam splitter. Multiple interferograms are generated by setting the probe and reference beams in off-axis alignment. The resulting intensity images as in Equation 4.9 are acquired over time using an area-scan camera[3]. Images are acquired at either 1024×1024 or 1536×1536 pixels[4]. With the method outlined in subsection 4.2.1, we can reconstruct the phases of the holograms available. This provides information on the fluctuations of the fluid surface caused by various factors such as vibrational noise, thermal effects, and external disturbances. In this study, we obtained data from a setup placed on a noise-isolating optical table.

Fluid surface profile

Figure 4.4(a) shows an example frame $\mathbf{Y}$ acquired in an experiment, and its spatial Fourier transform $\mathcal{F}[\mathbf{Y}]$ is displayed in Figure 4.4(b). Compared to the simulation in Figure 4.3, the empirical image contains many new features coming from the imperfect spatial profile of the expanded beam, specular reflections, and other experimental aspects not accounted for in our idealised simulation. They invariably taint the spectrum of the image, which also displays extra peaks from partial reflections at the optical components, mainly the beam-splitter. To assist in the identification of the relevant holographic peaks, we developed a graphical user interface that provides a live view of the SFD and allows for the real-time viewing of the reconstructed phase and interferograms. When the reference beam is blocked, the FB_j family holograms are the only remaining peaks, as they are generated by interference between the probe mirror and the fluid surface reflections. From Equation 4.11, we infer that the most prominent peak in the Fourier space is always the RB_1, while the brightest hologram in the FB_j family can be labelled as FB_1. Adjustments in the reference mirror alone keep the positions of FB_j fixed, while adjustments in the probe mirror leave the position of RF unaffected. This method enables the preliminary identification and labelling of the prominent peaks in the spatial-frequency domain of experimental data.

Once the peaks have been identified, their phase prefactors should follow Equation 4.12 and, hence, changes in the liquid surface $\delta h(t, \mathbf{r})$ can be computed with

[3] Basler acA2040-120um (12 bits, grayscale CMOS sensor) attached to fixed focal length lenses (Tuss Vision LV5028, 50 mm) with 0.3x effective magnification.

[4] The direct space equivalent pixel size is $11.2\,\mu\mathrm{m}$.

the reconstructed phases. In Figure 4.4(c-f), the height change of the order of just a few nanometres between two consecutive frames $12.5\,\mathrm{ms}$ apart is shown. This is done by computing the difference in phase between the two frames through the *relative reconstruction*, i.e., effectively computing $\delta h(t,\mathbf{r}) \equiv h(t,\mathbf{r}) - h(t-\delta t,\mathbf{r})$. As a result, any spatial features in those phases not varying or slowly varying in time, such as aberrations and speckles, are eliminated or reduced upon subtraction. Panels (c-f) in Figure 4.4 are ordered by decreasing peak intensity, with RB_1 being the bright-

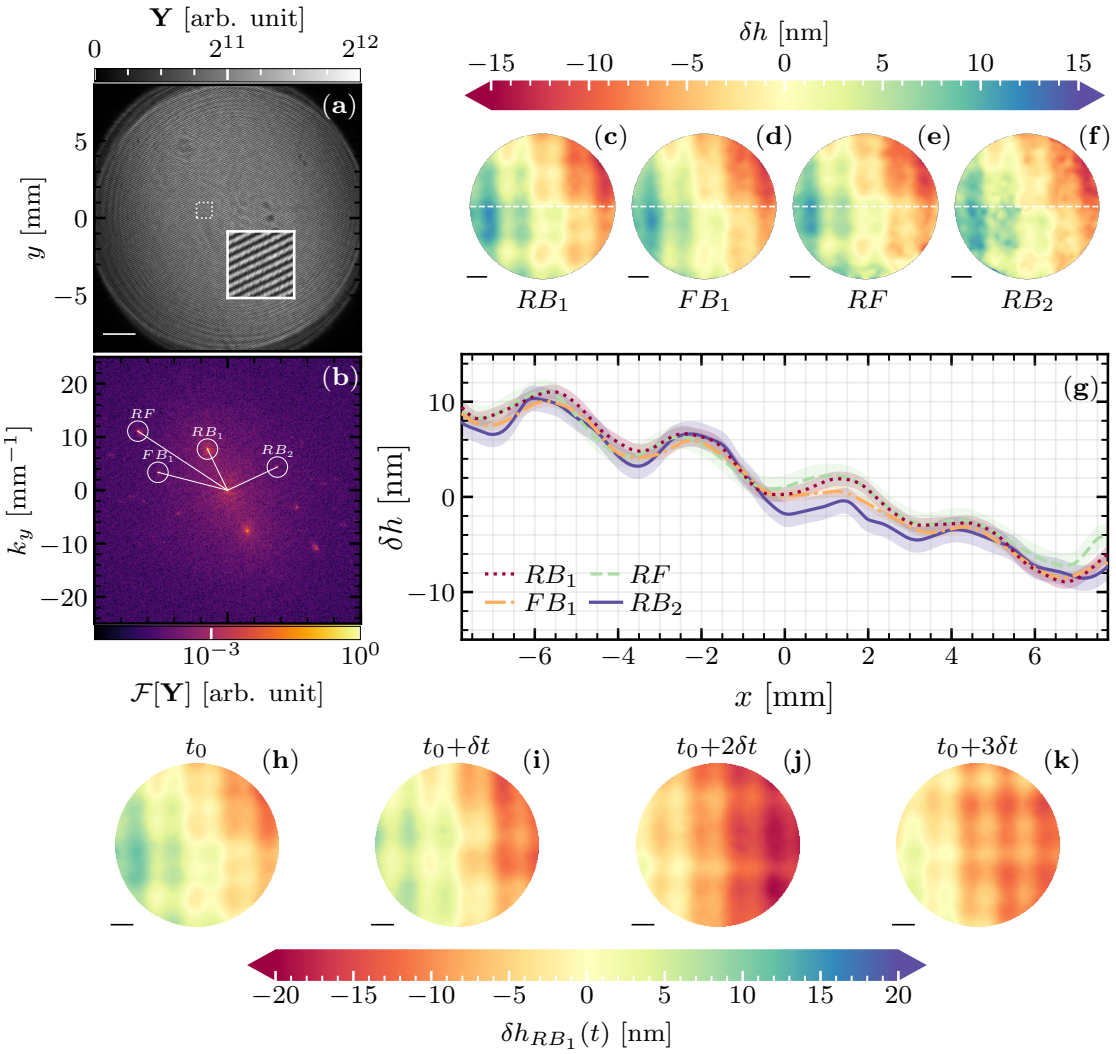

Figure 4.4: In (a), an acquired sample image frame with 1536×1536 pixels with a white line indicating a length of $2\,\mathrm{mm}$. The spatial-frequency domain of the image is shown in (b), with the four main peaks labelled by the procedure described in the text. Their reconstructed height changes, $\delta h(t,\mathbf{r}) \equiv h(t,\mathbf{r}) - h(t-\delta t,\mathbf{r})$, are shown in (c) − (f) using the inferred prefactors of (4.12). The white dashed line in (c)−(f) corresponds to a diameter of $15.5\,\mathrm{mm}$. In (g), we display a horizontal slice of δh for all labelled peaks. The shaded regions indicate the root mean square (RMS) deviation from the average reconstruction, $\delta h = \frac{1}{4}\sum_{AB}\delta h_{AB}$, of the four interferograms given by $RMS_{AB} = \sqrt{\langle|\delta h_{AB} - \delta h|^2\rangle_{\mathbf{r}}}$. (h) − (k) show the time evolution of the height changes retrieved from the RB_1 peak, with $\delta t = 12.5\,\mathrm{ms}$. In (b), the spatial-frequency resolution is $\delta k = 0.06\,\mathrm{mm}^{-1}$, and the frequency cutoffs used in the filters of each peak are $k_{c,RB_1} = 33\delta k$, $k_{c,RF} = 23\delta k$, $k_{c,FB_1} = 23\delta k$ and $k_{c,RB_2} = 23\delta k$.

est and RB_2 being the faintest. All four independent reconstructions show the same surface profile, but the reconstruction quality varies among the peaks. RB_2 has low intensity and is more likely to be affected by background noise, resulting in a noisier reconstruction, as seen in Figure 4.4(f). All curves in panel (g), depicting horizontal slices of the reconstructions, qualitatively and quantitatively recover the same interface with various degrees of noise. Although small, we see that the spatial shift introduced by the relative tilts between the sample and reference mirrors persists. The time evolution of four consecutive frames of the height change $\delta h_{RB_1}(t, \mathbf{r})$ reconstructed from the RB_1 peak is shown in panels (h)-(k) of Figure 4.4. The seemingly periodic signal showcased here is consistent with the eigenmodes of the square sample basin used in the experiment.

Depth change in fluids

Digital holography enables the monitoring of dynamic changes in the probe arm with nanometric scale resolution, as shown above. We offer now an alternative analysis for identifying peaks through data processing of acquired images. Here, our modelling is used to evaluate the time evolution of the average fluid depth relative to a reference time. In demonstrating the potential application of our methods in noisy environments, where careful alignment cannot be guaranteed, the reference and sample mirrors were coarsely aligned for the experiments discussed in what follows. Due to digital artefacts present in the acquired data – such as repeated peaks, aliasing, and spatial Fourier harmonics and folding [224] – not all peaks will appear in the SFD or be identified in the process.

To examine the depth change of the sample, we first note that it is directly proportional to the spatial average of the phases. That is, $\langle \delta h(t, \mathbf{r}) \rangle_{\mathbf{r}} \propto \langle \delta \phi^{(m)}(t, \mathbf{r}) \rangle_{\mathbf{r}}$ for a peak m. Since the spatial profile of the interface causes spatial modulations around an average phase, by looking at the complex value of the Fourier transform at the peak position, $A_m(t) \equiv \mathcal{F}[\mathbf{Y}](\mathbf{k}_m)$, we can infer $\langle \phi^{(m)}(\mathbf{r}, t) \rangle_{\mathbf{r}}$. By establishing an image reference $\mathbf{Y}_0$ at $t_0 = t - \delta t$, we can obtain the approximate change in the spatially-averaged phase of a hologram m at time t by $\langle \phi^{(m)}(t, \mathbf{r}) \rangle_{\mathbf{r}} \simeq \mathrm{Im}\{\log[\mathcal{F}[\mathbf{Y}](\mathbf{k}_m)(\mathcal{F}[\mathbf{Y}_0](\mathbf{k}_m))^*]\}$. By applying this alternative phase recovery procedure to all available peaks in the Fourier spectrum, we can compute the change in spatially averaged phases. With the PCA of subsection 4.3.3, we may identify the phase prefactors that result in the appropriate change of fluid depth over time. In the following case studies, the complex-valued peak amplitudes $A_m(t)$ are normalized by the brightest peak at the first frame ($t = 0$), denoted $A_0(t = 0)$, and represented by $\tilde{A}_m(t) \equiv |A_m(t)|/|A_0(t = 0)|$. The holograms are numbered according to their time-averaged normalised intensities, denoted $\langle \tilde{A}_m \rangle_t$, with hologram $m = 0$ corresponding to RB_1 and its prefactor identified

as $\alpha_0 = \lambda_0 \Delta n$, for $\Delta n = n_2 - n_1$. The largest label m refers to the dimmest peak, i.e., with the smallest average intensity.

Controlled change in volume We devised an experiment to verify the ability of our setup to monitor changes in the depth of a water sample. We injected a known volume $\mathrm{d}V$ and independently reconstructed the corresponding phase shifts $\mathrm{d}\phi^{(AB)}$, which should follow from Equation 4.12, i.e.,

$$\mathrm{d}\phi^{(AB)} = \frac{\mathrm{d}V}{2k_0 \alpha_{AB} A}. \tag{4.17}$$

Here, the cross-section area A of the basin was $70.6(2)\,\mathrm{cm}^2$. The spatially-averaged height $\langle h(t, \mathbf{r}) \rangle_{\mathbf{r}}$ obtained from the reconstructed phases is then compared with the predicted volume change. A syringe system attached to a remote-controlled stepper motor was used to steadily change the water level in the basin. Figure 4.5 (d) and (e) display the phase change for different holograms over 130 seconds and the rate of change in fluid volume, respectively.

By performing the PCA in time, we found that most of the reconstructed phases consistently correlated with a principal component with confidence of $\mathrm{sg}_p = 97.40\%$. In Figure 4.5(c), we show the resulting phase prefactors α_m normalised by the first, α_0. The RMS deviation of the reconstructed depth change $\langle h_m(t, \mathbf{r}) \rangle_{\mathbf{r}}$ of a peak m from the averaged result $h(t) = \left(\sum_{m=0}^{M-1} \langle h_m(t, \mathbf{r}) \rangle_{\mathbf{r}} \right) / M$ was used as a measure of uncertainty for the prefactors α_m (error bars in Figure 4.5(c)). The first, and brightest peak (see Figure 4.5(b)), should correspond to RB_1. Hence, its computed prefactor is $\alpha_0 = \lambda_0 \Delta n$, with $\Delta n = n_2 - n_1$, as per Equation 4.12. The holograms numbered 1, 8, 14, and 16 have similar prefactors to α_0, indicating that they sample the same height change as RB_1, and could be identified as Fourier foldings of RB_1. Holograms 2, 3, 4, and 15, with prefactors $2\alpha_0$, are artefacts of digital processing and consistent with the first harmonics of the RB_1 peak and its repetitions. We could not confidently identify peak 12 in our model. Holograms with prefactors smaller than α_0 are shown in grey in Figure 4.5(c), and are not used in the analysis of panel (d), as they are not well correlated to the depth change $\langle h(t, \mathbf{r}) \rangle_{\mathbf{r}}$.

Evaporation Rates We now present a study of the evaporation rates of liquids. We let the sample basin sit for 15 minutes on a noise-isolating table in a controlled laboratory environment, where air currents and temperature variations were negligible. With the same analysis procedure as in Figure 4.5, we performed the PCA in time for data acquired in water and isopropanol ($\mathrm{C_3H_7OH}$). Their results are condensed in Figure 4.6i and Figure 4.6ii, respectively. Panels (b) in Figure 4.6 display the overlapping reconstructed depth change $\langle h(t, \mathbf{r}) \rangle_{\mathbf{r}}$ over time for selected peaks in panel (a). The height change is measured with respect to the initial time $t = 0$. For the

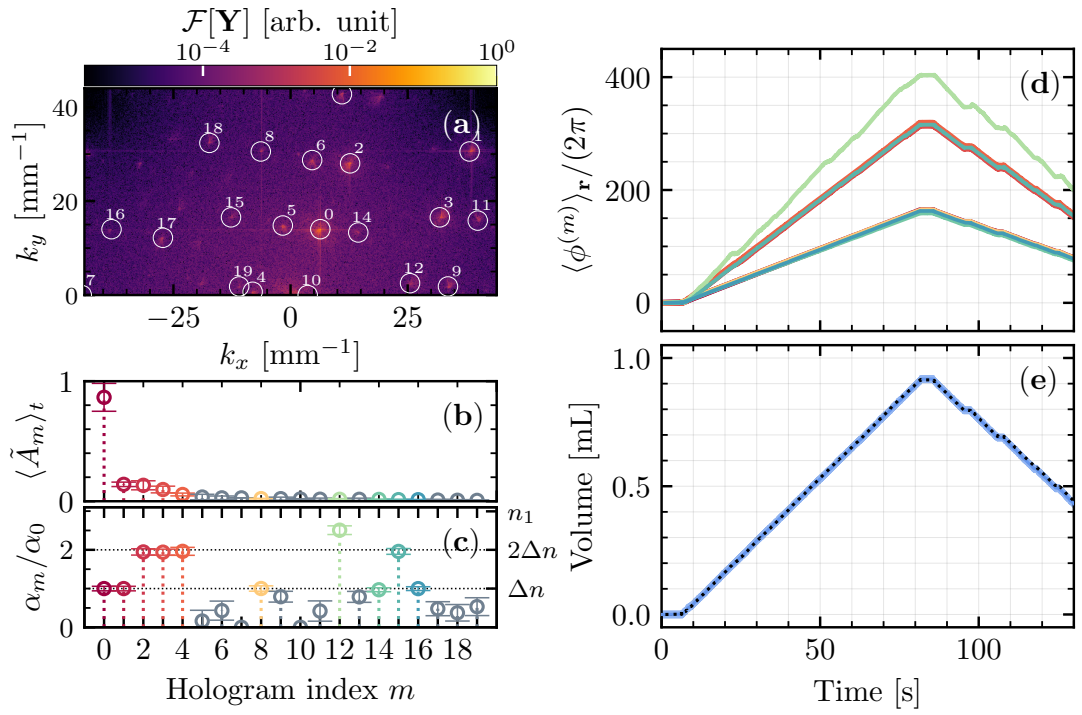

Figure 4.5: In (**a**), half of the SFD ($k_y > 0$) is shown for a sample image with 1024×1024 pixels and spatial frequency resolution $\delta k \simeq 0.09\,\mathrm{mm}^{-1}$. We label the peaks from $m = 0$ to $m = 19$ based on their intensities, as described in the text, and display their time-averaged relative intensities $\langle \tilde{A}_m(t) \rangle_t$ in (**b**). Error bars indicate the standard deviations of $\tilde{A}_m(t)$. The estimated prefactors α_m for each peak obtained from the temporal PCA with 97.40% confidence are shown in (**c**), normalised by the prefactor of the strongest peak, α_0. On the right-hand side of (**c**), we indicate the expected positions of the refractive indices corresponding to the prefactors in (4.12), and $\Delta n \equiv n_2 - n_1$. The phase changes retrieved from the identified peaks are displayed in (**d**). In (**e**), the blue line indicates the average volume change calculated from the reconstructed phases and the shaded region indicates the standard deviation. The dotted line shows the volume measurement done by tracking the movement of the syringe. The results are obtained from 7800 frames, acquired at 60 frames per second.

water sample in Figure 4.6i, the PCA confidence was $\mathrm{sg}_p = 99.94\%$, confirming that an overall depth change trend highly correlates to all phases. Similarly, data for the isopropanol sample in Figure 4.6ii showed a PCA confidence of 99.25%.

As previously, panel (d) in Figure 4.6i and Figure 4.6ii show the phase-prefactors α_m normalised by α_0. Similarly to Figure 4.5, the first peak $m = 0$ can be identified as RB_1, and hence $\alpha_0 = \lambda_0 \Delta n$ in both samples. For water, holograms 1, 3, 7, 11, 13, and 16 display the same prefactor as RB_1 and are likely repetitions of this peak. The largest prefactors appear for holograms 17 and 19, with their normalised prefactors staying close to $n_2/\Delta n$. Hence, they are candidates for the FB_1 family. Hologram 18 has normalised prefactor $\alpha_m/\alpha_0 \simeq n_1/\Delta n$ and is a candidate for an RF peak. The grey points in Figure 4.6i(d) correspond to peaks whose phases weakly correlate with the overall depth change. We are unable to classify them within our model and

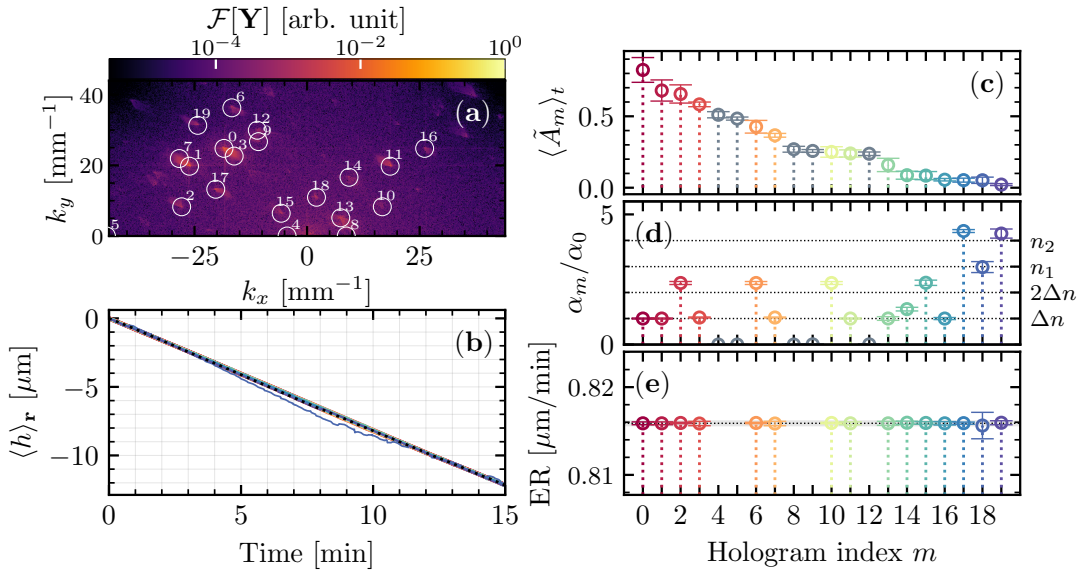

(i) Evaporation study in water. For this data set, 1800 images of 1024×1024 pixels were acquired at 2 frames per second. The SFD resolution in $(\mathbf{a})$ is $\delta k \simeq 0.09\,\mathrm{mm}^{-1}$. The average evaporation rate observed is $0.8159(2)\,\mu\mathrm{m\,min}^{-1}$, and the sample temperature was at $20.8(2)\,^{\circ}\mathrm{C}$. The refractive index of water is $n_2 = 1.333$ [225].

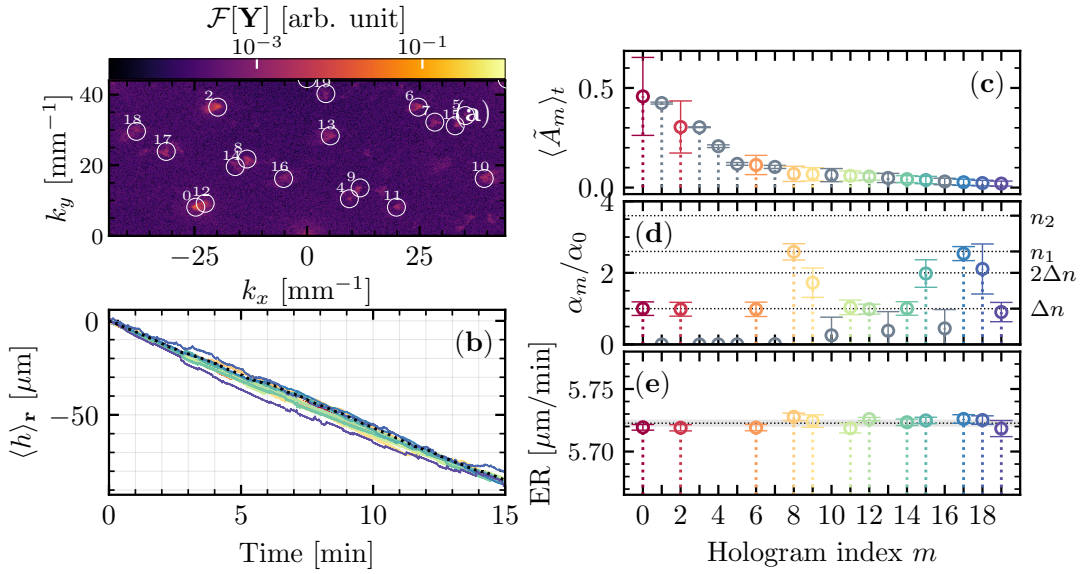

(ii) Evaporation study in isopropanol. For this data set, 9000 images of 1536×1536 pixels were acquired at 10 frames per second. The SFD resolution in $(\mathbf{a})$ is $\delta k \simeq 0.06\,\mathrm{mm}^{-1}$. The average evaporation rate observed is $5.720(1)\,\mu\mathrm{m\,min}^{-1}$, and the sample temperature was at $23.2(2)\,^{\circ}\mathrm{C}$. The refractive index of isopropanol is $n_2 = 1.377$ [226].

Figure 4.6: Panels $(\mathbf{a})$ show the SFD of a sample image. In $(\mathbf{b})$, we display the reconstructed depth changes for the various peaks and the dotted line gives their average trend. The time-averaged relative intensities $\langle \tilde{A}_m(t) \rangle_t$ of all the labelled peaks are shown in $(\mathbf{c})$. The peak identification and prefactor estimates from the PCA in time are given in $(\mathbf{d})$. Here, $\Delta n \equiv n_2 - n_1$. In $(\mathbf{e})$, we show the evaporation rates estimated from the slope of linear fits of the depth changes in $(\mathbf{b})$. The average evaporation rate is indicated by the dotted line.

their contribution can be disregarded. We can draw similar conclusions from the data acquired with the isopropanol sample.

Finally, we compare the average evaporation rates observed in our experiment with references for liquid evaporation in controlled conditions. Hisatake et al. [227, 228] register water evaporation rates in the range of $0.6 - 1.2\,\mu\mathrm{m\,min^{-1}}$, for low air-current speeds and similar ambient temperatures and sample surface area. We obtained an average of $0.8159(2)\,\mu\mathrm{m\,min^{-1}}$, which is well within the expected. For isopropanol, Mackay and van Wesenbeeck [229] observe rates in the range of $5 - 6\,\mu\mathrm{m\,min^{-1}}$, which again encompasses our average evaporation rate of $5.720(1)\,\mu\mathrm{m\,min^{-1}}$. The uncertainty of the empirical evaporation rates in Figure 4.6 does not account for the systematic error in the reference values of refractive indices and should be understood as the uncertainty in reconstructing the rate of change in optical path length from several holograms. Ultimately, these results confirm that the PCA is a useful tool for peak identification when labelling them during acquisition is not possible. Even without careful alignment and with an intricate and densely populated Fourier spectrum (as in Figure 4.6(a)), our proposed analysis still managed to recover the time variations in the surface of the fluids.

4.4 Summary and discussion

In this chapter, we discussed two detection schemes for the profilometry of fluid interfaces and surfaces. The first, which we referred to as Schlieren Fourier Transform Profilometry (FTP) [89], is considered one of the standard modern methods for free-surface measurements, and we used it in the experiment presented in Chapter 3. Here, we reviewed the underlying principles of this technique and argued it could be adapted for measurements of a two-fluid interface in a closed sample cell with the suitable configuration of the imaging system. We further discussed a general process for phase recovery from images of distorted checkerboard patterns, in line with the Fourier demodulation put forward by Takeda & Mutoh [169].

The second detection method used a Michelson interferometer to create a sensor for surface waves in fluids using multiplexed DH. We showed that a straightforward optical configuration combined with a data analysis based on FTP can reconstruct nanometric height variations. Additionally, we showed the potential application of this method in monitoring over time the depth of the fluid, in contrast with Schlieren FTP, which is insensitive to changes in the spatial average of the interface. In comparison with the latter method, whose application in Chapter 3 showed a lower bound in the order of micrometres, our DH profilometry shows an improvement of three orders of magnitude, with a lower bound around nanometres. One could utilise this digital holographic sensor to investigate the dynamics of fluid flows and the dispersion of

interfacial waves at scales inaccessible by conventional detection methods, such as Schlieren FTP.

Chapter 5

Observer dependence in EFT simulators: experimental proposal

We now move to another Effective Field Theory (EFT) introduced in Section 2.4, namely an analogue massless scalar field in a $(2+1)-$dimensional Minkowski spacetime. Here, we present an experimental proposal to probe one of the most fundamental predictions at the confluence between quantum physics and relativity, known as the Unruh effect, concerning the disjoint perception that inertial and non-inertial observers have of the quantum vacuum. By using a laser beam as a sensor of surface modes on superfluid helium-4, we show that this aspect of observer-dependent detector response can be measured in an experimental setup. We begin with a brief introduction of the Unruh effect and how our proposed simulator addresses the experimental challenges in detecting it. This is followed by the theoretical modelling supporting the proposal and a discussion on a possible experimental setup, with estimates for the empirical observables. This chapter is based on the preprint *"Third sound detectors in accelerated motion"* [4], written in collaboration with Cameron R D Bunney, Steffen Biermann, August Geelmuyden, Cisco Gooding, Grégoire Ithier, Xavier Rojas, Jorma Louko, and Silke Weinfurtner.

5.1 Inertial vs accelerated observers in Minkowski spacetime

Quantum Field Theory in Curved Spacetimes (QFTCS) [5] features a hall of intricate and elusive outcomes, such as the Unruh effect, Hawking radiation and gravitational backreaction, to cite a few. Many of these revolve around the ambiguity of defining a vacuum state of the underlying quantum fields in curved spacetimes. This is in contrast to Minkowski spacetime, where Poincaré invariance enjoyed by inertial observers allows for a unique definition of creation and annihilation operators for positive and negative

energy states [230]. Inevitably, the aforementioned ambiguity implies the lack of a unifying interpretation of the physical concept of a particle. This statement, however, is not restricted to curved spacetimes and may appear as well in Minkowski spacetime, as in the notable result of the Unruh effect [82].

In a nutshell, the Unruh effect anticipates that inertial and accelerated observers in flat spacetime perceive the particle content of the quantum vacuum differently. Naturally, to make sense of this assertion, the concept of a particle must be properly defined. This issue is resolved by introducing two-level particle detectors of a quantum field, known as Unruh-DeWitt detectors [5], such that we may interpret a particle as what makes them tick. With this setup, the energy gap between the ground and excited states of the two-level system is given by $\hbar\omega$, and the detector transitions as field quanta are absorbed and emitted at this frequency. Unruh showed that an observer in linear motion with constant acceleration a carrying an Unruh-DeWitt detector would see it transition between states with a probability rate $p(\omega)$ such that [82]

$$p(\omega) \propto \frac{\hbar\omega}{\exp\left(2\pi\omega c/a\right) - 1}, \tag{5.1}$$

where c is the speed of light in free space. The surprising side of this result comes by noting that this same transition rate would appear had the detector stood at rest immersed in a thermal bath at the so-called Unruh temperature

$$T_U = \frac{\hbar a}{2\pi c k_B}, \tag{5.2}$$

where k_B is the Boltzmann constant. Accordingly, from this outcome, it follows the interpretation that *"a uniformly accelerated observer will 'see' thermal radiation even though the field is in the vacuum state and, as far as inertial observers are concerned, no particles are detected whatever"* [5].

Despite its undeniable importance, the Unruh effect remains undetected, as its experimental observation encounters two significant challenges. Firstly, the acceleration prefactor $\hbar/(2\pi c k_B)$ in Equation 5.2 is of the order $10^{-21}\,\mathrm{K\,s^2\,m^{-1}}$. Consequently, the realisation of prohibitively large accelerations required for an appreciable temperature poses a technical obstacle. Secondly, and more fundamentally, the precise properties of the quantum vacuum state are essential but have yet to be fully explored. These properties serve to unify the perception of all non-accelerating observers travelling at any constant velocity. However, when the initial state differs from the quantum vacuum state, for example, in the form of a thermal state, the agreement among inertial observers is damaged by a Doppler-shifted spectrum determined by their respective velocities [83].

Here, we devise a quantum EFT simulator to address these two experimental imped-

iments with the goal of identifying observer dependence in the response of a detector. In line with the discussion of Chapter 2, we show that at the interface between thin-film superfluid helium-4 and helium vapour emerges a quantum EFT for long-wavelength interfacial perturbations, known as third sound [231]. Albeit low, the non-zero temperature of the helium sample allows us to scan a range of background thermal states, each with corresponding acceleration temperatures in line with Equation 5.2. Given this initial thermality, the theoretical framework put forward by Bunney & Louko [83] can then be used to distinguish between the inertial (Doppler) and acceleration (Unruh) signatures. Instead of two-level detectors, we build upon a previous proposal for ultracold atoms systems [81, 232], where it is shown that a laser acts as a continuous detector from which an acceleration-dependent signal can be extracted. By moving a localised beam on a circular trajectory through the sample, we construct an accelerated detector of third-sound quasi-particles.

5.2 Third sound on thin films of superfluid helium-4

The concept of *superfluidity* dates back to 1938 when Kapitza discovered the phenomenon [233], describing it as the property that liquid helium-4 develops below $2.17\,\mathrm{K}$ by flowing through narrow capillaries or gaps with what the author calls *"abnormally low viscosity"*. This critical temperature, referred to as the $\lambda-$point, characterises a second-order phase transition into a state also known as helium II, with remarkable properties where quantum effects may become noticeable. Our current theoretical understanding of the dynamics of superfluid helium is itself an EFT attributed to Landau [98]. With a coarse-grained prescription of the microscopic theory, heavily based on the available experimental results at that time, Landau develops a set of effective hydrodynamical equations describing the macroscopic motion of liquid helium below the $\lambda-$point. This phenomenological model relies on regarding the fluid as a mixture of normal and superfluid components. We emphasise, however, that the previous statement cannot be interpreted by means of a *chemical* mixture of species or substances, as treated in Chapters 2 and 3. Ultimately, the particles of liquid helium cannot be really separated into two types, and Landau's description refers to two possible fluid motions, the *superfluid* and *normal* ones.

Landau's two-fluid model has been extensively discussed in the literature, e.g. [90, 234, 235], and a few of its underlying concepts are central to our discussion here. Specifically, in this context, the *normal* flow is assumed to be well-described by the Navier-Stokes equations (see Equation 2.8) with fluid quantities labelled by a sub-index n, i.e., $\boldsymbol{v}_n,\ p_n,\ \rho_n,\ \nu_n$. We particularly note that a non-zero but small kinematic viscosity ν_n is attributed to the normal component [99]. Conversely, the *superfluid* component is inviscid and irrotational, $\nabla \times \boldsymbol{v}_x$, so its velocity may be written as

$\boldsymbol{v}_s = \nabla\phi_s$, for some velocity potential ϕ_s. Its properties are similarly labelled by a sub-index s, i.e., $\boldsymbol{v}_s,\ p_s,\ \rho_s$. The total density ρ of the liquid is also assumed to be the sum of each component, $\rho = \rho_n + \rho_s$. While ρ weakly depends on temperature, ρ_s and ρ_n independently relate strongly with temperature [99].

The incompressible flow of helium II decouples to two ordinary motions, namely that of an ideal (superfluid) and of a viscous (normal) fluid. On the other hand, the fluid flow of liquid helium may also be treated as compressible, and the propagation of sound waves can be considered, see e.g., §131 in [90]. With the standard procedure of linearising the hydrodynamical equations of motion for perturbations in the bulk, the usual sound waves arising from density-pressure oscillations appear, and the superfluid and normal components move in phase. Additionally, another sound-like type of wave inherent to superfluidity can be identified to leading order, with the components moving with opposite phases. In this case, in contrast with ordinary sound waves, pressure oscillations are negligible, and instead, the opposing superfluid and normal flows allow the propagation of temperature oscillations, which are referred to as *second* sound waves. As the temperature of helium II approaches the λ-point and the fraction of the superfluid component reduces, the speed of the second sound rapidly goes to zero. Accordingly, although the ordinary *first* sound persists above the λ-point, *second* sound waves only propagate if a superfluid flow exists.

Beyond first and second sounds, Atkins [231] suggests that a *third* sound exists in thin films of helium II. For this case, we recall the discussion of subsection 2.5.1, where we examined the dynamics of slightly viscous, enclosed fluids. Similarly, we consider a film of superfluid helium-4 with depth h_0 coating a flat substrate at the bottom of a closed basin and the interface $z = \xi(t, \boldsymbol{x})$ forming with the vapour phase enclosed. As required for viscous flows, the normal component must satisfy a no-slip boundary condition at the horizontal base. Hence, if the basin is at rest, we expect its flow velocity $\boldsymbol{v}_n$ to vanish within thin viscous boundary layers around solid walls. If we then consider surface waves propagating in liquid helium with a frequency ω, the boundary-layer thickness, or *penetration depth* of the wave [231], is $\ell_n \equiv \sqrt{\nu_n/\omega}$, as defined in Chapter 2.

A classical viscous fluid film with depth such that $h_0 \ll \ell_n$ cannot encounter waves propagating on its surface, as they will be heavily damped by the viscous adherence with the walls. On the other hand, helium II can sustain such waves through superfluidity. In this case, the normal (viscous) component remains clamped to the substrate, as required by the no-slip condition, while a superfluid flow forms on the layers above, allowing waves to propagate at the interface [236–238]. For typical values of kinematic viscosity $\nu_n \sim 1 \times 10^{-8}\,\mathrm{m^2\,s^{-1}}$ [99] and for frequencies around $1\,\mathrm{kHz}$, the penetration depth is such that $\ell_n \gtrsim 1\,\mu\mathrm{m}$, increasing in value for lower frequencies. Hence, the condition $h_0 \ll \ell_n$ can be readily achieved for films with submicron thickness, which

are well within the current technological standards [239]. For much higher frequencies or for thicker films, we rapidly leave the long-wavelength, third-sound regime, and damping may become non-negligible [240].

Let us now consider the dynamics of surface waves appearing on thin films of helium II. In the following, we use the notation introduced in Chapter 2 unless otherwise defined. The free surface of the film is located at $z = \xi(t, \boldsymbol{x})$, and its substrate is at $z = -h_0$. We first note that, as mentioned above, third sound is a type of long-wavelength interfacial perturbation similar to shallow-water waves in classical fluids (see Chapter 2). For the latter, however, the restoring force is gravity $-g_0\hat{\boldsymbol{z}}$, whereas, for the former, the forces that create the film dominate, particularly the strong intermolecular attraction between helium atoms and the substrate compounds due to van der Waals interactions [231]. Under these conditions, another heavily phenomenological description applies to the form of the potential energy density $U_{vdW}(\boldsymbol{x}, z)$ of these interactions, with experimental evidence suggesting $U_{vdW}(z) \simeq -\alpha_{vdW}(z + h_0)^{-3}$ for films of tenths of nanometers in thickness, see e.g. [241–243]. The van der Waals coefficient α_{vdW}, with dimensions $\mathrm{m}^5\,\mathrm{s}^{-2}$, can only be determined experimentally and varies with the material used for the substrate at $z = -h_0$. The resulting force density entering the equations of motion of the superfluid flow is then $\boldsymbol{f}_{vdW} = -\rho\nabla U_{vdW}(z) \equiv -f_{vdW}\hat{\boldsymbol{z}}$, with

$$f_{vdW} = \frac{3\rho\alpha_{vdW}}{(z + h_0)^4} \equiv 3\rho g_0 \left(\frac{\kappa_0}{z + h_0}\right)^4, \tag{5.3}$$

and κ_0 is defined as a characteristic length scale of the van der Waals interaction. At the average interface at $z = 0$, this force adds up to that of gravity, $-\rho g_0\hat{\boldsymbol{z}}$, and the liquid experiences an effective acceleration g given by

$$g \equiv g_0\left(1 + 3\left(\frac{\kappa_0}{h_0}\right)^4\right). \tag{5.4}$$

From the equation above, we see that, for thin films such that $h_0 \ll \kappa_0$, the second term rapidly dominates and the effective gravity is well described by $g \approx 3\alpha_{vdW}h_0^{-4}$.

In the following derivations for the equations of motion of third sound, some assumptions apply. We consider saturated films formed by coating a substrate immersed or protruding from a larger liquid helium sample under saturated vapour pressure, hence the name. These are typically thicker than 100 atomic layers, with $h_0 \gtrsim 10\,\mathrm{nm}$, and a hydrodynamical treatment of the incompressible flow applies for the frequencies and wavelengths considered here [237, 244]. We also operate at temperatures well below the λ-point, under $500\,\mathrm{mK}$, for which the superfluid component dominates over the normal. For reference, for temperatures beneath $1\,\mathrm{K}$, the superfluid density corresponds to more than 98% of the density of helium II [234, 245], i.e.,

$\rho_s/\rho > 0.98$, rapidly approaching 100% at even lower temperatures. Additionally, at these temperatures, the saturated vapour pressure is approximately zero [99]. Hence, the mean-free path between atoms in the vapour becomes so large that the hydrodynamical description is no longer applicable, and the equations for the film and the vapour decouple [239, 246], as for water and air. Accordingly, pressure gradients and evaporation-recondensation on the free surface are negligible [246]. Finally, we assume the experiment can be maintained in an isothermal state, in which the low-frequency wave propagation does not lead to heat transfer, and temperature gradients can also be neglected.

Conservation of mass within the film-vapour system and the equation of motion for the superfluid flow can be linearised in the regime described above for small height disturbances $\xi(t, \boldsymbol{x})$ [231, 237, 239], as follows,

$$\rho \frac{\partial \xi}{\partial t} + \rho_s h_0 \nabla \cdot \boldsymbol{v}_s|_{z=0} + J_m^{vap} \;=\; 0\,, \tag{5.5}$$

$$\left.\frac{\partial \boldsymbol{v}_s}{\partial t}\right|_{z=0} + g\nabla\xi - \frac{\sigma}{\rho}\nabla(\nabla^2\xi) + \frac{1}{\rho}\nabla p - s\nabla T \;=\; 0\,, \tag{5.6}$$

where J_m^{vap} is the rate of change in mass at the film-vapour interface per unit area, s is the average entropy of the film, and p and T are the pressure and temperature at the film interface, respectively. Now, using the aforementioned assumptions, we may neglect pressure and temperature gradients, i.e., $\nabla p \approx 0$ and $\nabla T \approx 0$, respectively, as well as changes in mass at the interface, i.e., $J_m^{vap} \approx 0$. By denoting the superfluid velocity potential ϕ_s evaluated at the interface by ϕ, i.e., $\phi \equiv \phi_s|_{z=0}$, and writing $\boldsymbol{v}_s|_{z=0} = \nabla\phi$, with the previous approximations, we find

$$\frac{\partial \xi}{\partial t} \;=\; -\,h_0\nabla^2\phi\,, \tag{5.7}$$

$$\frac{\partial \phi}{\partial t} \;=\; -\,g\xi + \frac{\sigma}{\rho}\nabla^2\xi\,, \tag{5.8}$$

where we used that $\rho_s \approx \rho$ for the temperatures considered here.

Equations (5.7) and (5.8) can be rewritten to return two separate equations for ϕ and ξ. It can be readily shown that the resulting equation of motion is the same for both fields and, for the observable ξ, it reads

$$-\frac{1}{h_0 g}\frac{\partial^2 \xi}{\partial t^2} + \nabla^2\xi - \frac{\sigma}{g\rho}\nabla^2(\nabla^2\xi) \;=\; 0\,. \tag{5.9}$$

This is the wave equation for the third sound. As in Chapter 2, it can be further simplified by noting that the interfacial height ξ can be decomposed into spatial eigenfunctions $\chi_a(\boldsymbol{x})$ satisfying the Helmholtz equation (2.18) with generalised time-dependent coordinates $\xi_a(t)$, i.e., $\xi = \sum_a \xi_a \chi_a$. Hence, from the equation above, it follows that

the mode amplitudes ξ_a propagate in harmonic motion with a frequency given by the dispersion relation,

$$\omega_a = \sqrt{g h_0 \left(1 + \ell_c^2 k_a^2\right)}\; k_a, \tag{5.10}$$

with $\ell_c = \sqrt{\sigma/(\rho g)}$, the capillary length of helium II, as in Equation 2.31 in Section 2.4 for shallow-water, gravity-capillary waves. We then restrict our analysis to interfacial modes ξ_a with long enough wavelengths so that $\ell_c^2 k_a^2 \ll 1$, i.e., interfacial modes out of the capillary regime. Thus, for thin films where the van der Waals forces dominate over gravity, the third-sound wave speed of propagation is well approximated by

$$c_3 = \frac{\omega_a}{k_a} \approx \sqrt{\frac{3\alpha_{vdW}}{h_0^3}}\ . \tag{5.11}$$

We note that, in contrast with the speed of shallow-water gravity waves, $c_0 = \sqrt{g_0 h_0}$, the speed of third sound reduces with increasing film thickness until $h_0 \sim \kappa_0$, for which gravity and van der Waals accelerations are comparable, reaching the limit of c_0 for $h_0 \gg \kappa_0$.

5.2.1 Analogue relativistic field in Minkowski spacetime

As presented in Section 2.4, with the approximations adopted above, the interfacial height ξ of thin-film helium II in the third-sound regime corresponds to a massless Klein-Gordon (KG) field in a $(2+1)-$dimensional Minkowski spacetime. Its effective Lagrangian density can then be written as

$$\mathcal{L}_3 \;=\; \frac{1}{2}\rho h_0 \left[\left(\frac{\partial \xi}{\partial t}\right)^2 - c_3^2 \left|\nabla \xi\right|^2\right]. \tag{5.12}$$

Conversely, we consider an alternative scenario where the fundamental analogue scalar field is given by the velocity potential ϕ at the interface, while the interfacial height ξ acts as the canonically conjugate momentum of ϕ. In this case, the effective Lagrangian for the fundamental field reads

$$\mathcal{L} \;=\; \frac{1}{2}\rho h_0 \left[\left(\frac{1}{c_3}\frac{\partial \phi}{\partial t}\right)^2 - \left|\nabla \phi\right|^2\right]. \tag{5.13}$$

By noting that Equation 5.8 reduces to $\partial_t \phi = -g\xi$ and that $c_3^2 = g h_0$ under the current (long-wavelength) approximations, we can define the conjugate momentum of ϕ, denoted π, as

$$\pi = \frac{\partial \mathcal{L}}{\partial(\partial_t \phi)} = \frac{\rho h_0}{c_3^2}\frac{\partial \phi}{\partial t} = -\rho \frac{g h_0}{c_3^2}\xi = -\rho \xi. \tag{5.14}$$

Hence, as anticipated, ξ is proportional to the conjugate momentum of the field ϕ in our derived EFT with Hamiltonian density

$$\mathcal{H} = \frac{1}{2}\rho\left[h_0\left|\nabla\phi\right|^2 + g\xi^2\right], \tag{5.15}$$

with the first and second terms corresponding to kinetic and potential energies per unit area of the interface.

In certain regimes, it is known that third sound waves behave as quantised quasi-particles [247–249]. Accordingly, we follow with a quantisation of the effective fields by requiring the canonical commutation relations $[\phi(t,\boldsymbol{x}),\rho\xi(t,\boldsymbol{x'})] = -i\hbar\delta(\boldsymbol{x}-\boldsymbol{x'})$ [109]. By promoting mode amplitudes b_k to quasi-particle annihilation-creation operators satisfying $[b_{\boldsymbol{k}}, b^\dagger_{\boldsymbol{k'}}] = \delta_{\boldsymbol{k},\boldsymbol{k'}}$, we may expand the field and its conjugate as follows

$$\phi(t,\boldsymbol{x}) = \frac{g}{\sqrt{2\Sigma}}\sum_{\boldsymbol{k}}\frac{A_k}{\omega_k}\left(b_{\boldsymbol{k}}\mathrm{e}^{-i(\omega_k t-\boldsymbol{k}\cdot\boldsymbol{x})} + \mathrm{h.c.}\right), \tag{5.16a}$$

$$\xi(t,\boldsymbol{x}) = \frac{-i}{\sqrt{2\Sigma}}\sum_{\boldsymbol{k}}A_k\left(b_{\boldsymbol{k}}\mathrm{e}^{-i(\omega_k t-\boldsymbol{k}\cdot\boldsymbol{x})} - \mathrm{h.c.}\right), \tag{5.16b}$$

with $k = |\boldsymbol{k}|$ and $\omega_k = c_3 k$,

$$A_k = \left(\frac{\hbar\omega_k}{\rho g}\right)^{1/2}, \tag{5.17}$$

and Σ is the horizontal cross-section area of the average interface. Here, the summations are performed over all allowed wavevectors $\boldsymbol{k}$ of the discretised interfacial modes, and the mode functions are normalised according to the standard Klein-Gordon (KG) scalar product [5], given by

$$(f_1, f_2) = -i\int d^2\boldsymbol{x}\left[f_1(\boldsymbol{x})\partial_t f_2^*(\boldsymbol{x}) - f_2^*(\boldsymbol{x})\partial_t f_1(\boldsymbol{x})\right], \tag{5.18}$$

for two solutions f_1 and f_2 of the $(2+1)-$dimensional massless KG equation.

We can reconnect the prescription above to an analogue $(2+1)-$dimensional Quantum Field Theory (QFT) by comparing the Lagrangian (5.13) with that of a quantised massless scalar field φ with effective speed of light c_3 given by

$$\mathcal{L}_{\mathrm{QFT}} = \frac{1}{2}\hbar^2\left[\left(\frac{1}{c_3}\frac{\partial\varphi}{\partial t}\right)^2 - \left|\nabla\varphi\right|^2\right]. \tag{5.19}$$

It then follows that the hydrodynamical and quantum field theoretical fields can be mapped into each other by the relation

$$\phi(t,\boldsymbol{x}) = \sqrt{\frac{\hbar^2 g}{\rho c_3^2}}\varphi(t,\boldsymbol{x}). \tag{5.20}$$

Later, we shall use the theoretical matching above to relate the results of an Unruh-DeWitt detector of φ particles in circular motion to a continuous detector of ϕ quasi-particles. Here, we derived this correspondence by treating both the analogue field ϕ and the effective field φ as quantised objects, but we will later examine how observables related to them behave in classical configurations.

5.3 Continuous quasi-particle laser detectors

In line with the proposal in [81] for cold-atom systems, we move now to build a simplified model for a continuous third-sound waves detector using an electromagnetic field instead of a two-level, Unruh-DeWitt detector. In the following, we consider that a laser field with a Gaussian (TEM_{00}) intensity profile travels through a thin film of helium II with its optical axis aligned with the $z-$direction, and, hence, perpendicular to the sample plane. We also require that the beam width at its intersection with the interface is much smaller than the characteristic dimensions of the sample and experimental parameters, in effect allowing us to regard the interaction between the laser and the superfluid as point-like. This condition will be further discussed in the section with experimental estimates.

We parametrise the electromagnetic field with a fixed polarisation $\hat{\boldsymbol{e}}_1$ using a vector potential $\boldsymbol{A}$ in the Coulomb gauge ($\nabla \cdot \boldsymbol{A} = 0$) given by $\boldsymbol{A}(t,z) = A(t,z)\ \hat{\boldsymbol{e}}_1$, with

$$A(t,z) = A_0 \cos\left(\omega_L t - k_L z + \psi(t,z)\right). \tag{5.21}$$

Here, ω_L is the optical frequency of the laser light, while k_L is its wavenumber in the medium, i.e., $k_L = 2\pi n/\lambda_L \equiv n k_0$, where n is the refractive index in the medium and λ_L is the laser wavelength in vacuum, given by $\lambda_L = 2\pi/k_0 = 2\pi c/\omega_L$, with c the speed of light in vacuum. In the equation above, we assumed that the amplitude A_0 is approximately constant. This is justified for small interface gradients, $\nabla\xi \ll 1$, such that the beam is not deflected as it goes through the sample. We also neglect changes in amplitude caused by reflection at the interface or absorption in the bulk of liquid helium, which can be treated as a dilute gas, so $n \approx 1$, to a good approximation [99, 219]. Ultimately, we allow the laser phase to fluctuate around the expected phase shift caused by changes in refractive index and parametrise these fluctuations by $\psi(t,z)$.

Let us now consider a control volume around the sample of liquid helium-4 and its surroundings, spanning in the vertical direction from $z = -h_0$ to a reference height $z = z_0$ above the interface at $z = \xi(t,\boldsymbol{x})$. Inside the helium sample ($-h_0 < z \leq \xi$), the refractive index is assumed to be a constant n for the fixed laser wavelength and one outside the liquid medium. Accordingly, the dielectric constant ϵ_r equals n^2 inside

helium and one outside, and we may write it as

$$\epsilon_r(t,\boldsymbol{x},z) = n^2\left[\Theta(z+h_0) - \Theta\left(z-\xi(t,\boldsymbol{x})\right)\right] + \left[\Theta\left(z-\xi(t,\boldsymbol{x})\right) - \Theta(z-z_0)\right], \tag{5.22}$$

where $\Theta(\cdot)$ denotes the the step-function. Under these conditions, the action functional of the electromagnetic field reads [247, 250]

$$S_{EM} = \int \mathrm{d}t\mathrm{d}^2\boldsymbol{x}\int_{-h_0}^{z_0}\mathrm{d}z\;\frac{1}{2\mu_0}\left[\frac{\epsilon_r(t,\boldsymbol{x},z)}{c^2}\left(\frac{\partial A(t,z)}{\partial t}\right)^2 - \left(\frac{\partial A(t,z)}{\partial z}\right)^2\right]. \tag{5.23}$$

This functional can be conveniently separated into two components, $S_{EM} = S_0 + S_{int}$, with S_0 including the free electromagnetic field Lagrangian in vacuum and S_{int} denoting an interaction term with the dielectric medium, liquid helium in our case. These actions are given by

$$S_0 = \int \mathrm{d}t\mathrm{d}^2\boldsymbol{x}\int_{-h_0}^{z_0}\mathrm{d}z\;\frac{1}{2\mu_0}\left[\frac{1}{c^2}\left(\frac{\partial A(t,z)}{\partial t}\right)^2 - \left(\frac{\partial A(t,z)}{\partial z}\right)^2\right], \tag{5.24a}$$

$$S_{int} = \int \mathrm{d}t\mathrm{d}^2\boldsymbol{x}\int_{-h_0}^{\xi(t,\boldsymbol{x})}\mathrm{d}z\;\frac{1}{2\mu_0}\left[\frac{n^2-1}{c^2}\left(\frac{\partial A(t,z)}{\partial t}\right)^2\right]. \tag{5.24b}$$

We can now use the ansatz in Equation 5.21 to linearise the actions (5.24). It should be noted that, for the free field in S_0, $k_L \equiv k_0$, i.e., the refractive index is one. In the following, we operate with time-averaged actions over the short period of typical optical frequencies ω_L. Hence, the time average components will be $\langle(\partial_t A)^2\rangle_{1/\omega_L} = A_0^2(\omega_L + \partial_t\psi)^2/2$ and $\langle(\partial_z A)^2\rangle_{1/\omega_L} = A_0^2(k_L + \partial_z\psi)^2/2$. The terms linear in $\partial_t\psi$ and $\partial_z\psi$ do not contribute to the free action S_0, as we assume the phase fluctuations ψ to be prescribed at the boundaries of the control volume and time. On the other hand, for the interacting part S_{int}, the phase ψ may be time-dependent at the interface $z = \xi$ and, hence, the linear terms contribute. The linearised time-averaged actions then read

$$\bar{S}_0 = \int \mathrm{d}t\mathrm{d}^2\boldsymbol{x}\int_{-h_0}^{z_0}\mathrm{d}z\;\frac{A_0^2}{4\mu_0}\left[\frac{1}{c^2}\left(\frac{\partial\psi(t,z)}{\partial t}\right)^2 - \left(\frac{\partial\psi(t,z)}{\partial z}\right)^2\right], \tag{5.25a}$$

$$\bar{S}_{int} = \int \mathrm{d}t\mathrm{d}^2\boldsymbol{x}\int_{-h_0}^{\xi(t,\boldsymbol{x})}\mathrm{d}z\;\frac{A_0^2}{4\mu_0}\left[\frac{n^2-1}{c^2}\left(\frac{\partial\psi(t,z)}{\partial t} + \omega_L\right)^2\right]. \tag{5.25b}$$

The variation of the action $\bar{S}_0$ results in the wave equation in vacuum for $\psi(t,z)$ over the entire control volume. Conversely, the interaction action is only valid over

the helium sample volume, and its variation reads

$$\begin{aligned}
\delta\bar{S}_{int} &= \int \mathrm{d}t\mathrm{d}^2\boldsymbol{x} \int_{-h_0}^{\xi(t,\boldsymbol{x})} \mathrm{d}z \; \frac{A_0^2}{2\mu_0}\frac{n^2-1}{c^2}\left(\frac{\partial\psi}{\partial t}+\omega_L\right)\frac{\partial\delta\psi}{\partial t} \\
&= \int \mathrm{d}t\mathrm{d}^2\boldsymbol{x} \int_{-h_0}^{\xi(t,\boldsymbol{x})} \mathrm{d}z \; \frac{A_0^2}{2\mu_0}\frac{n^2-1}{c^2}\left[\frac{\partial}{\partial t}\left(\frac{\partial\psi}{\partial t}\delta\psi+\omega_L\delta\psi\right)-\frac{\partial^2\psi}{\partial t^2}\delta\psi\right] \\
&= \int \mathrm{d}t\mathrm{d}^2\boldsymbol{x} \; \frac{A_0^2}{2\mu_0}\frac{1-n^2}{c^2}\left[\left(\left.\frac{\partial\psi}{\partial t}\right|_{z=\xi}+\omega_L\right)\frac{\partial\xi}{\partial t}\delta\psi|_{z=\xi}+\int_{-h_0}^{\xi(t,\boldsymbol{x})}\mathrm{d}z \; \frac{\partial^2\psi}{\partial t^2}\delta\psi\right] \\
&= \int \mathrm{d}t\mathrm{d}^2\boldsymbol{x} \int_{-h_0}^{z_0} \mathrm{d}z \; \frac{A_0^2}{2\mu_0}\frac{1-n^2}{c^2}\left[\left(\frac{\partial\psi}{\partial t}+\omega_L\right)\frac{\partial\xi}{\partial t}\delta(z-\xi)+\frac{\partial^2\psi}{\partial t^2}\Theta(\xi-z)\right]\delta\psi.
\end{aligned} \tag{5.26}$$

In the derivation above, between the second and third lines, we used the Leibniz integral rule[1] and boundary terms were taken to vanish throughout. The last line is written as a variation over the entire control volume and can be appropriately combined with the variation of the free action, $\delta\bar{S}_0$. We note that the phase fluctuation ψ is assumed to vary slowly, and its time derivative may be disregarded when compared to optical frequencies at the level of equations of motion, i.e., $\partial_t\psi \ll \omega_L$ in the last line. For the interfacial height perturbations ξ considered here, the following approximation holds $\delta(z-\xi) \approx \delta(z)$.

So far, we have ignored the $\boldsymbol{x}-$coordinates in the Lagrangians and integrated them over the entire horizontal cross-section of the control volume. However, as stated above, the interaction between the laser beam and the superfluid sample is point-like along a trajectory $\boldsymbol{x} = \boldsymbol{X}(t)$ that may vary in time. To localise the interaction to the position $\boldsymbol{x} = \boldsymbol{X}(t)$, we will introduce a delta function $\delta(\boldsymbol{x}-\boldsymbol{X}(t))$ inside the action, resulting in $\partial_t\xi(t,\boldsymbol{x}) = \partial_t\xi(t,\boldsymbol{X}(t))$. Finally, in the superfluid volume, the equations of motion for the phase fluctuations $\psi(t,z)$ read

$$-\frac{n^2}{c^2}\frac{\partial^2\psi}{\partial t^2}+\frac{\partial^2\psi}{\partial z^2} = k_0\frac{n^2-1}{c}\frac{\partial\xi(t,\boldsymbol{X}(t))}{\partial t}\delta(z). \tag{5.27}$$

The solution to the equation above can be separated into two contributions. The first solves the homogeneous problem and is denoted $\psi_0(t,z)$, while the particular solution can be obtained using the Green's function for the 1D wave equation, given by $G(t,z) = \frac{c}{2n}\Theta(t-n|z|/c)$. The resulting solution is then

$$\psi(t,z) \;=\; \psi_0(t,z) - \frac{n^2-1}{2n}k_0\xi(\tau,\boldsymbol{X}(\tau)), \tag{5.28}$$

[1] Upon using the Leibniz integral rule, a total derivative in time remains and is integrated over time inside the varied action $\delta\bar{S}_{int}$. The resulting terms are then evaluated at the boundaries of the time integration, where $\delta\psi$ is prescribed and vanishes.

where $\tau = t - n|z|/c$. Under the dilute gas approximation, which applies well to liquid helium in the visible and near-infrared spectra, the refractive index may be written as $n = 1 + \varepsilon$, with $\varepsilon \ll 1$. Hence, the prefactor $(n^2-1)/(2n)$ in the equation above, to leading order in ε, is $(n^2-1)/(2n) \approx \varepsilon = n - 1$, which gives the known phase shift obtained from a change of ξ in the optical path length at the interface [219].

Equation 5.28 shows that third-sound interfacial fluctuations are transduced into the phase field of the laser along its trajectory $\boldsymbol{x} = \boldsymbol{X}(t)$ intersecting the superfluid sample. In other words, the one-dimensional laser phase field $\psi(t,z)$ is subject to an interaction with the two-dimensional field $\xi(t,\boldsymbol{x})$ confined to the interface. The effective Lagrangian describing this process can be inferred from the action S_{int} and reads (cf. [81])

$$L_{int} = -\frac{A_0^2}{2\mu_0} k_0 \frac{n^2-1}{c} \frac{\partial\psi(t,0)}{\partial t} \xi\left(t, \boldsymbol{X}(t)\right). \tag{5.29}$$

In our analogue model, the laser phase field ψ encompasses the quantum fluctuations of the free electromagnetic field around a semi-classical coherent state. In this depiction, the analogue probing field ψ is in a ground state $|0\rangle$ representing the coherent phase state. Upon interaction with the height field ξ, which is in a thermal state $|\beta\rangle_T$ characterised by the temperature T of the helium sample, the phase field transitions to states $|1_{\bar\omega}\rangle$, given by $|1_{\bar\omega}\rangle = a^\dagger_{\bar\omega}|0\rangle$, where $a^\dagger_{\bar\omega}$ are the creation operators at frequencies $\bar\omega$ in the mode expansion of ψ [81, 82]. Similar to Equation 5.16a, the phase field at the interaction point can be written as,

$$\psi(t,0) \propto \int \frac{\mathrm{d}\bar\omega}{\sqrt{\bar\omega}} \left(a_{\bar\omega} \mathrm{e}^{-i\bar\omega t} + h.c.\right). \tag{5.30}$$

Using first-order time-dependent perturbation theory, we can compute the transition amplitude for the interaction resulting in the creation of a single third-sound quasi-particle $|1_{\boldsymbol{k}}\rangle$ of momentum $\boldsymbol{k}$ from the thermal state $|\beta\rangle_T$. The amplitude reads

$$\begin{aligned} c_{\bar\omega,\boldsymbol{k}} &\propto \int \mathrm{d}t \ \langle 1_{\bar\omega}| \partial_t\psi(t,0) |0\rangle \langle 1_{\boldsymbol{k}}| \xi(t,\boldsymbol{X}(t)) |\beta\rangle_T \\ &\propto \sqrt{\bar\omega} \int \mathrm{d}t \ \mathrm{e}^{i\bar\omega t} \langle 1_{\boldsymbol{k}}| \xi(t,\boldsymbol{X}(t)) |\beta\rangle_T . \end{aligned} \tag{5.31}$$

By summing over all possible final states $|1_{\boldsymbol{k}}\rangle$ of the height field ξ, one finds the transition rate of this continuous detector at a frequency $\bar\omega$ [81, 232], as follows

$$\begin{aligned} \Gamma(\bar\omega) &= \sum_{\boldsymbol{k}} |c_{\bar\omega,\boldsymbol{k}}|^2 \\ &\propto \bar\omega \int \mathrm{d}t \int \mathrm{d}t' \ \mathrm{e}^{-i\bar\omega(t-t')} \sum_{\boldsymbol{k}} {}_T\langle\beta|\xi(t,\boldsymbol{X}(t)) |1_{\boldsymbol{k}}\rangle \langle 1_{\boldsymbol{k}}| \xi(t',\boldsymbol{X}(t')) |\beta\rangle_T \\ &\equiv \bar\omega \int \mathrm{d}t \int \mathrm{d}t' \ \mathrm{e}^{-i\bar\omega(t-t')} W_T(t,t') = \bar\omega \int \mathrm{d}s \ \mathrm{e}^{-i\bar\omega s} W_T(s), \end{aligned} \tag{5.32}$$

where $W_T(s)$ is the thermal Wightman function at temperature T for the field ξ evaluated at the the trajectory $\boldsymbol{X}(t)$,

$$W_T(s) = \Big\langle \xi(s, \mathbf{X}(s))\xi(0, \mathbf{X}(0)) \Big\rangle_T , \tag{5.33}$$

corresponding to the unequal time and space two-point correlation function. The form of Equation 5.32 was obtained by assuming the trajectory is stationary, so $W_T(t, t') = W_T(t - t', 0) \equiv W_T(s)$, and the integration is performed over all times from $-\infty$ to ∞.

By recalling that the field ξ is the canonically conjugate momentum of the fundamental field ϕ at the interface, i.e., $\xi = \partial_t \phi / g$, it follows that

$$W_T(s) = \frac{1}{g^2}\Big\langle \partial_t\phi(s, \mathbf{X}(s))\partial_t\phi(0, \mathbf{X}(0)) \Big\rangle_T = \frac{\hbar^2}{\rho g c_3^2}\Big\langle \partial_t\varphi(s, \mathbf{X}(s))\partial_t\varphi(0, \mathbf{X}(0)) \Big\rangle_T . \tag{5.34}$$

In the equation above, we used the matching (5.20) between the hydrodynamical field ϕ and the analogue QFT field φ to express the Wightman function of ξ in terms of that of an analogue KG field in $(2+1)-$dimensional Minkowski spacetime. The latter case was examined in [83], where the authors discuss several aspects of the analogue Unruh effect for detectors in circular motion immersed in a thermal bath in $2 + 1$ dimensions. We will soon use their results to draw a parallel with our proposed setup.

5.3.1 Detector along circular trajectory

By treating the laser phase field as a continuous detector of third-sound quasi-particles in a thermal bath at temperature T, we may define its spectral response function, or susceptibility, as [5]

$$\mathcal{F}_\xi(\omega; T) = \int \mathrm{d}s \; e^{-i\omega s} W_T(s) = \frac{\hbar^2}{\rho g c_3^2}\mathcal{F}(\omega; T). \tag{5.35}$$

Here, the response function $\mathcal{F}(\omega; T)$ of the analogue scalar field φ corresponds to that developed in [83]. In line with their work, let us consider that the laser beam is point-like at the interface and moves in a circular trajectory with radius R and angular frequency Ω. Hence, the interaction point is parametrised by the curve $\boldsymbol{X}(t) = (R\cos(\Omega t), R\sin(\Omega t))$. Bunney & Louko show in [83] that the response function of the analogue field detector reads

$$\mathcal{F}(\omega; T) = \frac{1}{2}\frac{\omega^2}{\hbar}\sum_{m > \omega/\Omega} J_m^2\left(\left(m - \frac{\omega}{\Omega}\right)\frac{v}{c_3}\right)$$

$$+\frac{1}{2}\frac{\omega^2}{\hbar}\left[\sum_{m>\omega/\Omega}\frac{J_m^2\left(\left(m-\frac{\omega}{\Omega}\right)\frac{v}{c_3}\right)}{e^{\hbar(m\Omega-\omega)/k_BT}-1}+\sum_{m>-\omega/\Omega}\frac{J_m^2\left(\left(m+\frac{\omega}{\Omega}\right)\frac{v}{c_3}\right)}{e^{\hbar(m\Omega+\omega)/k_BT}-1}\right]. \quad (5.36)$$

In the second line of the equation above, we see the clear footprint of thermality of third-sound modes through the Bose distribution, which is inherently dependent on the sample temperature T. Conversely, the first line shows a vacuum contribution, independent of T. We also note the implicit dependence of the response on the acceleration through the angular frequency Ω, i.e., $a = \Omega^2 R$.

Bunney & Louko also record that a detector moving in linear inertial motion, say at constant velocity v, will experience a Doppler-shifted response, denoted $\mathcal{F}_{\text{Lin}}$, given by

$$\mathcal{F}_{\text{Lin}}(\omega;T)=\frac{1}{2}\frac{\omega^2}{\hbar}\left[\gamma_s\Theta\left(-\omega\right)+\frac{\gamma_s}{\pi}\int_{-\pi/2}^{\pi/2}\frac{\mathrm{d}\theta}{e^{\gamma_s^2(1+\frac{v}{c_3}\sin\theta)\hbar|\omega|/k_BT}-1}\right], \quad (5.37)$$

where $\gamma_s = (1 - v^2/c_3^2)^{-1/2}$ is the Lorentz factor. Again, the first term inside the brackets corresponds to the inertial vacuum contribution, which is the only remaining term when $T = 0$ [251]. It is related to the de-excitation rate of the two-level Unruh-DeWitt detector, which is expected to occur regardless of the temperature [5]. The authors show that one can obtain Equation 5.37 by considering a limiting case of Equation 5.36 in which the velocity v is kept fixed, while the radius R is taken to infinity and the angular velocity Ω to zero. We can use the formula above to conceptually distinguish between accelerated and inertial signals and quantitatively isolate them by defining a measure of their difference, as follows

$$\Delta\mathcal{F}_\xi(\omega;T)=\mathcal{F}_\xi(\omega;T)-\mathcal{F}_{\xi,\text{Lin}}(\omega;T) \quad (5.38)$$

In the following section, we will employ it in the discussion of the experimental proposal and its expected output signal.

From Equation 5.37, we can infer the response of a static continuous detector interacting with the height field ξ in a thermal bath. By taking $v = 0$ and $\gamma_s = 1$, we see that

$$\mathcal{F}_{\xi,v=0}(\omega;T)=\frac{\hbar\omega^2}{2\rho g c_3^2}\left[\Theta\left(-\omega\right)+\frac{1}{e^{\hbar|\omega|/k_BT}-1}\right]. \quad (5.39)$$

In the previous derivations, we implicitly assumed that the quantisation of third-sound modes was justified, which would be valid for $\hbar|\omega| \gtrsim k_BT$. However, we will see that the typical operation temperatures for the helium sample and the linear dispersive band limit $\ell_c^2 k^2 \ll 1$ could practically restrict our analysis to a regime where $k_BT \gg \hbar|\omega|$. This condition suggests a classical treatment of the response functions presented here. For the purpose of building intuition on this regime, we follow the standard approach in Quantum Mechanics of keeping leading order terms in $\hbar$, which is treated as a

negligible quantity in this classical limit, i.e., $\hbar \to 0$ [252]. Accordingly, the high ambient temperature case of Equation 5.39 reads

$$\mathcal{F}_{\xi,v=0}(\omega;T) \approx \frac{|\omega| k_B T}{2\rho g c_3^2} + \mathcal{O}(\hbar), \tag{5.40}$$

where we used

$$\frac{1}{e^{\hbar|\omega|/k_B T} - 1} \approx \frac{k_B T}{\hbar|\omega|}, \text{ for } k_B T \gg \hbar|\omega|. \tag{5.41}$$

The response function above agrees with the expectation of a fluctuating hydrodynamic interface by means of a fluctuation-dissipation relation at temperature T and frequencies below the capillary band [95, 96].

A similar analysis of this high-temperature regime applies to $\mathcal{F}_\xi$ and $\mathcal{F}_{\xi,\mathrm{Lin}}$ at arbitrary velocities v, in which cases both vacuum contributions in (5.36) and (5.37) can be neglected as they are of order $\hbar$. Nevertheless, to a leading order approximation, the accelerated and inertial response functions have non-vanishing contributions explicitly depending on a and v, respectively. Hence, we find that the formulas derived in [83] can be suitably adapted to our proposed setup to identify the signature of acceleration dependence in the detector response, in contrast with the Doppler-shifted signal of an inertial detector. Finally, they can be adequately applied even for finite temperatures of the helium sample, which can be realised in a laboratory. Our proposal for such an experiment is shown below.

5.4 Experimental proposal and estimates

With the theoretical framework of our proposal laid down in the previous sections, we will now discuss a candidate for an experimental setup to measure the observer dependence in a detector response. A depiction of it is shown in Figure 5.1, with a description of the core components required for an optical Mach-Zender interferometric configuration. Naturally, the liquid helium-4 sample shown in the drawing must be prepared in a low-temperature setting. Accordingly, in a cryostat with capacity for temperatures below $1\,\mathrm{K}$, a sample cell containing a bulk volume of helium II will be used to conduct the experiment. Inside it, a small quartz platform protrudes from the bottom and is coated by a fine layer of helium II, forming a superfluid thin-film. The van der Waals interaction coefficient between helium-4 and a quartz substrate was measured in [240], and yields a characteristic length scale of $\kappa_0 \simeq 717\,\mathrm{nm}$. When operating at saturated-vapour conditions, a typical film thickness within experimental reach lies in the order of $h_0 = 100\,\mathrm{nm}$ [240, 249, 253]. Hence, the thin-film condition for third-sound waves, $h_0 \ll \kappa_0$, is satisfied.

Typical physical properties of liquid helium-4 at $500\,\mathrm{mK}$ and our choices of exper-

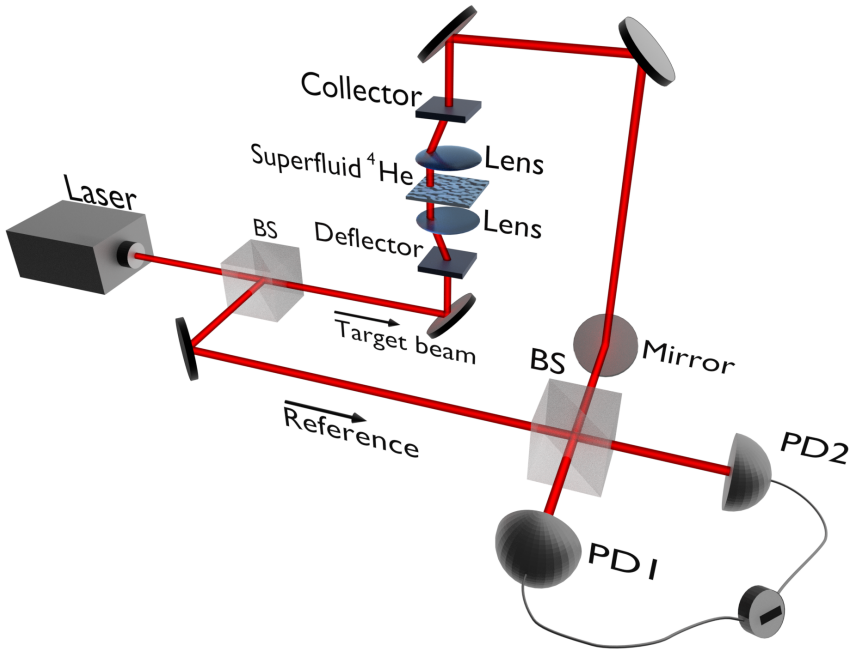

Figure 5.1: An input laser beam with a Gaussian profile is separated into two arms, namely a target and a reference, in a beam splitter (BS). An appropriate deflector-lens configuration steers the target beam on a circular trajectory through the superfluid helium sample with the optical axis perpendicular to the fluid surface. After the sample, a lens-collector combination, followed by a series of mirrors, brings the beam back to a static path and leads it to a second beam splitter (BS), where the target and reference arms are combined and interfere. The resulting beams are detected at two photodiodes (PD1) and (PD2). [4]

imental parameters are shown in Table 5.1. Below this temperature, these properties display very little variation. Hence, we use them as reference values and refer to [99] for the exact temperature dependence. For these values, the speed of propagation of third-sound modes in Equation 5.11 is $c_3 \approx 8.8\,\mathrm{cm\,s^{-1}}$. We also see that the capillary length is $\ell_c \approx 5.8\,\mu\mathrm{m}$, which provides the characteristic wavenumber $k_c \sim 1/\ell_c$ at which the surface modes enter the dispersive gravity-capillary regime, $\omega^2 = c_3^2(1+\ell_c^2 k^2)k^2$. The linear dispersion frequency of this transition is given by $\omega_c = c_3 k_c \approx (2\pi)2415\,\mathrm{Hz}$. We thus require that the detector must probe modes with frequencies $\omega \ll \omega_c$ so the analogy with a massless scalar field in flat spacetime remains valid.

The quartz substrate of the sample cell allows optical access, so the laser beam can interact with the thin-film of superfluid helium. To minimise optical absorption by the sample [254], we choose to operate with a laser in the near-infrared, $\lambda_L = 700\,\mathrm{nm}$, and with low power, $P = 500\,\mu\mathrm{W}$. We further assume that the beam can be focused on the interface to a spot with diameter $2r_0 = 10\,\mu\mathrm{m}$ with appropriate optical components outside the cryostat[2]. A beam deflector moves the interaction spot of the target beam

[2]We expect that the beam focused at the sample will spread over the Rayleigh range - possibly much larger than the thin-film thickness - around its waist [219], where its width is minimum, and its profile is ideally Gaussian. Although experimentally challenging, we hope to optimally align the focus point at the thin-film interface, hence keeping the desired assumptions.

Table 5.1: Physical properties of Helium-4 at $T = 500\,\mathrm{mK}$ [99] (ρ: density; n: optical density or refractive index; σ: surface tension) and experimental parameters (α_{vdW}: van der Waals coefficient; h_0: thin-film average depth). The effective gravitational acceleration g, the third-sound speed of propagation c_3 and the capillary length ℓ_c are also given for the chosen film depth. The van der Waals coefficient is given for a quartz substrate [240].

Property	**Value at $T = 500\,\mathrm{mK}$**	**Parameter**	**Value at $T = 500\,\mathrm{mK}$**
$\rho\ [\mathrm{kg\,m^{-3}}]$	145	$h_0\ [\mathrm{nm}]$	100
$n\ [\ ]$	1.025	$g\ [\mathrm{m\,s^{-2}}]$	77.8×10^3
$\sigma\ [\mathrm{mN\,m^{-1}}]$	0.379	$c_3\ [\mathrm{cm\,s^{-1}}]$	8.8
$\alpha_{vdW}\ [\mathrm{m^5\,s^{-2}}]$	2.6×10^{-24}	$\ell_c\ [\mu\mathrm{m}]$	5.8

on a circular trajectory at the interface. Bunney & Louko show in [83] that the effect of acceleration on the response of the detector is enhanced at "relativistic" speeds, i.e., $v \to c_3$. For that, we choose a fixed rotation speed of $v = 0.95c_3$ with trajectory radii R ranging from $20 - 100\,\mu\mathrm{m}$, corresponding to angular frequencies $\Omega/(2\pi)$ in the approximate range of $133 - 665\,\mathrm{Hz}$, which are well within achievable mechanical or electro-optical rotations.

At this point, it is clear that the order of the typical frequencies in our proposed system will lie in the range of $100\,\mathrm{Hz}$ to $1\,\mathrm{kHz}$. Following our discussion of the previous section, quantisation of non-capillary third-sound interfacial modes, $\hbar\omega > k_B T$, would require a superfluid sample at temperatures lower than $0.05\,\mu\mathrm{K}$ for modes in the kilohertz range, which is generally out of the current technological capabilities of a few millikelvins [248, 249]. In the following estimates, we will consider temperatures between $1\,\mu\mathrm{K}$ and $1\,\mathrm{K}$, which ensures the validity of our assumptions from Section 5.2.

5.4.1 Estimated detection readout and signal-to-noise ratio

For the purposes of this discussion, we only require that a suitable detection scheme, such as phase-referenced homodyne photodetection [255, 256], outputs a time series signal from which laser phase field correlations can be extracted, particularly the autocorrelation function [121, 160]

$$C_\psi(t) = \langle \psi(t)\psi(0) \rangle\ . \tag{5.42}$$

The expectation value above is left purposefully undefined as it could refer to a quantum expectation value of the field from the signal of the photodetectors followed by an experimental average over multiple realisations or the autocorrelation computed with the time-delayed average [160] of the classically extracted phase from an ensem-

ble of experiments. By appropriately referencing the phase, one can extract a phase shift ψ_S acquired at the interface $z = 0$ upon interaction with the height field ξ, as in Equation 5.28. If all possible measurement noise sources have been suppressed, the extracted laser phase is limited by quantum fluctuations only, i.e. shot-noise [255], which we denote by $\delta\psi_{SN}$. Reduction of this noise can be achieved by increasing the laser power, but one must be conscious of the amount of heat transferred to the fluid cell, which could lead to significant temperature changes or even the complete evaporation of the helium film. Accordingly, the shot-noise limited phase field extracted from the experiment should read

$$\psi(t) = \psi_S(t) + \delta\psi_{SN}(t). \tag{5.43}$$

From Equation 5.28, we note that the phase shift ψ_S at the interface is evaluated at the trajectory $\boldsymbol{X}(t)$. However, in the experimental setup, the laser beam is focused at the interface, so its Gaussian intensity profile has a waist of $2r_0$ at the interaction point. This property can be included in our model by noting that the phase couples with an effectively averaged height field $\bar{\xi}(t, \boldsymbol{X}(t))$ at the interaction point, i.e.,

$$\begin{aligned}\bar{\xi}(t, \boldsymbol{X}(t)) &= \frac{1}{2\pi r_0^2} \int \mathrm{d}^2\boldsymbol{x}\ \mathrm{e}^{-\frac{|\boldsymbol{x}-\boldsymbol{X}(t)|^2}{2r_0^2}} \xi(t, \boldsymbol{x}) \\ &= \frac{-i}{\sqrt{2\Sigma}} \sum_{\boldsymbol{k}} \mathrm{e}^{-\frac{1}{2}r_0^2k^2} A_k \left(b_{\boldsymbol{k}} \mathrm{e}^{-i(\omega_k t - \boldsymbol{k}\cdot\boldsymbol{X}(t))} - \mathrm{h.c.} \right),\end{aligned} \tag{5.44}$$

where we used the decomposition of the field ξ in Equation 5.16b. Here, we see that the Gaussian profile of the beam effectively depletes the contribution of high-momentum modes of the probed height field. The equation above confirms the intuitive statement that the laser beam cannot detect interfacial modes whose wavelengths are smaller than its width $2r_0$. In fact, wavenumbers as large as $k_{\max} = 2\pi/(2r_0)$ contribute as little as 0.7% to the spectrum of the measured height field $\bar{\xi}$. Accordingly, we argue that, for the long-wavelengths considered in the analogue scenario, the approximation $\bar{\xi}(t, \boldsymbol{X}(t)) \approx \xi(t, \boldsymbol{X}(t))$ is justified.

Under the approximations above, it follows that the phase shift relates to the height field by $\psi_S(t) \approx (n^2 - 1)k_0/2\ \xi(t, \boldsymbol{X}(t))$, as per Equation 5.28, and the phase autocorrelation function extracted from the experiment should read

$$C_\psi(t) \approx \frac{(n^2-1)^2k_0^2}{4} W_T(t) + \sigma_{SN}^2 \delta(t), \tag{5.45}$$

where $W_T(t)$ is the autocorrelation of the height field ξ, or the Wightman function, as defined in Equation 5.33, and $\sigma_{SN}^2 = \hbar\omega_L/P$ is the variance of shot-noise induced phase fluctuations on the laser with integrated power P [81]. Here, we assumed that

the phase noise $\delta\psi_{SN}$ is Gaussian and uncorrelated with the thermal excitations of the interfacial field ξ.

In order to relate the measured quantity with the response function of the analogue field detector, we inspect the time Fourier transform of C_ψ, known as the power spectral density (PSD), and defined as

$$S_\psi(\omega) = \int \mathrm{d}s\ C_\psi(s)\mathrm{e}^{-i\omega t}. \tag{5.46}$$

From Equation 5.45, we can relate the quantity above with the response function of the height field $\mathcal{F}_\xi$, which is in turn related to that of the analogue relativistic field by Equation 5.35. Hence, the PSD of the phase fluctuations reads

$$S_\psi(\omega) = \kappa\mathcal{F}(\omega;T) + \sigma^2_{SN}, \tag{5.47}$$

with $\mathcal{F}$ as defined in Equation 5.36 and the constant κ is given by

$$\kappa = \frac{(n^2-1)^2k_0^2\hbar^2}{4\rho g c_3^2}. \tag{5.48}$$

The PSD above shows a direct relation between the expected readout of an experiment and the response function of a field detector in circular motion. This confirms that an acceleration dependence is embedded in the measured signal, and thus this system could be used to probe the analogue of the Unruh effect in $2+1$ dimensions. On the other hand, as mentioned in subsection 5.3.1, we want to distinguish the acceleration-dependent signal from the Doppler-shifted one related to the relative motion of the detector with speed v in the sample's thermal bath. As discussed in subsection 5.3.1, the former is isolated in the response $\mathcal{F}_{\mathrm{Lin}}$ of a detector in linear inertial motion with constant speed v.

Unfortunately, the finite size of the sample prohibits an empirical measurement of a laser detector moving in a stationary linear trajectory, which would rapidly extrapolate the size of the probed system. We circumvent the issue of obtaining this linear response from an experiment by noting that $\mathcal{F}(\omega;T)$ and $\mathcal{F}_{\mathrm{Lin}}(\omega;T)$ share the same high-frequency $\omega \gg \Omega$ behaviour [83]. In other words, a third-sound mode with frequency $\omega_k \gg \Omega = v/R$ will have a wavelength $1/k \ll (c_3/v)R$. Hence, high-frequency, short-wavelength modes will experience the interaction with the laser along a circle with a virtually infinite radius, i.e., a straight line. This intuitive description is in line with the mathematical asymptotic analysis put forward in [83]. Here, we focus on the numerical confirmation of this statement by considering a circular trajectory with radius $R = 60\,\mu\mathrm{m}$ in a helium II sample at temperature $T = 10\,\mathrm{mK}$. Using formulas (5.36) and (5.37), we compute the response functions for the circular motion with frequency

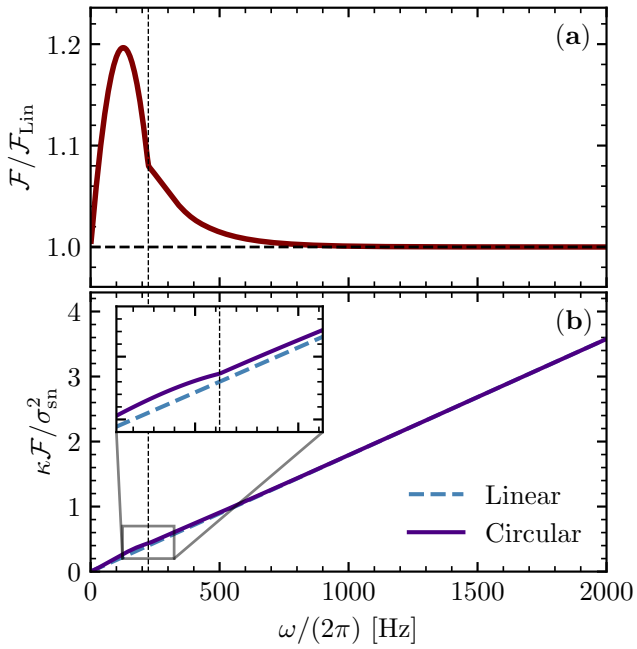

Figure 5.2: In $(\mathbf{a})$, we show the ratio between the circular motion response function $\mathcal{F}$ in Equation 5.36 and the linear motion one $\mathcal{F}_{\rm Lin}$ as in Equation 5.37. Panel $(\mathbf{b})$ displays the ratio of response to shot-noise variance for both circular and linear motions. The inset in $(\mathbf{b})$ shows that at low frequencies, the responses disagree as expected from deviation from unity in the ratio of panel $(\mathbf{a})$. A dashed vertical line indicates the rotation frequency $\Omega/(2\pi)$ in both panels.

$\Omega = v/R \approx (2\pi)222\,\mathrm{Hz}$ and the linear motion with speed v, respectively. We stress that $v = 0.95c_3$ is the same for both detectors. The numerical results are shown in Figure 5.2.

The discrepancies between the circular and linear responses for frequencies around the angular velocity Ω observed in Figure 5.2 are precisely the behaviour we want to observe in our system. We also note that the linear response $\mathcal{F}_{\rm Lin}$ is linear in ω for the low frequencies, hence the trend of the circular response $\mathcal{F}$ at higher ω can be extrapolated to infer the form of $\mathcal{F}_{\rm Lin}$ at lower ones. Accordingly, from an experimental measurement of S_ψ, and thus $\mathcal{F}$, we can infer $\mathcal{F}_{\rm Lin}$ and build the difference measure in Equation 5.38. We then define the difference PSD $S_\delta(\omega)$, as follows

$$S_\delta(\omega) \equiv S_\psi(\omega) - \left(\kappa\mathcal{F}_{\rm Lin}(\omega;T) + \sigma^2_{\rm sn}\right) = \kappa\Delta\mathcal{F}(\omega;T). \tag{5.49}$$

The above measure vanishes if the circular and linear responses agree, as expected for frequencies much higher than Ω, and it admits values greater or smaller than zero when an acceleration dependence exists.

In our ideal scenario in which all noise sources have been eliminated, and the measurement is limited only by fluctuations in the laser phase with variance σ^2_{SN}, we propose another quantitative measure to evaluate the feasibility of measuring S_δ in an

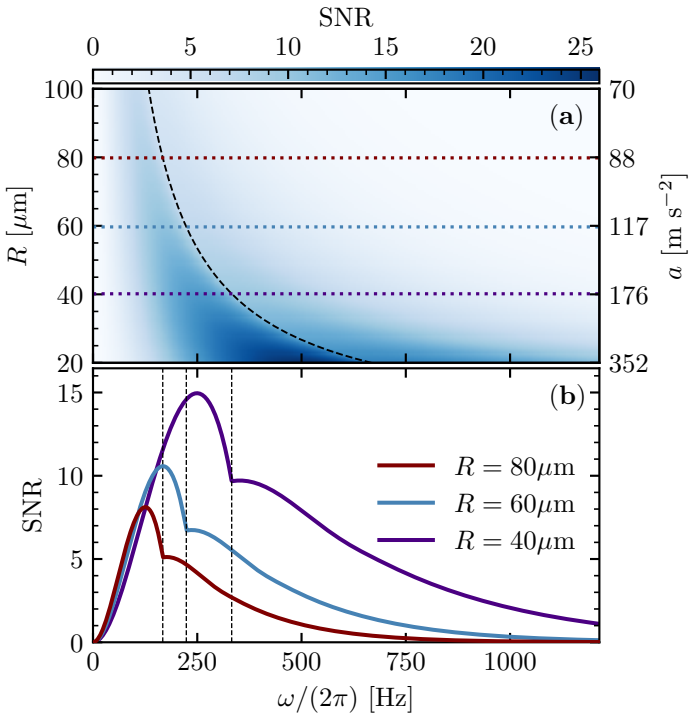

Figure 5.3: SNR (5.50) for $\mathcal{N} = 10^5$ realizations with a bandwidth of $\mathcal{B} = 1$. Superfluid temperature $T = 10\,\mathrm{mK}$, orbital speed $v = 0.95c_3$, orbital radius R as shown; the laser trajectory angular frequency and acceleration are determined in terms of these quantities by $\Omega = v/R$ and $a = v^2/R$. The horizontal axis is the frequency. $(\mathbf{a})$ Heatmap of computed SNR for orbital radii $20\,\mu\mathrm{m} \leq R \leq 100\,\mu\mathrm{m}$. The horizontal colorbar indicates the magnitude of the SNR. Dashed black curve is the orbital radius R for varying angular frequencies Ω with fixed $v = \Omega R$. Purple, blue and dark red dotted lines are lines of constant radii, whose SNRs are displayed in (b). $(\mathbf{b})$ Profile of computed SNR for constant radial slices in (a). Vertical black dashed lines represent orbital angular frequencies for $R = 40\,\mu\mathrm{m}$ (far right), $60\,\mu\mathrm{m}$, and $80\,\mu\mathrm{m}$ (far left). [4]

experiment. We use the following signal-to-noise ratio (SNR) [81]

$$\mathrm{SNR} = \sqrt{\frac{\mathcal{N}\mathcal{B}}{2}} \frac{S_\delta(\omega)}{\sigma_{\mathrm{sn}}^2 \sqrt{1 + 2\frac{S_\delta(\omega)}{\sigma_{\mathrm{sn}}^2} + 2\frac{S_\delta^2(\omega)}{\sigma_{\mathrm{sn}}^4}}}, \tag{5.50}$$

where $\mathcal{N}$ is the number of experimental realisations, and $\mathcal{B}$ is the dimensionless analysis bandwidth given in multiples of the measurement bandwidth $\mathcal{B}_m$ (in hertz). This measure follows from generalising the total variance of the measured signal when averaged over the spectral analysis bandwidth $\mathcal{B}\mathcal{B}_m$ for an ensemble of $\mathcal{N}$ repetitions, see [81] for derivation. Here, we assume that the measurement bandwidth of the spectral analyser or final filter used matches half of the capillary band frequency, i.e., $\mathcal{B}_m = \omega_c/2 \approx (2\pi)1200\,\mathrm{Hz}$. We further consider that the spectral analysis can be done over the entire measurement bandwidth, so $\mathcal{B} = 1$ in the following.

The SNR measure as defined in Equation 5.50 must be above one to indicate that

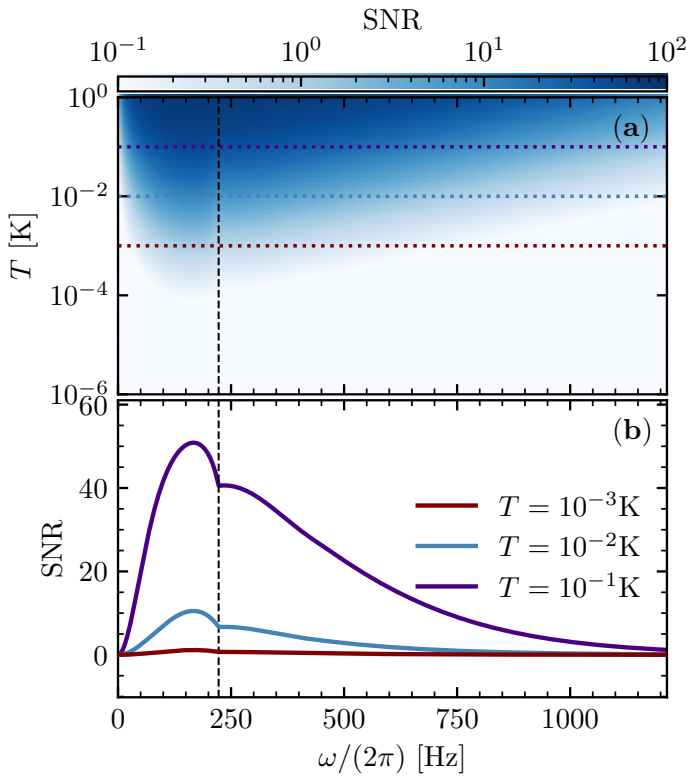

Figure 5.4: SNR (5.50) for $\mathcal{N} = 10^5$ realizations with a bandwidth of $\mathcal{B} = 1$. Orbital radius $R = 60\,\mu\mathrm{m}$, speed $v = 0.95c_3$, frequency on the horizontal axis as in Figure 5.3. Dashed vertical black line shows the orbital angular frequency Ω. (**a**) Heatmap of computed SNR for superfluid at temperatures $1\,\mu\mathrm{K} \leq T \leq 1\,\mathrm{K}$. Purple, blue and dark red dotted lines are lines of constant superfluid temperature, whose SNRs are displayed in (b). (**b**) Profile of computed SNR for constant temperature slices in (a). [4]

the acceleration-dependent signal S_δ can be observed out of the noise level σ^2_{SN} in a set of repeated experiments. We illustrate the use of the proposed quantifier by numerically estimating its value in a range of possible experimental parameters. We first consider that the helium sample is kept at a fixed temperature $T = 10\,\mathrm{mK}$, and compute the SNR for a range of orbital accelerations a by varying the trajectory radius, as shown in Figure 5.3. For the fixed velocity $v = 0.95c_3$, as the radius decreases, the acceleration $a = v^2R^{-1}$ increases and, with it, the acceleration-dependent signal, as seen in panel (a) of Figure 5.3. This observation generalises the concept behind the Unruh effect, which anticipates that the temperature experienced by the detector as it travels through empty space at zero temperature should increase with its acceleration.

A core aspect of our system is the non-zero temperature bath, where the analogue relativistic field is immersed in. To evaluate the influence of the sample's temperature on the SNR, we fix the trajectory radius to $R = 60\,\mu\mathrm{m}$ and, instead, vary the temperature of the thin film of superfluid helium. As mentioned before, we choose a range of operating temperatures within the current technological standards for helium-4 cryostats, namely T between $1\,\mu\mathrm{K}$ and $1\,\mathrm{K}$. With these parameters, the numerical

estimates for the SNR are shown in Figure 5.4. One striking feature appears in this result: the acceleration-dependent signal increases as the sample's temperature rises. Bunney & Louko [83] argue, however, that the detector probing a fixed energy scale (small range of ω) observes an effective reduction in temperature, which is then interpreted as a "colder" thermal bath. They further show that this effect gets enhanced as the ambient (sample) temperature increases. As the authors put it: *"where there is little, the Unruh effect gives; and where there is plenty, the Unruh effect takes."*

5.5 Summary and discussion

Supported by the theoretical modelling presented here, we proposed an experiment that displays an analogue of the circular-motion Unruh effect on the vapour-liquid interface of thin-film superfluid helium-4. In this configuration, a laser serves as a continuous probing field, effectively acting as a local detector of surface fluctuations. Our setup enables the sampling of the superfluid interface along an accelerated trajectory, particularly a circular path. With a suitable choice of experimental parameters, surface modes are within the third-sound regime, where they behave as an effective relativistic field. As the laser phase interacts with this field, the information about the accelerations along the circular trajectory is carried by the detector response function, which can, in turn, be extracted from correlations in the measured signal.

We further examined a signal-to-noise quantifier with the intent of isolating acceleration dependence in the response. Using a range of viable experimental parameters, we numerically estimated the SNR (5.50) for various temperatures and orbital radii, as shown in Figures 5.3 and 5.4. It is important to reiterate that the initial state in our helium-4 setup is thermal, markedly distinct from the vacuum state featured in conventional textbook descriptions of the Unruh effect. Despite this distinction, our results bring two significant conclusions. We first noted that SNR scales proportionally with the acceleration of the detector, confirming the intuition brought from the standard Unruh effect. Second, we have observed that not only an acceleration-dependent signal persists in the presence of background thermality in the probed field, but it also increases with the temperature of the superfluid sample.

It is worth noting that the experimental proposal relied on an entirely novel theoretical framework for quantum field detectors in (2+1) dimensions immersed in a thermal bath [83] and for continuous local field detectors as an alternative to the usual two-level Unruh-DeWitt detectors [251]. The estimates presented here consider a "high-temperature" limit, $k_B T \gg \hbar\omega$, of these more general descriptions. Nevertheless, it is possible to increase the propagation speed of third-sound modes by reducing the film thickness, which could potentially allow for the investigation of high enough frequencies, $k_B T \lesssim \hbar\omega$, so that third-sound quantisation might be visible.

Chapter 6

Conclusion

In this thesis, we have established new kinds of interacting field theory simulators on liquid-liquid and liquid-gas interfaces, tackling problems that, so far, have only been simulated in Bose gases [70–74]. We initially motivated our work with recent developments in quantum simulators and analogue gravity, seeking to extend the research programme to explore generalised Effective Field Theories (EFTs), not necessarily linear ones, that we cannot exactly calculate or numerically simulate. Given the historical relevance and practical versatility of experiments on fluid surfaces, we derived an effective theoretical framework for interfacial dynamics. We then used it to devise proof-of-principle experimental setups to emulate and examine fundamental aspects of the emergent field theories and their counterparts in Quantum Field Theory in Curved Spacetimes (QFTCS).

Our empirical investigations showed that the interface between two classical liquids can be the stage for simulations of non-equilibrium dynamics in the early Universe. The effective field-theoretical description supporting our findings can be directly transferred to quantum liquids, such as helium-3 and helium-4. Indeed, the experimental simulator recently reported in [78] systematically explores, in line with our work, the EFT emerging from the surface dynamics of a vortex flow in superfluid helium-4. Foreseeing this new generation of experiments on classical and quantum fluid interfaces, we briefly reviewed and presented detection methods for reconstructing entire spatial regions of the fluid interfacial height, the central observable of our EFTs. Complementarily, by considering a local detector built from an effective interaction between a laser and superfluid helium-4, we opened a new path for studying the fundamental principle of observer dependence in QFTCS as predicted by the Unruh effect. In the following, we briefly review our main results and offer outlooks on future avenues of research.

In Chapter 2, we have discussed the theoretical framework for constructing EFT simulators using fluid interfaces. This description was further used in the following chapters to specialise to scalar field theories in cosmological scenarios and flat spacetime. Our discussion on including non-idealised features in the formulation reveals the

critical advantage of this process: the model can be iteratively improved to better describe the underlying physical system while keeping the field-theoretical framework. This approach extrapolates the standard treatment of analogue gravity, relying on exact mathematical equivalences between the target and the simulator. Instead, it permits a systematic analysis of the impact that realistic experimental features have on the emergent dynamics of the EFT. In turn, an element of robustness appears in investigating the target process idealised in astrophysical settings. After all, if a phenomenon prediction can "survive" the various intricacies of different systems, such as dissipation and dispersion, it might have something more fundamental to it worth delving into.

Building on these previous statements, our results in Chapter 3 speak for the convergence of two somewhat unrelated theories - the cosmological model of preheating and the evolution of non-linear Faraday waves - through the dynamical similarities in their field-theoretical descriptions. As an initial step, we used statistical measures to characterise the emergent EFT and demonstrate the efficacy of our approximate non-linear model in accurately recovering the evolution of the primary instability. We further established a conceptual relation to the preheating scenario by investigating secondary instabilities resulting from the decay of the dominant mode. Our findings highlight that the key non-linear dynamical features of the astrophysical theory can be observed in a strongly interacting and damped system, reinforcing the robustness of the phenomena in line with our statement above. Moreover, we note that the two-fluid interface hosts infinitely many modes fitting the basin, and our EFT predicts that just as many interaction "channels" are available. This offers a powerful platform to investigate the time evolution of more intricate interacting scenarios that numerical simulations of an approximate EFT would struggle to replicate.

The developments of Chapter 3 illustrate the need for precise and accurate reconstruction of the interfacial height in order to obtain a trustworthy characterisation of the emergent EFT. Accordingly, we presented two detection schemes in Chapter 4, also envisioning further experimental analogue simulations in fluid interfaces. The first, Schilieren Fourier Transform Profilometry (FTP), is primarily limited by the spatial frequency of the periodic pattern and the imaging system only. Despite being successfully used in the experiments of Chapter 3 and resolving wave amplitudes from micro to millimetres, we could not observe the interface departing its stochastic initial state, as that is expected to happen way below our lower resolution bound. In this sense, the second method, Digital Holography (DH) profilometry, may help future studies by allowing the reconstruction of the entire dynamical evolution of the interface. With this, we could examine the influence, if any, of the initial state on the non-linear behaviour at later times, which is a known problem in far-from-equilibrium field theories.

Expanding on the reconstruction methods of Chapter 4 covering a region of the

sample, we employed local analogue field detectors in Chapter 5. The proposed experiment would simulate a different type of interacting field theory, touching the concept of particle detectors in QFTCS. The third-sound quasi-particles in helium-II are analogous to a free massless scalar field in (2+1)-dimensional Minkowski space. However, in defining a quasi-particle detector, we had to establish an effective interaction term between the probing and analogue fields. This was critical for the mapping between the EFT and the target Quantum Field Theory (QFT). Leveraging the measurement system and the analogue correspondence, our experimental proposal would be the first to observe the acceleration dependence in detector response, in line with the Unruh effect, but in the presence of background thermality.

Conceiving such a setup whose sample is always at a finite temperature requires considering a thermal state instead of the quantum vacuum in the relevant QFT. In other words, the theory of the target scenario had to be suitably extended to the experimental requirements of the simulator, even revealing novel aspects of the circular-motion Unruh effect, as presented by Bunney and Louko [83]. Accordingly, besides the relevance of the potential observation of the phenomenon, this proposal represents a prime instance of the symbiotic relation between the physics of the target and the simulator, even at an early conceptual and developmental stage.

We argue that two factors ultimately determine the utility and efficacy of gravity and early Universe simulators. Firstly, a thorough understanding of the EFT, extending beyond the description of the analogical framework, is needed. This comprehension must encompass an ability to quantitatively assess potential deviations and ascertain whether they can be translated into relevant and interesting features of non-equilibrium and fundamental processes. This was shown through the development of the general EFT in fluid interfaces, the experimental investigations of our preheating dynamics simulations, and the proposal of empirical observation of the analogue Unruh effect.

Secondly, the refinement and optimisation of gravity simulators for broader applications require precisely extracting the dynamics of the simulated field. In turn, this entails a comprehensive characterisation of the emergent EFT and its suitability in describing empirical data. Our measurement schemes, both for interfacial reconstruction over a spatial region and for local detection of surface waves, were devised to facilitate the development of gravity simulators in fluids. Ultimately, these two facets of analogue simulations are interconnected. Hence, future developments should be guided by a comprehensive theoretical description of the underlying physics governing the simulation, as well as enhanced experimental control mechanisms and detection methods.

In light of the discussion above, future work should concentrate on applying the framework of interacting field theories developed here to challenging QFTCS problems, building on the proof-of-principle experiment and proposal presented in this

thesis. Our results of Chapter 3 indicate that a classical liquid-liquid interface can be appropriately used for early Universe simulations. However, a question remains on what relevant aspects of non-equilibrium dynamics can be observed in a classical setup in contrast with quantum simulators in condensed matter. One route for answering this question would be to conduct experiments in the two-fluid system of Chapter 3 to investigate universal behaviour in the late-time non-linear interfacial dynamics using our effective field-theoretical description. The results could then be compared to previous experiments in Bose gases [70–72], allowing differences and similarities to be drawn.

Following with early Universe simulators, due to its abnormally low viscosity, thin films of superfluid helium could be used for mimicking the inflationary expansion of the Universe with enough e-folds to observe mode freezing way before interfacial waves are viscously damped, similar to the proposal of Fifer et al. [79] for magnetised liquids. For such an experiment, the DH profilometry method developed in Chapter 4 would be of great use as it could be readily implemented in low-temperature setups. Overlapping with the proposal in Chapter 5, the method should be employed in reconstructing the spectrum of third sound waves on thin films of helium-II, which can then be used as input for numerical studies to be compared with the experiment. At low frequencies, the holographic measurement would serve as a benchmark for developing the phase-referenced laser detector required for the experimental implementation suggested in Chapter 5.

As we look forward, it is evident that the combination of theoretical advances and experimental innovations in fluid interfaces holds great promise for analogue gravity. The compelling opportunity of experimentally simulating EFTs with astrophysical origins in the presence of intricate real-world conditions leaves us optimistic about future research prospects. Our work builds on the solid foundation laid by previous analogue black-hole and early Universe simulators to offer the stepping stones for a new generation of experiments on classical and quantum fluid interfaces that we anticipate will dive deeper into fundamental physics questions.

Appendix A

Fluid-fluid interfacial dynamics: derivations and useful formulae

This appendix condenses a series of derivations and useful formulae relevant to all chapters but primarily to the model presented in Chapter 2. Some of these are based off [1] and standard textbook references in Fluid Dynamics [15, 90, 100, 108].

A.1 Limits of Navier-Stokes equations

Here, we discuss the approximate limits of the Navier-Stokes equations (2.8) and some of their solutions relevant to the conditions and setup of Section 2.2.

A.1.1 Stress Balance condition

Following the Helmholtz decomposition of Equation 2.2, the normal stress condition at the interface (2.12) reads

$$\begin{aligned}\hat{\boldsymbol{n}}_\Gamma \cdot \left(\overleftrightarrow{\boldsymbol{\pi}}_1\Big|_{\Gamma=0^-} - \overleftrightarrow{\boldsymbol{\pi}}_2\Big|_{\Gamma=0^+}\right)\cdot\hat{\boldsymbol{n}}_\Gamma = -\left(p_1|_{\Gamma=0^-} - p_2|_{\Gamma=0^+}\right)\\ + \frac{2}{|\nabla\Gamma|}\left[\mu_1\varepsilon_{1,zz}|_{\Gamma=0^-} - \mu_2\varepsilon_{2,zz}|_{\Gamma=0^+} - (2\hat{\boldsymbol{z}} - \nabla\xi)\cdot\left(\mu_1\,\overleftrightarrow{\boldsymbol{\varepsilon}}_1\,|_{\Gamma=0^-} - \mu_2\,\overleftrightarrow{\boldsymbol{\varepsilon}}_2\,|_{\Gamma=0^+}\right)\cdot\nabla\xi\right]\\ = -\sigma\nabla\cdot\hat{\boldsymbol{n}}_\Gamma, \quad \text{(A.1)}\end{aligned}$$

where $|\nabla\Gamma| = \sqrt{1+|\nabla\xi|^2}$, $\overleftrightarrow{\boldsymbol{\varepsilon}}_j$ denotes the strain rate tensor of fluid j, and $\varepsilon_{j,kl}$ its components in the (kl) directions. Similarly, the tangential stress condition reads

$$\mu_1\hat{\boldsymbol{n}}_\Gamma\cdot\left(\overleftrightarrow{\boldsymbol{\varepsilon}}_1\Big|_{\Gamma=0^-}\right)\times\hat{\boldsymbol{n}}_\Gamma = \mu_2\hat{\boldsymbol{n}}_\Gamma\cdot\left(\overleftrightarrow{\boldsymbol{\varepsilon}}_2\Big|_{\Gamma=0^+}\right)\times\hat{\boldsymbol{n}}_\Gamma. \quad \text{(A.2)}$$

We note that the normal stress condition recovers the usual Young-Laplace law [97] in the absence of viscosity and non-linearities. Under the same conditions, the tangential stress equation vanishes, indicating the continuity of tangential components across the interface.

A.1.2 Non-linear inviscid regime

By disregarding any viscous components of the velocity, i.e., setting $\boldsymbol{U}_j \equiv \boldsymbol{0}$, in equations (2.4) and (2.7), we directly obtain (2.15b) and (2.15c). To derive equation (2.15d), we first note that the convective term of the Navier-Stokes equation (2.8) can be re-expressed as follows

$$(\boldsymbol{u}_j \cdot \nabla)\, \boldsymbol{u}_j = \frac{1}{2}\nabla|\boldsymbol{u}_j|^2 - \boldsymbol{u}_j \times (\nabla \times \boldsymbol{u}_j) = \nabla\left(\frac{1}{2}|\nabla\phi_j|^2\right), \tag{A.3}$$

where we used that the curl of a gradient vanishes. The divergence of the stress tensor $\overset{\leftrightarrow}{\varepsilon}_j$ reads

$$\nabla\cdot \overset{\leftrightarrow}{\varepsilon}_j = -\nabla p_j + \mu_j \nabla^2 \boldsymbol{u}_j = -\nabla p_j + \mu_j \underbrace{\nabla^2 \nabla\phi_j}_{\nabla(\nabla^2\phi_j)=0} = -\nabla p_j. \tag{A.4}$$

Equation 2.8 can then be written as

$$\nabla\left[\rho_j \frac{\partial\phi_j}{\partial t} + \frac{1}{2}|\nabla\phi_j|^2 + \rho_j g(t) z + p_j\right] = 0, \tag{A.5}$$

from which we recover Bernoulli's equation in both fluids

$$\rho_j \frac{\partial\phi_j}{\partial t} + \frac{1}{2}|\nabla\phi_j|^2 + \rho_j g(t) z + p_j = \text{const.} \tag{A.6}$$

By evaluating this equation at the interface $\Gamma = z - \xi(t, \boldsymbol{x}) = 0$ in each fluid and computing their difference, we obtain (2.15d).

A.1.3 Linear, slightly viscous regime

For linearised perturbations of the Navier-Stokes equations (2.8) in the presence of small viscosities in both fluids, we may describe the linear dynamics in terms of inviscid (irrotational) solutions $\nabla\phi_j$ with small viscous (solenoidal or rotational) corrections $\boldsymbol{U}_j$ relevant around the boundary layers at solid walls and the interface [90]. In the absence of external forcing, we assume that the velocity potentials satisfy the linearised Bernoulli's equation, which evaluates to the following at the interface,

$$\frac{\partial}{\partial t}\left(\rho_1\phi_1 - \rho_2\phi_2\right)\Big|_{z=0} + (\rho_1 - \rho_2) g_0 \xi - \sigma\nabla^2\xi = 0. \tag{A.7}$$

Additionally, it follows from Equation 2.8 that the Stokes' boundary layer velocities $\boldsymbol{U}_j$ satisfy

$$\frac{\partial \boldsymbol{U}_j}{\partial t} - \nu_j \nabla^2 \boldsymbol{U}_j = 0. \tag{A.8}$$

Under these assumptions, the kinematic boundary condition at the interface (2.7) for the inviscid solution reads

$$\frac{\partial\xi}{\partial t} = \frac{\partial\phi_1}{\partial z}\Big|_{z=0} = \frac{\partial\phi_2}{\partial z}\Big|_{z=0}. \tag{A.9}$$

From this equation, by employing the spectral decompositions for ϕ_j and ξ in equations (2.20) and (2.21), we recover a map between the interfacial modes ξ_a and $\phi_{j,a}$ in Equation 2.24. Accordingly, Equation 2.56 follows directly from this relation. For the rotational velocities $\boldsymbol{U}_j$, the kinematic boundary condition yields Equation 2.57d and the remaining constraints are given in Equation 2.57.

Around rigid walls and the interface, Equation 2.57b and Equation 2.57d require that the solenoidal velocities must vanish along the direction of the normal and, thus, are always tangential to the boundaries. In line with [86], we write the boundary layer velocities around a rigid wall $\bar{S}_B$ as

$$\boldsymbol{U}_{j,B} = -\nabla_{\parallel_B}\phi_j\big|_{\bar{S}_B} F(\zeta_{j,B}), \tag{A.10}$$

where $\nabla_{\parallel_B}$ denotes the gradient along the tangential coordinates of $\bar{S}_B$, and $\zeta_{j,B}$ is the dimensionless coordinate in the direction of the normal $\hat{\boldsymbol{n}}_B$, as given in Equation 2.58. It follows that the velocity above satisfies the no-slip condition (2.57c) identically if $F(\zeta_{j,B}=0)=1$.

Now, the only remaining component of the rotational velocity to be determined is F. For that, we must solve the equation of motion Equation 2.57f with boundary condition $F(\zeta_{j,B}=0)=1$ and requiring the Stokes form, i.e., $\boldsymbol{U}_{j,B}$ must vanish rapidly far from the boundary, so $F\to 0$, as $\zeta_{j,B}\to\infty$. Hence the solution follows,

$$\begin{aligned}
\ell_j^2\nabla^2\boldsymbol{U}_{j,B} = \ell_j^2\left(\nabla_{\parallel_B}^2+\frac{\partial^2}{\partial n_B^2}\right)\boldsymbol{U}_{j,B} &= \left(\ell_j^2\nabla_{\parallel_B}^2+\frac{\partial^2}{\partial\zeta_{j,B}^2}\right)\boldsymbol{U}_{j,B} = -i\,\mathrm{sgn}(\omega_a)\boldsymbol{U}_{j,B}\\
\implies 0 = \left(\ell_j^2\nabla_{\parallel_B}^2+\frac{\partial^2}{\partial\zeta_{j,B}^2}+i\,\mathrm{sgn}(\omega_a)\right)\boldsymbol{U}_{j,B} &\approx \left(\frac{\partial^2}{\partial\zeta_{j,B}^2}+i\,\mathrm{sgn}(\omega_a)\right)\boldsymbol{U}_{j,B}\\
\implies \left(\frac{\partial^2}{\partial\zeta_{j,B}^2}+i\,\mathrm{sgn}(\omega_a)\right)F(\zeta_{j,B}) &= 0\\
\implies F(\zeta_{j,B}) = \mathrm{e}^{-\Delta\zeta_{j,B}},\ \text{for}\ \Delta = \frac{1-i\,\mathrm{sgn}(\omega_a)}{\sqrt{2}}&.
\end{aligned} \tag{A.11}$$

Here, in the first line, n_B stands for the dimensionful coordinate along the direction of the normal $\hat{\boldsymbol{n}}_B$ and related to $\zeta_{j,B}$ through Equation 2.58. In the second line, we only kept leading order terms of the small boundary layer thickness ℓ_j. With the function F above applied to (A.10), one recovers the leading order solution in Equation 2.59.

At the interface $\bar{I}$, two boundary layers effectively form, one in each fluid. From the boundary conditions (2.57d) and (2.57e), it is still reasonable to assume that the solenoidal velocity $\boldsymbol{U}_{j,I}$ is separable and depends on the dimensionless coordinates $\zeta_{j,I}$ though the same function $F(\zeta_{j,I})$ as $\boldsymbol{U}_{j,B}$ in Equation 2.59. Hence, we write the ansatz for the interfacial boundary layer velocity in each fluid as

$$\boldsymbol{U}_{j,I} = \boldsymbol{W}_j(\boldsymbol{x})F(\zeta_{j,I}), \tag{A.12}$$

where $\boldsymbol{W}_j$ are vector functions depending only on the horizontal coordinates of the interface $\boldsymbol{x}$ and with no vertical component, i.e., $\hat{\boldsymbol{z}}\cdot\boldsymbol{W}_j=0$. These functions can be found by solving the continuity conditions (2.57e) and (2.57g) at the interface, i.e.,

$$\nabla_{\boldsymbol{x}}\phi_1|_{z=0} + \boldsymbol{W}_1 = \nabla_{\boldsymbol{x}}\phi_2|_{z=0} + \boldsymbol{W}_2, \tag{A.13}$$

$$\rho_1\nu_1\frac{\partial}{\partial z}\left(\boldsymbol{W}_1(\boldsymbol{x})F(\zeta_{1,I})\right)_{z=0} = \rho_2\nu_2\frac{\partial}{\partial z}\left(\boldsymbol{W}_2(\boldsymbol{x})F(\zeta_{2,I})\right)_{z=0}. \tag{A.14}$$

The solutions of this system yield

$$\boldsymbol{W}_j(\boldsymbol{x}) = (-1)^j\frac{1}{\rho_j\sqrt{\nu_j}}\left(\frac{1}{\rho_1\sqrt{\nu_1}}+\frac{1}{\rho_2\sqrt{\nu_2}}\right)^{-1}\nabla_{\boldsymbol{x}}\left(\phi_1-\phi_2\right)_{z=0}, \tag{A.15}$$

which recovers Equation 2.60.

A.2 Variation of the kinematic boundary action

We consider the action defined in equation (2.16),

$$\begin{aligned} I_j &= \frac{(-1)^{j+1}}{2\Sigma}\iiint_{V_j}(\nabla\phi_j)^2\,\mathrm{d}\Sigma\,\mathrm{d}z - \frac{1}{\Sigma}\iint\frac{1}{|\nabla\Gamma|}\frac{\partial\xi}{\partial t}\,\phi_j|_{z=\xi}\,\mathrm{d}\Sigma \\ &= \frac{(-1)^{j+1}}{2\Sigma}\iint\mathrm{d}\Sigma(-1)^{j+1}\int_{h_j}^{\xi}\mathrm{d}z\;\left(\nabla\phi_j\right)^2 - \frac{1}{\Sigma}\iint\frac{1}{|\nabla\Gamma|}\frac{\partial\xi}{\partial t}\,\phi_j|_{z=\xi}\,\mathrm{d}\Sigma. \end{aligned} \tag{A.16}$$

The variation of the action with respect to ϕ_j is then given by

$$\begin{aligned} \delta I_j &= \frac{(-1)^{j+1}}{\Sigma}\iiint_{V_j}\mathrm{d}\Sigma\mathrm{d}z\;\nabla\phi_j\cdot\nabla(\delta\phi_j) - \frac{1}{\Sigma}\iint\mathrm{d}\Sigma\;\frac{1}{|\nabla\Gamma|}\frac{\partial\xi}{\partial t}\,\delta\phi_j|_{z=\xi} \\ &= \frac{(-1)^{j+1}}{\Sigma}\iiint_{V_j}\mathrm{d}\Sigma\mathrm{d}z\;\left[\nabla\cdot(\delta\phi_j\nabla\phi_j) - \delta\phi_j\nabla^2\phi_j\right] - \frac{1}{\Sigma}\iint\mathrm{d}\Sigma\;\frac{1}{|\nabla\Gamma|}\frac{\partial\xi}{\partial t}\,\delta\phi_j|_{z=\xi} \\ &= \frac{(-1)^{j}}{\Sigma}\iiint_{V_j}\mathrm{d}\Sigma\mathrm{d}z\;\left(\nabla^2\phi_j\right)\delta\phi_j + \frac{(-1)^{j+1}}{\Sigma}\oiint_{\partial V_j}\mathrm{d}S_{\hat{\boldsymbol{n}}}\;\left[(\hat{\boldsymbol{n}}\cdot\nabla\phi_j)\,\delta\phi_j\right]_{\partial V_j} \\ &\qquad - \frac{1}{\Sigma}\iint\mathrm{d}\Sigma\;\frac{1}{|\nabla\Gamma|}\frac{\partial\xi}{\partial t}\,\delta\phi_j|_{z=\xi}. \end{aligned} \tag{A.17}$$

The vector $\hat{\boldsymbol{n}}$ denotes all outwardly directed normal unit vectors of the boundaries ∂V_j of volume V_j of each fluid with $S_{\hat{\boldsymbol{n}}}$ their respective area element. We distinguish the boundaries into rigid ones, $\bar{S}$, and the moving interface at $\Gamma = 0$. For the latter, the outwardly directed normal $\hat{\boldsymbol{n}}_{\Gamma,j}$ of each fluid can be written as $\hat{\boldsymbol{n}}_{\Gamma,j} = (-1)^{j+1}\hat{\boldsymbol{n}}_\Gamma = (-1)^{j+1}\nabla\Gamma/|\nabla\Gamma|$, i.e., the interface's normal points upwards in fluid 1 and downwards in 2. Hence, the variation of the action results in

$$\begin{aligned} \delta I_j = \frac{(-1)^{j}}{\Sigma}\iiint_{V_j}\mathrm{d}\Sigma\mathrm{d}z\;\left(\nabla^2\phi_j\right)\delta\phi_j + \frac{(-1)^{j+1}}{\Sigma}\iint_{\bar{S}}\mathrm{d}S_{\hat{\boldsymbol{n}}}\;\left[(\hat{\boldsymbol{n}}\cdot\nabla\phi_j)\,\delta\phi_j\right]_{\overline{\partial V_j}} \\ + \frac{1}{\Sigma}\iint\mathrm{d}\Sigma\frac{1}{|\nabla\Gamma|}\left[\nabla\Gamma\cdot\nabla\phi_j - \frac{\partial\xi}{\partial t}\right]_{z=\xi}\delta\phi_j|_{z=\xi}. \end{aligned} \tag{A.18}$$

Hence, by imposing $\delta I_j = 0$, we see that the integrals in the equation above respectively recover Laplace's equation (2.3) for ϕ_j, the no-penetration conditions (2.4) at rigid boundaries, and the kinematic condition (2.7) at the interface.

A.3 Matrices, their integral coefficients and useful relations

By comparing equation (2.22) with (2.16), we can obtain the form of the $\mathbf{K}_j$ and $\mathbf{D}_j$ matrices. The matrix coefficients of $\mathbf{D}_j$, denoted $\mathrm{d}_{ab}^{(j)}$, are defined by

$$\mathrm{d}_{ab}^{(j)} = \frac{1}{\Sigma}\iint \mathrm{d}\Sigma\ \frac{\chi_a\chi_b}{\sqrt{1+|\nabla\xi|^2}}\frac{\cosh[k_b(\xi-h_j)]}{\cosh(k_b h_j)}. \tag{A.19}$$

This definition indicates that $\mathbf{D}_j$ is an asymmetric, dimensionless, square matrix. Under the assumption that $|\xi| \ll |h_j|$, we may right the hyperbolic cosines above as

$$\frac{\cosh[k_b(\xi-h_j)]}{\cosh(k_b h_j)} = 1 + (-1)^{j+1}T_{j,b}k_b\xi + \frac{1}{2}k_b^2\xi^2 + \cdots, \tag{A.20}$$

with $T_{j,a} \equiv \tanh(k_a|h_j|)$ and we used $h_j = (-1)^j|h_j|$. We must also account for the square root in the denominator of equation (A.19), which for small slopes of the interface, i.e., $|\nabla\xi| \ll 1$, reads

$$\frac{1}{\sqrt{1+|\nabla\xi|^2}} = 1 - \frac{1}{2}|\nabla\xi|^2 + \cdots = 1 - \frac{1}{2}\sum_{c,d}\nabla\chi_c\cdot\nabla\chi_d\xi_c\xi_d + \cdots. \tag{A.21}$$

From the equation above and (2.21), we see that

$$\mathrm{d}_{ab}^{(j)} = \delta_{ab} + (-1)^{j+1}k_b T_{j,b}\sum_c \mathbb{C}_{cab}\xi_c + \frac{1}{2}\sum_{c,d}\left(k_b^2\mathbb{C}_{cdab} - \mathbb{D}_{abcd}\right)\xi_c\xi_d + \cdots, \tag{A.22}$$

with

$$\mathbb{C}_{cab} = \frac{1}{\Sigma}\iint \mathrm{d}\Sigma\ \chi_c\chi_a\chi_b, \tag{A.23a}$$

$$\mathbb{C}_{cdab} = \frac{1}{\Sigma}\iint \mathrm{d}\Sigma\ \chi_c\chi_d\chi_a\chi_b, \tag{A.23b}$$

and

$$\mathbb{D}_{abcd} = \frac{1}{\Sigma}\iint \mathrm{d}\Sigma\ \chi_a\chi_b\nabla\chi_c\cdot\nabla\chi_d\ . \tag{A.23c}$$

Similarly, the matrix coefficients of $\mathbf{K}_j$, denoted $\mathrm{k}_{ab}^{(j)}$, are defined by

$$\mathrm{k}_{ab}^{(j)} = \frac{(-1)^{j+1}}{\Sigma}\iiint_{V_j}\mathrm{d}\Sigma\mathrm{d}z\ \nabla\psi_a\cdot\nabla\psi_b = \frac{1}{\Sigma}\int_{h_j}^{\xi}\mathrm{d}z\iint\mathrm{d}\Sigma\ \nabla\psi_a\cdot\nabla\psi_b. \tag{A.24}$$

It is worth noting that in fluid 2 the integration in z should span from ξ to h_2, hence requiring a negative sign, which cancels off the sign in equation (2.16). $\mathbf{K}_j$ is also a square matrix, but symmetric in its entries and with the dimension of inverse length.

By using the definitions in the main text, the equation above expands to

$$\mathrm{k}_{ab}^{(j)} = \frac{\operatorname{sech}(k_a|h_j|)}{\Sigma\cosh(k_b|h_j|)}\int_{h_j}^{\xi}\mathrm{d}z\iint\mathrm{d}\Sigma\,\Big\{\nabla\chi_a\cdot\nabla\chi_b\cosh[k_a(z-h_j)]\cosh[k_b(z-h_j)] + k_ak_b\chi_a\chi_b\sinh[k_a(z-h_j)]\sinh[k_b(z-h_j)]\Big\}, \tag{A.25}$$

and upon integration of the $z-$components, reduces to

$$\mathrm{k}_{ab}^{(j)} = \frac{1}{2\Sigma}\iint\mathrm{d}\Sigma\,\Big\{\mathcal{K}_{ab}^{(j,+)} + \mathcal{K}_{ab}^{(j,-)}\Big\}, \tag{A.26}$$

with

$$\mathcal{K}_{ab}^{(j,\pm)} = \frac{\operatorname{sech}(k_a|h_j|)}{\cosh(k_b|h_j|)}\frac{\sinh[(k_a\pm k_b)(\xi-h_j)]}{k_a\pm k_b}\Big\{\nabla\chi_a\cdot\nabla\chi_b\pm k_ak_b\chi_a\chi_b\Big\}. \tag{A.27}$$

And again, under the assumption that $|\xi|\ll|h_j|$, we find that

$$\frac{\sinh[(k_a\pm k_b)(\xi-h_j)]}{k_a\pm k_b} = (-1)^{j+1}\frac{\sinh[(k_a\pm k_b)|h_j|]}{k_a\pm k_b} + \xi\cosh[(k_a\pm k_b)|h_j|] + \frac{(-1)^{j+1}}{2}(k_a\pm k_b)\xi^2\sinh[(k_a\pm k_b)|h_j|]+\cdots, \tag{A.28}$$

which leads to

$$\begin{aligned}\mathcal{K}_{ab}^{(j,\pm)} &= (-1)^{j+1}\frac{T_{j,a}\pm T_{j,b}}{k_a\pm k_b}\Big\{\nabla\chi_a\cdot\nabla\chi_b\pm k_ak_b\chi_a\chi_b\Big\}\\ &\quad+(1\pm T_{j,a}T_{j,b})\sum_c\xi_c\Big\{\chi_c\nabla\chi_a\cdot\nabla\chi_b\pm k_ak_b\chi_c\chi_a\chi_b\Big\}\\ &+\frac{(-1)^{j+1}}{2}(k_a\pm k_b)(T_{j,a}\pm T_{j,b})\sum_{c,d}\xi_c\xi_d\Big\{\chi_c\chi_d\nabla\chi_a\cdot\nabla\chi_b\pm k_ak_b\chi_c\chi_d\chi_a\chi_b\Big\}+\cdots.\end{aligned} \tag{A.29}$$

By rearranging terms and defining new auxiliary integral coefficients, we find that the matrix coefficients $\mathrm{k}_{ab}^{(j)}$ up to second-order in ξ simplify to

$$\begin{aligned}\mathrm{k}_{ab}^{(j)} =&(-1)^{j+1}k_aT_{j,a}\delta_{ab}+\sum_c(\mathbb{D}_{cab}+k_aT_{j,a}k_bT_{j,b}\mathbb{C}_{cab})\xi_c\\ &+\frac{(-1)^{j+1}}{2}\sum_{c,d}\Big[(k_aT_{j,a}+k_bT_{j,b})\mathbb{D}_{cdab}+(k_a^2k_bT_{j,b}+k_b^2k_aT_{j,a})\mathbb{C}_{cdab}\Big]\xi_c\xi_d+\cdots,\end{aligned} \tag{A.30}$$

with

$$\mathbb{D}_{cab} = \frac{1}{\Sigma}\iint\mathrm{d}\Sigma\;\chi_c\nabla\chi_a\cdot\nabla\chi_b \text{ and } \mathbb{D}_{cdab} = \frac{1}{\Sigma}\iint\mathrm{d}\Sigma\;\chi_c\chi_d\nabla\chi_a\cdot\nabla\chi_b\,. \tag{A.31}$$

In deriving the equations above, one should note that the boundary condition on rigid boundaries (2.18) is required when setting boundary terms in the integrals to zero. Thus, if those conditions change, one should account for that when re-deriving the

form of the matrix elements $\mathrm{k}_{ab}^{(j)}$. We also note that matrix $\mathbf{K}_j$ in equation (A.30) agrees with the result from Miles [84] for the fluid $j = 1$, however, matrix $\mathbf{D}_j$ in equation (A.22) diverges from that of Miles by a term proportional to $\mathbb{D}_{abcd}$.

To obtain the $\mathbf{L}_j$ matrix coefficients, we must first compute the inverse of $\mathbf{K}_j$, which can be done by employing a matrix inversion identity (e.g., the Woodbury identity) or computing each term of the inverse perturbatively for a given small parameter. We opt for the latter and suppose that there exists a square matrix $\mathbf{F}_j$ such that $\mathbf{F}_j\mathbf{K}_j = \mathbf{I}$, where $\mathbf{I}$ is the identity matrix, and hence $\mathbf{F}_j \equiv (\mathbf{K}_j^{-1})^{\mathrm{T}}$. Similar to equation (A.30), we may write the matrix coefficient of $\mathbf{F}_j$, denoted $\mathrm{f}_{ab}^{(j)}$, as a series expansion in powers of ξ_a, as follows,

$$\mathrm{f}_{ab}^{(j)} = \mathrm{f}_{ab}^{(j,0)} + \sum_c \mathrm{f}_{abc}^{(j,1)}\xi_c + \sum_{c,d} \mathrm{f}_{abcd}^{(j,2)}\xi_c\xi_d + \cdots . \tag{A.32}$$

By solving the equality $\sum_c \mathrm{f}_{ac}^{(j)}\mathrm{k}_{cb}^{(j)} = \delta_{ab}$ up to second order in ξ_a, we find

$$\begin{aligned}
\mathrm{f}_{ab}^{(j)} = {}& \frac{(-1)^{j+1}}{k_a T_{j,a}}\delta_{ab} - \sum_c \left(\frac{\mathbb{D}_{cab}}{k_a T_{j,a} k_b T_{j,b}} + \mathbb{C}_{cab}\right)\xi_c \\
& + (-1)^j \frac{1}{2k_a T_{j,a} k_b T_{j,b}} \sum_{c,d} \Big[(k_a T_{j,a} + k_b T_{j,b})\mathbb{D}_{cdab} + (k_a^2 k_b T_{j,b} + k_b^2 k_a T_{j,a})\mathbb{C}_{cdab}\Big]\xi_c\xi_d \\
& - (-1)^j \sum_{c,d,e} \frac{(\mathbb{D}_{cae} + k_a T_{j,a} k_e T_{j,e}\mathbb{C}_{cae})(\mathbb{D}_{deb} + k_e T_{j,e} k_b T_{j,b}\mathbb{C}_{deb})}{k_a T_{j,a} k_b T_{j,b} k_e T_{j,e}}\xi_c\xi_d + \cdots .
\end{aligned} \tag{A.33}$$

Finally, the matrix elements $\mathrm{l}_{ab}^{(j)}$ can be found by computing $\mathrm{l}_{ab}^{(j)} = \sum_c \mathrm{f}_{ac}^{(j)}\mathrm{d}_{bc}^{(j)}$, which results in

$$\begin{aligned}
\mathrm{l}_{ab}^{(j)} = {}& \frac{(-1)^{j+1}}{k_a T_{j,a}}\delta_{ab} - \sum_c \frac{\mathbb{D}_{cab}}{k_a T_{j,a} k_b T_{j,b}}\xi_c \\
& + (-1)^{j+1} \sum_{c,d} \Bigg[-\frac{k_b}{2T_{j,b}}\mathbb{C}_{cdab} - \frac{k_a T_{j,a} + k_b T_{j,b}}{2k_a T_{j,a} k_b T_{j,b}}\mathbb{D}_{cdab} - \frac{1}{2k_a T_{j,a}}\mathbb{D}_{abcd} \\
& \qquad + \sum_e \frac{\mathbb{D}_{deb}}{k_a T_{j,a} k_b T_{j,b} k_e T_{j,e}}(\mathbb{D}_{cae} + k_a T_{j,a} k_e T_{j,e}\mathbb{C}_{cae})\Bigg]\xi_c\xi_d + \cdots .
\end{aligned} \tag{A.34}$$

The elements $\mathcal{A}_{ab}^{(j)}$ of matrix $\mathbf{A}_j$ may be computed in a similar way as $\mathbf{L}_j$ and $\mathbf{F}_j$ by defining it from the series expansion in powers of ξ_a, i.e.,

$$\mathcal{A}_{ab}^{(j)} = (-1)^{j+1}\mathcal{A}_{ab}^{(j,0)} + \sum_c \mathcal{A}_{cab}^{(j)}\xi_c + \frac{1}{2}(-1)^{j+1}\sum_{c,d} \mathcal{A}_{cdab}^{(j)}\xi_c\xi_d + \cdots , \tag{A.35}$$

with

$$\mathcal{A}_{ab}^{(j,0)} = \frac{1}{k_a T_{j,a}}\delta_{ab} , \tag{A.36a}$$

$$\mathcal{A}_{cab}^{(j)} = \mathbb{C}_{cab} - \frac{\mathbb{D}_{cab}}{k_a T_{j,a} k_b T_{j,b}} , \tag{A.36b}$$

$$\mathcal{A}_{cdab}^{(j)} = -\frac{k_a T_{j,a} + k_b T_{j,b}}{k_a T_{j,a} k_b T_{j,b}}\left(\mathbb{D}_{abcd} + \mathbb{D}_{cdab}\right) + 2\sum_e \frac{\mathbb{D}_{cae}\mathbb{D}_{deb}}{k_a T_{j,a} k_b T_{j,b} k_e T_{j,e}} . \tag{A.36c}$$

And the integral coefficient $\mathcal{B}_{abcd}$ is given by

$$\mathcal{B}_{abcd} = \frac{1}{\Sigma} \iint \mathrm{d}\Sigma \left(\nabla\chi_a \cdot \nabla\chi_b\right)\left(\nabla\chi_c \cdot \nabla\chi_d\right) \ . \tag{A.37}$$

A.4 Mathieu equation in the two-fluid system

In the setup of Chapter 3, the linear evolution of interfacial modes ξ_a in the presence of an external forcing of the form $F_0(t) = F_0\cos(\omega_\mathrm{d} t)$ is given by Equation 3.1, which we re-write as follows,

$$\ddot{\xi}_a + 2\gamma_a\dot{\xi}_a + A_{12}g_0\left(1 + \ell_c^2 k_a^2 - \frac{F_0}{g_0}\cos(\omega_\mathrm{d} t)\right) k_a \tanh(k_a h_0)\xi_a = 0, \tag{A.38}$$

where $A_{12} = (\rho_1 - \rho_2)/(\rho_1 + \rho_2)$ is the dimensionless Atwood number, γ_a is the linear damping of the mode, and $\ell_c = \sqrt{\sigma/(\rho_1 - \rho_2)g_0}$ is the capillary length. We now employ the following variable definitions

$$\omega_a^2 = A_{12}g_0(1 + \ell_c^2 k_a^2)k_a \tanh(k_a h_0), \tag{A.39a}$$
$$F_a^2 = A_{12}F_0 k_a \tanh(k_a h_0), \tag{A.39b}$$
$$\tau = \omega_\mathrm{d} t, \tag{A.39c}$$
$$c = \frac{2\gamma_a}{\omega_\mathrm{d}}, \tag{A.39d}$$
$$\delta = \left(\frac{\omega_a}{\omega_\mathrm{d}}\right)^2, \tag{A.39e}$$
$$\epsilon = \left(\frac{F_a}{\omega_\mathrm{d}}\right)^2. \tag{A.39f}$$

The set of dimensionless variables $(\tau, c, \delta, \epsilon)$ allows us to write Equation A.38 as in Kovacic et al. [112] (cf. equation (45) in [112]), i.e.,

$$\ddot{x} + c\dot{x} + (\delta + \epsilon\cos\tau)\, x = 0, \tag{A.40}$$

where the dots denote differentiation with respect to τ, and $x(\tau) \equiv \xi_a(\tau/\omega_\mathrm{d})$.

For the typical experimental parameters of Chapter 3, some of the dimensionless coefficients of the dominant mode $(m, n) = (4, 1)$ are small, $c_{4,1} \approx 0.06 \ll 1$ and $\epsilon_{4,1} \approx 0.09 \ll 1$. In such conditions, Kovacic et al. [112] solve the damped Mathieu equation perturbatively to find that the first instability band is centred around $\delta = 1/4$ and has transition boundaries to stable solutions at $\delta_\pm$ given by

$$\delta_\pm = \frac{1}{4} \pm \frac{1}{2}\sqrt{\epsilon^2 - c^2}. \tag{A.41}$$

The authors also compute the approximate value of the dimensionless Floquet coefficient $\bar{\lambda} = \lambda/\omega_\mathrm{d}$ of the slow time exponential envelope $\exp(\bar{\lambda}\epsilon\tau)$. The approximate dimensionful coefficient λ at the centre of the first resonance band ($\delta = 1/4$) is given by

$$\lambda \approx -\frac{\omega_\mathrm{d} c}{2} + \frac{\omega_\mathrm{d}\epsilon}{2} = \frac{F_a^2}{2\omega_\mathrm{d}} - \gamma_a. \tag{A.42}$$

Appendix B

Numerical Methods

B.1 Determination of Floquet coefficients and instability bands

The equation of motion for the two-fluid interfacial dynamics approximately reduces to the Mathieu equation for the linear evolution, which in its dimensionless form, reads

$$\ddot{x} + c\dot{x} + (\delta + \epsilon\cos\tau)\, x = 0. \tag{A.40}$$

We perform the stability analysis of our system by numerically solving the system of equations obtained from Floquet's theorem applied to the equation above. The forcing term is periodic with period 2π, and we look for unstable solutions of the Floquet form, as in Equation 3.3,

$$x(\tau) = \sum_n A_n \exp\left(\lambda\tau + i\frac{n}{2}\tau\right). \tag{B.1}$$

By applying this form to the Mathieu equation and balancing terms in the summation accordingly, one finds that Equation A.40 reduces to

$$\sum_n \mathrm{e}^{\left(\lambda\tau + i\frac{n}{2}\tau\right)} \left[M_n A_n + \frac{\epsilon}{2}A_{n-2} + \frac{\epsilon}{2}A_{n+2}\right] = 0, \tag{B.2a}$$

with

$$M_n \equiv \left(\lambda + \frac{in}{2}\right)^2 + c\left(\lambda + \frac{in}{2}\right) + \delta. \tag{B.2b}$$

In Equation B.2a, each term of the summation must vanish independently, resulting in a system of quadratic equations in λ for each n, as follows,

$$\lambda^2 A_n + (in + c)\lambda A_n + \left(\delta - \frac{n^2}{4} + \frac{icn}{2}\right) A_n + \frac{\epsilon}{2}(A_{n-2} + A_{n+2}) = 0. \tag{B.3}$$

We then define the column vector of coefficients $\boldsymbol{A}$ given by

$$\boldsymbol{A} = (\ldots, A_{-1}, A_0, A_1, \ldots)^T, \tag{B.4}$$

and represent the system of equations above in matrix notation as follows,

$$\left(\lambda^2\mathbf{I} + \lambda\mathbf{D} + \mathbf{K}\right)\boldsymbol{A} = 0, \tag{B.5a}$$

where $\mathbf{I}$ is the identity matrix, and $\mathbf{D}$ and $\mathbf{K}$ are diagonal and tridiagonal matrices, respectively, given by

$$\mathbf{D} = \mathrm{diag}\left(\dots,\ c-in,\dots,\ c-i,\ c,\ c+i,\dots,\ c+in,\dots\right), \tag{B.5b}$$

and

$$\mathbf{K} = \begin{pmatrix}
\ddots & \ddots & \ddots & \ddots & \ddots & \ddots & & & & & \\
 & 0 & \frac{\epsilon}{2} & 0 & \kappa_{-n} & 0 & \frac{\epsilon}{2} & 0 & & & \\
 & & \ddots & \ddots & \ddots & \ddots & \ddots & \ddots & \ddots & & \\
 & & & 0 & \frac{\epsilon}{2} & 0 & \kappa_0 & 0 & \frac{\epsilon}{2} & 0 & \\
 & & & & \ddots & \ddots & \ddots & \ddots & \ddots & \ddots & \ddots \\
 & & & & & 0 & \frac{\epsilon}{2} & 0 & \kappa_n & 0 & \frac{\epsilon}{2} \\
 & & & & & & \ddots & \ddots & \ddots & \ddots & \ddots
\end{pmatrix}, \tag{B.5c}$$

with $\kappa_n \equiv \delta - \frac{n^2}{4} + \frac{icn}{2}$. When truncated for numerical implementation at an integer N such that $|n| \leq N$, $\mathbf{D}$ and $\mathbf{K}$ are square matrices with $(2N+1)\times(2N+1)$ elements.

The quadratic eigenvalue problem in Equation B.5a can be further simplified for numerical convenience by noting that it can be written as a generalised eigenvalue problem, as follows,

$$\begin{pmatrix} \mathbf{0} & \mathbf{I} \\ \mathbf{K} & \mathbf{D} \end{pmatrix} \begin{pmatrix} \boldsymbol{A} \\ \lambda \boldsymbol{A} \end{pmatrix} = \lambda \begin{pmatrix} \mathbf{I} & \mathbf{0} \\ \mathbf{0} & -\mathbf{I} \end{pmatrix} \begin{pmatrix} \boldsymbol{A} \\ \lambda \boldsymbol{A} \end{pmatrix}. \tag{B.6}$$

Both block matrices on each side have $(4N+2)\times(4N+2)$ elements when the numerical truncation is implemented, and we denote the one on the right-hand side as $\mathbf{B}$. The latter is an idempotent matrix, and hence its inverse is given by

$$\mathbf{B} \equiv \begin{pmatrix} \mathbf{I} & \mathbf{0} \\ \mathbf{0} & -\mathbf{I} \end{pmatrix} = \mathbf{B}^{-1}, \tag{B.7}$$

and the generalised eigenvalue problem reduces to a simple one, as follows,

$$\begin{pmatrix} \mathbf{0} & \mathbf{I} \\ -\mathbf{K} & -\mathbf{D} \end{pmatrix} \begin{pmatrix} \boldsymbol{A} \\ \lambda \boldsymbol{A} \end{pmatrix} = \lambda \begin{pmatrix} \boldsymbol{A} \\ \lambda \boldsymbol{A} \end{pmatrix}. \tag{B.8}$$

The system in Equation B.8 can be readily diagonalised with any standard numerical package, such as NumPy or Scipy. Numerical performance is improved by employing any package optimised for sparse matrices, such as the block matrix above. The real part of the eigenvalues λ in Equation B.8 determines the unstable growth of the mode considered in obtaining Equation A.40. We recall that the dimensionless coefficients $c,\ \delta$ and ϵ are, in fact, mode-dependent. The truncation error is rapidly suppressed for $N > 10$, and by looping over different values of $c,\ \delta$ and ϵ, one can obtain a map of Floquet coefficients λ.

The instability bands are traced by transition curves where the unstable evolution becomes stable, that is when $\lambda = 0$. For fixed values of damping c and forcing amplitude ϵ, we can determine the stiffness parameters δ for which Equation B.3 is satisfied with $\lambda = 0$. In other words, we write another eigenvalue problem as follows,

$$\mathbf{K}|_{\delta=0}\, \boldsymbol{A} = -\delta \boldsymbol{A}. \tag{B.9}$$

Another option is to solve a generalised eigenvalue problem by fixing δ instead and determining ϵ, i.e.,

$$\mathbf{K}|_{\epsilon=0}\, \boldsymbol{A} = -\epsilon\, \mathbf{K}|_{\epsilon=1,\delta=0} \boldsymbol{A}. \tag{B.10}$$

By solving any of these systems, one can trace the instability transition curves shown in Chapter 3. The matrices above have $(2N+1)^2$ elements, four times less than the block matrices for the Floquet coefficients λ.

B.2 Simulations of non-linear evolution

For the numerical simulations of the non-linear evolution in Chapter 3 given by

$$\ddot{\xi}_a + (2\gamma_a + \tilde{\gamma}_a[\xi])\, \dot{\xi}_a + \left(\omega_a^2(t) + \tilde{\delta}_a[\xi]\right) \xi_a = \eta_a(t) + \tilde{\eta}_a[\xi], \tag{3.9}$$

we employed a fourth-order Runge-Kutta (RK) step solver. In the following discussion, we drop the sub-index a denoting the mode label and define the solution vector as

$$\boldsymbol{X} \equiv \begin{pmatrix} \xi_a \\ \dot{\xi}_a \end{pmatrix}. \tag{B.11}$$

The non-linear terms will be denoted as implicit functions of the vector X and are given by the appropriate formulas in Chapter 3. The system above can be written in matrix notation as follows

$$\frac{\mathrm{d}\boldsymbol{X}}{\mathrm{d}t} = \begin{pmatrix} 1 & 0 \\ -\left(\omega^2(t) + \tilde{\delta}[\boldsymbol{X}]\right) & -(2\gamma + \tilde{\gamma}[\boldsymbol{X}]) \end{pmatrix} \boldsymbol{X} + \begin{pmatrix} 0 \\ \eta(t) + \tilde{\eta}[\boldsymbol{X}] \end{pmatrix} \equiv \boldsymbol{f}\left(\boldsymbol{X}(t), t\right). \tag{B.12}$$

The vector function $\boldsymbol{f}$ is the input for the numerical solver, and the initial value at $t = 0$ of the solution $\boldsymbol{X}$ is set to $\mathbf{0}$. The evolution is triggered by the stochastic noise term $\eta(t)$, which we sample from a central distribution estimated from the experimental data, as explained in Chapter 3.

We consider the numerical solver evolves from an initial time $t = 0$ with N_t steps equally spaced in time with duration h each. We then use the fourth-order RK method to compute the slope approximations up to the fourth order at some time t_0, as follows,

$$\begin{cases} \boldsymbol{k}_1 = \boldsymbol{f}\left(\boldsymbol{X}(t_0), t_0\right), \\ \boldsymbol{k}_2 = \boldsymbol{f}\left(\boldsymbol{X}(t_0) + \frac{h}{2}\boldsymbol{k}_1, t_0 + \frac{h}{2}\right), \\ \boldsymbol{k}_3 = \boldsymbol{f}\left(\boldsymbol{X}(t_0) + \frac{h}{2}\boldsymbol{k}_2, t_0 + \frac{h}{2}\right), \\ \boldsymbol{k}_4 = \boldsymbol{f}\left(\boldsymbol{X}(t_0) + h\boldsymbol{k}_3, t_0 + h\right). \end{cases} \tag{B.13}$$

We then estimate the solution at $t_0 + h$ by using the weighted average of the slopes,

given by

$$\boldsymbol{k}_0 = \frac{1}{6}\left(\boldsymbol{k}_1 + 2\boldsymbol{k}_2 + 2\boldsymbol{k}_3 + \boldsymbol{k}_4\right). \tag{B.14}$$

Hence, the approximate solution after the step is

$$\boldsymbol{X}(t_0 + h) \approx \boldsymbol{X}(t_0) + \boldsymbol{k}_0 h. \tag{B.15}$$

We stress again that, at each RK step, the random stochastic function η is sampled, effectively sourcing the evolution despite the initial being identically zero. The simulations for the primary mode only have contributions from the stochastic term as $\tilde{\eta}$ vanishes. On the other hand, the secondary mode is sourced both by the random noise and by the evolution of the primary appearing through $\tilde{\eta}$.

Bibliography

[1] Barroso, V. S., Bunney, C. R. D., and Weinfurtner, S. Non-linear effective field theory simulators in two-fluid interfaces. *Journal of Physics: Conference Series*, 2531(1):012003, June 2023.

[2] Barroso, V. S., Geelmuyden, A., Fifer, Z., Erne, S., Avgoustidis, A., Hill, R. J. A., and Weinfurtner, S. Primary thermalisation mechanism of Early Universe observed from Faraday-wave scattering on liquid-liquid interfaces. *arXiv e-prints*, art. arXiv:2207.02199, July 2022.

[3] Barroso, V. S., Geelmuyden, A., Ajithkumar, S. C., Kent, A. J., and Weinfurtner, S. Multiplexed digital holography for fluid surface profilometry. *Applied Optics*, 62(27):7175–7184, September 2023.

[4] Bunney, C. R. D., Biermann, S., Barroso, V. S., Geelmuyden, A., Gooding, C., Ithier, G., Rojas, X., Louko, J., and Weinfurtner, S. Third sound detectors in accelerated motion. *arXiv e-prints*, art. arXiv:2302.12023, February 2023.

[5] Birrell, N. D. and Davies, P. C. W. *Quantum Fields in Curved Space*. Cambridge Monographs on Mathematical Physics. Cambridge University Press, February 1982. ISBN 9780521278584.

[6] Howl, R., Hackermüller, L., Bruschi, D. E., and Fuentes, I. Gravity in the quantum lab. *Advances in Physics X*, 3(1):1383184, January 2018.

[7] Barceló, C., Liberati, S., and Visser, M. Analogue Gravity. *Living Reviews in Relativity*, 8(1):12, December 2005.

[8] Faccio, D., Belgiorno, F., Cacciatori, S., Gorini, V., Liberati, S., and Moschella, U. *Analogue gravity phenomenology : analogue spacetimes and horizons, from theory to experiment*, volume 870. Springer International Publishing, 2013. ISBN 978-3-319-00265-1.

[9] Jacquet, M. J., Weinfurtner, S., and König, F. The next generation of analogue gravity experiments. *Philosophical Transactions of the Royal Society of London Series A*, 378(2177):20190239, August 2020.

[10] Unruh, W. G. Experimental black-hole evaporation? *Physical Review Letters*, 46(21):1351–1353, May 1981.

[11] Hawking, S. W. Black hole explosions? *Nature*, 248(5443):30–31, March 1974.

[12] Hawking, S. W. Particle creation by black holes. *Communications in Mathematical Physics*, 43(3):199–220, August 1975.

[13] Field, G. E. The latest frontier in analogue gravity: New roles for analogue experiments. *philsci e-prints*, art. philsci:20365, June 2021.

[14] Almeida, C. R. and Jacquet, M. J. Analogue gravity and the Hawking effect: historical perspective and literature review. *arXiv e-prints*, art. arXiv:2212.08838, December 2022.

[15] White, F. M. *Fluid Mechanics*. McGraw-Hill International Editions. WCB/McGraw-Hill, December 1999. ISBN 9780070697164.

[16] Schützhold, R. and Unruh, W. G. Gravity wave analogues of black holes. *Physical Review D*, 66(4):044019, August 2002.

[17] Novello, M., Visser, M., and Volovik, G. *Artificial Black Holes*. World Scientific, October 2002. ISBN 9789810248079.

[18] Volovik, G. E. and Press, O. U. *The Universe in a Helium Droplet*. International Series of Monographs on Physics. Clarendon Press, February 2003. ISBN 9780198507826.

[19] Visser, M. Essential and Inessential Features of Hawking Radiation. *International Journal of Modern Physics D*, 12(4):649–661, January 2003.

[20] Wilson, C. M., Johansson, G., Pourkabirian, A., Simoen, M., Johansson, J. R., Duty, T., Nori, F., and Delsing, P. Observation of the dynamical Casimir effect in a superconducting circuit. *Nature*, 479(7373):376–379, November 2011.

[21] Jaskula, J. C., Partridge, G. B., Bonneau, M., Lopes, R., Ruaudel, J., Boiron, D., and Westbrook, C. I. Acoustic Analog to the Dynamical Casimir Effect in a Bose-Einstein Condensate. *Physical Review Letters*, 109(22):220401, November 2012.

[22] Hung, C.-L., Gurarie, V., and Chin, C. From Cosmology to Cold Atoms: Observation of Sakharov Oscillations in a Quenched Atomic Superfluid. *Science*, 341 (6151):1213–1215, September 2013.

[23] Philbin, T. G., Kuklewicz, C., Robertson, S., Hill, S., König, F., and Leonhardt, U. Fiber-optical analog of the event horizon. *Science*, 319(5868):1367–1370, March 2008.

[24] Rousseaux, G., Mathis, C., Mäissa, P., Philbin, T. G., and Leonhardt, U. Observation of negative-frequency waves in a water tank: a classical analogue to the hawking effect? *New Journal of Physics*, 10(5):053015, May 2008.

[25] Weinfurtner, S., Tedford, E. W., Penrice, M. C., Unruh, W. G., and Lawrence, G. A. Measurement of stimulated hawking emission in an analogue system. *Physical Review Letters*, 106(2):021302, January 2011.

[26] Belgiorno, F., Cacciatori, S. L., Clerici, M., Gorini, V., Ortenzi, G., Rizzi, L., Rubino, E., Sala, V. G., and Faccio, D. Hawking radiation from ultrashort laser pulse filaments. *Physical Review Letters*, 105(20):203901, November 2010.

[27] Lahav, O., Itah, A., Blumkin, A., Gordon, C., Rinott, S., Zayats, A., and Steinhauer, J. Realization of a sonic black hole analog in a bose-einstein condensate. *Physical Review Letters*, 105(24):240401, December 2010.

[28] Steinhauer, J. Observation of quantum hawking radiation and its entanglement in an analogue black hole. *Nature Physics*, 12(10):959–965, October 2016.

[29] Nguyen, H. S., Gerace, D., Carusotto, I., Sanvitto, D., Galopin, E., Lemaître, A., Sagnes, I., Bloch, J., and Amo, A. Acoustic black hole in a stationary hydrodynamic flow of microcavity polaritons. *Physical Review Letters*, 114(3): 036402, January 2015.

[30] Euvé, L. P., Michel, F., Parentani, R., Philbin, T. G., and Rousseaux, G. Observation of noise correlated by the hawking effect in a water tank. *Physical Review Letters*, 117(12):1–11, September 2016.

[31] Choudhary, A. and König, F. Efficient frequency shifting of dispersive waves at solitons. *Optics Express*, 20(5):5538, February 2012.

[32] Rubino, E., McLenaghan, J., Kehr, S. C., Belgiorno, F., Townsend, D., Rohr, S., Kuklewicz, C. E., Leonhardt, U., König, F., and Faccio, D. Negative-frequency resonant radiation. *Physical Review Letters*, 108(25):253901, June 2012.

[33] McLenaghan, J. and König, F. Few-cycle fiber pulse compression and evolution of negative resonant radiation. *New Journal of Physics*, 16(6):063017, June 2014.

[34] Muñoz de Nova, J. R., Golubkov, K., Kolobov, V. I., and Steinhauer, J. Observation of thermal hawking radiation and its temperature in an analogue black hole. *Nature*, 569(7758):688–691, May 2019.

[35] Človečko, M., GaŽo, E., Kupka, M., and Skyba, P. Magnonic analog of black- and white-hole horizons in superfluid he 3 -b. *Physical Review Letters*, 123(16): 161302, October 2019.

[36] Drori, J., Rosenberg, Y., Bermudez, D., Silberberg, Y., and Leonhardt, U. Observation of stimulated hawking radiation in an optical analogue. *Physical Review Letters*, 122(1):010404, January 2019.

[37] Petty, J. and König, F. Optical analogue gravity physics: resonant radiation. *Philosophical Transactions of the Royal Society of London Series A*, 378(2177): 20190231, August 2020.

[38] Rousseaux, G. and Kellay, H. Classical hydrodynamics for analogue space-times: open channel flows and thin films. *Philosophical Transactions of the Royal Society of London Series A*, 378(2177):20190233, August 2020.

[39] Kolobov, V. I., Golubkov, K., Muñoz de Nova, J. R., and Steinhauer, J. Observation of stationary spontaneous Hawking radiation and the time evolution of an analogue black hole. *Nature Physics*, 17(3):362–367, January 2021.

[40] Torres, T., Patrick, S., Coutant, A., Richartz, M., Tedford, E. W., and Weinfurtner, S. Rotational superradiant scattering in a vortex flow. *Nature Physics*, 13(9):833–836, September 2017.

[41] Zel'Dovich, Y. B. Generation of Waves by a Rotating Body. *Soviet Journal of Experimental and Theoretical Physics Letters*, 14:180, August 1971.

[42] Zel'Dovich, Y. B. Amplification of Cylindrical Electromagnetic Waves Reflected from a Rotating Body. *Soviet Journal of Experimental and Theoretical Physics*, 35:1085, January 1972.

[43] Brito, R., Cardoso, V., and Pani, P. *Superradiance*, volume 906 of *Lecture Notes in Physics*. Springer International Publishing, Cham, 2015. ISBN 978-3-319-18999-4.

[44] Braidotti, M. C., Prizia, R., Maitland, C., Marino, F., Prain, A., Starshynov, I., Westerberg, N., Wright, E. M., and Faccio, D. Measurement of Penrose Superradiance in a Photon Superfluid. *Physical Review Letters*, 128(1):13901, January 2022.

[45] Vocke, D., Maitland, C., Prain, A., Wilson, K. E., Biancalana, F., Wright, E. M., Marino, F., and Faccio, D. Rotating black hole geometries in a two-dimensional photon superfluid. *Optica*, 5(9):1099, September 2018.

[46] Solnyshkov, D. D., Leblanc, C., Koniakhin, S. V., Bleu, O., and Malpuech, G. Quantum analogue of a kerr black hole and the penrose effect in a bose-einstein condensate. *Physical Review B*, 99:214511, June 2019.

[47] Torres, T., Patrick, S., Richartz, M., and Weinfurtner, S. Quasinormal mode oscillations in an analogue black hole experiment. *Physical Review Letters*, 125 (1):011301, July 2020.

[48] Eckel, S., Kumar, A., Jacobson, T., Spielman, I. B., and Campbell, G. K. A Rapidly Expanding Bose-Einstein Condensate: An Expanding Universe in the Lab. *Physical Review X*, 8(2):021021, April 2018.

[49] Wittemer, M., Hakelberg, F., Kiefer, P., Schröder, J.-P., Fey, C., Schützhold, R., Warring, U., and Schaetz, T. Phonon Pair Creation by Inflating Quantum Fluctuations in an Ion Trap. *Physical Review Letters*, 123(18):180502, November 2019.

[50] Chen, C.-A., Khlebnikov, S., and Hung, C.-L. Observation of Quasiparticle Pair Production and Quantum Entanglement in Atomic Quantum Gases Quenched to an Attractive Interaction. *Physical Review Letters*, 127(6):060404, August 2021.

[51] Steinhauer, J., Abuzarli, M., Aladjidi, T., Bienaimé, T., Piekarski, C., Liu, W., Giacobino, E., Bramati, A., and Glorieux, Q. Analogue cosmological particle creation in an ultracold quantum fluid of light. *Nature Communications*, 13: 2890, May 2022.

[52] Banik, S., Galan, M. G., Sosa-Martinez, H., Anderson, M., Eckel, S., Spielman, I. B., and Campbell, G. K. Accurate Determination of Hubble Attenuation and Amplification in Expanding and Contracting Cold-Atom Universes. *Physical Review Letters*, 128(9):090401, March 2022.

[53] Viermann, C., Sparn, M., Liebster, N., Hans, M., Kath, E., Parra-López, Á., Tolosa-Simeón, M., Sánchez-Kuntz, N., Haas, T., Strobel, H., Floerchinger, S., and Oberthaler, M. K. Quantum field simulator for dynamics in curved spacetime. *Nature*, 611(7935):260–264, November 2022.

[54] Dardashti, R., Hartmann, S., Thébault, K., and Winsberg, E. Hawking radiation and analogue experiments: A Bayesian analysis. *Studies in the History and Philosophy of Modern Physics*, 67:1–11, August 2019.

[55] Evans, P. W. and Thébault, K. P. Y. On the limits of experimental knowledge. *Philosophical Transactions of the Royal Society of London Series A*, 378(2177): 20190235, August 2020.

[56] Crowther, K., Linnemann, N. S., and Wüthrich, C. What we cannot learn from analogue experiments. *Synthese*, 198:3701–3726, 2021.

[57] Weinfurtner, S. Superfluid system hosts early-Universe dynamics. *Nature*, 611 (7935):238–239, November 2022.

[58] Bain, J. 224 Effective Field Theories. In *The Oxford Handbook of Philosophy of Physics*. Oxford University Press, 02 2013. ISBN 9780195392043.

[59] Petrov, A. A. and Blechman, A. E. *Effective Field Theories*. WORLD SCIENTIFIC, 2016.

[60] Dubovsky, S., Hui, L., Nicolis, A., and Son, D. T. Effective field theory for hydrodynamics: thermodynamics, and the derivative expansion. *Physical Review D*, 85:085029, 2012.

[61] Crossley, M., Glorioso, P., and Liu, H. Effective field theory of dissipative fluids. *JHEP*, 09:095, 2017.

[62] Torres, T. Estimate of the superradiance spectrum in dispersive media. *Philosophical Transactions of the Royal Society of London Series A*, 378(2177): 20190236, 2020.

[63] Patrick, S. and Weinfurtner, S. Superradiance in dispersive black hole analogues. *Physical Review D*, 102(8):084041, 2020.

[64] Patrick, S. Rotational superradiance with Bogoliubov dispersion. *Classical and Quantum Gravity*, 38(9):095010, May 2021.

[65] Bain, J. The emergence of spacetime in condensed matter approaches to quantum gravity. *Studies in History and Philosophy of Science Part B: Studies in History and Philosophy of Modern Physics*, 44(3):338–345, August 2013.

[66] Cirac, J. I. and Zoller, P. Goals and opportunities in quantum simulation. *Nature Physics*, 8(4):264–266, April 2012.

[67] Bloch, I., Dalibard, J., and Nascimbène, S. Quantum simulations with ultracold quantum gases. *Nature Physics*, 8(4):267–276, April 2012.

[68] Schweigler, T., Kasper, V., Erne, S., Mazets, I., Rauer, B., Cataldini, F., Langen, T., Gasenzer, T., Berges, J., and Schmiedmayer, J. Experimental characterization of a quantum many-body system via higher-order correlations. *Nature*, 545 (7654):323–326, May 2017.

[69] Zache, T. V., Schweigler, T., Erne, S., Schmiedmayer, J., and Berges, J. Extracting the field theory description of a quantum many-body system from experimental data. *Physical Review X*, 10(1):11020, January 2020.

[70] Prüfer, M., Kunkel, P., Strobel, H., Lannig, S., Linnemann, D., Schmied, C.-M., Berges, J., Gasenzer, T., and Oberthaler, M. K. Observation of universal dynamics in a spinor Bose gas far from equilibrium. *Nature*, 563(7730):217–220, November 2018.

[71] Erne, S., Bücker, R., Gasenzer, T., Berges, J., and Schmiedmayer, J. Universal dynamics in an isolated one-dimensional bose gas far from equilibrium. *Nature*, 563(7730):225–229, November 2018.

[72] Glidden, J. A. P., Eigen, C., Dogra, L. H., Hilker, T. A., Smith, R. P., and Hadzibabic, Z. Bidirectional dynamic scaling in an isolated Bose gas far from equilibrium. *Nature Physics*, 17(4):457–461, January 2021.

[73] Gałka, M., Christodoulou, P., Gazo, M., Karailiev, A., Dogra, N., Schmitt, J., and Hadzibabic, Z. Emergence of isotropy and dynamic scaling in 2d wave turbulence in a homogeneous bose gas. *Physical Review Letters*, 129:190402, November 2022.

[74] Prüfer, M., Zache, T. V., Kunkel, P., Lannig, S., Bonnin, A., Strobel, H., Berges, J., and Oberthaler, M. K. Experimental extraction of the quantum effective action for a non-equilibrium many-body system. *Nature Physics*, 16 (10):1012–1016, October 2020.

[75] Aguirre, A. Eternal Inflation, past and future. *arXiv e-prints*, art. arXiv:0712.0571, December 2007.

[76] Fialko, O., Opanchuk, B., Sidorov, A. I., Drummond, P. D., and Brand, J. Fate of the false vacuum: Towards realization with ultra-cold atoms. *Europhysics Letters*, 110(5):56001, June 2015.

[77] Braden, J., Johnson, M. C., Peiris, H. V., and Weinfurtner, S. Towards the cold atom analog false vacuum. *Journal of High Energy Physics*, 2018(7):14, July 2018.

[78] Švančara, P., Smaniotto, P., Solidoro, L., MacDonald, J. F., Patrick, S., Gregory, R., Barenghi, C. F., and Weinfurtner, S. Exploring the Quantum-to-Classical Vortex Flow: Quantum Field Theory Dynamics on Rotating Curved Spacetimes. *arXiv e-prints*, art. arXiv:2308.10773, August 2023.

[79] Fifer, Z., Torres, T., Erne, S., Avgoustidis, A., Hill, R. J., and Weinfurtner, S. Analog cosmology with two-fluid systems in a strong gradient magnetic field. *Physical Review E*, 99(3):031101, March 2019.

[80] Berges, J. Introduction to nonequilibrium quantum field theory. *AIP Conference Proceedings*, 739(1):3–62, December 2004.

[81] Gooding, C., Biermann, S., Erne, S., Louko, J., Unruh, W. G., Schmiedmayer, J., and Weinfurtner, S. Interferometric unruh detectors for bose-einstein condensates. *Physical Review Letters*, 125:213603, July 2020.

[82] Unruh, W. G. Notes on black-hole evaporation. *Physical Review D*, 14(4): 870–892, August 1976.

[83] D Bunney, C. R. and Louko, J. Circular motion analogue Unruh effect in a 2+1 thermal bath: robbing from the rich and giving to the poor. *Classical and Quantum Gravity*, 40(15):155001, August 2023.

[84] Miles, J. W. Nonlinear surface waves in closed basins. *Journal of Fluid Mechanics*, 75(3):419–448, June 1976.

[85] Miles, J. W. Nonlinear faraday resonance. *Journal of Fluid Mechanics*, 146: 285–302, September 1984.

[86] Case, K. M. and Parkinson, W. C. Damping of surface waves in an incompressible liquid. *Journal of Fluid Mechanics*, 2(2):172–184, March 1957.

[87] Herreman, W., Nore, C., Guermond, J.-L., Cappanera, L., Weber, N., and Horstmann, G. M. Perturbation theory for metal pad roll instability in cylindrical reduction cells. *Journal of Fluid Mechanics*, 878:598–646, November 2019.

[88] Horstmann, G. M., Herreman, W., and Weier, T. Linear damped interfacial wave theory for an orbitally shaken upright circular cylinder. *Journal of Fluid Mechanics*, 891:A22, May 2020.

[89] Wildeman, S. Real-time quantitative schlieren imaging by fast fourier demodulation of a checkered backdrop. *Experiments in Fluids*, 59(6):97, June 2018.

[90] Landau, L. D. and Lifshitz, E. M. *Fluid Mechanics: Course of Theoretical Physics, Volume 6*. Elsevier Science, 2013. ISBN 9781483161044.

[91] Rousseaux, G., Mäissa, P., Mathis, C., Coullet, P., Philbin, T. G., and Leonhardt, U. Horizon effects with surface waves on moving water. *New Journal of Physics*, 12:095018, September 2010.

[92] Patrick, S., Coutant, A., Richartz, M., and Weinfurtner, S. Black hole quasibound states from a draining bathtub vortex flow. *Physical Review Letters*, 121 (6):061101, August 2018.

[93] Torres, T., Coutant, A., Dolan, S., and Weinfurtner, S. Waves on a vortex: Rays, rings and resonances. *Journal of Fluid Mechanics*, 857:291–311, December 2018.

[94] Israelachvili, J. N. *Intermolecular and Surface Forces*. Intermolecular and Surface Forces. Elsevier Science, 2011. ISBN 9780123919335.

[95] Flekkøy, E. G. and Rothman, D. H. Fluctuating fluid interfaces. *Physical Review Letters*, 75(2):260–263, July 1995.

[96] Flekkøy, E. G. and Rothman, D. H. Fluctuating hydrodynamic interfaces: Theory and simulation. *Physical Review E*, 53(2):1622–1643, February 1996.

[97] de Gennes, P. G., Brochard-Wyart, F., and Quere, D. *Capillarity and Wetting Phenomena: Drops, Bubbles, Pearls, Waves*, volume 41. Springer New York, May 2003. ISBN 9780387005928.

[98] Landau, L. Theory of the superfluidity of helium ii. *Physical Review*, 60(4): 356–358, August 1941.

[99] Donnelly, R. J. and Barenghi, C. F. The observed properties of liquid helium at the saturated vapor pressure. *J. Phys. Chem. Ref. Data*, 27:1217, November 1998.

[100] Batchelor, G. K. *An Introduction to Fluid Dynamics*, volume 76 of *Cambridge Mathematical Library*. Cambridge University Press, October 1967. ISBN 9780521663960.

[101] Serrin, J. Mathematical principles of classical fluid mechanics. *Fluid Dynamics I/Strömungsmechanik I*, 3:125–263, 1959.

[102] Prandtl, L. Uber flüssigkeitsbewegung bei sehr kleiner reibung. chronik des iii. In Krazer, A., editor, *Internationalen Mathematiker-Kongresses in Heidelberg 1904*, 1905.

[103] Drazin, P. G., Riley, N., and Society, L. M. *The Navier-Stokes Equations: A Classification of Flows and Exact Solutions*. Number v. 13 in London Mathematical Society Lecture Note Series. Cambridge University Press, June 2006. ISBN 9780521681629.

[104] Day, M. A. The no-slip condition of fluid dynamics. *Erkenntnis*, 33(3):285–296, November 1990.

[105] Lauga, E., Brenner, M., and Stone, H. Microfluidics: The no-slip boundary condition. In *Springer Handbooks*, pages 1219–1240. Springer, January 2007.

[106] Kumar, K. and Tuckerman, L. S. Parametric instability of the interface between two fluids. *Journal of Fluid Mechanics*, 279:49–68, November 1994.

[107] Luke, J. C. A variational principle for a fluid with a free surface. *Journal of Fluid Mechanics*, 27(2):395–397, February 1967.

[108] Lamb, H. *Hydrodynamics*. Dover Books on Physics. Dover publications, May 1945. ISBN 9780486602561.

[109] Peskin, M. E. and Schroeder, D. V. *An Introduction to Quantum Field Theory*. Advanced book classics. Avalon Publishing, May 1995. ISBN 9780201503975.

[110] Hawking, S. W. and Ellis, G. F. R. *The Large Scale Structure of Space-Time*. Cambridge Monographs on Mathematical Physics. Cambridge University Press, May 1973. ISBN 9780521099066.

[111] Weinfurtner, S., Jain, P., Visser, M., and Gardiner, C. W. Cosmological particle production in emergent rainbow spacetimes. *Classical and Quantum Gravity*, 26 (6):065012, February 2009.

[112] Kovacic, I., Rand, R., and Sah, S. M. Mathieu's equation and its generalizations: Overview of stability charts and their features. *Applied Mechanics Reviews*, 70 (2):020802, March 2018.

[113] Magnus, W. and Winkler, S. *Hill's Equation*. Dover phoenix editions. Dover Publications, 2013. ISBN 9780486150291.

[114] Faraday, M. Xvii. on a peculiar class of acoustical figures; and on certain forms assumed by groups of particles upon vibrating elastic surfaces. *Philosophical Transactions of the Royal Society of London*, 121:299–340, June 1831.

[115] Gazzola, F. Brief history of suspension bridges. *Modeling, Simulation and Applications*, 15:1–41, 2015.

[116] Biran, A. and López-Pulido, R. Chapter 9 - stability in waves. In Biran, A. and López-Pulido, R., editors, *Ship Hydrostatics and Stability (Second Edition)*, pages 221–241. Butterworth-Heinemann, Oxford, second edition edition, 2014. ISBN 978-0-08-098287-8.

[117] Kofman, L., Linde, A., and Starobinsky, A. A. Reheating after inflation. *Physical Review Letters*, 73(24):3195–3198, December 1994.

[118] Shtanov, Y., Traschen, J. H., and Brandenberger, R. H. Universe reheating after inflation. *Physical Review D*, 51:5438–5455, May 1995.

[119] Mukhanov, V. *Physical foundations of cosmology*. Cambridge University Press, January 2005. ISBN 9780511790553.

[120] Baumann, D. *The Physics of Inflation*. CreateSpace Independent Publishing Platform, 2015. ISBN 9781506124629.

[121] Gardiner, C. W. *Handbook of stochastic methods for physics, chemistry and the natural sciences*, volume 13 of *Springer Series in Synergetics*. Springer-Verlag, Berlin, third edition, 2004. ISBN 3-540-20882-8.

[122] Bouchiat, M. A. and Meunier, J. Spectre des fluctuations thermiques de la surface libre d'un liquide simple. *Journal de Physique*, 32(7):561–571, July 1971.

[123] Loudon, R. Theory of thermally induced surface fluctuations on simple fluids. *Proceedings of the Royal Society of London. A. Mathematical and Physical Sciences*, 372(1749):275–295, August 1980.

[124] Loudon, R. Liquid surface and interface waves. *Le Journal de Physique Colloques*, 45(C5):5–93, April 1984.

[125] Gross, M., Cates, M. E., Varnik, F., and Adhikari, R. Langevin theory of fluctuations in the discrete boltzmann equation. *Journal of Statistical Mechanics: Theory and Experiment*, 2011(03):P03030, March 2011.

[126] Smith, E. R., Müller, E. A., Craster, R. V., and Matar, O. K. A langevin model for fluctuating contact angle behaviour parametrised using molecular dynamics. *Soft Matter*, 12(48):9604–9615, December 2016.

[127] Mitsui, T. and Aoki, K. Measurements of liquid surface fluctuations at sub-shot-noise levels with michelson interferometry. *Physical Review E*, 87(4):042403, April 2013.

[128] Aoki, K. and Mitsui, T. Thermal interface fluctuations of liquids and viscoelastic materials. *Exp. Phys*, 2018(11):43–44, April 2018.

[129] Sudo, S. and Otsuka, K. Measurements of liquid surface fluctuations using a self-mixing solid-state laser. *Journal of Applied Physics*, 115(23):233103, June 2014.

[130] Goldstein, H. *Classical Mechanics*. Pearson Education, 2002. ISBN 9788177582833.

[131] Mei, C. C. and Liu, L. F. The damping of surface gravity waves in a bounded liquid. *Journal of Fluid Mechanics*, 59(2):239–256, June 1973.

[132] Henderson, D. M. and Miles, J. W. Surface-wave damping in a circular cylinder with a fixed contact line. *Journal of Fluid Mechanics*, 275:285–299, September 1994.

[133] MARTEL, C., NICOLÁS, J. A., and VEGA, J. M. Surface-wave damping in a brimful circular cylinder. *Journal of Fluid Mechanics*, 360:213–228, April 1998.

[134] MILES, J. W. and HENDERSON, D. M. A note on interior vs. boundary-layer damping of surface waves in a circular cylinder. *Journal of Fluid Mechanics*, 364:319–323, June 1998.

[135] Ibrahim, R. A. *Liquid Sloshing Dynamics: Theory and Applications*. Cambridge University Press, Cambridge, May 2005. ISBN 9780521838856.

[136] Miles, J. W. Surface-Wave Damping in Closed Basins. *Proceedings of the Royal Society of London Series A*, 297(1451):459–475, March 1967.

[137] Keulegan, G. H. Energy dissipation in standing waves in rectangular basins. *Journal of Fluid Mechanics*, 6(1):33–50, July 1959.

[138] Herrada, M. A., Montanero, J. M., and Vega, J. M. Surface wave damping. *Understanding Complex Systems*, pages 349–361, 2013.

[139] Ziener, C. H., Kurz, F. T., Buschle, L. R., and Kampf, T. Orthogonality, lommel integrals and cross product zeros of linear combinations of bessel functions. *SpringerPlus*, 4(1), August 2015.

[140] Dussan, E. B. On the spreading of liquids on solid surfaces: Static and dynamic contact lines. *Annual Review of Fluid Mechanics*, 11(1):371–400, January 1979.

[141] Cocciaro, B., Faetti, S., and Festa, C. Experimental investigation of capillarity effects on surface gravity waves: non-wetting boundary conditions. *Journal of Fluid Mechanics*, 246:43–66, January 1993.

[142] Hocking, L. M. The damping of capillary–gravity waves at a rigid boundary. *Journal of Fluid Mechanics*, 179:253–266, June 1987.

[143] Kidambi, R. Meniscus effects on the frequency and damping of capillary-gravity waves in a brimful circular cylinder. *Wave Motion*, 46(2):144–154, March 2009.

[144] Kidambi, R. Capillary damping of inviscid surface waves in a circular cylinder. *Journal of Fluid Mechanics*, 627:323–340, May 2009.

[145] Jiang, L., Perlin, M., and Schultz, W. W. Contact-line dynamics and damping for oscillating free surface flows. *Physics of Fluids*, 16(3):748–758, February 2004.

[146] Nguyem Thu Lam, K. D. and Caps, H. Effect of a capillary meniscus on the faraday instability threshold. *The European Physical Journal E 2011 34:10*, 34 (10):1–5, June 2011.

[147] Viola, F. and Gallaire, F. Theoretical framework to analyze the combined effect of surface tension and viscosity on the damping rate of sloshing waves. *Physical Review Fluids*, 3(9):94801, September 2018.

[148] Viola, F., Brun, P.-T., and Gallaire, F. Capillary hysteresis in sloshing dynamics: a weakly nonlinear analysis. *Journal of Fluid Mechanics*, 837:788–818, February 2018.

[149] Horstmann, G. M., Wylega, M., and Weier, T. Measurement of interfacial wave dynamics in orbitally shaken cylindrical containers using ultrasound pulse-echo techniques. *Experiments in Fluids*, 60(4):56, April 2019.

[150] Kofman, L., Linde, A., and Starobinsky, A. A. Towards the theory of reheating after inflation. *Physical Review D - Particles, Fields, Gravitation and Cosmology*, 56(6):3258–3295, September 1997.

[151] Berges, J. and Serreau, J. Parametric resonance in quantum field theory. *Physical Review Letters*, 91(11):111601, June 2003.

[152] Jaeger, H. M. and Liu, A. J. Far-From-Equilibrium Physics: An Overview. *arXiv e-prints*, art. arXiv:1009.4874, September 2010.

[153] Kovacic, I. and Cartmell, M. P. Special issue on parametric excitation: Applications in science and engineering:. *Proceedings of the Institution of Mechanical Engineers, Part C: Journal of Mechanical Engineering Science*, 226(8):1909–1911, June 2012.

[154] Miles, J. and Henderson, D. Parametrically forced surface waves. *Annual Review of Fluid Mechanics*, 22:143–165, January 1990.

[155] Miles, J. W. Resonantly forced surface waves in a circular cylinder. *Journal of Fluid Mechanics*, 149:15–31, December 1984.

[156] Ciliberto, S. and Gollub, J. P. Chaotic mode competition in parametrically forced surface waves. *Journal of Fluid Mechanics*, 158:381–398, September 1985.

[157] King, G. C. *Vibrations and Waves*. Manchester Physics Series. Wiley, June 2013. ISBN 9781118681787.

[158] French, A. P. *Vibrations and Waves*. M.I.T. introductory physics series. Taylor & Francis, December 1971. ISBN 9780748744473.

[159] Rashid, M. H. *Power Electronics Handbook*. Elsevier Science, 2011. ISBN 9780123820372.

[160] Proakis, J. G. *Digital Signal Processing: Principles, Algorithms, And Applications, 4/E*. Pearson Education, 2007. ISBN 9788131710005.

[161] ISO. *ISO 16063-21:2003 - Methods for the calibration of vibration and shock transducers – Part 21: Vibration calibration by comparison to a reference transducer*. International Organization for Standardization (ISO), August 2003.

[162] Harris, D. M. and Bush, J. W. Generating uniaxial vibration with an electrodynamic shaker and external air bearing. *Journal of Sound and Vibration*, 334: 255–269, January 2015.

[163] ISO. *ISO 80369-7:2021 - Small-bore connectors for liquids and gases in healthcare applications – Part 7: Connectors for intravascular or hypodermic applications*. International Organization for Standardization (ISO), May 2021.

[164] Jajoo, V. *Faraday instability in binary fluids*. Theses, Université de Bordeaux, December 2017.

[165] Scase, M. M., Baldwin, K. A., and Hill, R. J. A. Magnetically induced rayleigh-taylor instability under rotation: Comparison of experimental and theoretical results. *Physical Review E*, 102(4):43101, October 2020.

[166] Salabat, A. and Hashemi, M. Liquid-liquid equilibria for aliphatic alcohols + water + potassium carbonate systems; experiment and correlation. *Physics and Chemistry of Liquids*, 45(2):231–239, April 2007.

[167] Hansen, F. K. and Rødsrud, G. Surface tension by pendant drop: I. a fast standard instrument using computer image analysis. *Journal of Colloid and Interface Science*, 141(1):1–9, June 1991.

[168] Moisy, F., Rabaud, M., and Salsac, K. A synthetic schlieren method for the measurement of the topography of a liquid interface. *Experiments in Fluids*, 46 (6):1021–1036, June 2009.

[169] Takeda, M., Ina, H., and Kobayashi, S. Fourier-transform method of fringe-pattern analysis for computer-based topography and interferometry. *Journal of the Optical Society of America (1917-1983)*, 72(1):156, January 1982.

[170] Brigham, E. *The Fast Fourier Transform and Its Applications*, volume 26 of *Prentice-Hall Signal Processing Series: Advanced monographs*. Prentice Hall, February 1988. ISBN 9780133075052.

[171] Rioul, O. and Vetterli, M. Wavelets and signal processing. *IEEE Signal Processing Magazine*, 8(4):14–38, October 1991.

[172] Zinn-Justin, J. *Quantum Field Theory and Critical Phenomena: Fifth Edition*. International series of monographs on physics. Oxford University Press, 2021. ISBN 9780198834625.

[173] Marcinkiewicz, J. and Zygmund, A. On the summability of double fourier series. *Fundamenta Mathematicae*, 32:122–132, 1939.

[174] Douady, S. Experimental study of the faraday instability. *Journal of Fluid Mechanics*, 221(5):383–409, December 1990.

[175] Edwards, W. S. and Fauve, S. Patterns and quasi-patterns in the faraday experiment. *Journal of Fluid Mechanics*, 278(II):123–148, June 1994.

[176] Zhang, W. and Viñals, J. Square patterns and quasipatterns in weakly damped faraday waves. *Physical Review E*, 53(5):R4283, May 1996.

[177] Zhang, W. and Viñals, J. Pattern formation in weakly damped parametric surface waves. *Journal of Fluid Mechanics*, 336:301–330, June 1997.

[178] Chen, P. and Viñals, J. Amplitude equation and pattern selection in faraday waves. *Physical Review E*, 60(1):559, June 1999.

[179] Chen, P. Nonlinear wave dynamics in faraday instabilities. *Physical Review E*, 65(3):36308, June 2002.

[180] Garih, H., Estivalezes, J. L., and Casalis, G. On the transient phase of the faraday instability. *Physics of Fluids*, 25(12):124104, June 2013.

[181] Gonçalves, F. A. and Kestin, J. The viscosity of na2co3 and k2co3 aqueous solutions in the range 20–60°c. *International Journal of Thermophysics*, 2(4): 315–322, December 1981.

[182] Khattab, I. S., Bandarkar, F., Fakhree, M. A. A., and Jouyban, A. Density, viscosity, and surface tension of water+ethanol mixtures from 293 to 323k. *Korean Journal of Chemical Engineering*, 29(6):812–817, June 2012.

[183] Salabat, A. and Hashemi, M. Temperature effect on the liquid-liquid equilibria for some aliphatic alcohols + water + k2co3 systems. *Journal of Chemical and Engineering Data*, 51(4):1194–1197, July 2006.

[184] Villers, D. and Platten, J. K. Temperature dependence of the interfacial tension between water and long-chain alcohols. *The Journal of Physical Chemistry*, 92 (14):4023–4024, July 1988.

[185] Zache, T. V., Kasper, V., and Berges, J. Inflationary preheating dynamics with two-species condensates. *Physical Review A*, 95(6):063629, June 2017.

[186] Robertson, S., Michel, F., and Parentani, R. Nonlinearities induced by parametric resonance in effectively 1d atomic bose condensates. *Physical Review D*, 98(5): 056003, September 2018.

[187] Tipton, C. R. and Mullin, T. An experimental study of faraday waves formed on the interface between two immiscible liquids. *Physics of Fluids*, 16(7):2336–2341, May 2004.

[188] Butera, S. and Carusotto, I. Numerical studies of back reaction effects in an analog model of cosmological preheating. *Physical Review Letters*, 130:241501, June 2023.

[189] Wang, Z. Review of real-time three-dimensional shape measurement techniques. *Measurement*, 156:107624, May 2020.

[190] Gomit, G., Chatellier, L., and David, L. Free-surface flow measurements by non-intrusive methods: a survey. *Experiments in Fluids*, 63(6):94, June 2022.

[191] Takeda, M. and Mutoh, K. Fourier transform profilometry for the automatic measurement of 3-d object shapes. *Applied Optics*, 22(24):3977, December 1983.

[192] Cobelli, P. J., Maurel, A., Pagneux, V., and Petitjeans, P. Global measurement of water waves by fourier transform profilometry. *Experiments in fluids*, 46(6): 1037–1047, June 2009.

[193] Przadka, A., Cabane, B., Pagneux, V., Maurel, A., and Petitjeans, P. Fourier transform profilometry for water waves: how to achieve clean water attenuation with diffusive reflection at the water surface? *Experiments in fluids*, 52:519–527, February 2012.

[194] Tahara, T., Quan, X., Otani, R., Takaki, Y., and Matoba, O. Digital holography and its multidimensional imaging applications: a review. *Microscopy*, 67(2):55–67, 02 2018.

[195] Yu, X., Hong, J., Liu, C., and Kim, M. K. Review of digital holographic microscopy for three-dimensional profiling and tracking. *Optical Engineering*, 53 (11):112306, April 2014.

[196] Su, X. and Chen, W. Fourier transform profilometry:: a review. *Optics and lasers in Engineering*, 35(5):263–284, May 2001.

[197] SUTHERLAND, B. R., DALZIEL, S. B., HUGHES, G. O., and LINDEN, P. F. Visualization and measurement of internal waves by 'synthetic schlieren'. part 1. vertically oscillating cylinder. *Journal of Fluid Mechanics*, 390:93–126, July 1999.

[198] Schardin, H. *Die Schlierenverfahren und ihre Anwendungen*, volume 20, pages 303–439. Springer Berlin Heidelberg, Berlin, Heidelberg, December 1942. ISBN 978-3-540-77207-1.

[199] Burton, R. A. A modified schlieren apparatus for large areas of field. *J. Opt. Soc. Am.*, 39(11):907–908, November 1949.

[200] Fifer, Z. *Analog cosmology with two-fluid systems*. PhD thesis, University of Nottingham, July 2022.

[201] Mcclellan, J. H. and Parks, T. W. A unified approach to the design of optimum fir linear-phase digital filters. *IEEE Transactions on Circuit Theory*, 20(6):697 – 701, 1973. Cited by: 216.

[202] Herráez, M. A., Burton, D. R., Lalor, M. J., and Gdeisat, M. A. Fast two-dimensional phase-unwrapping algorithm based on sorting by reliability following a noncontinuous path. *Applied Optics*, 41(35):7437–7444, December 2002.

[203] Zhang, X. An algorithm for calculating water surface elevations from surface gradient image data. *Experiments in fluids*, 21(1):43–48, May 1996.

[204] Gabor, D. A new microscopic principle. *Nature*, 161(4098):777–778, May 1948.

[205] Gabor, D. Microscopy by reconstructed wave-fronts. *Proceedings of the Royal Society of London. Series A. Mathematical and Physical Sciences*, 197(1051): 454–487, July 1949.

[206] Gabor, D. Microscopy by reconstructed wave fronts: Ii. *Proceedings of the Physical Society. Section B*, 64(6):449–469, June 1951.

[207] Schnars, U. and Jüptner, W. Direct recording of holograms by a ccd target and numerical reconstruction. *Applied Optics*, 33(2):179–181, January 1994.

[208] Leith, E. N. and Upatnieks, J. Reconstructed wavefronts and communication theory∗. *Josa*, 52(10):1123–1130, October 1962.

[209] Cuche, E., Bevilacqua, F., and Depeursinge, C. Digital holography for quantitative phase-contrast imaging. *Optics Letters*, 24(5):291–293, March 1999.

[210] Shaked, N. T., Micó, V., Trusiak, M., Kuś, A., and Mirsky, S. K. Off-axis digital holographic multiplexing for rapid wavefront acquisition and processing. *Advances in Optics and Photonics*, 12(3):556–611, September 2020.

[211] Dardikman, G. and Shaked, N. T. Is multiplexed off-axis holography for quantitative phase imaging more spatial bandwidth-efficient than on-axis holography? *Journal of the Optical Society of America A*, 36(2):A1, February 2019.

[212] Z. Huang, L. C. High bandwidth-utilization digital holographic multiplexing: An approach using kramers–kronig relations. *Advanced Photonics Research*, 3(2): 2100273, 2022.

[213] Rubin, M., Dardikman, G., Mirsky, S. K., Turko, N. A., and Shaked, N. T. Six-pack off-axis holography. *Optics Letters*, 42(22):4611, November 2017.

[214] Sha, B., Liu, X., Ge, X.-L., and Guo, C.-S. Fast reconstruction of off-axis digital holograms based on digital spatial multiplexing. *Optics Express*, 22(19): 23066–23072, September 2014.

[215] Kühn, J., Colomb, T., Montfort, F., Charrière, F., Emery, Y., Cuche, E., Marquet, P., and Depeursinge, C. Real-time dual-wavelength digital holographic microscopy with a single hologram acquisition. *Optics express*, 15(12):7231–7242, June 2007.

[216] Yuan, C., Situ, G., Pedrini, G., Ma, J., and Osten, W. Resolution improvement in digital holography by angular and polarization multiplexing. *Applied Optics*, 50(7):B6–b11, March 2011.

[217] Colomb, T., Krivec, S., Hutter, H., Akatay, A. A., Pavillon, N., Montfort, F., Cuche, E., Kühn, J., Depeursinge, C., and Emery, Y. Digital holographic reflectometry. *Opt. Express*, 18(4):3719–3731, February 2010.

[218] Colomb, T. and Emery, Y. Digital holographic reflectometry for semi-transparent multilayers topography measurement. In *2012 International Symposium on Optomechatronic Technologies (ISOT 2012)*, pages 1–2. IEEE, October 2012.

[219] Lahiri, A. *Basic Optics: Principles and Concepts*. Elsevier Science, 2016. ISBN 9780128053577.

[220] Pereyra, P. and Robledo-Martinez, A. On the equivalence of the summation and transfer-matrix methods in wave propagation through multilayers of lossless and lossy media. *European Journal of Physics*, 30(2):393, February 2009.

[221] Kim, M. K. Principles and techniques of digital holographic microscopy. *SPIE Reviews*, 1(1):018005, April 2010.

[222] Jolliffe, I. T. Principal component analysis: a beginner's guide–i. introduction and application. *Weather*, 45(10):375–382, October 1990.

[223] Jolliffe, I. *Principal Component Analysis*. Springer Series in Statistics. Springer New York, October 2013. ISBN 9781475719048.

[224] Sundararajan, D. *Digital image processing: a signal processing and algorithmic approach*. Springer, 2017. ISBN 9789811061127.

[225] Daimon, M. and Masumura, A. Measurement of the refractive index of distilled water from the near-infrared region to the ultraviolet region. *Appl. Opt.*, 46(18): 3811–3820, June 2007.

[226] Moutzouris, K., Papamichael, M., Betsis, S. C., Stavrakas, I., Hloupis, G., and Triantis, D. Refractive, dispersive and thermo-optic properties of twelve organic solvents in the visible and near-infrared. *Applied Physics B*, 116:617–622, September 2014.

[227] Hisatake, K., Fukuda, M., Kimura, J., Maeda, M., and Fukuda, Y. Experimental and theoretical study of evaporation of water in a vessel. *Journal of applied physics*, 77(12):6664–6674, June 1995.

[228] Hisatake, K., Tanaka, S., and Aizawa, Y. Evaporation rate of water in a vessel. *Journal of applied physics*, 73(11):7395–7401, June 1993.

[229] Mackay, D. and van Wesenbeeck, I. Correlation of chemical evaporation rate with vapor pressure. *Environmental science & technology*, 48(17):10259–10263, September 2014.

[230] Parker, L. and Toms, D. *Quantum Field Theory in Curved Spacetime: Quantized Fields and Gravity*. Cambridge Monographs on Mathematical Physics. Cambridge University Press, September 2009. ISBN 9780521877879.

[231] Atkins, K. R. Third and fourth sound in liquid helium ii. *Physical Review*, 113 (4):962–965, February 1959.

[232] Unruh, W. G. Black holes, acceleration temperature and low temperature analog experiments. *J. Low Temp. Phys.*, 208(1-2):196–209, July 2022.

[233] Kapitza, P. Viscosity of liquid helium below the $\l ambda$-point. *Nature*, 141 (3558):74, January 1938.

[234] Mc McClintock, P. V. E., Meredith, D. J., and Wigmore, J. K. *Liquid helium-4*, pages 151–189. Springer Netherlands, Dordrecht, 1992. ISBN 978-94-011-2276-4.

[235] Tilley, D. R. and Tilley, J. *Superfluidity and Superconductivity*. Adam Hilger, Bristol, July 1990. ISBN 9780203737897.

[236] Everitt, C. W., Atkins, K. R., and Denenstein, A. Third Sound in Liquid Helium Films. *Physical Review*, 136(6A):1494–1499, December 1964.

[237] Atkins, K. and Rudnick, I. Chapter 2 third sound. volume 6 of *Progress in Low Temperature Physics*, pages 37–76. Elsevier, 1970.

[238] Schechter, A. M. R., Simmonds, R. W., Packard, R. E., and Davis, J. C. Observation of 'third sound' in superfluid ^{3}He. *Nature*, 396(6711):554–557, December 1998.

[239] White, I. *Third Sound in Thin Film Superfluid ^{3}He*. PhD thesis, University of Manchester, 2006.

[240] Roche, P., Deville, G., Keshishev, K. O., Appleyard, N. J., and Williams, F. I. B. Low damping of micron capillary waves on superfluid ^{4}he. *Physical Review Letters*, 75(18):3316–3319, October 1995.

[241] Sabisky, E. S. and Anderson, C. H. Onset for superfluid flow in He^4 films on a variety of substrates. *Physical Review Letters*, 30:1122–1125, May 1973.

[242] Sabisky, E. S. and Anderson, C. H. Verification of the lifshitz theory of the van der waals potential using liquid-helium films. *Physical Review A*, 7:790–806, February 1973.

[243] DZYALOSHINSKII, I., LIFSHITZ, E., PITAEVSKII, L., and Priestley, M. 34 - the general theory of van der waals forces – reprinted with permission from advances in physics 10, part 38, 165, 1961. In Pitaevski, L., editor, *Perspectives in Theoretical Physics*, pages 443–492. Pergamon, Amsterdam, 1992. ISBN 978-0-08-036364-6.

[244] Rutledge, J. E., McMillan, W. L., Mochel, J. M., and Washburn, T. E. Third sound, two-dimensional hydrodynamics, and elementary excitations in very thin helium films. *Physical Review B*, 18:2155–2168, September 1978.

[245] Andronikashvili, E. E11 - a direct observation of two kinds of motion in helium ii**j. phys. (u.s.s.r.) 10, 201 (1946). In Galasiewicz, Z. M., editor, *Helium 4*, pages 154–165. Pergamon, 1971. ISBN 978-0-08-015816-7.

[246] Brouwer, P. W., Draisma, W. A., van Beelen, H., and Jochemsen, R. On the propagation of third sound in 4he films. *Physica B: Condensed Matter*, 215(2): 135–152, October 1995.

[247] Agarwal, G. S. and Jha, S. S. Theory of optomechanical interactions in superfluid he. *Physical Review A*, 90(2):23812, August 2014.

[248] Shkarin, A. *Quantum Optomechanics with Superfluid Helium*. PhD thesis, Yale University, 2018.

[249] Harris, G. I., McAuslan, D. L., Sheridan, E., Sachkou, Y., Baker, C., and Bowen, W. P. Laser cooling and control of excitations in superfluid helium. *Nature Phys.*, 12(8):788–793, August 2016.

[250] Stratton, J. *Electromagnetic Theory*. Swedenborg Press, October 2010. ISBN 9781446517390.

[251] Biermann, S., Erne, S., Gooding, C., Louko, J., Schmiedmayer, J., Unruh, W. G., and Weinfurtner, S. Unruh and analogue unruh temperatures for circular motion in 3+1 and 2+1 dimensions. *Physical Review D*, 102(8):85006, October 2020.

[252] Merzbacher, E. *Quantum Mechanics*, volume 69. Wiley, January 1998. ISBN 9780471887027.

[253] Hoffmann, J. A., Penanen, K., Davis, J. C., and Packard, R. E. Measurements of attenuation of third sound: Evidence of trapped vorticity in thick films of superfluid 4 he. *J. Low Temp. Phys.*, 135:177–202, May 2004.

[254] Kashkanova, A. D. *Optomechanics with Superfluid Helium*. PhD thesis, Yale University, 2017.

[255] Walls, D. F. and Milburn, G. J. *Quantum Optics*. Springer, 2008. ISBN 9783540285731.

[256] Stefszky, M. S., Mow-Lowry, C. M., Chua, S. S. Y., Shaddock, D. A., Buchler, B. C., Vahlbruch, H., Khalaidovski, A., Schnabel, R., Lam, P. K., and McClelland, D. E. Balanced homodyne detection of optical quantum states at audio-band frequencies and below. *Class. Quantum Grav.*, 29(14):145015, June 2012.